

Quantitative Measures for Gastrointestinal MRI

by

Hannah Grace Williams, M.Phys

Thesis submitted to
The University of Nottingham
for the degree of
Doctor of Philosophy

September 2019

Abstract

The use of Magnetic Resonance Imaging (MRI) as both a clinical and research tool has increased substantially over the last 40 years. However, one area of use that has seen a smaller benefit from this increase is the structure and function of the gastrointestinal system. Faster acquisition methods and improved computer analysis techniques now mean that measures that are routinely made outside of the abdomen can start to be utilised in the gastrointestinal system.

The aim of this thesis was to address key gaps in the availability of quantitative measures in the gastrointestinal system using MRI. Whilst there are many challenges that could have been addressed, three areas which all relate to inflammatory gastrointestinal diseases were chosen.

The first relates to the lymphatic system which plays an essential role in all inflammatory diseases. Quantitative measures of the lymphatic system in the abdomen could provide further insight into GI diseases. In this thesis methods to visualise the abdominal lymph nodes were developed and significant differences between the lymph nodes in patients with inflammatory gastrointestinal disease and healthy volunteers were measured.

The second area of focus was the bowel wall which is implicated in many inflammatory gastrointestinal diseases. Its relatively small size and unpredictable motion have meant that common MRI measures such as T1 and T2 have never been made in the non-enlarged bowel wall. In this thesis T2 was shown to correlate with the current standard measures of bowel wall permeability providing a new non-invasive method of investigating the structure of the bowel wall.

The third and final area was the quantification of fat in the abdomen. Whilst this topic has largely been tackled in the liver at low field strengths the confounding factors that effect its measurement have not been taken into account outside the liver or at higher field strengths. The current methods of fat quantification were tested and found to not be appropriate for use in the colon at 3T due to the large field inhomogeneities present. The first *in vivo* fat quantification maps at 7T were generated using in-house fitting methods which was found to perform better than the current vendor product for fat quantification.

Bringing these three topics together provides a good starting block for tackling the deficiencies currently present in quantitative GI MRI and the tools developed throughout this thesis will be applicable across many diseases that impact the gastrointestinal system.

Contents

1	Introduction	13
1.1	Overview of Thesis	13
2	MRI Theory	16
2.1	Nuclear Magnetic Resonance	16
2.1.1	Spin and Nuclear Magnetism	16
2.1.2	Nuclei in an External Magnetic Field	17
2.1.3	Bulk Magnetism	20
2.1.4	Excitation	22
2.1.5	Relaxation and the Free Induction Decay	24
2.1.6	T1 Relaxation	26
2.1.7	T2 Relaxation	27
2.1.8	T2* Relaxation	30
2.1.9	Correlation Time	31
2.1.10	Chemical Shift	33
2.1.11	Susceptibility	34
2.2	Magnetic Resonance Image Encoding	34
2.2.1	Slice Selection	35
2.2.2	Frequency Encoding	36
2.2.3	Phase Encoding	38
2.2.4	k Space	39
2.2.5	Partial Fourier Imaging	42
2.2.6	Parallel Imaging	42
2.2.7	Multiband Imaging	45
2.3	Magnetic Resonance Image Acquisition Schemes	45
2.3.1	Turbo Spin Echo	45
2.3.2	Echo Planar Imaging	46
2.3.3	Gradient Echoes and Steady State Imaging	49
2.3.4	Spoiled Gradient Echo (FLASH)	51

2.3.5	Balanced Turbo Field Echo (bTFE)	53
2.3.6	Diffusion Weighted Imaging	55
2.3.7	Spectroscopy	60
2.3.8	Fat Suppression Techniques	61
2.3.9	Dixon Imaging	65
2.3.10	Field Mapping	67
2.4	Conclusion of Chapter	69
3	The Gastrointestinal System	73
3.1	Introduction	73
3.2	Ingestion and the Stomach	73
3.3	The Liver	74
3.4	The Gall Bladder and the Pancreas	75
3.5	The Small Intestine	75
3.6	The Large Intestine	76
3.7	The Structure of the GI Tract	77
3.8	Diseases of the GI Tract	78
3.8.1	Coeliac Disease	78
3.8.2	Crohn's Disease	78
3.8.3	Diverticulitis	79
3.8.4	Helicobacter Pylori	80
3.8.5	Hepatitis B and C	81
3.8.6	Liver Cirrhosis	81
3.9	The Lymphatic System	82
3.10	Conclusion of Chapter	85
4	Abdominal Lymph Nodes	91
4.1	Introduction	91
4.2	Lymph Nodes in Disease	92
4.3	Lymph Nodes and MRI	93
4.4	Development of MRI of Abdominal Lymph Nodes	98
4.4.1	Abdominal Nodes at 1.5T	98

4.4.2	Pelvic Nodes at 3T	100
4.4.3	Abdominal Nodes at 3T	102
4.5	Measuring Healthy Abdominal Lymph Nodes	105
4.5.1	Study Design and Healthy Volunteer Cohort	106
4.5.2	Scanning Protocol	106
4.5.3	Analysis Methods	107
4.5.4	Results	110
4.5.5	Discussion	113
4.6	Measuring Lymph Nodes in GI Diseases	114
4.6.1	Cohort and Study Design	115
4.6.2	MAL Protocol	117
4.6.3	Analysis	117
4.6.4	Results	119
4.6.5	Inter Observer Reproducibility	127
4.7	Discussion	130
4.8	Conclusion	132
5	Bowel Wall and the PerMinH Study	138
5.1	Introduction	138
5.2	Measuring Bowel Wall Permeability	140
5.3	MRI and the Bowel Wall	141
5.4	Study Overview and Design	142
5.4.1	Study Objectives	143
5.4.2	Study Design	143
5.4.3	Studied Cohort	145
5.4.4	PerMinH Imaging Protocol	147
5.4.5	Lactulose:Mannitol Ratio Test	149
5.5	Calculating T1 and T2 of the Small Bowel Wall	149
5.5.1	Motion Correction	150
5.5.2	Masking the Bowel	154
5.5.3	Creating a Mask of the Bowel Wall	159
5.5.4	Manual Quality Control Step	164

5.5.5	Fitting to the Data	166
5.5.6	Bowel Wall Segment Size	169
5.6	PerMinH Results	172
5.6.1	T1	172
5.6.2	T2	173
5.7	Inter Observer and Intra Subject Reproducibility	179
5.8	Discussion of PerMinH	182
5.9	Improving on the PerMinH Study Design	185
5.9.1	Optimising Inversion Times to Measure T1	186
5.9.2	Discussion	190
5.10	Conclusion and future work	190
6	Fat Quantification using Multi-Echo MRI in Non Standard Situations	199
6.1	Introduction	199
6.2	Quantification using the Dixon Method	201
6.2.1	Two Point Dixon	201
6.2.2	Three Point Dixon	202
6.2.3	Multi-Echo Dixon	203
6.3	Methods	211
6.3.1	General Simulation Method	212
6.3.2	General <i>In Vivo</i> Methods	215
6.3.3	Simulations for the Liver a 3T	216
6.3.4	Fat Phantom Measurements at 3T	217
6.3.5	Liver Fat Measurements at 3T	218
6.3.6	Simulations for the Liver at 7T	219
6.3.7	Liver Fat Measurements at 7T	220
6.3.8	Simulations for the Colon at 3T	221
6.3.9	Colonic Fat Measurements at 3T	222
6.4	Results	222
6.4.1	Simulations in the Liver a 3T	223
6.4.2	Fat Phantom Measurements at 3T	228

Contents

6.4.3	<i>In Vivo Liver Fat Measurements at 3T</i>	229
6.4.4	Simulations for the Liver at 7T	234
6.4.5	<i>In Vivo Liver Fat Measurements at 7T</i>	237
6.4.6	Simulations for the Colon at 3T	242
6.4.7	<i>In Vivo Colonic Fat Measurements at 3T</i>	244
6.5	Discussion	246
6.6	Conclusion	249
7	Conclusions	259
7.1	Future Work	261

Acknowledgements

Firstly I would like to thank my supervisors Professor Penny Gowland and Dr Luca Marciani without their support, guidance and encouragement this thesis would not have been possible. I would also like to thank Dr Caroline Hoad from whom I have learnt everything that I needed to know over the last four years. I would also like to thank my colleagues at the Nottingham Digestive Diseases Centre for their invaluable knowledge and the assistance that they have given. Secondly I would like to thank my friends at the SPMIC (with an extra special thanks to the below the neck team) for providing the most enjoyable working environment that could be imagined. A mention must be given to Dr Andrew Peters, I'm sorry that I broke so many things and my appreciation for your help in fixing them is endless. Likewise I would like to thank Chris Bradley for answering the phone every time I had a problem with the scanner and helping me without hesitation. A thesis acknowledgement is not complete without thanking Lesley, without whom the centre would be lost. A special thanks goes to Emma for being the most supportive office pal that anyone could ask for, and for making the long days, late nights and weekends enjoyable. I would also like to thank Charlotte for every tea break and Portland walk, for every pity party and white wine spritzer that we have shared, I couldn't have done it without you.

Outside of work I would like to thank the Postgraduate netball team. Every training session, match and doughnut has helped me through the hardest stages of this process. I must also thank my friends further afield, Aimee, Emily, Jen and Liz for being the best group of intelligent and inspirational friends that anyone could ask for and for their friendship and support from the start of this process right through until the end.

I would also like to thank my family for listening and nodding along for these last few years even when you weren't sure what I was talking about. Your unwavering faith in me has got me where I am today, and for that I will forever be grateful.

My last thank you is to Jamie, for all your encouragement, advice, love and support but most importantly for all the bolognese, meatballs and burgers you

Contents

have made me over the last four years.

Abbreviations

ADC Apparent Diffusion Coefficient

bFFE Balanced Fast Field Echo

bTFE Balanced Turbo Field Echo

BRC Biomedical Research Centre

CE Contrast Enhanced

CHESS CHEmical Shift Selective pulse

CLE Confocal Laser Endoscopy

CT Computed Tomography

CF Cystic Fibrosis

DREAM Dual Refocusing Echo Acquisition Mode

DWI Diffusion Weighted Imaging

DWIBS Diffusion Weighted whole body Imaging with Background body Suppression

ECM Extra Cellular Matrix

EPI Echo Planer Imaging

ETL Echo Train Length

FSE Fast Spin Echo

FFE Fast Field Echo

FLASH Fast Low Angle SHot

FISP Fast Imaging with Steady state free Precession

FID Free Induction Decay

GI GastroIntestinal

GRAPPA GeneRalized Auto-calibrating Partial Parallel Acquisition

HASTE Half-fourier Acquisition Single-shot Turbo spin Echo

HIV Human Immunodeficiency Viruses

HV Healthy Volunteer

IBD Irritable Bowel Disease

IBS Irritable Bowel Syndrome

IDEAL Iterative Decomposition of water and fat with Echo Asymmetry and Least-squares estimation

IP In Phase
LMR Lactulose Mannitol Ratio
MaRIA Magnetic Resonance Index of Activity
MRI Magnetic Resonance Imaging
MRL Magnetic Resonance Lymphangiography
MRS Magnetic Resonance Spectroscopy
NAFLD Non-Alcoholic Fatty Liver Disease
NMR Nuclear Magnetic Resonance
OP Opposed Phase
PDFF Proton Density Fat Fraction
PIS Patient Information Sheet
RF Radio Frequency
ROI Region Of Interest
SAR Specific Absorption Rate
SENSE SENSitivity Encoding
SNR Signal to Noise Ratio
SSH-TSE Single SHot Turbo Spin Echo
STARD STAndards of Reporting of Diagnostic Accuracy
STIR Short TI Inversion Recovery
TE Echo Time
TR Repetition Time
TSE Turbo Spin Echo

1 Introduction

Gastrointestinal (GI) diseases are a major burden on the UK health care system with around 1 in 6 hospital admissions and 1 in 6 surgical procedures relating to gastrointestinal diseases. GI diseases also have a huge impact on the quality of life of patients with symptoms ranging from mild abdominal pain to malnutrition and severe pain. The incidences of most gastrointestinal diseases are increasing in the UK (1). Currently there is a lack of non-invasive methods to study and monitor gastrointestinal diseases with patients undergoing endoscopies, colonoscopies and biopsies in order to be diagnosed and monitored.

Magnetic Resonance Imaging (MRI) has the potential to meet the shortfall in non-invasive methods to diagnose, assess and research gastrointestinal diseases. Hardware deficiencies meant that initially radio frequency (RF) drop out was common in the centre of the abdomen until dual transmit systems were introduced. Despite this being resolved quantitative MRI measures of the structure of the GI system fall far behind their counterparts based outside of the abdomen. This is probably due to the increased difficulty in the acquisition and analysis of images from the abdomen because of respiratory motion and peristalsis.

The overall aim of this thesis was to develop quantitative MRI measures of the gastrointestinal system which are applicable to a range of gastrointestinal diseases and where possible to investigate the variation of these measures between healthy volunteers and patients.

1.1 Overview of Thesis

Chapter 2 provides the theoretical background required for the work carried out in this thesis. It covers the principles of Nuclear Magnetic Resonance (NMR), Magnetic Resonance Imaging and the image acquisition methods used throughout this thesis.

Chapter 3 provides the medical background relevant to this thesis. Included is a description of the gastrointestinal system, its structure and function and a

basic description of the GI diseases investigated throughout this thesis.

Chapter 4 provides details of experimental work that was aimed at developing quantitative measures of the lymph nodes in the abdomen and the optimisation of the acquisition techniques used. The chapter details the first quantitative measures of the abdominal lymph nodes that have been acquired in healthy volunteers. It then progresses to detail a patient study that compared quantitative measures of lymph nodes between healthy volunteers and patients with a range of gastrointestinal diseases.

Chapter 5 describes the first quantitative T1 and T2 measures of the healthy bowel wall. The main focus of the chapter was not the acquisition of the images, which is relatively straight forward, but the development of an automated analysis package which could serve as a clinical tool to make T1 and T2 measurements of the bowel wall. The developed programme was used in a healthy volunteer provocation study aimed at measuring small changes in the bowel wall and in a follow up study measuring the inter observer and intra subject reproducibility of these measures.

Chapter 6 describes the use of fat quantification in regions which do not fall into the target areas for vendor fat quantification products which are optimised to work mainly in the liver at 1.5T and 3T. Outside of the liver and at higher field strengths it is unlikely that vendor products use fully optimised algorithms which could result in a decreased accuracy in fat quantification. Two key areas were selected for fat quantification, the liver at 7T and the colon at 3T. Monte Carlo simulations were used to test currently used liver fat quantification methods at 3T and 7T. The aim of the simulations was to determine whether currently used methods and the assumptions that accompany them can be made in more difficult to image areas such as the colon at 3T and in the liver at 7T. The first *in vivo* liver fat quantification at 7T is presented along with preliminary *in vivo* measurements of colonic fat at 3T.

Chapter 7 summarises the experimental work and key findings presented in this thesis and the future work that will stem from this thesis is discussed.

References

- [1] J G Williams, S E Roberts, M F Ali, W Y Cheung, D R Cohen, G Demery, A Edwards, M Greer, M D Hellier, H A Hutchings, B Ip, M F Longo, I T Russell, H A Snooks, and J C Williams. Gastroenterology Services in the UK. The Burden of Disease, and the Organisation and Delivery of Services for Gastrointestinal and Liver Disorders: A Review of the Evidence. *Gut*, 56(suppl 1):1–113, feb 2007. ISSN 0017-5749. doi: 10.1136/GUT.2006.117598.

2 MRI Theory

2.1 Nuclear Magnetic Resonance

Nuclear Magnetic Resonance (NMR) was first described by Bloch and Purcell in 1946 (1, 2). NMR describes the interaction of a nucleus with an external magnetic field. For their work they were both awarded the Nobel Prize for Physics in 1952. Lauterbur and Mansfield later went on to apply the principles of NMR to the field of medicine, bringing about a new medical imaging technique, Magnetic Resonance Imaging (MRI), which in 2003 won them the Nobel Prize in Medicine (3, 4). This chapter firstly describes the basic principles of NMR and how these are used to produce magnetic resonance images. The MRI techniques that are used in the experimental chapters of this thesis are also described.

2.1.1 Spin and Nuclear Magnetism

NMR describes the interaction between a nucleus, which possesses an intrinsic property called spin, with an external magnetic field. A nucleus with a spin, \mathbf{I} , is said to have a spin angular momentum, \mathbf{J} , which can be calculated as

$$\mathbf{J} = \hbar\sqrt{\mathbf{I}(\mathbf{I} + 1)} \quad (2.1)$$

where here \hbar is $h/2\pi$, where h is Plank's constant.

Both \mathbf{J} and \mathbf{I} are quantum numbers with \mathbf{I} being restricted to integer, or half integer values. Paired nucleons within a nucleus cancel each other out, therefore only nuclei with an odd number of protons or neutrons possess an overall non-zero spin. For a proton $\mathbf{I} = 1/2$. As protons are charged the spin angular momentum produces a magnetic moment $\boldsymbol{\mu}$,

$$\boldsymbol{\mu} = \gamma\mathbf{J}. \quad (2.2)$$

where γ is the gyromagnetic ratio of the nucleus and is dependent on the charge

and mass of the nuclei. In classical physics γ is calculated as

$$\gamma = \frac{q}{2m}. \quad (2.3)$$

Due to its high abundance in the human body the hydrogen nucleus is used to generate the majority of magnetic resonance (MR) images. It has a gyromagnetic ratio of 42.58 MHzT^{-1} , the highest of any nucleus. Another commonly used nucleus in the body is sodium which has a gyromagnetic ratio of 11.27 MHzT^{-1} . A high gyromagnetic ratio gives a high signal to noise ratio in an MR image. All work in this thesis uses ^1H protons.

2.1.2 Nuclei in an External Magnetic Field

Without the presence of an external magnetic field spins are randomly orientated which, in large spin systems, produces a net magnetization of zero. However, when an external magnetic field is applied the spins either align along the direction of the external field (parallel) or against it (anti-parallel) (Figure 2.1).

The magnetic dipole moment, as described by the quantum model, has a restricted number of orientations limited by its spin quantum number m_I . The number of orientations is given by $2I + 1$, for example a nucleus with spin I can take on the values $m_I = -I, (-I+1), (-I+2), \dots, 0, \dots, (I-2), (I-1), I$. Therefore for a hydrogen nucleus with spin number $I = 1/2$, two orientations exist, $m_I = +1/2$ or $m_I = -1/2$.

Using m_I the angular momentum of the spin in an external field, μ_z , is calculated as

$$\mu_z = \gamma \hbar m_I \quad (2.4)$$

where z is the direction of the external magnetic field B_0 . This gives rise to two possible angular momentum states in which hydrogen nuclei can exist: $\mu_z = +1/2$ giving $\boldsymbol{\mu} = +\gamma \hbar / 2 \hat{z}$, or $\mu_z = -1/2$ giving $\boldsymbol{\mu} = -\gamma \hbar / 2 \hat{z}$.

In an external magnetic field both these states have an energy associated

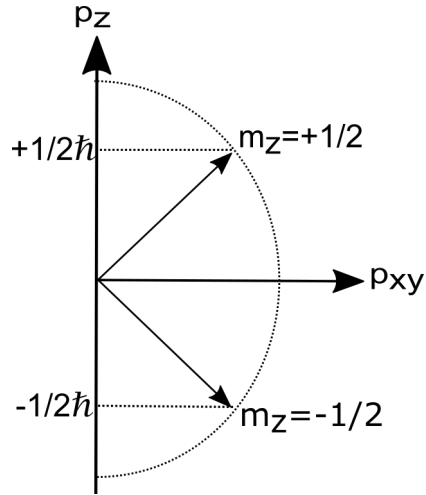


Figure 2.1: In an external magnetic field spins can exist in the up state where $m_z = +1/2$ or in the down state where $m_z = -1/2$.

with them which is calculated as

$$E = -\boldsymbol{\mu} \cdot \mathbf{B}. \quad (2.5)$$

In MRI the external field, B_0 , is applied in the z direction, giving

$$E = -\mu_z B_0 = -\gamma \hbar m_I B_0. \quad (2.6)$$

The spins aligned along the magnetic field have a lower energy than those that are aligned against the field and thus an energy difference, ΔE , exists between the two states.

$$\Delta E = \gamma \hbar B_0. \quad (2.7)$$

The spins will tend to exist in the lower energy state, and it is the difference in the number of spins between the low and high energy states that gives rise to the bulk magnetism which is utilised in magnetic resonance imaging.

As the nuclei have an angular momentum, they experience a torque, $\boldsymbol{\tau}$, when placed in an external magnetic field \mathbf{B} , which is given by

$$\boldsymbol{\tau} = \boldsymbol{\mu} \times \mathbf{B}. \quad (2.8)$$

2. MRI Theory

The torque is equal to the change in angular momentum over time,

$$\boldsymbol{\tau} = \frac{d\mathbf{J}}{dt} \quad (2.9)$$

which can also be expressed as

$$\boldsymbol{\tau} = \frac{d\mathbf{J}}{dt} = \boldsymbol{\mu} \times \mathbf{B} = \gamma \mathbf{J} \times \mathbf{B} = \gamma \mathbf{J} B_0 \sin\theta. \quad (2.10)$$

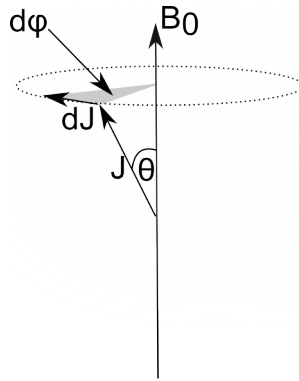


Figure 2.2: Mechanics of the spins in the up state where the angular momentum vector \mathbf{J} oscillates around the direction of the external magnetic field, B_0 . The change in momentum is given by $d\mathbf{J}$ and the change in angle of the vector is given by $d\phi$.

From the geometry in Figure 2.2 it can be shown that

$$d\mathbf{J} = \mathbf{J} \sin\theta d\phi. \quad (2.11)$$

The precessional frequency, ω , is given by the rate of change in ϕ ,

$$\omega = \frac{d\phi}{dt} \quad (2.12)$$

which when combined with Equations 2.10 and 2.11 gives

$$\omega = \gamma B_0. \quad (2.13)$$

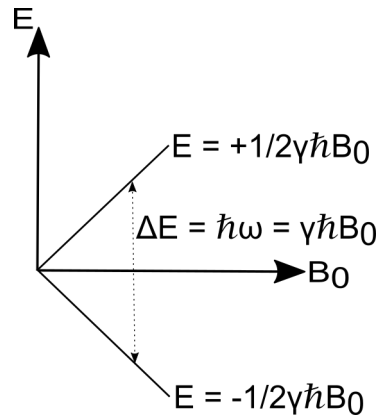


Figure 2.3: Energy level diagram for a proton in an external magnetic field, B_0 .

This rate of precession can also be calculated from the energy difference between the two states (Figure 2.3). Using Planck's equation

$$\Delta E = \hbar\omega \quad (2.14)$$

and

$$\Delta E = \gamma\hbar B_0 \quad (2.15)$$

the frequency of radiation required to excite between the two states can be defined as

$$\omega = \gamma\mathbf{B}. \quad (2.16)$$

This frequency, known as the Larmor frequency, is directly related to the strength of the external magnetic field. When energy is applied at or near the Larmor frequency, magnetic resonance is said to occur; when the system absorbs the energy allowing the spins to transition between the two states. As this energy is absorbed more spins will begin to reside in the higher energy state. Once the source of energy is removed the system will return to its equilibrium state.

2.1.3 Bulk Magnetism

In order to calculate the bulk magnetism of a spin system (Figure 2.4) we must refer to Boltzmann statistics to calculate the probability of the spins existing in

2. MRI Theory

each state. This requires the assumption that the spin system has a temperature well above absolute zero. At equilibrium the ratio of spins in the up state (aligned along the external magnetic field) to those in the down state (aligned against the external magnetic field) is given by

$$\frac{N_{\uparrow}}{N_{\downarrow}} = \exp\left(\frac{\Delta E}{k_b T}\right) \quad (2.17)$$

where T is the temperature of the system and k_b is Boltzmann's constant. The energy difference between the spin states is small and Equation 2.17 can be approximated to

$$\frac{N_{\uparrow}}{N_{\downarrow}} \approx 1 + \frac{\Delta E}{k_b T}. \quad (2.18)$$

Combining this with Equation 2.7 gives

$$N_{\uparrow} - N_{\downarrow} = N_{\downarrow} \frac{\gamma \hbar B_0}{k_B T}. \quad (2.19)$$

Assuming that the population difference is small N_{\downarrow} can be approximated by $N/2$, where N is the total number of spins. The difference in population, n , can then be expressed as

$$n = N_{\uparrow} - N_{\downarrow} = N \frac{\gamma \hbar B_0}{2k_B T}. \quad (2.20)$$

The net magnetization, M_0 , in the z direction (along the external field) can be calculated by summing the magnetic field due to all the spins in the system,

$$M_0 = \sum_{n=1}^N \mu_z. \quad (2.21)$$

As the up and down spins cancel each other out only the magnetization from n spins needs to be taken into consideration, giving

$$M_0 = n\mu_z. \quad (2.22)$$

Therefore, using Equation 2.20, M_0 can be calculated as

$$M_0 = \frac{\gamma^2 \hbar^2 B_0 N}{4k_b T} \hat{z}. \quad (2.23)$$

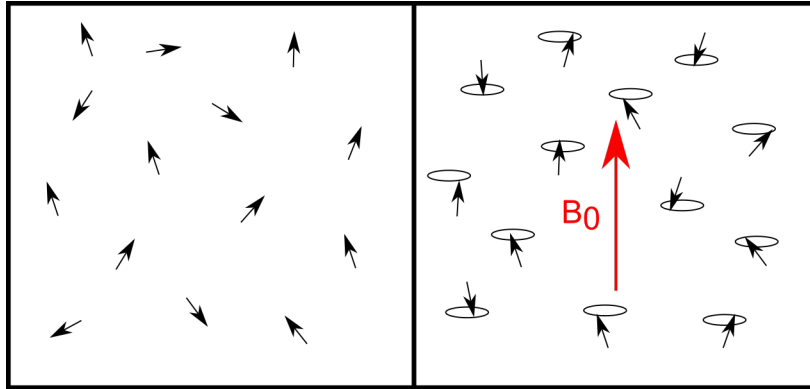


Figure 2.4: Left: A spins system with no external magnetic field applied. The spins are randomly orientated resulting in no net magnetization. Right: A spin system with an external magnetic field applied, spins either align with the field or against it, resulting in a bulk magnetization.

2.1.4 Excitation

M_0 is extremely small in comparison with the external field B_0 , and so measuring it when aligned with the external field is difficult. By rotating M_0 by 90° into the transverse plane it can be measured much more easily. In order to do this energy in the form of a radio frequency (RF) pulse must be put into the system. When a radio frequency pulse is applied, providing that the frequency of the pulse matches the Larmor frequency, some of the spins absorb the energy and transfer from the lower energy state into the higher energy state. Over time more and more spins absorb the energy and transfer into the higher energy state. This results in the bulk magnetic field being rotated away from the direction of the external field. The effects of a radio frequency pulse, known as the B_1 field, can be more easily visualised by moving from the laboratory frame into a rotating frame (Figures 2.5 and 2.6).

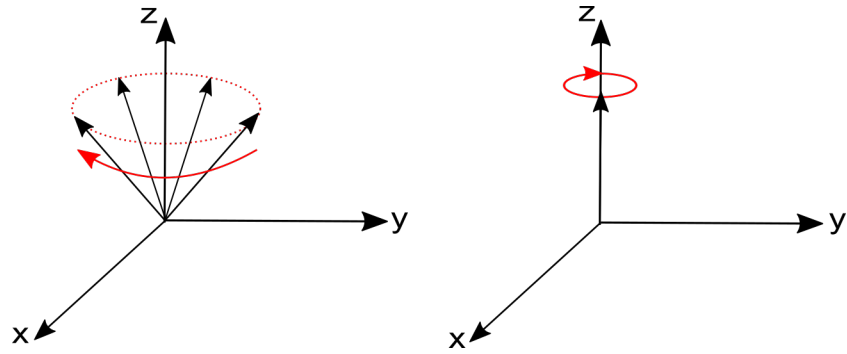


Figure 2.5: Left: Magnetization vector in the lab frame. Right: Magnetization vector in the rotating frame.

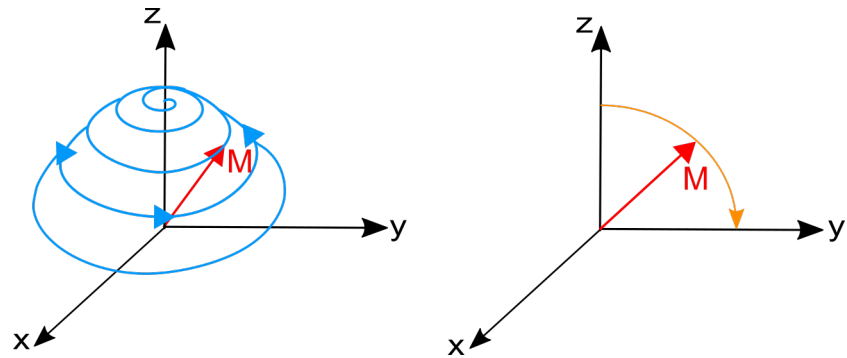


Figure 2.6: Evolution of the magnetization vector, \mathbf{M} , when an RF pulse is applied in the lab frame (left) and the rotating frame (right).

The B_1 field can be described in the laboratory frame (x, y, z) by

$$\mathbf{B}_1(\mathbf{t}) = \begin{pmatrix} B_1(t) \cos(\omega t) \\ -B_1(t) \sin(\omega t) \\ 0 \end{pmatrix}. \quad (2.24)$$

The rotating frame (x', y', z') is related to the lab frame by the following equations:

$$\begin{aligned} x' &= x \cos(\omega t) - y \sin(\omega t) \\ y' &= x \sin(\omega t) + y \cos(\omega t) \\ z' &= z. \end{aligned} \quad (2.25)$$

2. MRI Theory

Using these the oscillating B_1 field can be transformed into the rotating frame:

$$\begin{pmatrix} B_{1,x'} \\ B_{1,y'} \\ B_{1,z'} \end{pmatrix} = \begin{pmatrix} \cos(\omega_0 t) & -\sin(\omega_0 t) & 0 \\ \sin(\omega_0 t) & \cos(\omega_0 t) & 0 \\ 0 & 0 & 1 \end{pmatrix} \begin{pmatrix} B_1(t) \cos(\omega t) \\ -B_1(t) \sin(\omega t) \\ 0 \end{pmatrix}. \quad (2.26)$$

Evaluating this when the B_1 field frequency matches that of the Larmor frequency gives

$$\mathbf{B}_1 = \begin{pmatrix} B_1(t) \\ 0 \\ 0 \end{pmatrix}. \quad (2.27)$$

On resonance, in the rotating frame the B_1 field appears stationary in the $x'y'$ plane (e.g. points along the x' axis). When on resonance the B_1 field will cause the magnetization vector to rotate around the x' axis. The rate of rotation can be calculated as

$$\omega = \frac{d\theta}{dt} = \gamma B_1(t) \quad (2.28)$$

$$\theta = \int \gamma B_1(t). \quad (2.29)$$

From this the angle, θ , through which the magnetization vector rotates when a B_1 field is applied for a time t is given by

$$\theta = \gamma B_1 t. \quad (2.30)$$

It is common to refer to RF pulses by the angle through which they rotate \mathbf{M} . For example a 90° pulse will rotate \mathbf{M} by 90° . This rotation of the magnetic field vector away from its equilibrium point is known as excitation. The radio frequency pulse also has the effect of bringing all the spins into a coherent phase.

2.1.5 Relaxation and the Free Induction Decay

After an RF pulse is switched off the magnetization returns to its equilibrium state. This decay is known as the free induction decay (FID) of the observable

2. MRI Theory

magnetization, and can be measured by receive coils surrounding the spin system (Figure 2.7). Two types of relaxation occur, longitudinal relaxation and transverse relaxation. Longitudinal, spin-lattice or T1 relaxation is due to the spins returning to their equilibrium magnetization, M_0 , and involves the emission of energy obtained from the RF pulse into the surrounding spin system. Transverse, spin-spin or T2 relaxation is due to the phase of the spins returning to randomly phased states with respect to one another. T1 and T2 are time constants and are dependent on the structure and environment of the spin system.

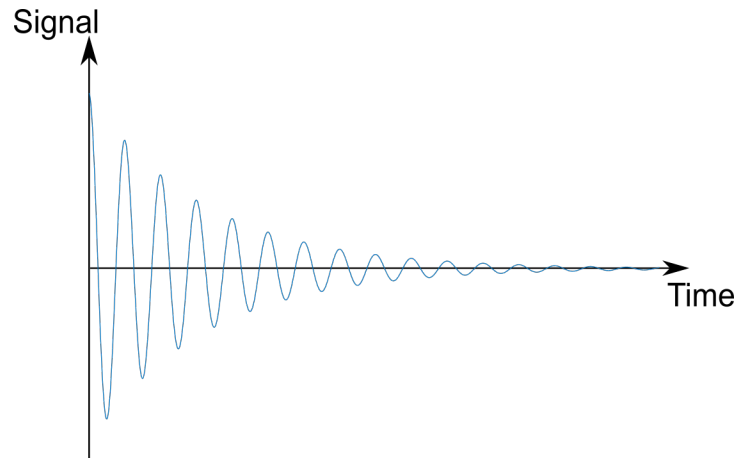


Figure 2.7: A free induction decay of the signal after the B_1 field is removed.

The change in the magnetization of the spin system over time was originally described by Bloch as

$$\frac{d\mathbf{M}}{dt} = \gamma[\mathbf{M} \times \mathbf{B}]. \quad (2.31)$$

Bloch also took account of the free induction decay which, in the rotating frame, can be expressed as

$$\frac{d\mathbf{M}}{dt} = \gamma(\mathbf{M} \times \mathbf{B}) - \frac{(M_z - M_0)}{T_1} \hat{z} - \frac{M_x \hat{x} + M_y \hat{y}}{T_2}. \quad (2.32)$$

These equations are known as the Bloch equations.

2.1.6 T1 Relaxation

Longitudinal, spin-lattice, or T1, relaxation refers to the relaxation of the magnetization in the longitudinal, or z axis. T1 decay is the process by which the system returns to thermal equilibrium. When the RF pulse is removed the spin states are in a higher energy level than at equilibrium, the spins then return to their equilibrium state, emitting the energy difference which is absorbed by the surrounding lattice. This process is termed spin-lattice relaxation. The net longitudinal magnetization vector M_z follows an exponential recovery, gradually returning to its equilibrium position M_0 (Figure 2.8). The z component of Equation 2.32 can be used to obtain the following relationship:

$$\frac{dM_z(t)}{dt} = -\frac{(M_z - M_0)}{T_1} \quad (2.33)$$

which gives the magnetization in the z direction at time t as

$$M_z(t) = M_0(1 - e^{-\frac{t}{T_1}}) + M_z(0)e^{-\frac{t}{T_1}}. \quad (2.34)$$

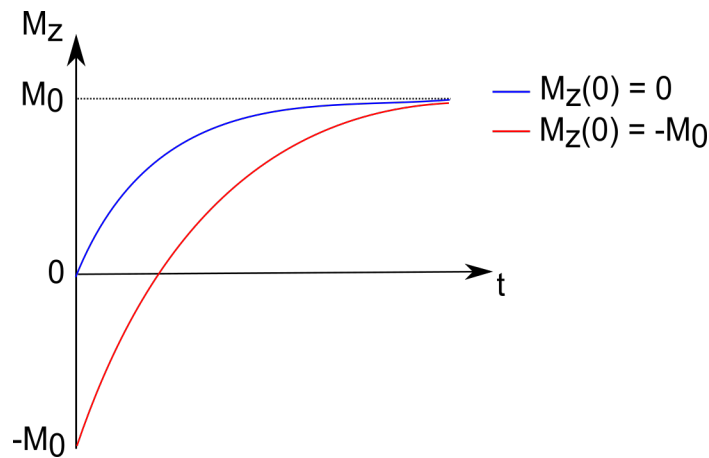


Figure 2.8: Longitudinal relaxation after an inversion pulse (red) and a 90° pulse (blue).

In order to measure T1, an inversion recovery sequence can be used (Figure 2.9). An inversion recovery sequence involves applying a 180° pulse and waiting

an inversion time (TI) before measuring the signal. The signal is measured by applying a 90° pulse to rotate the magnetization from the z plane into the xy plane. This allows the M_z component of the signal at TI to be measured. Due to the 180° pulse, at $t = 0$ $M_z(0) = -M_0$ and thus Equation 2.34 becomes

$$M_z(t) = M_0 \left(1 - 2e^{-\frac{t}{T_1}} \right). \quad (2.35)$$

Repeating this process for a range of different TI values allows for T1 to be calculated by fitting Equation 2.35 to the measured signal.

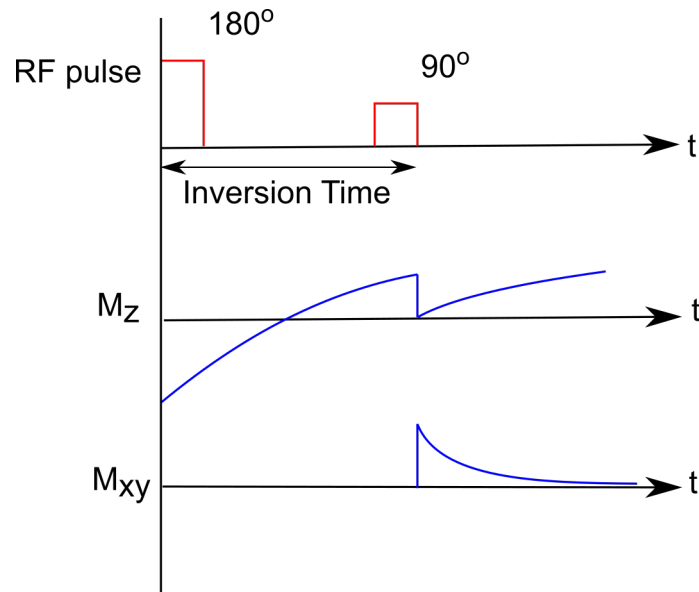


Figure 2.9: Schematic of a T1 inversion recovery sequence where an initial inversion pulse is applied followed by a 90° pulse after waiting for a set inversion time (TI).

2.1.7 T2 Relaxation

T2, or transverse relaxation, refers to the dephasing of the spins in the xy plane. The application of an RF pulse brings all the spins into phase with each other, however after its removal the spins will all have slightly different precessional frequencies. This results in the transverse magnetization dephasing over time,

2. MRI Theory

and returning to its equilibrium state of zero (Figure 2.10).

The Bloch equations characterising this dephasing can be summarised as

$$\frac{dM_{xy}(t)}{dt} = -\frac{M_{xy}(t)}{T2}, \quad (2.36)$$

which means that the xy magnetization at a given time is

$$M_{xy}(t) = M_0 e^{-\frac{t}{T2}}. \quad (2.37)$$

By applying a 180° pulse the spins can be forced to come back into phase (Figure 2.11). This is known as a spin echo (5) and it is used to measure $T2$. To do this a 90° pulse is applied, then after waiting a set time a 180° pulse is used to get the spins back in phase. The time that the echo occurs is known as the echo time (TE) and is twice the length from the 90° pulse to the 180° pulse. By repeating this for a number of different echo times the exponential decay described in Equation 2.37 can be sampled and $T2$ calculated (Figure 2.12).

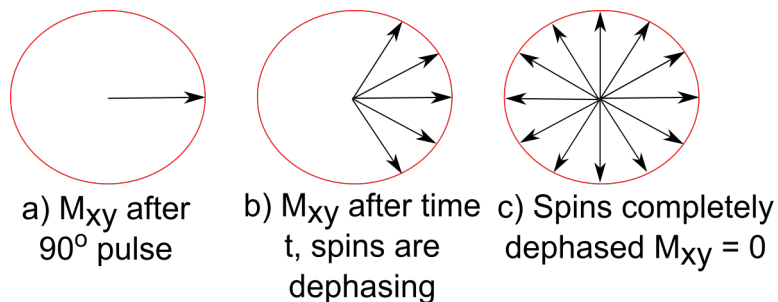


Figure 2.10: a) Immediately after a 90° pulse the spins are in phase. b) The spins start to dephase according to $T2$. c) The spins are completely dephased.

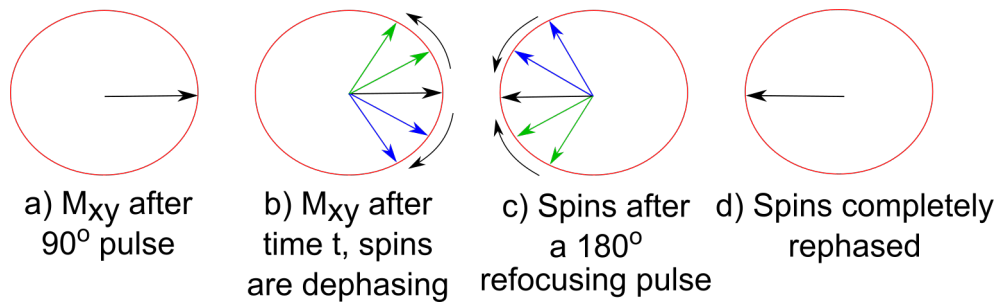


Figure 2.11: a) Immediately after a 90° pulse the spins are in phase. b) The spins start to dephase according to T_2 . c) After a 180° refocusing pulse the spins start to come back into phase. d) The spins are completely in phase.

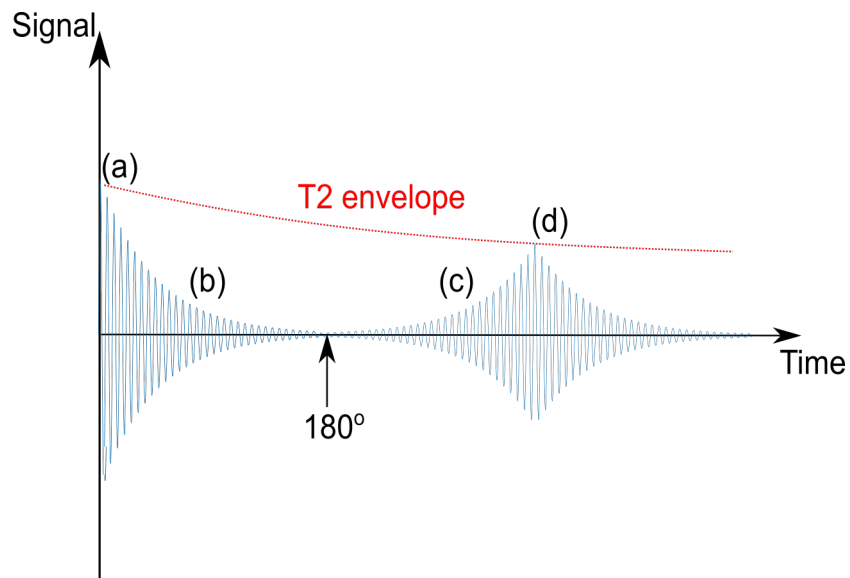


Figure 2.12: An FID followed by a spin echo with the T_2 decay envelope shown. Points a, b, c, and d match those in Figure 2.11.

2.1.8 T2* Relaxation

In reality it is not just the spin system itself that causes the spins to dephase. Inhomogeneities in the B_0 field can accelerate the dephasing making T2 appear shorter than theoretically predicted. This faster dephasing is called T2* decay and encompasses both the T2 decay and the effects of field inhomogeneities such that

$$\frac{1}{T2^*} = \frac{1}{T2} + \frac{1}{T2'}. \quad (2.38)$$

The T2' effects are static in relation to time and thus can be reversed allowing for T2 to be measured. In the spin echo sequence in Figure 2.12 the dephasing effects caused by B_0 inhomogeneities are reversed by the 180° pulse and therefore pure T2 is measured. In order to measure T2* the decay of the FID over time is measured.

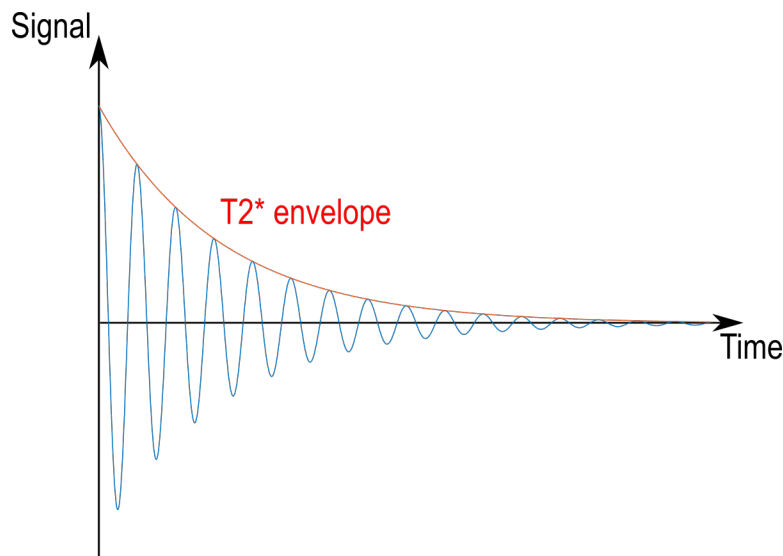


Figure 2.13: An FID shown with the T2* decay of the signal which occurs once the RF pulse is removed.

T2* is measured from the FID decay, or using a gradient echo for imaging. After the application of a 90° pulse, rather than apply a 180° pulse and wait for a spin echo to form, the formation of a gradient echo can be forced. This is done by applying a dephasing gradient which causes the spins to become less coherent

and then applying the same gradient but in the opposite direction. This reversed gradient forces the spins into phase forming a gradient echo. The rephasing that occurs does not undo the dephasing caused by T2 decay as this is due to random processes that cannot be undone by the gradients. By repeating the process the decay of the FID can be measured giving T2*. For imaging it is preferred to have symmetric signal which gives a real Fourier transform, i.e. the exact phase at $t = 0$ does not matter. So a gradient echo is used rather than an FID for imaging if possible.

2.1.9 Correlation Time

The relaxation times that are measured are determined by the properties of the spin system. In the spin system the rotational motion of the molecules causes interactions between spins and their surroundings which determine the relaxation times of the system. Each molecule has its own magnetic dipole moment which, when close enough together, can interact with each other in so called dipole-dipole interactions. The most prominent features of the spins which influences the dipole-dipole interactions in proton NMR is the rate at which they tumble.

For T1 relaxation to occur a magnetic interaction at the Larmor frequency is required to cause it to revert back to the lower energy state. This interaction is in the form of dipole-dipole interactions. As the Larmor frequency increases with field strength the T1 of the spin system will be longer at higher field strengths.

T2 relaxation is due to interactions that cause different spins to experience slightly different magnetic fields, resulting in different spins precessing at different frequencies. In liquids these magnetic fields fluctuate much more rapidly than in solids. The fluctuating fields in liquids results in the dephasing occurring much more slowly as the fluctuating fields average out (long T2), whereas in solids the fields are much more static and therefore dephasing occurs much faster (short T2). T2 is mainly unaffected by field strength however at high field strengths such as 7T diffusion effects can shorten the measured T2.

Quantitatively these effects can be explained by looking at the motion of molecules in the spin system. The rotational motion of a molecule, or its molec-

2. MRI Theory

ular tumbling, is determined by its correlation time τ_c , defined as the time it takes the molecule to rotate by 1 radian. Small molecules will rotate faster than larger ones and hence have a shorter correlation time. The correlation time of a molecule depends on its kinetic energy, which is not identical for each identical molecule. The spectral density function $J(\omega)$, the probability of finding a molecule tumbling at a given frequency, is proportional to this function. For a spherical molecule

$$J(\omega) = \frac{\tau_c}{1 + \omega^2\tau_c^2}. \quad (2.39)$$

In 1955 Solomon gave a model which explained and could predict the T1 and T2 of protons (6):

$$\frac{1}{T1} = \frac{6}{20} \cdot \frac{\hbar^2\gamma^4}{r^6} \cdot \left(\frac{\tau_c}{1 + \omega^2\tau_c^2} + \frac{4\tau_c}{1 + 4\omega^2\tau_c^2} \right), \quad (2.40)$$

$$\frac{1}{T2} = \frac{3}{20} \cdot \frac{\hbar^2\gamma^4}{r^6} \cdot \left(3\tau_c + \frac{5\tau_c}{1 + \omega^2\tau_c^2} + \frac{2\tau_c}{1 + 4\omega^2\tau_c^2} \right). \quad (2.41)$$

From these equations the relationships between tumbling rate and T1 and T2 can be demonstrated (Figure 2.14).

From Figure 2.14 it can be seen that solids which have a slow molecular tumbling rate will have a high T1 and low T2 whereas free water will have a long T1 and T2.

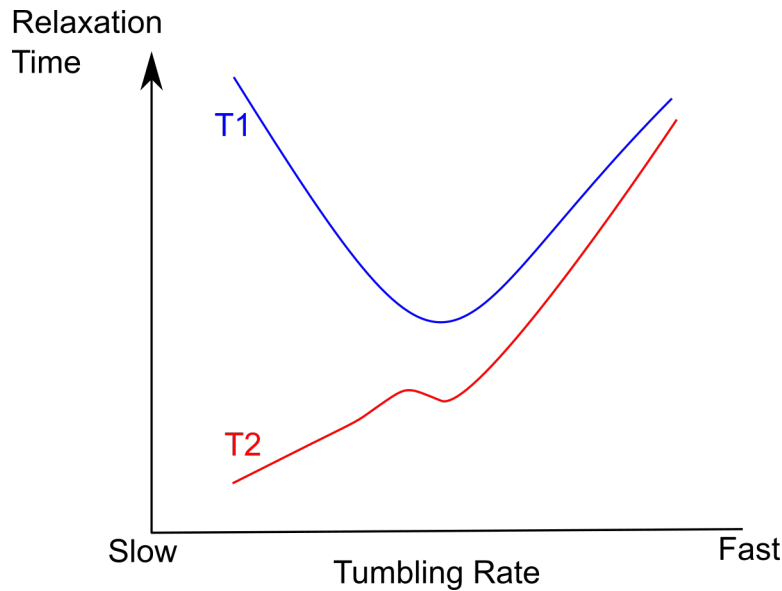


Figure 2.14: Relationship between the tumbling rate of a molecule and its T1 and T2.

2.1.10 Chemical Shift

The Larmor frequency of a nucleus is dependent on the magnetic field in which it sits. The magnetic field which a nucleus experiences is called the local magnetic field B_{loc} , and it differs from the external magnetic field B_0 due to the local chemical environment. Electrons in the chemical to which the nucleus belongs can shield them from the magnetic field resulting in a difference between B_{loc} and B_0 . Therefore a hydrogen nucleus attached to a water molecule will experience a different magnetic field to one attached to a fat molecule and will therefore resonate at a different frequency. The field experienced can be expressed as

$$B_{loc} = B_0(1 - \sigma) \quad (2.42)$$

where σ is the shielding factor.

Differences in the Larmor frequency can be utilised in Magnetic Resonance Spectroscopy (MRS) in order to identify the relative abundance of a certain chemical in the species being imaged. To do this a spectral frequency is collected

2. MRI Theory

and the peaks compared to a reference standard. The chemical shift of a species, which is usually expressed in parts per million, can be calculated as

$$\delta = (f_{sample} - f_{reference})/f_{reference}. \quad (2.43)$$

Here f_{sample} is the frequency of the sample, and $f_{reference}$ is the frequency of the external reference. The chemical shift values of many species are readily available for identification of the chemicals contained within a sample.

2.1.11 Susceptibility

The extent to which a substance is magnetized by an external magnetic field is determined by its magnetic susceptibility, χ . The susceptibility of the substance can influence the surrounding magnetic field, B_{eff} which can be calculated as

$$B_{eff} = (1 + \chi)B_0. \quad (2.44)$$

These changes in the local magnetic field can cause artefacts in MR images. Two common causes of susceptibility artefacts in gastrointestinal MRI are the presence of iron in the liver and the presence of air in the gut. These cause variations in the local magnetic field which in turn creates variations in the precessional frequencies of the surrounding substances. This causes livers with iron overload to appear very dark on MR images due to rapid dephasing caused by the varying precessional frequencies.

2.2 Magnetic Resonance Image Encoding

In the 1970s Mansfield and Lauterbur put NMR to use in the field of medical imaging (3, 4). Using magnetic field gradients they were able to localise NMR signals and produce *in vivo* images of human tissue. Since those first images, the field has grown to produce faster, higher resolution and more complex images of the human body. In this section basic image encoding methods are discussed.

2.2.1 Slice Selection

With the use of magnetic field gradients a particular imaging slice can be selected (7). In order to achieve this a magnetic field gradient is applied perpendicular to the desired slice (Figure 2.15). A radio frequency pulse is then applied such that the frequency of the pulse matches the Larmor frequency of the nuclei within the desired slice.

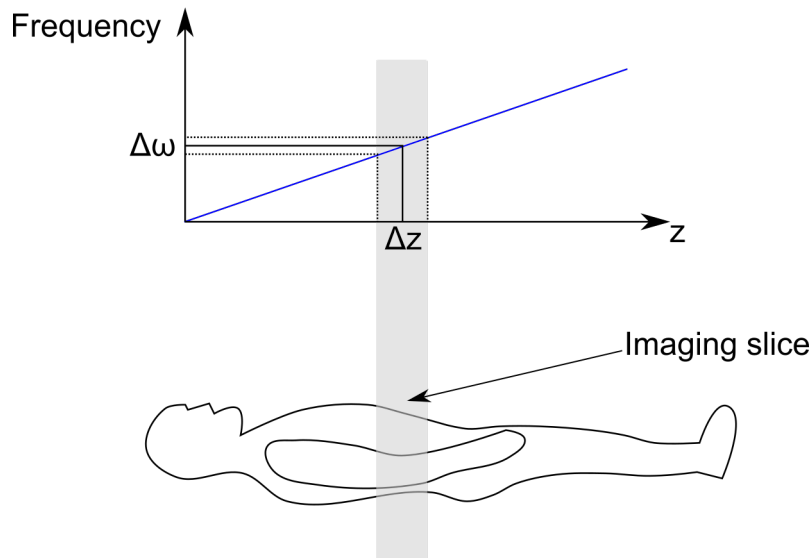


Figure 2.15: A gradient applied in the z direction gives spatially dependent Larmor frequencies in the z direction. Only those spins that have a Larmor frequency matching that of the imaging slice region are excited. A slice of width Δz is excited with the spins within the slice having a frequency range of $\Delta\omega$ which is known as the bandwidth.

If a gradient G_z is applied then the Larmor frequency is given as

$$\omega(z) = \gamma(B_0 + zG_z). \quad (2.45)$$

The slice required will have a finite thickness chosen by the user, corresponding to a range of Larmor frequencies within the slice. This requires that the radio frequency pulse has a finite bandwidth. The bandwidth required to create a slice

of thickness Δz is given by

$$\Delta\omega = \Delta z\gamma G_z. \quad (2.46)$$

A smaller slice thickness requires a smaller band width or a larger magnetic field gradient, the increase of both demand more from the MR hardware.

In general a rectangular slice is required which can be achieved by using a sinc RF pulse with an infinite number of side lobes. However due to time restriction the sinc pulse is truncated which can lead to an imperfect imaging slice (Figure 2.16). Typical RF pulses are in the MHz range and are applied for a few milliseconds.

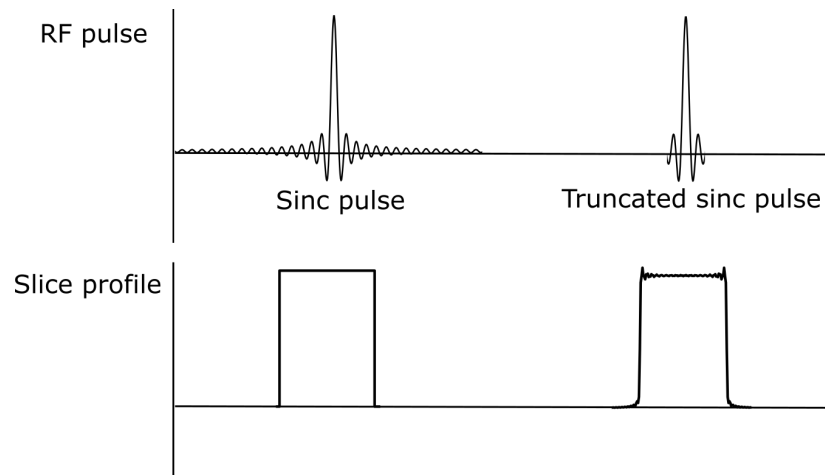


Figure 2.16: Example of a sinc pulse which created a rectangular slice profile and a truncated sinc pulse which creates a imperfect slice profile.

2.2.2 Frequency Encoding

Frequency encoding uses the same principles as slice selection to allow the localisation of the signal in the x direction (Figure 2.17). In frequency encoding a gradient is applied in the x plane such that the Larmor frequency of nuclei in the x plane varies as

$$\omega(x) = \gamma(B_0 + xG_x). \quad (2.47)$$

The signal can now be expressed as a function of position, r and sample time t

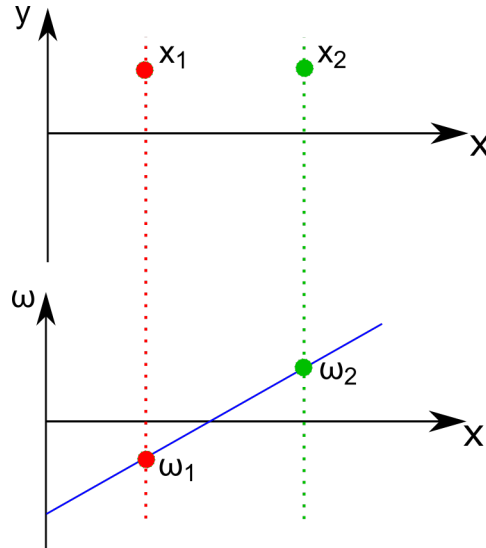


Figure 2.17: A gradient applied in the x direction produces spatially dependent Larmor frequencies which can be used to determine the location of a spin in the x direction.

as

$$S(r, t) \propto \rho(r) \exp^{i \int_0^t \omega(r, \tau) d\tau} \quad (2.48)$$

where τ is time, $\omega(r, \tau)$ is the Larmor frequency of the spins and $\rho(r)$ is the density of the spins. This can be extended to the signal acquired from the whole sample of volume V as

$$S(t) \propto \int_V \rho(r) \exp^{i \int_0^t \omega(r, \tau) d\tau} dV. \quad (2.49)$$

The magnetic field experienced by the spin which determines the frequency at which it precesses, therefore Equation 2.49 can be expressed in terms of the magnetic field gradients.

$$S(t) \propto \int_V \rho(r) \exp^{(i\gamma \int_0^t r \cdot G(\tau) d\tau)} dV, \quad (2.50)$$

where $\mathbf{G}(\tau)$ is the gradient applied in all directions. These gradients can be

used to describe the evolution of the phase of the spins over time such that

$$k(t) = \gamma \int_0^t \mathbf{G}(\tau) d\tau \quad (2.51)$$

where k is the wave number. Combining the above equations gives

$$S(k) \propto \int_V \rho(k) \exp(i\mathbf{r} \cdot \mathbf{k}(t)) dV. \quad (2.52)$$

This equation is an inverse Fourier Transform. The Fourier Transform of the signal results in the proton density. By acquiring the signal at a range of different frequencies the Fourier transform can be solved and the proton density calculated i.e. the image.

$$\rho(r) = \int S(k) \exp(-i\mathbf{r} \cdot \mathbf{k}(t)) dV. \quad (2.53)$$

2.2.3 Phase Encoding

In order to encode the signal in the third dimension phase encoding is used. When a gradient is applied to the spin system the resonant frequency of the spins temporarily changes. Once removed the spins return to their original resonant frequency but their phase will have changed. The amount by which the phase will have changed is dependent on the strength of the gradient and the amount of time it is applied for.

The precession frequency can be calculated as

$$\omega(y) = \gamma(B_0 + yG_y). \quad (2.54)$$

Therefore the phase acquired over the time of the gradient application can be calculated as

$$\phi(y) = \gamma y \int_0^t G_y(t) dt. \quad (2.55)$$

Using Equation 2.51 this can be further simplified to

$$\phi = yk_y. \quad (2.56)$$

2.2.4 k Space

This leads onto the concept of k space. k space is the 2D Fourier transform of the image space (Figure 2.18). It allows the visualisation of the spatial frequencies contained within the MR image. Images are acquired in k space, and are then Fourier Transformed to give the MR image in Cartesian coordinates.

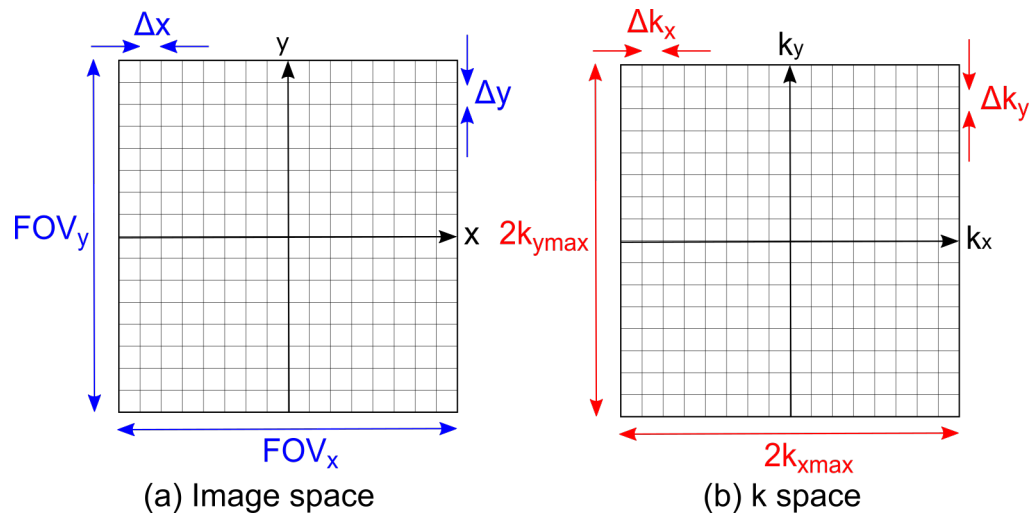


Figure 2.18: The relationship between image space (a) and k space (b).

k is a characteristic of the signal being collected. It is the wave number (the number of waves per unit space (spatial frequency)) and is inversely related to wavelength. This is akin to the temporal frequency which is the number of waves per unit time. k space and the image space are linked. k_x is typically taken to be the frequency encoding direction and k_y the phase encoding direction. The number of frequency encoding steps determines how many times the echo is sampled. The phase encoding steps determine how many echoes are sampled. Each sample of signal that is taken corresponds to a location in k space. High spatial frequencies in k space represent edges and details in the image whilst low spatial frequencies represent the general image contrast and shape. Therefore collecting only the centre of k space gives a rough representative image but the outer regions of k space are required for the finer details. The field of view of

the image is given by

$$FOV_x = \frac{1}{\Delta k_x} \quad FOV_y = \frac{1}{\Delta k_y}. \quad (2.57)$$

After the application of the slice select gradient spins are in phase and sampling begins at the centre of k space. The spin system can be moved away from the centre of k space by applying the relevant gradients in the x and y planes. During a constant gradient along the x axis k space sampling will move linearly along the k_x axis, and similarly for gradients in the y direction. Spin warp imaging is the simplest acquisition method and fills a single line of k space per repetition time (TR) (Figure 2.19).

After an RF pulse and slice selection gradient, a phase encoding gradient is applied. This is followed by a longer frequency encoding gradient. After a time TR the process is repeated. Each phase encoding gradient moves up a line in k space whilst the frequency encoding gradient moves the sampling along the frequency encoding direction. This results in one line of k space filled for each repetition time (Figure 2.20).

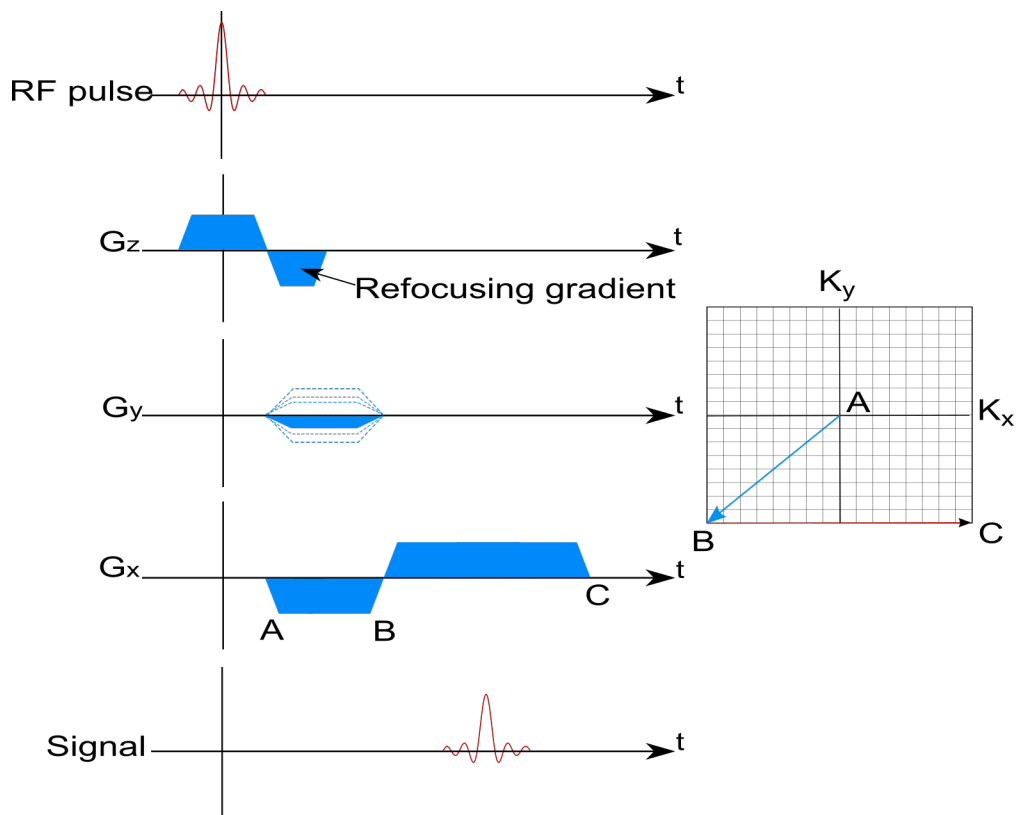


Figure 2.19: A Spin echo sequence. On the left is the pulse sequence with the corresponding k space trajectory shown on the right. The gradient in the x direction determines the position on the k_x axis with the gradient in the y direction determining the position on the k_y axis. Each of the dashed lines on the G_y gradient refer to a new line in k space (Figure 2.20).

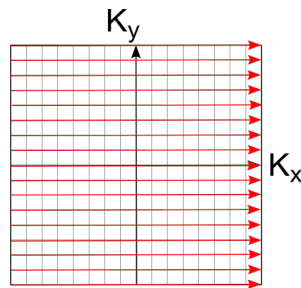


Figure 2.20: k space trajectory during a spin echo imaging sequence. Each new line occurs with the repetition of the pulse sequence shown in Figure 2.19 after a given repetition time.

2.2.5 Partial Fourier Imaging

Partial Fourier Imaging stems from a property of k space called conjugate symmetry. Conjugate symmetry means that each point in k space has a conjugate pair. Say, for example, a point in k space is at $a + bi$, its conjugate pair will exist at $a - bi$. This symmetry can be exploited and allows the collection of as little as half of k space to reduce the acquisition time, however problems do arise from Partial Fourier imaging. Phase effects cannot be corrected by only collecting half of k space, therefore around 60-70% of k space is usually collected to allow for a phase correction map to be generated. The time saved must be balanced with the signal to noise ratio (SNR) loss which is reduced by around 30%. Two different types of symmetry can be used: phase-symmetry and read symmetry. Phase encoding direction symmetry under samples in the phase encoding direction, this is known as Half-scan on Philips systems. Read encoding direction symmetry under samples in the frequency encoding direction and only samples part of the echoes. This allows for a reduction in the echo time, known as Partial Echo on Philips systems.

2.2.6 Parallel Imaging

In non-parallel imaging multiple surface coils are sometimes used to collect the MR signal, which are then combined to produce the full signal. Having multiple coils improves the SNR but does not make use of the varying sensitivity of each coil. The signal from each surface coil can be processed separately in 'parallel' providing some spatial information. In parallel imaging the number of phase encoding steps is reduced which results in a wrap around effect. These wrapped images are then 'unwrapped' by using the relative sensitivities of the coils (Figure 2.21). The sensitivity maps are made from low resolution images that are acquired separately for each coil. They are then normalised by dividing them by a low resolution image from the body coil. These maps give a relevant weight to the signal in each voxel for each coil. A voxel far away from the coil will have a low weight in that coil, whilst a voxel close to the coil will have a higher weight. This ensures voxels will have their final signal dictated mainly by

2. MRI Theory

the closest coil.

Two methods to unwrap the images commonly exist, SENSE (SENSitivity Encoding (8)) and GRAPPA (GeneRalized Auto-calibrating Partial Parallel Acquisition (9)). SENSE unwraps the images in the image domain whereas GRAPPA unwraps the images in the k space domain. In this thesis only SENSE is used and so shall be explained here in more detail.

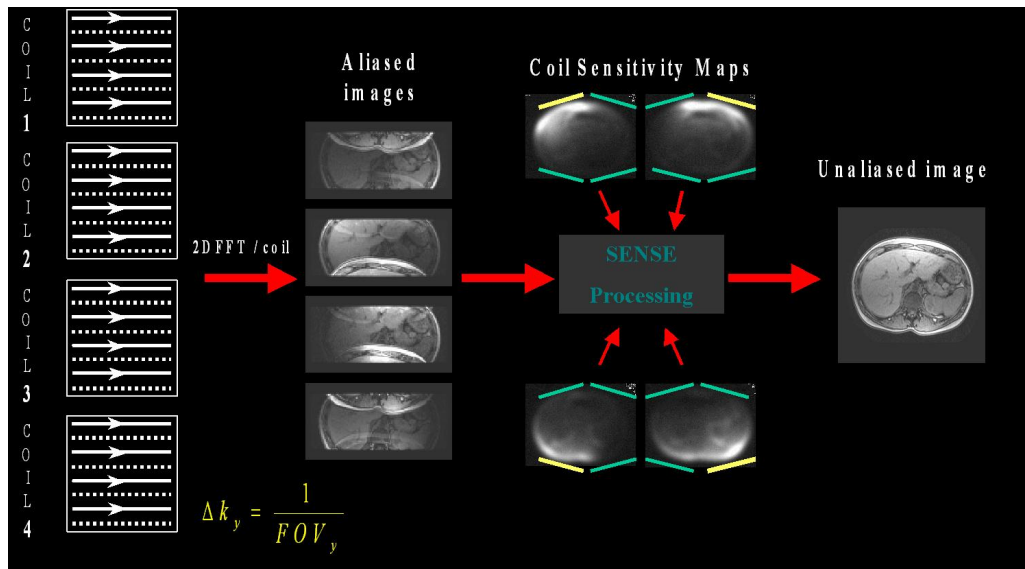


Figure 2.21: SENSE coil sensitivities. Four coils are used in this example each producing their own image. The images are then combined with a weighting for the relative sensitivities for the locations within each image for each coil (10).

There are two main benefits to parallel imaging: firstly, the acquisition time is accelerated, with the amount of acceleration achieved described by the acceleration factor (R). The acceleration is achieved by acquiring fewer lines of k space in the phase encoding direction. An acceleration factor of 2 is achieved by acquiring every other line of k space.

Secondly, the amount of susceptibility artefacts are reduced in echo planar imaging (EPI). This is due to the lower amount of phase encoding steps acquired. There are also two main drawbacks to parallel imaging: there is a reduction in SNR, for example when $R = 2$ the reduction in SNR is around 40%. Secondly,

parallel imaging artefacts (Figure 2.22) arise from errors in the coil sensitivities. These artefacts appear as fold over artefacts in the phase encoding direction of the reconstructed image.

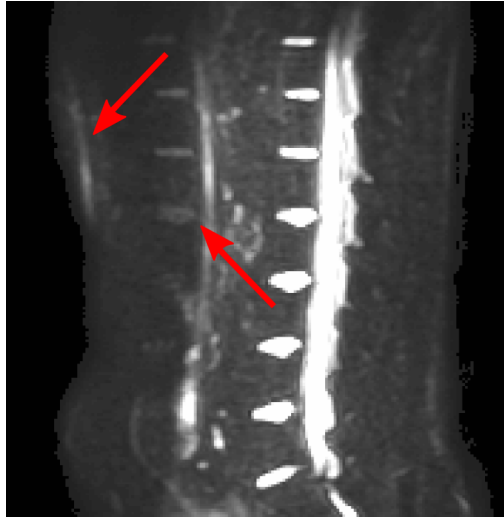


Figure 2.22: SENSE artefacts of the spine are shown by the red arrows.

In SENSE each coil has its own sensitivity map. These are generated before each acquisition that uses SENSE. The image is then acquired and the signals from each coil digitised separately and reconstructed into separate images.

After the images are acquired they are combined using matrix inversions. An example of how unfolding works is as follows: if there are two voxels A and B at locations 1 and 2 and two coils 1 and 2. The signals from these two voxels wrap around. Therefore the signal P measured in locations 1 and 2 is measured as

$$\begin{aligned} P_1 &= A.S_{1A} + B.S_{1B} \\ P_2 &= A.S_{2A} + B.S_{2B} \end{aligned} \tag{2.58}$$

where S is the sensitivity of each coil. Knowing the relative sensitivities and the measured values of P , the true signal from voxels A and B can be calculated. In the Philips systems used through this thesis 32 coil sensitivity maps are used.

2.2.7 Multiband Imaging

Multiband imaging is a relatively new technique which allows for multiple slices to be acquired at the same time. A complex B_1 field is used to excite slices in different spatial locations. Coil encoding is combined with gradient or RF encoding to distinguish the two slices (11). By encoding multiple slices simultaneously the acquisition time can be reduced or alternatively more data can be acquired in the same amount of time.

2.3 Magnetic Resonance Image Acquisition Schemes

The way that k space is sampled in magnetic resonance imaging is widely varied with different acquisition methods suiting different purposes. The different acquisition methods used in this thesis are discussed here.

2.3.1 Turbo Spin Echo

Turbo Spin Echo (TSE), also known as Fast Spin Echo (FSE), originated from the RARE (Rapid Acquisition with Relaxation Enhancement) sequence proposed by Hennig in 1986 (9). It is commonly used and in this thesis is put to use as a T2 weighted anatomical scan. In conventional spin echo sequences one line of k space is filled for each repetition time. Turbo spin sequences differ from this as they fill several lines of k space in one repetition time, speeding up the acquisition process (Figure 2.23). In order to do this, in one repetition time rather than have one refocusing 180° pulse creating one echo, several 180° refocusing pulses are applied. Each 180° pulse has a different phase encoding gradient allowing a new line of k space to be filled for each refocusing pulse. This allows several lines of k space to be filled in a single TR. The number of echoes per repetition time is known as the turbo factor or TSE factor. The echo time of the sequence is given as the time at which the centre of k space is traversed. Using a long TR and a long TE a T2 weighted image can be obtained.

TSE can also be performed in a single shot. This acquisition is known as HASTE (Half-Fourier Acquisition Single-shot Turbo spin Echo) or SSH-TSE

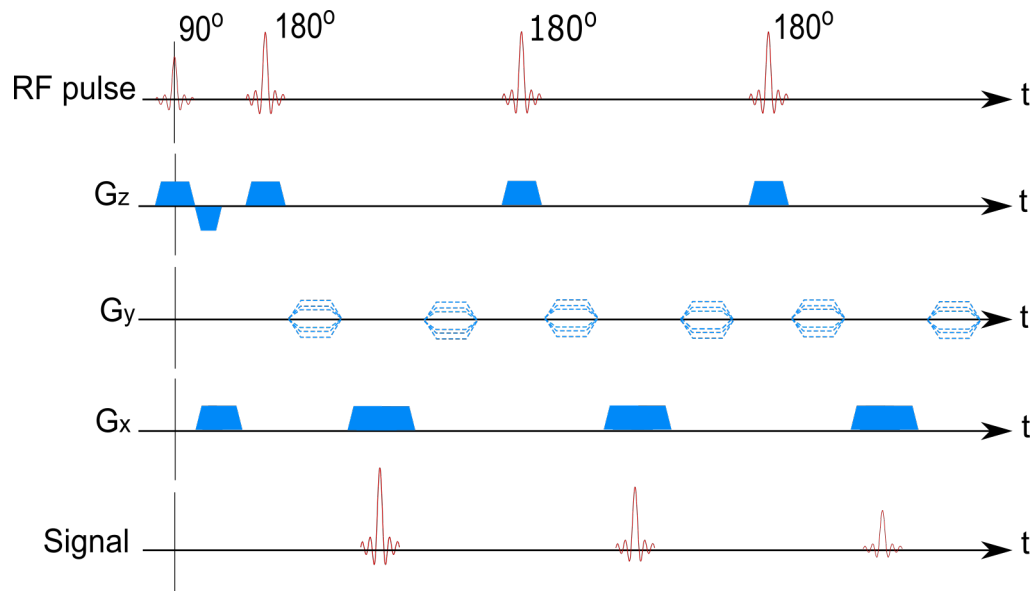


Figure 2.23: Schematic of the pulse sequence used in a Turbo Spin Echo sequence.

(Single Shot Turbo Spin Echo). This single shot acquisition makes use of phase conjugate symmetry (Section 2.2.5) to reduce the amount of k space that needs to be sampled. This allows for half of k space to be acquired after a single excitation by the use of long echo chains. These extremely short scans are often used when time is the most important factor in obtaining the image, for example in patients who cannot stay still for very long or non-breath held abdominal imaging.

2.3.2 Echo Planar Imaging

Echo Planar Imaging (EPI) was first proposed by Mansfield in the 1970s (12). EPI provides a method to collect the whole of k space in a single repetition time (Figures 2.24 and 2.25). Compared with spin warp imaging the new acquisition method was significantly faster allowing new insights into physiological function. Typically, EPI allows for the whole of k space to be sampled in under a second. It is of particular use in this thesis as abdominal imaging is affected by respiratory motion. This fast acquisition method allows abdominal images to be acquired

2. MRI Theory

in a single breath hold, eliminating the blurring effects of respiratory motion. EPI is used as a read out method in this thesis for diffusion weighted imaging of the abdominal lymph nodes.

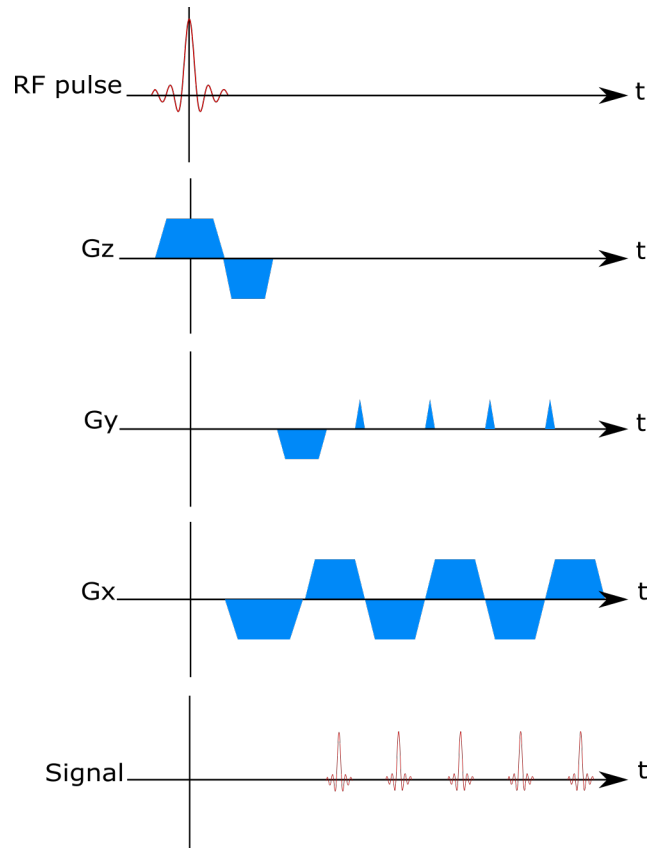


Figure 2.24: Schematic of the pulse sequence used in an EPI acquisition.

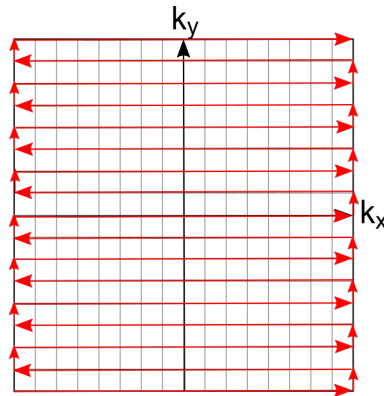


Figure 2.25: k space trajectory during an EPI sequence. The whole of k space is traversed in a single repetition time.

EPI makes use of a fast switching gradient in the frequency encoding direction along with a blipped gradient in the phase encoding direction. The resulting trajectory in k space is a zigzag path starting at the bottom of k space and working its way to the top. The large phase encoding gradient applied at the start of the readout ensures that the encoding starts at the edge of k space. This collection method is known as single shot EPI, however multishot EPI can also be used to collect all of k space in a small number of shots. On a Philips scanner the term EPI factor refers to the number of lines of k space that are collected in a single shot, this is also known as the Echo Train Length (ETL).

As the whole of k space is sampled following a single RF pulse, EPI is particularly susceptible to artefacts. Any field inhomogeneities or susceptibility effects can effect the evolution of the phase which is propagated through the whole of k space. A common example of an EPI artefact is the misregistration of fat (Figure 2.26). Fat and water have a phase difference caused by the different precessional frequencies of the two chemicals. This phase difference in EPI imaging is propagated throughout the whole collection of k space which can cause large differences in the phases of fat and water. There is a low bandwidth in the phase encoding direction which causes fat and water become separated by several pixels in the phase encoding direction. This is often seen in abdominal imaging due to the presence of subcutaneous and visceral fat (Figure 2.26).

These effects can be overcome by using a lower resolution image, changing the frequency and phase encoding directions or reducing the echo time.

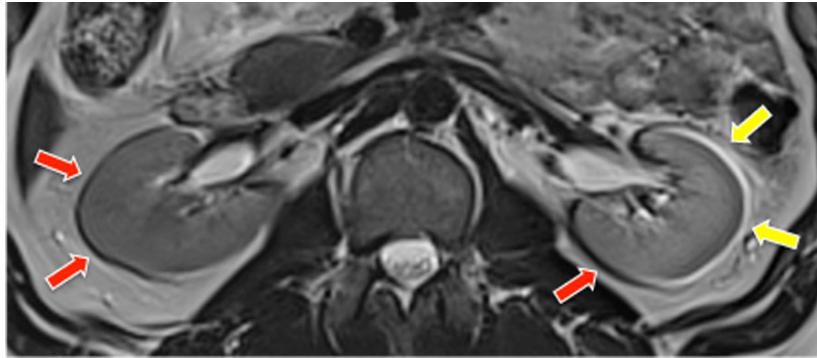


Figure 2.26: Fat misregistration on an EPI image. The yellow arrows show where the fat signal has moved to the right of the image by a few voxels creating areas of white where the signal has been added to that of other tissue and areas of black where it originated from (red arrows) (13).

2.3.3 Gradient Echoes and Steady State Imaging

Gradient echo sequences (Figure 2.27) employ a dephasing gradient followed by a rephasing gradient to produce gradient echoes. The application of these gradients rather than a refocusing RF pulse allows an echo to be produced much more rapidly than in a spin echo sequence. If a low flip angle is used then recovery of the signal requires a short time and thus short repetition times can be used. These factors mean imaging that requires fast acquisitions often use gradient echo sequences. The gradient echo does not undo any dephasing caused by field inhomogeneities or susceptibility issues, and therefore can exhibit artefacts related to these effects. Gradient echoes can be acquired in multiple shots providing that T_2^* decay has not significantly diminished the signal by the time the secondary echoes have been acquired.

In a gradient echo sequence several types of echo occur. Firstly there is the gradient echo mentioned above. Secondly there is a spin echo that is created by a pair of RF pulses. The third type is a Stimulated Echo.

2. MRI Theory

Three main types of gradient echo acquisitions exist. Firstly, one which only refocuses the FID (called FFE), secondly ones which refocus the echoes (T2 - FFE) and thirdly those which refocus both the FID and echoes (bFFE).

The first group, called 'coherent gradient echo sequences', retain the M_{xy} magnetization. The second group use spoiler gradients to dephase and hence diminish the M_{xy} magnetization. Spoiling gradients aim to completely dephase any transverse magnetization that exists before the application of the next RF pulse, i.e. the coherence in the xy plane is 'spoiled'. This thesis uses both of these types of gradient echo sequence and they are described in Sections 2.3.4 and 2.3.5.

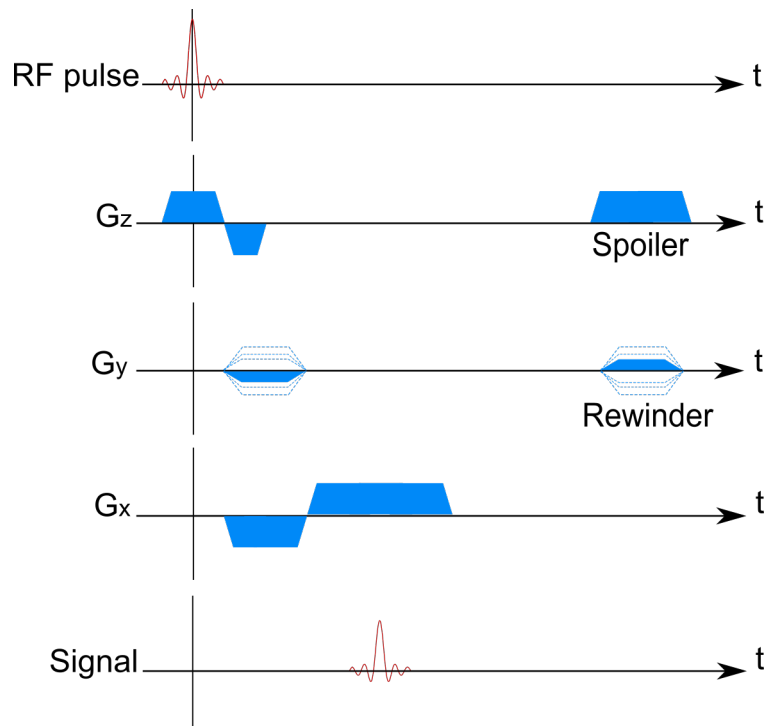


Figure 2.27: Schematic of the pulse sequence used in a steady state gradient echo sequence.

If the repetition time in a gradient echo sequence is sufficiently short the system can reach what is known as a steady state (Figure 2.28). In this state the magnetization does not reach equilibrium before the next pulse occurs. After a

number of RF excitations (with the number being dependent on T1, T2 and flip angle) the amount of M_z magnetization that is present before the next RF pulse becomes constant, i.e. the signal is at steady state. By imaging in the steady state we do not have to wait for the full T1 recovery and T2 decay to occur before collecting the next echo, allowing a reduction in the acquisition time.

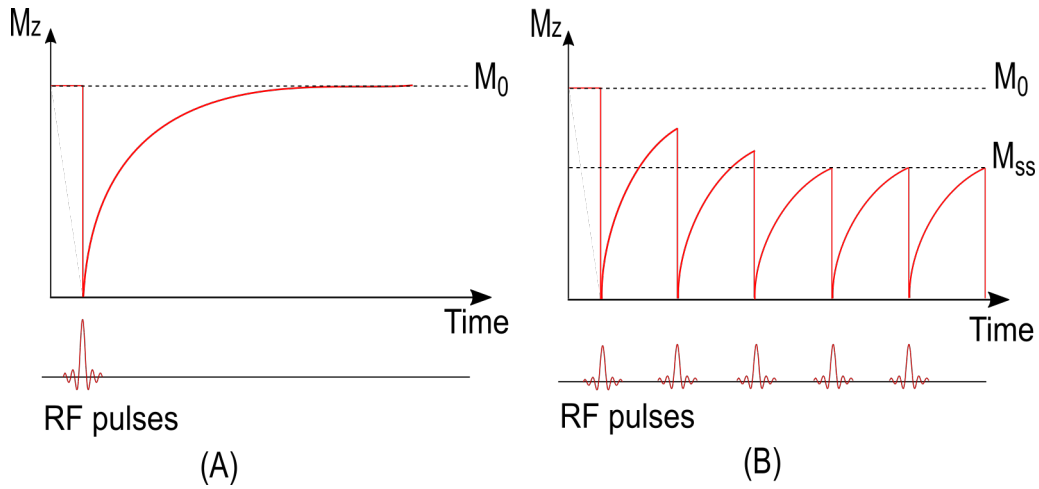


Figure 2.28: A) Magnetisation that fully recovers after a single RF pulse. B) Magnetization after repeated RF pulses are applied before the magnetization has returned to its equilibrium state. The magnetization reaches a steady state after several applications of the RF pulse.

2.3.4 Spoiled Gradient Echo (FLASH)

In this thesis a spoiled gradient echo sequence was used to measure the T1 of the small bowel wall. Spoiled gradient echo, also known as FLASH (Fast Low Angle SHot), uses low flip angles and short TRs to reach the steady state along with spoiler gradients to dephase the transverse magnetization before the application of a new RF pulse (14). RF spoiling can also be used to dephase the transverse magnetization, in this case a different phase is used for each RF pulse which effectively dephases the transverse magnetization. T2 decay can be used as a means to dephase the transverse magnetization but the use of spoiler gradients means that the dephasing occurs much faster than it would naturally. In the

2. MRI Theory

FLASH sequence the magnetization after the first RF pulse is given by

$$M_z = M_0 \cos(\theta) \quad (2.59)$$

$$M_{xy} = M_0 \sin(\theta) \quad (2.60)$$

where θ is the angle of the RF pulse (typically around 15° for this sequence). After the application of the first RF pulse M_z begins to recover towards its equilibrium value. However, before it can reach this state a second RF pulse is applied. The process is repeated until the steady state is reached (around 12 echoes). The longitudinal magnetization in the steady state is given by

$$M_{ss} = \frac{M_0 \left(1 - \exp\left(-\frac{TR}{T_1}\right)\right)}{1 - \exp\left(-\frac{TR}{T_1}\right) \cos(\theta)} \quad (2.61)$$

and the transverse magnetization is given by

$$M_{xy} = M_{ss} \sin(\theta) \exp\left(-\frac{t}{T_2^*}\right). \quad (2.62)$$

To calculate the maximum signal that is theoretically obtainable in the xy plane after the application of an RF pulse we solve

$$\frac{d}{d\theta} M_{ss} \sin(\theta) = 0. \quad (2.63)$$

Substituting M_{ss} from Equation 2.61 gives

$$\theta_E = \cos^{-1} \left(\exp^{-\frac{TR}{T_1}} \right). \quad (2.64)$$

This gives the angle, θ_E , of the RF pulse which produces the maximum signal to be sampled, known as the Ernst angle. When $TR \ll T_1$ two approximations can be used, $\cos(\theta) \approx 1 - \frac{\theta^2}{2}$ and $\exp(x) \approx 1 + x$ (the first for small angles and the second for exponentials of small numbers).

Using these the Ernst angle can be approximated as

$$\theta_E = \sqrt{\frac{2TR}{T_1}}. \quad (2.65)$$

The FLASH readout is put to use after an inversion recovery in this thesis as a way of measuring T1 of the small bowel wall. FLASH was chosen as it provides a fast method of sampling k space in the restricted time of a single breath hold.

2.3.5 Balanced Turbo Field Echo (bTFE)

In this thesis balanced turbo field echoes (bTFEs), or FISPs (Fast Imaging with Steady-state Precession), (15) are used to measure the apparent T2 of the small bowel wall. bTFE is a gradient echo acquisition however unlike FLASH does not use spoiler gradients to destroy the transverse magnetization but refocuses it completely or to some extent. This results in the steady state magnetization being reliant on T2 as well as flip angle, TR and T1. The steady state magnetization is also dependent on the angle through which the phase precesses between each RF pulse, β , which can cause banding artefacts (Figure 2.29). Inhomogeneities in the field or imperfect gradients mean that this rotation through β may not always be perfectly refocused. If the β differences are spatially dependent then banding artefacts can be seen in the image.

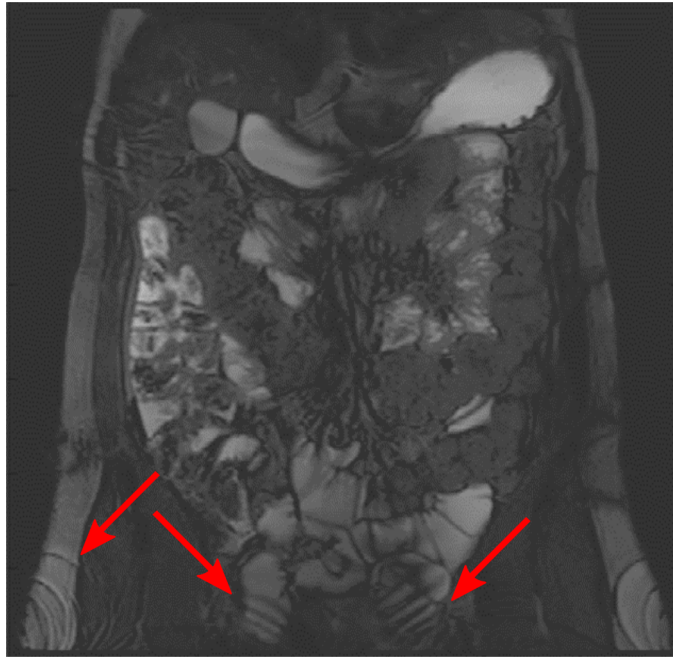


Figure 2.29: Banding artefacts (red arrows) seen in the lower half of a bTFE image.

In the case where the gradients are balanced the phase of the transverse magnetization is maintained throughout the acquisition i.e. the phase during one TR is the same throughout all other TRs. The computation of the steady state magnetization is much more complex compared to FLASH. The signal obtained from this balanced state can be shown to be

$$S_{bal} \propto \sin(\theta) \frac{1}{1 + \cos(\theta) + (1 - \cos(\theta)) \frac{T_1}{T_2}} \exp^{-\frac{TE}{T_2}}. \quad (2.66)$$

It can be shown that this is maximum at the optimal angle

$$\theta = \cos^{-1} \left(\frac{T_1/T_2 - 1}{T_1/T_2 + 1} \right). \quad (2.67)$$

Therefore the optimal angle for bTFE is dependent on the ratio of T1/T2.

2.3.6 Diffusion Weighted Imaging

Diffusion is the random motion of molecules due to their thermal energy. It was first observed as Brownian motion by Robert Brown (16) and then later described mathematically by Albert Einstein (17). The diffusion coefficient, D , gives the rate of flux of molecules. For example free water collides with a relatively low number of molecules in a given amount of time and so its diffusion distance is relatively long. In comparison a molecule in a viscous fluid will undergo many more collisions and so its diffusion distance will be much shorter. Therefore free water has a much higher diffusion coefficient ($3.0 \times 10^{-3} \text{ mm}^2/\text{s}$) than biological tissue ($\approx 1.0 \times 10^{-3} \text{ mm}^2/\text{s}$). The diffusion coefficient, D , can be described by the Stokes-Einstein equation (17).

$$D = \frac{k_B T}{6\pi r \eta}, \quad (2.68)$$

where T is the temperature of the system, r is the radius of the particle and η is the viscosity of the medium. From this coefficient the distance that a molecule in a liquid of temperature T would move in a particular time, t , can be calculated. In one dimension the distance moved by a molecule is given by

$$\sqrt{2Dt}. \quad (2.69)$$

It has been shown that the diffusion coefficient of a tissue can change with disease. In necrotic tissue the cellularity is reduced and the cell membrane integrity decreases which causes the diffusion coefficient to be increased (18). In inflammation and highly cellular tumours the intracellular space is reduced and therefore the diffusion coefficient is also decreased (19, 20). Structures such as nerves allow diffusion to occur more freely in one direction than others which creates an anisotropy in the diffusion coefficient. In this thesis only the average diffusion coefficient over three dimensions is used but the anisotropy of diffusion coefficients in different directions can provide insight into structures such as tracts in the brain.

2. MRI Theory

In 3D the diffusion tensor can be expressed as

$$\mathbf{D} = \begin{pmatrix} D_{xx} & D_{xy} & D_{xz} \\ D_{yx} & D_{yy} & D_{yz} \\ D_{zx} & D_{zy} & D_{zz} \end{pmatrix}. \quad (2.70)$$

For a perfectly isotropic system the diffusion tensor is given by

$$\mathbf{D} = \begin{pmatrix} D & 0 & 0 \\ 0 & D & 0 \\ 0 & 0 & D \end{pmatrix}. \quad (2.71)$$

The diffusion acquisition sequence makes use of a pair of identical diffusion gradients either side of a 180° pulse (Figure 2.30).

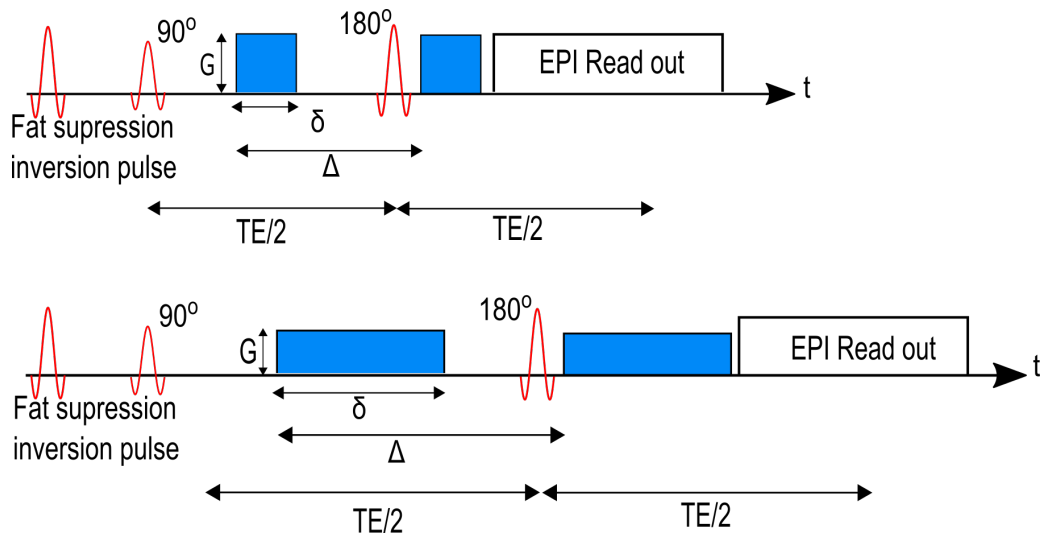


Figure 2.30: Diffusion weighted imaging pulse sequence. The diffusion weighting, b , is related to the gyromagnetic ratio of the nuclei, γ , the strength of the gradient G , the interval between the two gradients Δ , and the length of each gradient δ . If the echo time is increased the length of the gradients is also increased.

2. MRI Theory

The diffusion weighting, b , for a trapezoid set of pulses (Figure 2.30) is given by

$$b = \gamma^2 G^2 \left[\delta^2 (\Delta - \delta/3) + \epsilon^3/30 - \delta\epsilon^2/6 \right]. \quad (2.72)$$

The application of the first gradient causes the spins to dephase. The second gradient then causes rewinding of the phase caused by the first gradient. This rewind only occurs perfectly if the spins do not move between the gradient applications. This means that any spins that have moved will experience a different gradient after the 180° and will not experience a full rewind of the dephasing. This results in attenuation of the signal. The result of this is that tissue with a low diffusion coefficient will appear bright on the MR image and anything with a high diffusion coefficient will appear dark. The phrase Apparent Diffusion Coefficient (ADC) is used rather than diffusion coefficient as the measured value is dependent on the experimental conditions. The signal measured can be expressed as

$$M = M_0 \left(1 - \exp\left(-\frac{TR}{T_1}\right) \right) \exp\left(-\frac{TE}{T_2}\right) \exp^{-b.ADC}. \quad (2.73)$$

This is often simplified to

$$M = M_0' \exp^{-b.ADC}. \quad (2.74)$$

From equation 2.74 the ADC can be calculated, assuming a mono exponential decay, as

$$ADC = -\frac{1}{b} \ln \left(\frac{M}{M_0'} \right). \quad (2.75)$$

By measuring the signal at a range of different b values and fitting a straight line to the log of the signals ADC can be measured.

As seen from equation 2.73 the magnetization is dependent on TR, T1, TE, T2, b and ADC. In traditional DWI sequences TR and TE are chosen so that the T1 and T2 terms are constant and don't need to be taken into account. However, if T2 is long enough T2 shine through can occur for high ADC tissues. The long T2 means that the tissue appears bright even if its ADC is high, a

common example of this in abdominal imaging is the spinal fluid appearing bright on DWI scans even though the diffusion coefficient of fluid is high.

DWI traditionally uses an EPI readout to overcome the effects of motion on phase encoding which would be exaggerated by the bipolar diffusion gradients. Whilst being fast, EPI has the disadvantage of distortions occurring in the readout direction and suffers from susceptibility artefacts. EPI is generally less 'blurred' than FSE and has a very high SNR per unit time.

Diffusion Weighted Whole Body Imaging with Background Body Suppression, also known as DWIBS, is a commonly used free breathing DWI sequence first proposed by Takahara *et al* (21). Originally it was thought that using free breathing during diffusion weighted scans would compromise the image quality as respiratory motion is much larger than motion due to diffusion. However Takahara *et al* used DWIBS finding that high quality images were achievable. The image quality in DWIBS is not diminished by free breathing as the motion caused by respiration is coherent within a voxel. This results in the phase change being the same throughout the voxel and so the signal is phase shifted but not attenuated. Diffusion motion is incoherent within a voxel and so the phase changes lead to signal attenuation.

DWI scans can be used to help identify low ADC structures that would otherwise not be easily identified using other acquisition methods. In this thesis such a problem arose when imaging lymph nodes and DWI was employed to identify lymph nodes and measure their T2 value.

On a standard Philips DWI sequence if the echo time is increased the gradients are lengthened and their amplitude reduced (Figure 2.30). However, in order to measure T2 from a DWI, fixed diffusion gradients around the 180° pulse are required. This is due to the fact that ADC is dependent on the time over which the diffusion is measured as the probability of the nuclei colliding with structures within the cell increases with the measurement time. Therefore both the ADC and T2 should be measured using gradients with a consistent diffusion time. To measure T2 using a DWI sequence a new sequence had to be programmed on the scanner. The use of the in-house programmed sequences is

2. MRI Theory

commonly referred to as using a “patch”. The patch in this case allowed full user control of the strength and timing of the diffusion gradients. An example of this is shown in Figure 2.31.

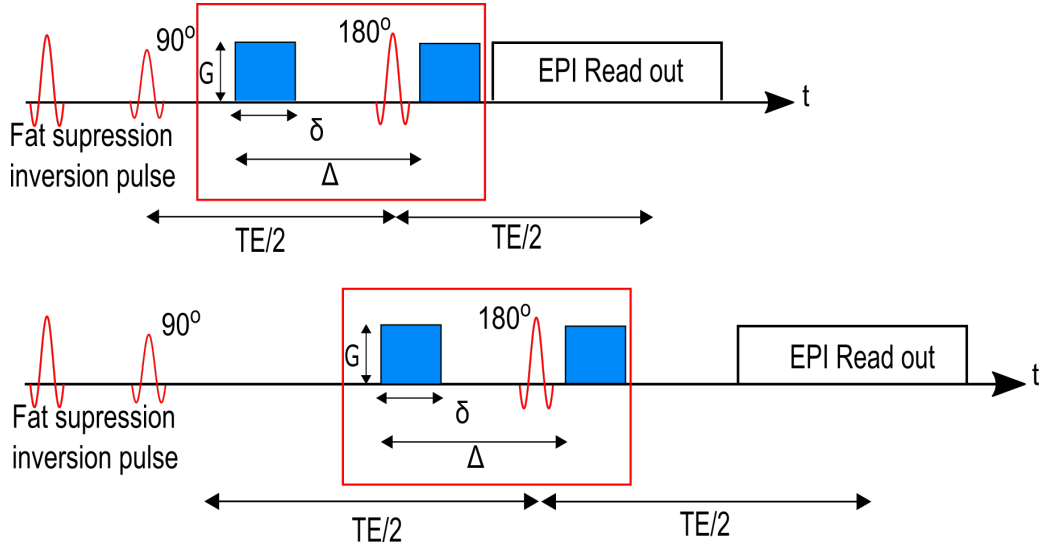


Figure 2.31: Diffusion weighted image sequence used to calculate T2 with a fixed diffusion weighting. All diffusion gradient parameters (those inside the red box) are fixed when the echo time is changed. The fixing of the gradients required the coding of the sequence on the scanner to be altered as the original code changes the gradients which changes the diffusion time.

When performing DWI with a low b value perfusion effects must be taken into account as they may contribute to signal loss (Figure 2.32). The effects of perfusion on the magnetization can be seen as a faster than expected attenuation of the signal at low b values. These effects are collectively known as Intra Voxel Incoherent Motion (IVIM) and can be included in the DWI signal as

$$S = S_0 f e^{-b(D^*+D)} + (1 - f) e^{-bD} \quad (2.76)$$

where f is the fraction of the voxel that is occupied by perfusing blood, D is the diffusion coefficient, D^* is the pseudodiffusion coefficient and describes dephasing due to perfusion.

At high b values an effect known as kurtosis comes into effect and reduces

the signal attenuation to a rate lower than expected. The kurtosis effect comes from the fact that in complex tissues the distribution of diffusion displacements does not follow a Gaussian distribution as they do in free water due to structural restrictions (e.g. cell walls). In this thesis the b values used do not reach high enough values to incorporate the kurtosis effect which adds an extra term to Equation 2.76.

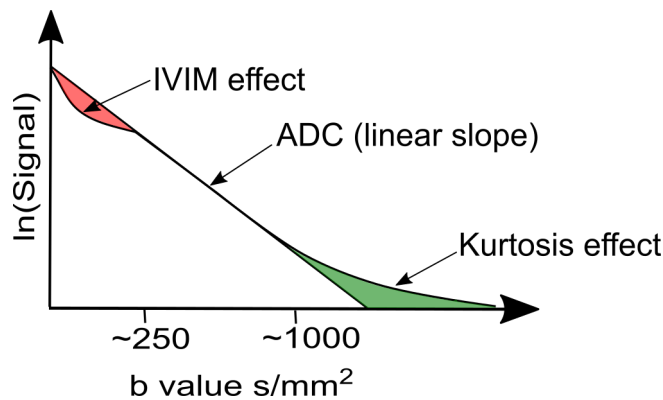


Figure 2.32: Diffusion over a range of b values with the IVIM effect shown at low b values and the kurtosis effect shown at high b values.

2.3.7 Spectroscopy

Magnetic Resonance Spectroscopy (MRS) differs from Magnetic Resonance Imaging in the fact that the aim is not to form an image of the tissue in the body but to analyze the chemical spectra of the tissue in a small spatial location. In spectroscopy the desired voxels are excited and the free induction decay sampled. Frequency encoding is not used as the frequency differences are used to produce a frequency spectra of the chemicals within the species (Figure 2.33). The peaks observed in the spectra allow for the chemical composition of the tissue to be determined. The spectra are traditionally displayed in parts per million rather than frequency as ppm is independent of field strength.

The area under each peak represents the amount of signal originating from a particular chemical. As water is the most abundant chemical in the body it is often suppressed to allow for smaller concentration chemicals to be identified.

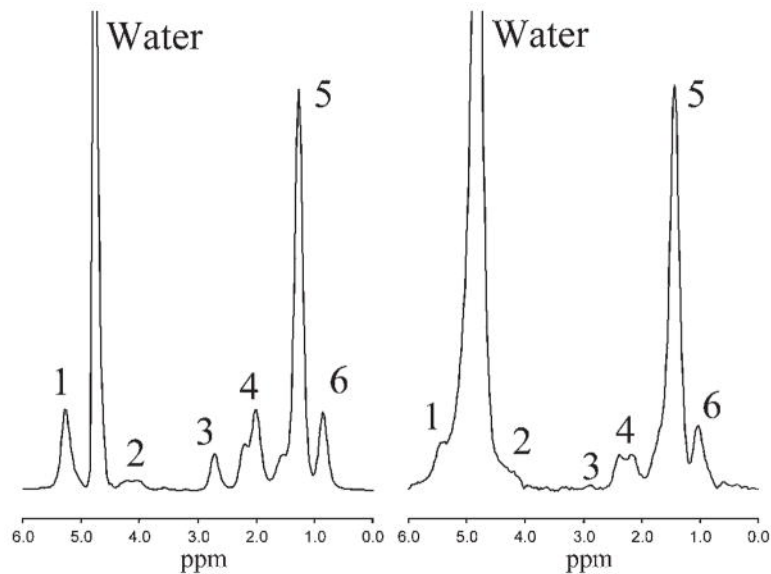


Figure 2.33: Fat spectra taken from Hamilton *et al* (22) showing the spectra in a fat emulsion phantom (left) and the liver from a patient with fatty liver disease (right). Fat peak assignment: 1, $-\text{CH}=\text{CH}-$ and $-\text{CH}-\text{O}-\text{CO}-$; 2, $-\text{CH}_2-\text{O}-\text{CO}-$; 3, $-\text{CH}=\text{CH}-\text{CH}_2-\text{CH}=\text{CH}-$; 4, $-\text{CO}-\text{CH}_2-\text{CH}_2-$ and $-\text{CH}_2-\text{CH}=\text{CH}-\text{CH}_2-$; 5, $-\text{CO}-\text{CH}_2-\text{CH}_2-$ and $-(\text{CH}_2)_n-$; 6, $-(\text{CH}_2)_n-\text{CH}_3$. Of the six fat peaks resolvable by spectroscopy at 3T, *in vivo* peaks 1 and 2 are buried within the water peak, and peak 3 is small and rarely seen in the human liver clinically.

The frequency shift in ppm is given by

$$\delta = \frac{\text{Chemical shift (Hz)} \times 10^6}{\text{Reference frequency}} \quad (2.77)$$

with the reference frequency being that of a proton.

2.3.8 Fat Suppression Techniques

Fat can often cause artefacts in images due to misregistration of its signal. Therefore fat suppression techniques are often used, especially in the abdomen. Two commonly used fat suppression techniques are STIR and CHESS. STIR (Short TI Inversion Recovery, Figure 2.34) is an inversion recovery sequence that makes use of the T1 of fat in order to suppress it. A 180° pulse is applied inverting all protons in the imaging plane. A wait time, corresponding to the

null point in the fat signal in the longitudinal plane, is then applied before the main image acquisition begins. This means that when the excitation pulse is applied the longitudinal signal of fat is 0 and therefore the fat signal is not excited and is suppressed from the image. STIR images also suppress any tissue with a similar T1 to fat, which in the case of this thesis is a benefit as the bowel has a similar T1 to fat and the STIR pulse suppresses fat and bowel in images aimed at visualising lymph nodes.

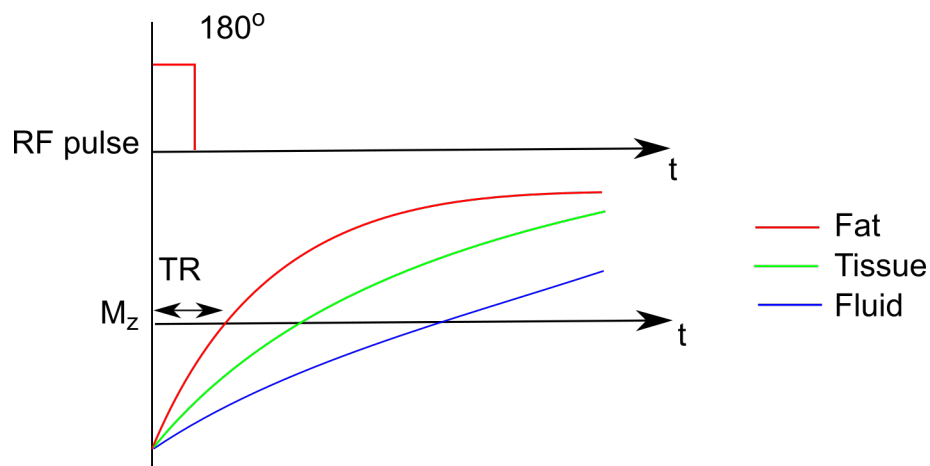


Figure 2.34: Schematic of the inversion recoveries used in STIR fat suppression.

The second commonly used fat suppression method is known as CHESS (CHEmical Shift Selective pulse, Figure 2.35). This technique makes use of the chemical shift of fat. An RF pulse with the resonant frequency of fat, and a narrow bandwidth is applied to the imaging plane, tipping the fat signal into the transverse plane. Immediately after this pulse the imaging sequence begins. This means that there is no longitudinal fat magnetization to excite during the acquisition and thus fat is suppressed from the image. To prevent the fat signal from producing an echo spoiler gradients are used to dephase the fat signal.

Philips' systems offer two other fat suppression techniques called SPIR (Spectral Presaturation with Inversion Recovery) and SPAIR (Spectral Attenuated Inversion Recovery). Both techniques are hybrid methods which combine the STIR and CHESS principles. An inversion pulse is applied at the the resonant

2. MRI Theory

frequency of fat (similar to CHESS) and then an inversion delay time is waited before the main imaging sequence is applied (similar to STIR). SPAIR differs from SPIR in that it uses an adiabatic inversion pulse making it less sensitive to B1 inhomogeneities. In this thesis the SPIR fat suppression technique is used in diffusion weighted imaging of the lymph nodes (Chapter 4).

2. MRI Theory

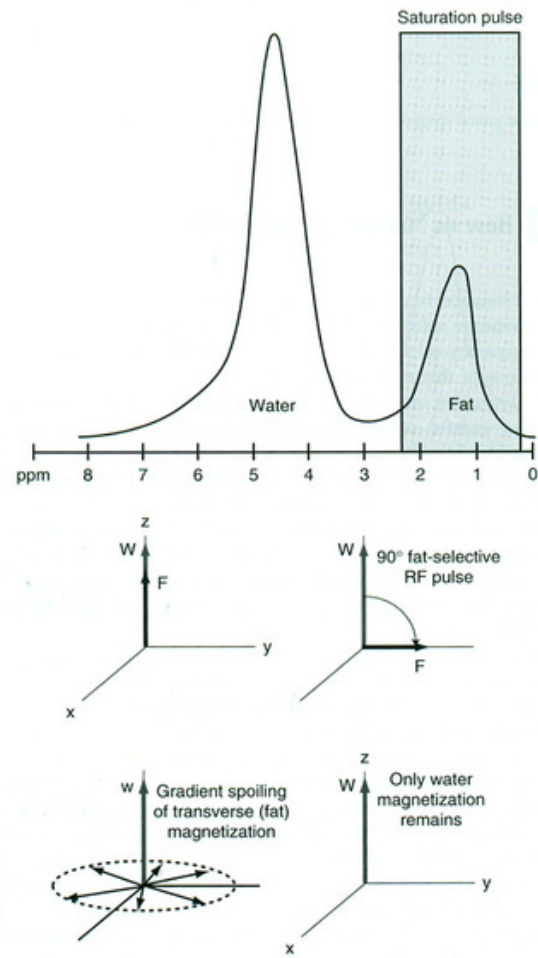


Figure 2.35: CHES fat suppression. The fat (or water) peak may be selectively saturated by a narrow-bandwidth radio frequency (RF) pulse. Fat-Sat pulses on most commercial images function according to the general method pictured here (23).

2.3.9 Dixon Imaging

Dixon imaging makes use of the chemical shift properties of fat in order for separate fat and water images to be produced. The Dixon method is used in Chapter 6 of this thesis as a fat quantification technique. The method, first proposed in 1984 (24), makes use of the different resonant frequencies of fat and water. Due to the different resonant frequencies, fat and water signals go in and out of phase. Two images are collected in traditional Dixon imaging, the first being at an echo time when fat (F) and water (W) are at opposed phases (OP) and the second when they are in phase (IP) (Figure 2.36). The signals from these can be written as

$$\begin{aligned} S_{IP} &= S_W + S_F \\ S_{OP} &= S_W - S_F. \end{aligned} \tag{2.78}$$

Rearranging these, fat and water only images can be calculated as

$$\begin{aligned} S_W &= \frac{1}{2}(S_{IP} + S_{OP}) \\ S_F &= \frac{1}{2}(S_{IP} - S_{OP}). \end{aligned} \tag{2.79}$$

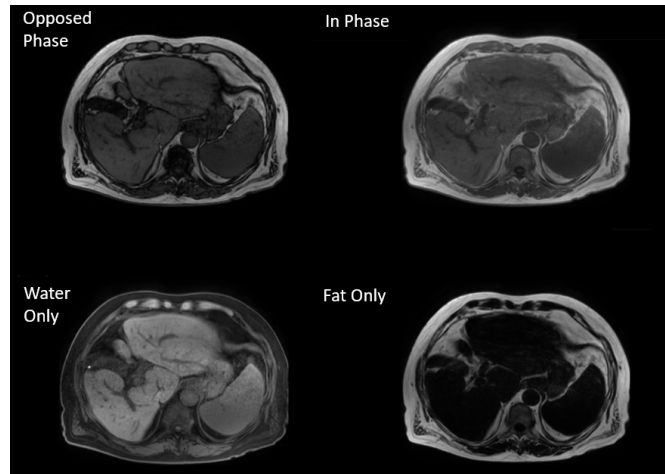


Figure 2.36: mDixon images over the liver.

2. MRI Theory

Modern Dixon techniques use 3 echoes, the third being at opposed-phase which allows for corrections of B_0 inhomogeneities. On Philips systems these are known as mDixon scans and the method of B_0 correction is unknown to users. mDixon acquisitions produce 4 images: in phase, out of phase, water and fat. Occasionally in these images fat and water can be misregistered causing a swap of the fat and water signals (Figure 2.37).

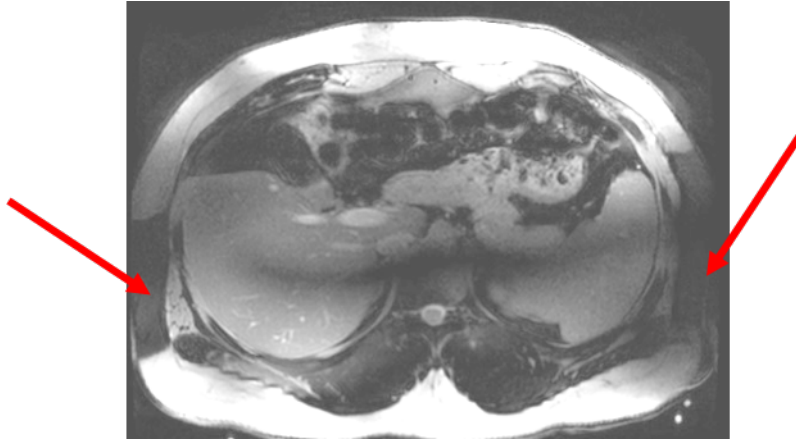


Figure 2.37: Fat only image acquired at 7T where fat and water have been misregistered. The red arrows show the dark areas indicating that the subcutaneous fat has been improperly registered. The liver in this image should appear dark.

Dixon imaging can also be used for more accurate fat quantification by collecting more echoes (usually 6 or 9). The signal from a single species in a voxel measured during Dixon imaging can be expressed as

$$S = S_0 e^{i\omega t} e^{-R2^* t} e^{i\psi t} e^{i\phi} \quad (2.80)$$

where ω is the resonant frequency, ψ is the frequency offset (the deviation of the magnetic field from B_0) and ϕ is the phase offset. Water is considered to be on resonance and thus $\omega_{water} = 0$.

Therefore when a voxel contains both fat and water the signal becomes

$$S = \left[W e^{-R2_w^* t} + \sum_1^n F_n e^{i\omega_n t} e^{-R2_f^* t} \right] e^{i\psi t} e^{i\phi} \quad (2.81)$$

where W and F are the signals of fat and water at $t=0$ respectively. Each of the n fat peaks have different resonant frequencies, ω_n .

2.3.10 Field Mapping

Quantitative MRI is reliant on homogeneous and accurate B_0 and B_1 fields. Unfortunately due to hardware imperfections and effects of the sample on the magnetic field B_0 is never perfectly homogeneous. Achieving homogeneous radio frequency deposition is dependent on the size and shape of the participant undergoing the scan. Corrections to the B_1 field are made using shimming however these are not always sufficient to achieve homogeneous RF deposition. Quantitative measures are reliant on B_0 and B_1 being consistent with the assumed values. Maps of the two respective fields are often calculated to check this assumption, and in some cases, the measured field maps are used in place of the assumed values. Field mapping is used in Chapters 5 and 6 of this thesis where accurate flip angles and the B_0 field are required for quantitative measures of the GI system.

B_0 Mapping

In quantitative MRI knowledge of the exact magnetic field experienced by the nuclei within a voxel is often required. A B_0 map provides this information by calculating the variation in the magnetic field across the field of view. The map is acquired using a gradient echo sequence with two different echo times separated by a time ΔTE . The difference in the phase, $\Delta\phi$, of the nuclei at the two different echo times, is directly related to the B_0 field inhomogeneity and is given by

$$\Delta\phi(r) = \gamma\Delta B_z(r)\Delta TE. \quad (2.82)$$

By measuring the phase difference the local deviation of the B_0 field can be calculated as

$$\Delta B_z(r) = \frac{\Delta\phi(r)}{\gamma\Delta TE}. \quad (2.83)$$

B₁ Mapping

B₁ mapping is necessary when the angle through which the magnetization vector is rotated needs to be precisely known. A common method of B₁ mapping is the dual TR method or 'Actual Flip Angle Imaging' method developed by Yarnykh (25). The acquisition (Figure 2.38) consists of two identical RF pulses, the first followed by TR₁ and the second by TR₂. The method requires that TR₁ < TR₂ < T1, allowing for the assumption that relaxation effects are negligible to be made and the magnetization to be at steady state. The solution to the Bloch equations for the steady state magnetization before the excitation pulses are as follows

$$M_{z,1} = M_0 \frac{1 - E_2 + (1 - E_1)E_2 \cos \alpha}{1 - E_1 E_2 \cos^2 \alpha} \quad (2.84)$$

$$M_{z,2} = M_0 \frac{1 - E_1 + (1 - E_2)E_2 \cos \alpha}{1 - E_1 E_2 \cos^2 \alpha} \quad (2.85)$$

where $E_{1,2} = \exp^{-TR_{1,2}/T1}$.

The signal measured after each of the excitation pulses is given by

$$S_{1,2} = M_{x1,2} \exp^{-TE/T2^*} \sin \alpha. \quad (2.86)$$

Using the first order approximation that $\exp(x) = 1 + x$, and the assumption that TR₁ < TR₂ < T1 it can be shown that the ratio of the two signals, r , is given as

$$r = \frac{s_2}{s_1} \approx \frac{1 + n \cos \alpha}{n + \cos \alpha} \quad (2.87)$$

where $n = TR_2/TR_1$. Therefore the actual flip angle that is applied during the sequence is given by

$$\alpha = \cos^{-1} \left(\frac{rn - 1}{n - r} \right). \quad (2.88)$$

The B₁ map can be used to correct for the flip angle assumed in any quantification.

Other B₁ mapping techniques exist such as DREAM (Dual Refocusing Echo

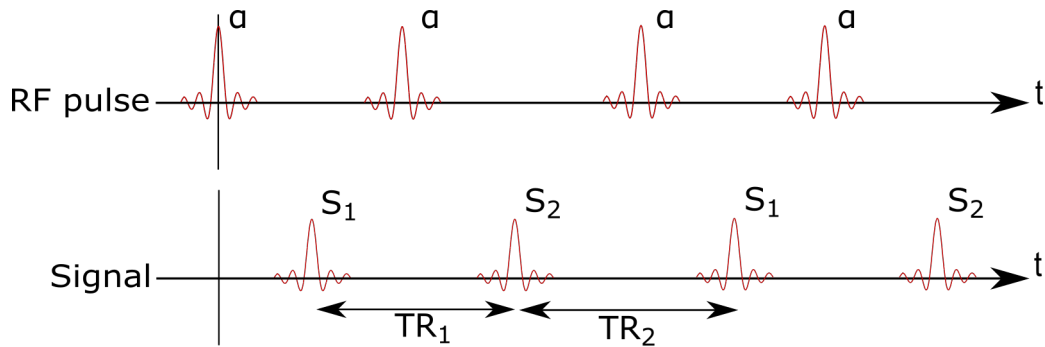


Figure 2.38: RF pulses used in a Dual TR sequence.

Acquisition Mode). This technique provides a faster method of B_1 mapping making it less sensitive to motion.

2.4 Conclusion of Chapter

This section introduced the principles of physics that underlie the MRI acquisition techniques and measurements that are used throughout this thesis. It has introduced the basics of NMR that are required to understand how MRI works. The techniques used in acquiring images were also discussed along with possible quantitative measures that may be of use in the gastrointestinal system including T1, T2, diffusion coefficient and fat quantification.

References

- [1] F Bloch. Nuclear Induction. *Phys. Rev.*, 70(7-8):460–474, oct 1946. doi: 10.1103/PhysRev.70.460.
- [2] E M Purcell, H C Torrey, and R V Pound. Resonance Absorption by Nuclear Magnetic Moments in a Solid. *Phys. Rev.*, 69(1-2):37–38, jan 1946. doi: 10.1103/PhysRev.69.37.
- [3] P Mansfield and P K Grannell. NMR 'Diffraction' in Solids? *Journal*

References

- of Physics C: Solid State Physics*, 6(22):L422—L426, nov 1973. doi: 10.1088/0022-3719/6/22/007.
- [4] P C Lauterbur. Image Formation by Induced Local Interactions: Examples Employing Nuclear Magnetic Resonance. *Nature*, 242(5394):190–191, mar 1973. ISSN 0028-0836. doi: 10.1038/242190a0.
- [5] E L Hahn. Spin Echoes. *Physical Review*, 80(4):580–594, nov 1950. ISSN 0031-899X. doi: 10.1103/PhysRev.80.580.
- [6] I Solomon. Relaxation Processes in a System of Two Spins. *Physical Review*, 99(2):559–565, jul 1955. ISSN 0031-899X. doi: 10.1103/PhysRev.99.559.
- [7] A N Garroway, P K Grannell, and P Mansfield. Image Formation in {NMR} by a Selective Irradiative Process. *Journal of Physics C: Solid State Physics*, 7(24):L457—L462, dec 1974. doi: 10.1088/0022-3719/7/24/006.
- [8] K P Pruessmann, M Weiger, M B Scheidegger, and P Boesiger. SENSE: Sensitivity Encoding for Fast MRI. Technical report.
- [9] M A Griswold, P M Jakob, R M Heidemann, M Nittka, V Jellus, J Wang, B Kiefer, and A Haase. Generalized Autocalibrating Partially Parallel Acquisitions (GRAPPA). *Magn Reson Med*, 47:1202–1210, 2002. doi: 10.1002/mrm.10171.
- [10] biac:pulsesequences:3t [Brain Imaging & Analysis Center]. URL <https://wiki.biac.duke.edu/biac:pulsesequences:3t>.
- [11] M Barth, F Breuer, P J Koopmans, D G Norris, and B A Poser. Imaging Methodology - Review Simultaneous Multislice (SMS) Imaging Techniques. *Magnetic Resonance in Medicine*, (75):63–81, 2016. doi: 10.1002/mrm.25897.

References

- [12] P Mansfield. Multi-Planar Image Formation using NMR Spin Echoes. *Journal of Physics C: Solid State Physics*, 10(3):L55—L58, feb 1977. doi: 10.1088/0022-3719/10/3/004.
- [13] A Elster. Chemical Shift Artifact Questions and Answers in MRI, 2018. URL <http://mriquestions.com/chemical-shift-artifact.html>.
- [14] A Haase, J Frahm, D Matthaei, and K-D Merboldt. FLASH Imaging. Rapid NMR Imaging Using Low Flip-Angle Pulses. Technical report, 1986.
- [15] A Oppelt, R Graumann, H Barfuss, H Fischer, W Hartl, and W Schajor. FISP - A New Fast MRI Sequence, 1986.
- [16] R Brown. *A Brief Account of Microscopical Observations Made ... on the Particles Contained in the Pollen of Plants, and on the General Existence of Active Molecules in Organic and Inorganic Bodies*. 1828.
- [17] A Einstein and A D Cowper. Investigations on the Theory of the Brownian Movement. Technical report.
- [18] T C Kwee, T Takahara, R Ochiai, R A J Nievelstein, and P R Luijten. Diffusion-weighted whole-body imaging with background body signal suppression (DWIBS): features and potential applications in oncology. *European Radiology*, 18(9):1937–1952, 2008. doi: 10.1007/s00330-008-0968-z.
- [19] P A Bonaffini, D Ippolito, A Casiraghi, V Besostri, C T Franzesi, and S Sironi. Apparent Diffusion Coefficient Maps Integrated in Whole-Body MRI Examination for the Evaluation of Tumor Response to Chemotherapy in Patients with Multiple Myeloma. *Academic Radiology*, 22(9):5–7, 2015. ISSN 10766332. doi: 10.1016/j.acra.2015.05.011.
- [20] S Kawada, T Takahara, T Ichikawa, H Yamamuro, Y Nagata, T Nagata, T Aizawa, T C Kwee, K Mori, Y Imai, and Philips Healthcare. The Apparent Diffusion Coefficient (ADC) as a Potential Marker of Inflammation Associated with Body Abscesses. Technical Report 1, 2017.

References

- [21] T Takahara, Y Imai, T Yamashita, S Yasuda, S Nasu, and M Van Cauteren. Diffusion Weighted Whole Body Imaging with Background Body Signal Suppression (DWIBS): Technical Improvement using Free Breathing, STIR and High Resolution 3D Display. *Radiation medicine*, 22(4):275–282, 2004. ISSN 0288-2043.
- [22] G Hamilton, T Yokoo, M Bydder, I Cruite, M E Schroeder, C B Sirlin, and M S Middleton. In Vivo Characterization of the Liver Fat 1H MR Spectrum. *NMR in biomedicine*, 24(7):784–90, aug 2011. ISSN 1099-1492. doi: 10.1002/nbm.1622.
- [23] A Elster. Fat Sat Pulses Questions and Answers in MRI.
- [24] W T Dixon. Simple Proton Spectroscopic Imaging. *Radiology*, 153(1):189–194, oct 1984. ISSN 0033-8419. doi: 10.1148/radiology.153.1.6089263.
- [25] V L Yarnykh. Actual Flip-Angle Imaging in the Pulsed Steady State: A Method for Rapid Three-Dimensional Mapping of the Transmitted Radiofrequency Field. *Magnetic Resonance in Medicine*, 57(1):192–200, jan 2007. ISSN 07403194. doi: 10.1002/mrm.21120.

3 The Gastrointestinal System

3.1 Introduction

The digestive system is split into two groups, the gastrointestinal tract (GI), a continuous structure that runs from the mouth to the anus, and the accessory digestive organs (Figure 3.1). It serves to digest food, absorb nutrients and excrete waste. The accessory digestive organs (excluding the teeth) lie off the gastrointestinal tract and are joined through ducts which allow secretions from the organs into the tract (1). Overall the digestive system has six basic functions: ingestion, secretion, mixing and propulsion, digestion, absorption and defecation. During gastrointestinal disease the structure of the tract and its functions can be disrupted. Common symptoms of gastrointestinal problems can often include nausea, constipation, diarrhoea and malabsorption (2).

3.2 Ingestion and the Stomach

The GI tract starts at the mouth where ingestion of food and liquid begins. In the mouth digestion is initiated by two different mechanisms. The teeth and tongue begin the mechanical breakdown of food while the enzyme amylase, which is found in saliva, starts the chemical breakdown of carbohydrates (4). At this stage saliva acts as a lubricant to assist the passage of food from the mouth into the oesophagus. The pharynx links the oral cavity to the oesophagus and provides the site for the start of the swallowing process. The oesophagus is a tubular structure which connects the pharynx to the stomach. A series of contractions and relaxations of muscles along the oesophagus continue the swallowing process, transporting food into the stomach.

The stomach, an expandable bag, provides the location for the next stage of digestion and also acts as a storage space for food (5). The storage space is required as the intestines digest and absorb food at a much slower rate than the rate at which it can be consumed. Whilst in the stomach, the food is mixed with secretions from the gastric glands by peristaltic movements of the stomach walls.

3. The Gastrointestinal System

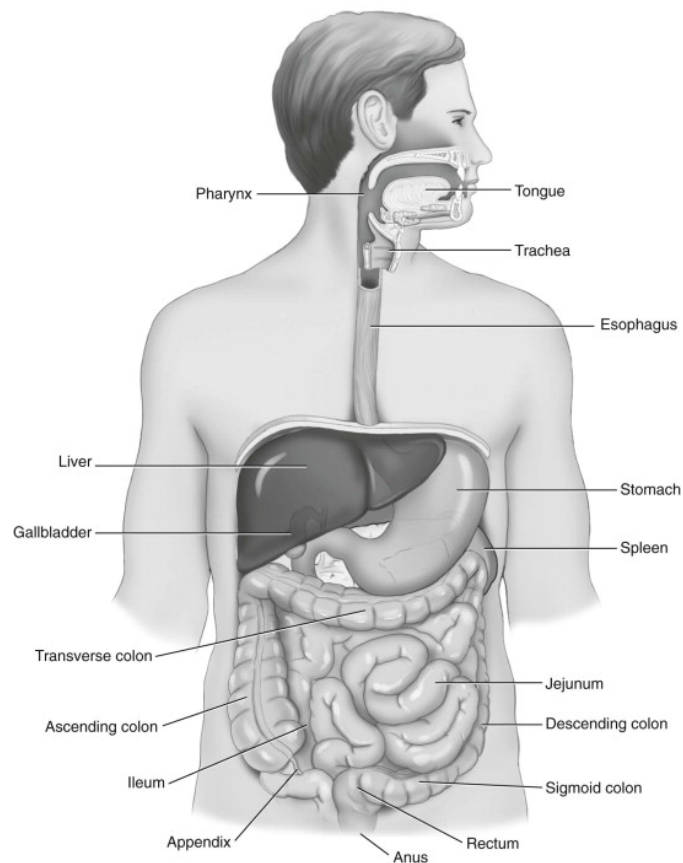


Figure 3.1: The gastrointestinal tract with key features and organs labelled (3).

This dilution causes the contents of the stomach to turn from the semisolid state they are received in into a liquid called chyme. In the stomach, enzymes such as pepsin begin the breakdown of proteins which continues in the small intestine. The pyloric sphincter connects the stomach with the duodenum, the start of the small intestine. With each wave of mixing in the stomach the pyloric sphincter allows small amounts of chyme to pass into the duodenum.

3.3 The Liver

The liver is one of the largest organs in the body and is comprised of two main lobes, the large right lobe and the smaller left lobe. Each of these is split into many smaller lobes called lobules. The blood supply to the liver is served by

3. The Gastrointestinal System

the hepatic artery, with the hepatic vein removing the blood. The portal vein delivers blood from the intestines to allow the liver to break down nutrients and remove toxins.

A large portion of the liver consists of hepatocytes (liver cells) which absorb nutrients from the blood and also remove potentially harmful substances. The liver has many functions including processing nutrients absorbed in the GI tract, regulating blood volume, maintaining levels of lipids, cholesterol and glucose in the body and assisting the immune system (1). Nutrients that are broken down in the liver are transported to the rest of the body via the hepatic vein. The liver also serves an important role in immunity. It provides a location to detect and destroy pathogens that are absorbed through the GI tract.

3.4 The Gall Bladder and the Pancreas

The gall bladder and the pancreas are accessory organs of the digestive tract and digestion in the small intestine is reliant on both.

The gall bladder is a sac that sits beneath the liver and can store around 50 mL of bile (6). Bile contains acids which help emulsify lipids in the small intestine to assist enzyme action. Bile also contains aged red blood cells, the contents of which are either recycled and absorbed in the intestines or excreted in faeces.

The pancreas is a large gland that produces secretions including insulin and glucagon. Ducts connect the pancreas to the duodenum where its secretions join the chyme in the GI tract. The secretions from the pancreas are alkaline and act to alter the acidic pH of the chyme leaving the stomach so that intestinal enzymes can function in the chyme (5). It also contains some protein and carbohydrate digesting enzymes (1).

3.5 The Small Intestine

The small intestine provides the location for most of the digestion and absorption in the GI tract. In order to maximise absorption along the intestine, the surface

3. The Gastrointestinal System

layer of the wall contains many folds called villi (Figure 3.2). The small intestine is a long tube split into three main sections: the duodenum, the entrance to the small intestine, followed by the jejunum and finally the ileum (6). The duodenum releases the hormone secretin into the blood stream which, in turn, triggers the secretion of pancreatic juices into the duodenum. The jejunum and ileum are mobile and are joined to the abdominal wall by the mesentery. The jejunum is located in the upper part of the abdominal cavity and has a thicker wall than the ileum. In the jejunum digestion and secretion of enzymes occur along with the absorption of fully digested carbohydrates and proteins. In the ileum the primary function is to absorb vitamin B12, bile salts and other nutrients not absorbed by the jejunum. The final section of the ileum, known as the terminal ileum connects the small intestine with the large intestine (1).

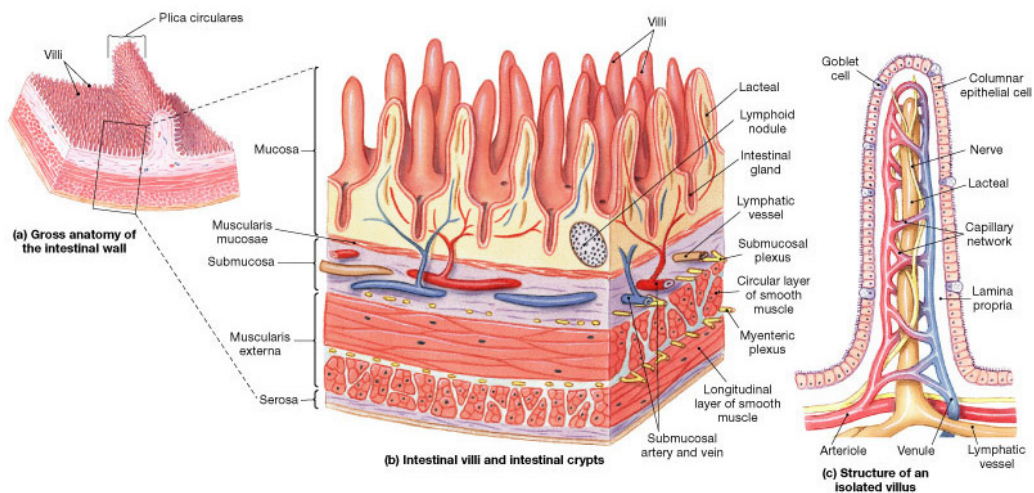


Figure 3.2: The villi along the wall of the small intestine (7).

3.6 The Large Intestine

There are four main sections of the large intestine: the cecum, colon, rectum and the anal canal. The terminal ileum is connected to the cecum via the ileocecal sphincter. Here the process of compression of food material into faecal matter begins (3). Attached to the lower end of the cecum is the appendix,

3. The Gastrointestinal System

composed of lymphatic tissue the appendix plays a role in immunity (5). Above the ileocecal sphincter the cecum joins with the colon, which is in turn split into four segments: the ascending, transverse, descending and sigmoid colon. The main function of the colon is to absorb water and electrolytes, any products not absorbed by this point then become faecal matter which is stored in the rectum (6). Faecal matter finally passes through the rectum and into the anal canal for excretion (1).

3.7 The Structure of the GI Tract

The GI tract has the same basic structure throughout its length. The tract has four main layers: the mucosa, submucosa, muscularis and serosa (Figure 3.3).

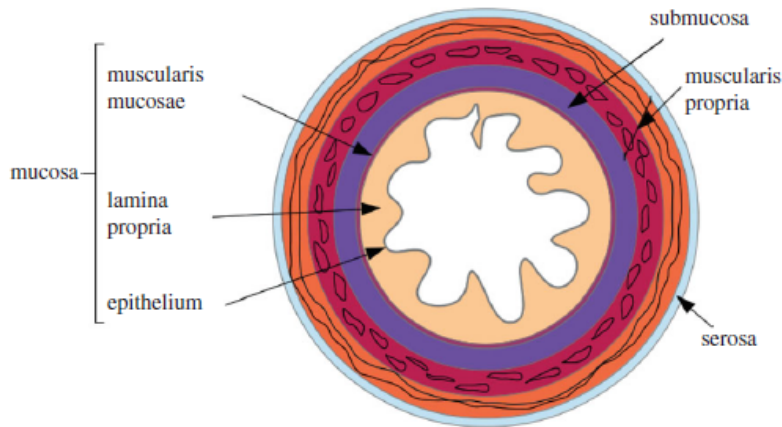


Figure 3.3: The structure of the GI tract with the main layers labelled (8).

The mucosa is the innermost layer of the tract and is split in turn into three layers: the epithelium, the lamina propria and the muscularis mucosa. The epithelium is the part of the tract that is in contact with the contents of the lumen which, in the small intestine forms the many folds in the surface (8). The lamina propria contains the blood vessels and lymphatic capillaries (see section 3.9). The muscularis mucosa is a muscle layer (1).

The submucosa contains the large blood and lymphatic vessels along with nerves (5). The muscularis contains muscle which helps the breakdown of food

and propels the contents along the GI tract. Finally the serosa is the outer layer of connective tissue and epithelial cells (1).

3.8 Diseases of the GI Tract

Inflammation can be split into two categories; acute inflammation and chronic inflammation. Acute inflammation is a healthy response by the body which helps recovery after injury whilst chronic or recurrent inflammation can be harmful to the body (3). In this thesis 6 chronic/recurrent inflammatory gastrointestinal diseases were investigated, the mechanisms of which are detailed in brief below.

3.8.1 Coeliac Disease

Coeliac disease is an autoimmune disease in which the body mistakes gluten for a harmful substance. The body attacks the gluten resulting in damage to the small intestine and chronic inflammation (9). The prevalence of the disease is increasing with current figures quoting around 1/100 in the western world. Common symptoms include diarrhoea, abdominal pain, bloating and constipation (10). Testing for the disease may involve looking at antibodies in the blood, genetic testing or a biopsy. The immune response is caused when gliadin, a protein found in gluten, undergoes a chemical reaction with the enzyme transglutaminase. It is transglutaminase that the immune system mistakenly responds to (11). The immune response causes atrophy of the intestinal villi which in turn causes the symptoms of coeliac disease. The current treatment for coeliac disease is a gluten free diet for the rest of the patient's life (12).

3.8.2 Crohn's Disease

Crohn's disease is an inflammatory disease affecting mainly the tissue of the bowel, although extra-intestinal occurrences of the disease have been found. There is no known cause of Crohn's disease but the current consensus is that the immune system and genetic factors may both play a role. Symptoms can include diarrhoea, stomach ache, blood in stool, tiredness and weight loss. Complica-

3. *The Gastrointestinal System*

tions of the disease can include ulcers, fistulas, malnutrition and an increased risk of colon cancer. Diagnosis mainly occurs before the age of 40, with the most common locations of disease manifestation being in the terminal ileum and the colon (13). Crohn's disease is currently diagnosed using a combination of several procedures which can include colonoscopies, CT scans, MRI scans and endoscopies (14). The inflammation in Crohn's disease is described in the literature as 'segmented granulomatous' (15). Segmented refers to the fact that the disease is not continuous along the bowel but rather occurs in patches. Granulomatous refers to the type of inflammation that is seen in the tissue and is defined by the presence of certain cells including histiocytes and leukocytes (16). Currently no cure exists for Crohn's disease. Treatment may take one of several forms including steroids (to reduce the inflammation), immunosuppressants and surgery amongst other methods (17).

3.8.3 Diverticulitis

Diverticula are small bulges or pockets that occur along the intestines and stick outwards. The diverticula themselves do not always cause symptoms (Figure 3.4). Once symptoms occur the patient is said to have diverticula disease or diverticulosis. Symptoms can include abdominal pain, bloating, constipation and diarrhoea amongst others (18). Prevalence of diverticula increases with age with a >50% prevalence in those over the age of 50 in the western world. Diverticula are thought to form when weak sections of the bowel wall are forced outwards by high pressures caused by dysmotility. Diverticulitis refers to the inflammation of the diverticula which can cause increased and often more severe symptoms. Inflammation is thought to occur when the diverticula become blocked off, allowing bacteria to ferment. This in turn increases the pressure in the diverticula, which causes pain (11). Complications can occur if the excessive pressure causes perforation. Treatment for diverticulitis is usually a course of antibiotics although surgery may be required for severe cases (19).

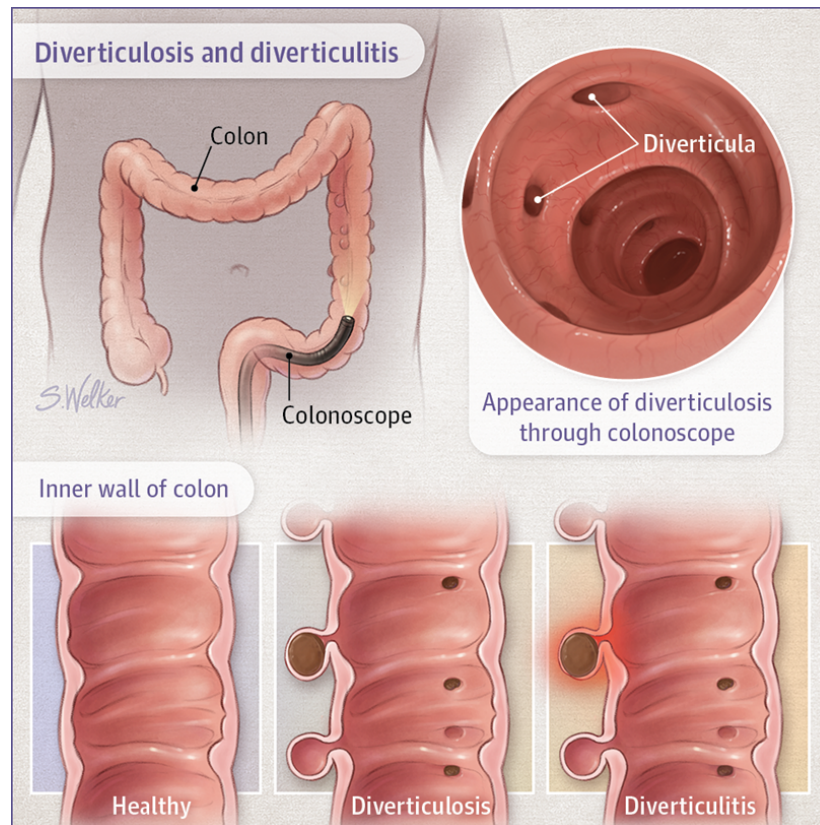


Figure 3.4: Diverticula are pockets of bowel that line the intestinal tract. When the presence of non-inflamed diverticula are found the patient is said to have diverticulosis. If the diverticula become inflamed the patient is said to have diverticulitis (18).

3.8.4 Helicobacter Pylori

Helicobacter pylori (H pylori) is a bacteria that is well suited to living in an acidic environment such as the human stomach. Its prevalence ranges from 20% to 80% and it is found throughout the world (20). Most carriers of the bacteria do not show any symptoms of having H pylori but those who do often present with abdominal pain, nausea and loss of appetite amongst others symptoms. Complications can include ulcers, inflammation of the stomach lining and stomach cancer (4). Tests for the infection include breath tests, stool tests and blood tests. H pylori colonises the gastric mucosa with the consequence of chronic

3. *The Gastrointestinal System*

gastritis and inflammation of the stomach lining. *H pylori* can bring about cell death, cell proliferation (the process that increases the number of cells and is higher in tumours) and destruction of cell junctions (21). The infection is treated with antibiotics (4).

3.8.5 Hepatitis B and C

Hepatitis is the inflammation of liver tissue. There are several causes of hepatitis including the hepatitis B and hepatitis C viruses, both of which are diagnosed with a blood test.

Hepatitis B is spread through blood or bodily fluids (22). In epidemic areas, which includes China and Africa, the prevalence is around 50% (11). Hepatitis C has a prevalence of around 0.5% in the UK but is much higher in countries such as Egypt and eastern European countries (23). The virus is most commonly spread through sharing needles and poor health care practises. For both viruses there are often no symptoms however after long exposure (~3 months) flu like symptoms can occur (11). The viruses invoke an immune response in the host which in turn causes inflammation and liver fibrosis. It can also promote carcinoma in the hepatic cells (24). In patients with no symptoms the body's natural defences can fight off the infection. Chronic hepatitis patients are given medication to keep control of the virus but they may not cure the virus (11).

3.8.6 Liver Cirrhosis

Liver cirrhosis is the final stage of scarring of the liver that can be caused by long term liver damage. For example fatty liver disease, hepatitis and alcoholism can all cause cirrhosis. Fibrosis is the precursor of cirrhosis and is defined as the accumulation of extra cellular matrix (ECM) proteins (25). Non-alcoholic fatty liver disease is the leading cause of cirrhosis in the western world. After undergoing injury the liver regenerates and replaces the damaged cells. During the recovery, inflammatory responses occur and ECM proteins are deposited in the liver, including collagen. Eventually with repeated damage the normal liver tissue is replaced with the collagen becoming cirrhotic and is then said to be in

the final stage of liver scarring. Degeneration of the liver function and necrosis of the liver cells are common to cirrhosis regardless of the initial cause of the liver damage (26). Symptoms of liver cirrhosis do not always occur, but can include fatigue, jaundice and loss of appetite amongst many others. Diagnosis is usually by a blood test, biopsy, endoscopy or imaging. The scarring cannot be reversed but lifestyle changes or treating the underlying cause can prevent further scarring. In the worst cases of liver scarring a transplant is required (27).

3.9 The Lymphatic System

The lymphatic system is made up of a series of vessels, capillaries, ducts and nodes. Lymph capillaries have dead ends and are found in interstitial space (the area that surrounds cells). Interstitial fluid consists mainly of water, plasma proteins and electrolytes. The exact composition of the fluid depends on the local environment and can vary with disease and inflammation (28). The lymphatic capillaries drain the interstitial fluid into larger lymphatic vessels which, in turn, drain into the blood stream. Once the fluid enters the lymphatic system it is known as lymph. Lymphatic vessels are found in most areas of the body (Figure 3.5) excluding the brain, bone marrow and tissue which does not contain vasculature (e.g. cartilage) (29). Lymph drained from the right upper portion of the body enters the blood stream in the right brachiocephalic vein whereas lymph from the lower and upper left part of the body is drained into the left brachiocephalic vein (1). All lymph from the lower part of the body including the abdomen is drained through the thoracic duct. Before reaching the thoracic duct, lymph from the intestinal, hepatic and lumbar areas drains through the cisterna chyli, a sac like structure located at the lower end of the thoracic duct (30).

Unlike the vasculature system, the lymphatic system does not contain a pump to propel lymph through the vessels and capillaries. The lymphatic system instead relies on a series of valves, to prevent back flow of lymph, and pressure gradients for lymph propulsion. Flow into the capillaries is driven by pressure differences between the lymphatic system and the interstitium (30). An

3. The Gastrointestinal System

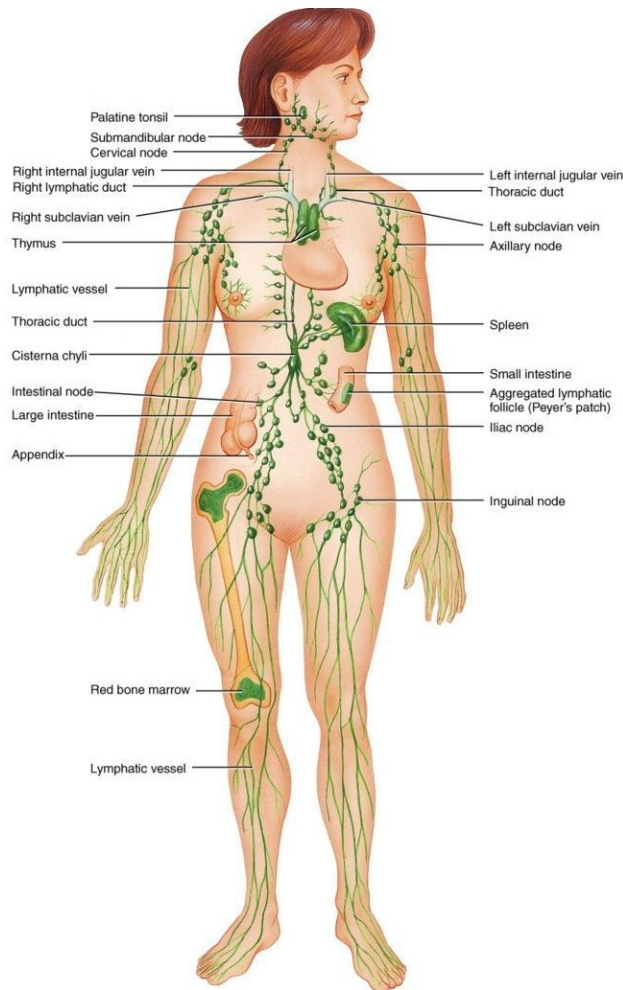


Figure 3.5: Lymphatics in the human body (1).

increase in the capillary pressure at the source of drainage causes the pressure in the system to increase and hence moves fluid further along the system. Interstitial fluid pressure can be influenced by many factors including exercise, blood pressure and tissue metabolism (31).

Lymph nodes (Figure 3.6), 0.1-2.5 cm kidney shaped structures, lie in groups along the routes of lymphatic vessels (32). Several vessels drain into a single node and the lymph leaves the node through one or two vessels. The nodes provide the location for the facilitation of immune responses to lymph.

Inside the nodes the lymph is screened by lymphocytes (33). Three types of

3. The Gastrointestinal System

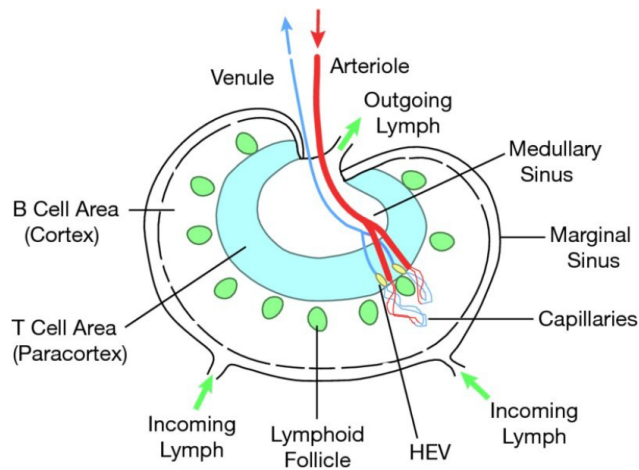


Figure 3.6: Lymph node structure (32). Red and blue arrows indicate blood flow into and out of the node.

lymphocytes exist, B cells, T cells and Natural killer cells. B cells are developed from stem cells shortly after birth (34). These immature B cells travel to the lymph nodes, liver and spleen. Once in the nodes, the B cells transform into plasma cells which can then secrete antibodies or immunoglobulins (1). T cells originate in bone marrow as pre-T cells, which then travel to the thymus to develop. These are then activated in the lymphatic tissue with different types of T cells performing different immune responses (33). Natural killer cells circulate in the blood and detect and destroy harmful substances before T cells arrive in the lymph nodes (35).

Lymph nodes have three main compartments: the superficial cortex, the deep cortex and the medulla. The superficial cortex is made up of mainly B cells, the deep cortex is made up of mainly T cells and the medulla contains plasma cells. In the medulla antibodies are secreted by the plasma cells to destroy antigens passing through the lymph node.

An inflammatory response occurs in the nodes when the presence of an antigen in the local tissue is detected. This response causes several changes in the local tissue with the aim of eliminating any toxins, micro-organisms or dead tissue. Blood flow to the area is increased, increasing the amount of interstitial fluid which, in turn, increases the amount of liquid drained by the

lymph capillaries (36). During disease the number of lymphocytes in the local nodes increases in order to assist in the destruction of antigens. This, along with the increase in the drainage volume, causes the nodes to swell. For example, the swelling of cervical nodes in the neck is commonly seen in cases of influenza (32). If the rate of drainage is insufficient during inflammation, oedema can occur (31). Because of the filtration process that occurs in lymph nodes and the fact that lymph flow is relatively slow, cancerous cells often remain in the nodes which can then become the site of secondary tumours (29).

In the small intestine specialised lymphatic capillaries exist to allow the transport of lipids from the gastrointestinal system into the blood stream (37). These specialised capillaries are called lacteals. The fluid transported through lacteals has a milky colour due to the presence of lipids, compared with the clear coloured lymph found elsewhere in the body. To distinguish this fat carrying lymph from ordinary lymph the fluid is often referred to as chyle (29). The small intestine also contains Payer's patches, lymphoid tissue clusters, similar to the tonsils. These specialised nodules are designed so that antigens pass through the surface and into the nodule. Antigens that are deemed to be harmful are killed by the lymphocytes and an immune response is triggered. Food allergies can occur if these nodes incorrectly 'decide' that a particular nutrient is dangerous (33). The lymphatics of the liver are rich in immune cells to tackle the influx of harmful substances that may be absorbed by the GI tract (38).

3.10 Conclusion of Chapter

The gastrointestinal system is a complex structure serving a crucial role within the body. Disruption of its homeostasis can cause a wide range of symptoms from fatigue to intense pain. Many of these symptoms can affect the quality of life of the patient suffering from them. Diagnosis of gastrointestinal disease is often difficult due to the large overlap in symptoms that GI diseases can cause. MRI is already embedded in the diagnosis and monitoring of several digestive diseases however quantitative measurements of the GI tract lag behind similar measures outside of the abdomen. The difficulties in obtaining MRI measures of

the GI tract must be overcome due to the scale of the potential benefits that non-invasive MRI offers. Once developed, quantitative measures would also enable long term studies of the gastrointestinal system which have not previously been possible due to the invasive nature of current measures.

The aim of this thesis is to address some of the shortages in quantitative MRI measures of the structure of the GI tract in the hope that future diagnosis and monitoring of GI diseases could move away from invasive and uncomfortable procedures and towards non-invasive MRI.

References

- [1] G J Tortora and S R Grabowski. *Principles of Anatomy and Physiology*. John Wiley & Sons, 2000. ISBN 9780471366928.
- [2] B E Lacy, M D Crowell, and J K DiBaise. *Functional and Motility Disorders of the Gastrointestinal Tract : a Case Study Approach*. 2015. ISBN 9781493914982.
- [3] J C Paz. Chapter 8 - Gastrointestinal System. In Jaime C Paz and Michele P West, editors, *Acute Care Handbook for Physical Therapists (Fourth Edition)*, pages 201–223. W.B. Saunders, St. Louis, fourth edition, 2014. ISBN 978-1-4557-2896-1. doi: <https://doi.org/10.1016/B978-1-4557-2896-1.00008-1>.
- [4] M J Fedoruk and S Hong. Gastrointestinal System. In Philip Wexler, editor, *Encyclopedia of Toxicology (Third Edition)*, pages 702–705. Academic Press, Oxford, third edit edition, 2014. ISBN 978-0-12-386455-0. doi: <https://doi.org/10.1016/B978-0-12-386454-3.00026-9>.
- [5] I Peate. *Fundamentals of Anatomy and Physiology*. John Wiley & Sons, 2016. ISBN 9781119063728.
- [6] R S Snell. *Clinical Anatomy for Medical Students*. Lippincott Williams & Wilkins, 2000. ISBN 0781715741.

References

- [7] R Droual. Digestive System. URL <http://droualb.faculty.mjc.edu/lecturenotes/unit6/spring06digestivesystemwithfigures.htm>.
- [8] V Balbi and P Ciarletta. Morpho-Elasticity of Intestinal Villi. *Journal of The Royal Society Interface*, 10(82), 2013. doi: 10.1098/rsif.2013.0109.
- [9] V Pascual, R Dieli-Crimi, N López-Palacios, A Bodas, L M Medrano, and C Núñez. Inflammatory Bowel Disease and Celiac Disease: Overlaps and Differences. *World journal of gastroenterology*, 20(17):4846–56, may 2014. ISSN 2219-2840. doi: 10.3748/wjg.v20.i17.4846.
- [10] N Gujral, H J Freeman, and A B R Thomson. Celiac Disease: Prevalence, Diagnosis, Pathogenesis and Treatment. *World Journal of Gastroenterology*, 18(42):6036, 2012. ISSN 1007-9327. doi: 10.3748/wjg.v18.i42.6036.
- [11] D W Hay. *The Little Black Book of Gastroenterology*. Jones & Bartlett Learning, 2011. ISBN 9780763777630.
- [12] B Lebowl, D S Sanders, and P H R Green. Coeliac Disease. *The Lancet*, 391(10115):70–81, 2018. ISSN 0140-6736. doi: [https://doi.org/10.1016/S0140-6736\(17\)31796-8](https://doi.org/10.1016/S0140-6736(17)31796-8).
- [13] H J Freeman. Natural History and Long-Term Clinical Course of Crohn's Disease. *World Journal of Gastroenterology*, 20(1):31, 2014. ISSN 1007-9327. doi: 10.3748/wjg.v20.i1.31.
- [14] G Van Assche, A Dignass, J Panes, L Beaugerie, J Karagiannis, M Allez, T Ochsenkühn, T Orchard, G Rogler, E Louis, L Kupcinkas, G Mantzaris, S Travis, and E Stange. The Second European Evidence-Based Consensus on the Diagnosis and Management of Crohn's Disease: Definitions and Diagnosis. *Journal of Crohn's and Colitis*, 4(1):7–27, 2010. ISSN 1873-9946. doi: 10.1016/j.crohns.2009.12.003.
- [15] J R Dillman, S D Swanson, L A Johnson, D S Moons, J Adler, R W Stidham, and P D R Higgins. Comparison of Noncontrast MRI Magnetization

References

- Transfer and T2-Weighted Signal Intensity Ratios for Detection of Bowel Wall Fibrosis in a Crohn's Disease Animal Model. doi: 10.1002/jmri.24815.
- [16] K K Shah, B S Pritt, and M P Alexander. Histopathologic Review of Granulomatous Inflammation. *Journal of Clinical Tuberculosis and Other Mycobacterial Diseases*, 7:1–12, may 2017. ISSN 24055794. doi: 10.1016/j.jctube.2017.02.001.
- [17] T Kuhbacher and U R Fölsch. Practical Guidelines for the Treatment of Inflammatory Bowel Disease. *World journal of gastroenterology*, 13(8): 1149–55, feb 2007. ISSN 1007-9327. doi: 10.3748/WJG.V13.I8.1149.
- [18] A E Thompson. Diverticulosis and Diverticulitis JAMA Patient Page. *JAMA*, 316(10):1124, 2016. ISSN 0098-7484. doi: 10.1001/jama.2016.3592.
- [19] T Wilkins, K Embry, and R George. Diagnosis and Management of Acute Diverticulitis. *American family physician*, 87(9):612–20, may 2013. ISSN 1532-0650.
- [20] S K Patel, C B Pratap, A K Jain, A K Gulati, and G Nath. Diagnosis of Helicobacter Pylori : What Should be the Gold Standard? *World Journal of Gastroenterology*, 20(36):12847, 2014. ISSN 1007-9327. doi: 10.3748/wjg.v20.i36.12847.
- [21] S Alzahrani, T T Lina, J Gonzalez, I V Pinchuk, E J Beswick, and V E Reyes. Effect of Helicobacter Pylori on Gastric Epithelial Cells. *World Journal of Gastroenterology*, 20(36):12767, 2014. ISSN 1007-9327. doi: 10.3748/wjg.v20.i36.12767.
- [22] D G Wild. 9.17.1 Hepatitis A Virus, 2013.
- [23] M Sunbul. Hepatitis B Virus Genotypes: Global Distribution and Clinical Importance. *World Journal of Gastroenterology*, 20(18):5427, 2014. ISSN 1007-9327. doi: 10.3748/wjg.v20.i18.5427.

References

- [24] G J Buckley and B L Strom, editors. *Eliminating the Public Health Problem of Hepatitis B and C in the United States*. National Academies Press, Washington, D.C., 2016. ISBN 978-0-309-43799-8. doi: 10.17226/23407.
- [25] R Bataller and D A Brenner. Liver Fibrosis. *The Journal of clinical investigation*, 115(2):209–18, feb 2005. ISSN 0021-9738. doi: 10.1172/JCI24282.
- [26] W Zhou, Q Zhang, and L Qiao. Pathogenesis of Liver Cirrhosis. *World Journal of Gastroenterology*, 20(23):7312, 2014. ISSN 1007-9327. doi: 10.3748/wjg.v20.i23.7312.
- [27] A Pascher, M Nebrig, and P Neuhaus. Irreversible Liver Failure: Treatment by Transplantation: Part 3 of a Series on Liver Cirrhosis. *Deutsches Arzteblatt international*, 110(10):167–73, mar 2013. ISSN 1866-0452. doi: 10.3238/arztebl.2013.0167.
- [28] H Wiig and M A Swartz. Interstitial Fluid and Lymph Formation and Transport: Physiological Regulation and Roles in Inflammation and Cancer. *Physiological Reviews*, 92(3):1005–1060, 2012. ISSN 0031-9333. doi: 10.1152/physrev.00037.2011.
- [29] R L Drake, K Moses, A W Vogl, and A W M Mitchell. Gray's Anatomy for Students, Third Edition. *Gray's Anatomy for Students*, pages 1–121, 2014. ISSN 1098-6596. doi: 10.1017/CBO9781107415324.004.
- [30] M A Swartz. The Physiology of the Lymphatic System. *Advanced Drug Delivery Reviews*, 50(1-2):3–20, 2001. ISSN 0169-409X.
- [31] J S Alexander, V C Ganta, P A Jordan, and M H Witte. Gastrointestinal lymphatics in health and disease. *Pathophysiology*, 17(4):315–335, 2010. doi: <http://dx.doi.org/10.1016/j.pathophys.2009.09.003>.
- [32] L M Sompayrac. *How the Immune System Works*. Wiley, 2011. ISBN 9781118298626.

References

- [33] V C Scanlon and T Sanders. *Essentials of Anatomy and Physiology*. 2014. ISBN 0803643756.
- [34] Lippincott, Williams, and Wilkins. *Anatomy \& physiology Made Incredibly Visual!*. Wolters Kluwer Health/Lippincott Williams & Wilkins, 2009. ISBN 9780781786867.
- [35] J A Campbell and L N Carayannopoulos. Natural Killer Cells. *Comprehensive Toxicology*, pages 53–85, jan 2010. doi: 10.1016/B978-0-08-046884-6.00604-7.
- [36] K Haworth. L Stockslager, R Cheli, editor. *Anatomy and Physiology*. Lippincott professional guides. Ambler, [Pennsylvania], 2nd ed. edition, 2002.
- [37] A B Kohan, S M Yoder, and P Tso. Physiology \& Behavior using the Lymphatics to Study Nutrient Absorption and the Secretion of Gastrointestinal Hormones. *Physiology & Behavior*, 105(1):82–88, 2011. ISSN 0031-9384. doi: 10.1016/j.physbeh.2011.04.056.
- [38] V Racanelli and B Rehermann. The Liver as an Immunological Organ. 2006. doi: 10.1002/hep.21060.

4 Abdominal Lymph Nodes

4.1 Introduction

The lymphatic system has three main functions: to drain excess interstitial fluid, to transport lipids from the digestive system into the blood stream and to facilitate immune responses. Inflammatory conditions such as Crohn's disease cause changes in the lymphatics including enlargement and necrosis (1). The presence of inflamed nodes has also been used in the staging of several diseases and can be used to determine the prognosis of treatment of cancers (2, 3). Lymph nodes, therefore, have the potential to be a useful biomarker of local inflammatory responses with the number, size and location of the nodes being potentially useful in determining the location and severity of disease. In order for lymph nodes to become a novel MRI biomarker, their state in the healthy body first needs to be evaluated to provide a bench mark against which disease can be compared. Some information is available in the literature about lymph nodes but this is mainly focused on cancer. A handful of studies have evaluated nodes in inflammatory gastrointestinal diseases but the amount of quantitative information is severely restricted. To our knowledge, no data has been published which has given quantitative MRI measures of lymph nodes in healthy volunteers. This may be due to the difficulty in visualising healthy lymph nodes *in vivo*. This chapter focuses on the development of MRI to evaluate non-enlarged abdominal lymph nodes in healthy participants and then details the use of the developed methods in patients with a range of inflammatory gastrointestinal diseases. All image acquisitions were performed by Hannah Williams, with initial assistance from Dr Caroline Hoad (Senior Research Fellow). The ethical approval for the patient study was written by Hannah Williams and recruitment was done with the assistance of the research nurses from the Biomedical Research Centre. The work presented in this chapter has been presented as a poster presentation at the annual conference of the International Society of Magnetic Resonance Imaging (ISMRM) 2017 and 2019 and the European Crohn's and Colitis Organisation

2019, and as an oral presentation at the Post graduate symposium of the British Chapter of ISMRM 2019. All image analysis was performed by the author of this thesis. Additional analysis to allow inter observer reproducibility to be evaluated was performed by Iyad Naim (PhD Student).

4.2 Lymph Nodes in Disease

The occurrence of enlarged lymph nodes is common in many diseases. In gastrointestinal disease the main patient groups in which lymph node involvement have been reported are Crohn's patients, liver cirrhosis patients and patients with coeliac disease.

Lymph Nodes in Crohn's Disease: Enlarged lymph nodes have been noted in Crohn's disease since its original descriptions (4). In 1946 it was noted that diseased tissue was more prominent in portions of the bowel where there was a higher number of lymph nodes (5). Despite this there has been little investigation into the involvement of the lymphatic system in Crohn's disease until recent years. The presence of enlarged nodes on T2 weighted images now forms part of the Magnetic Resonance Index of Activity (MaRIA) score which is used as a predictor of the severity of Crohn's disease (6). The use of nodes in the MaRIA score is purely qualitative, however having quantitative measures of nodes may provide more insights into the nature of the lymph nodes in the diseased state. Differences between patient groups have also been seen. For example, Noltheinushas *et al* have shown that Crohn's patients with proctitis (inflammation of the rectum) have larger lymph nodes than those Crohn's patients without proctitis (7).

Lymph Nodes in Coeliac Disease: Patients with Coeliac disease have been reported to have cavitation in their lymph nodes. Cavitation of lymph nodes is described as a 'central necrosis of mesenteric lymph nodes', the presence of which may indicate a poor prognosis (8). Changes such as necrosis should, in theory, be detectable using diffusion weighted imaging, with the necrosis pre-

senting as a high ADC region in the lymph node.

Lymph Nodes in Liver Cirrhosis: Changes in the lymphatic system have also been identified in patients with liver cirrhosis. Using Magnetic Resonance Lymphangiography (MRL), an invasive MRI technique which utilises contrast agents to image lymph flow, changes in the thoracic duct have been observed in liver cirrhosis patients. Differences in the length of the duct were seen between healthy volunteers and patients with alcoholic cirrhosis (9). This difference in length was not observed in patients with non-alcoholic liver cirrhosis suggesting that the length of the thoracic duct may be used as an indicator as to whether a patient has alcoholic or non-alcoholic liver cirrhosis.

4.3 Lymph Nodes and MRI

Lymph nodes have been described in several MRI studies however there is a lack of quantitative measures of lymph nodes, especially in gastrointestinal diseases. This is likely to be due to the difficulty in visualising abdominal nodes, repeated measurements are also difficult due to their small size and motion due to peristalsis and respiration. From the literature it is apparent that the main focus of lymph node imaging using MRI has been based around cancerous nodes, with a large amount of these studies focusing on the head, neck and breasts with little attention focusing on the abdominal lymph nodes. Currently Computed Tomography (CT) is the main method for staging malignant lymphoma (10). MRI, unlike CT, does not involve the use of ionising radiation and could therefore provide a safer method for diagnostics and staging and also allow longitudinal studies to be carried out. Many MRI studies involving the lymphatics use a contrast agent. However, studies have shown that enlarged and malignant lymph nodes are visible on non-contrast enhanced (CE) MRI and can be used to differentiate between benign and malignant lymph nodes (11).

Abdominal Nodes: In many non-CE MRI studies diffusion weighted imaging has been employed, however studies of malignant nodes in the abdomen have

4. Abdominal Lymph Nodes

reported poor visualisation of nodes. A study in which DWI was performed followed by surgical removal of gastric tissue in patients with gastric adenocarcinoma found that visualisation of lymph nodes was low with as little as 7% of removed nodes having been identified on the images (12). Mesmann *et al* conducted an investigation to determine whether Diffusion Weighted Imaging (DWI) or Diffusion Weighted whole body Imaging with Background body Suppression (DWIBS) was more successful in imaging thoracic lymph nodes, concluding that DWIBS allowed better visualisation of the lymph nodes. Free breathing and respiratory triggering were also compared, finding that respiratory triggering added a time penalty to the process but did not provide a significant increase in image quality (13).

A sensitivity of 77-80% has been achieved when imaging prostate lymph nodes using the method presented by Takahara *et al* in patients with prostate cancer (14). Kwee *et al* initially reported that in a small number of cases using lymph nodes imaged with DWIBS led to incorrect staging of lymphoma (10). However, a follow up study which utilized a much larger sample size found that staging using MRI was equivalent to using CT and thus could provide an alternative method of staging in cases where radiation exposure should be avoided (15).

We can draw on several studies of abdominal lymph nodes for methods to image enlarged nodes. A study of the visualisation of mediastinal lymph nodes concluded that they are better observed using short inversion recovery time sequences than using fat suppression techniques. It was reported that, in general, fat suppression techniques do improve the visibility of lymph nodes but around the mediastinal lymph nodes the field is often inhomogeneous and so visibility is enhanced more with short inversion recovery techniques (16). A study by Arrivé *et al* found that if the mediastinal lymph nodes are surrounded by mediastinal fat then T1 weighted images provide good contrast between the node and the fat (17). Arrivé *et al* used an interesting technique in a second study to image lymph nodes; pineapple juice, which has a high concentration of manganese was drunk by the patients prior to imaging to reduce the signal from liquid in the

4. Abdominal Lymph Nodes

bowel on T2 weighted images (18). The manganese has the effect of shortening the relaxation times of the liquid content in the bowel, making them appear darker. A study by Akduman *et al* compared the ADC of lymph nodes in patients with a range of diseases including Crohn's disease. The study highlighted that there was a significant difference in the ADC between these nodes and cancerous nodes. The nodes were all enlarged and no comparison was made with healthy nodes (19).

Nodes Outside the Abdomen: The use of MRI to visualise lymph nodes has mainly been focused outside of the abdomen. Around the lungs for example, Onhu *et al* used contrast enhanced short TI inversion recovery (STIR) turbo spin echo (TSE) to successfully image both healthy and metastatic lymph nodes. They were able to differentiate between healthy and metastatic lymph nodes both qualitatively and quantitatively by comparing the signal in the node with the signal in a phantom (20). Xu *et al* used DWIBS to image lymph nodes using the diffusion coefficient as an identifier of the spread of lung cancer into surrounding nodes. It was demonstrated that the lower diffusion coefficient of the malignant nodes made their visualisation easier with 100% of the malignant nodes being identified. In comparison, fewer than 50% of benign nodes were visualised (21). The result that <50% of benign enlarged lymph nodes were identified demonstrates that benign lymph nodes may be difficult to image even when they are enlarged.

A small amount of literature was found that included semi-quantitative T2 measures of lymph nodes. Kim *et al* calculated the relative T2 of nodes by comparing the signal in the lymph nodes on a T2 weighted image to the signal in muscle on the same image (22). They showed that the relative T2 could distinguish between metastatic and non-metastatic lymph nodes in breast cancer. Li *et al* measured the T2* of lymph nodes in breast cancer patients finding that the T2* of benign nodes was significantly lower than that of metastatic nodes. They suggest that the T2* value, due to its specificity, sensitivity and easiness of measurement, has a high potential for use in clinical practice (23).

4. Abdominal Lymph Nodes

From the literature it is clear that there is a lack of quantitative measures of abdominal lymph nodes. In order for the lymph nodes to be used in MRI as a biomarker, comparisons of values between patients and healthy volunteers must be obtained. There is a very small amount of data on healthy nodes and thus the potential for them to be used as a biomarker is minimal at this stage. The literature mainly focuses on using diffusion weighted imaging as the main method to study lymph nodes. This is due to the difficulty imaging them using other acquisition techniques. One potential alternative method is to use mDIXON imaging which had been noted on previously collected in-house data to show lymph nodes in diverticulitis patients with a high volume of visceral fat. Figure 4.1 shows nodes joined by lymphatic capillaries. mDixon scans provide fat only and water only images which provides the contrast between the lymph nodes and the surrounding visceral fat.

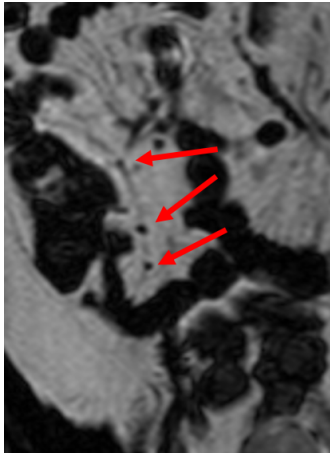


Figure 4.1: mDixon fat only scan in a patient with diverticulitis. Fat appears white with the lymph nodes (red arrows) appearing black, some lymph vessels are also seen joining the lymph nodes.

Identifying nodes in volunteers with a large amount of visceral fat is significantly easier than identifying them in volunteers with little visceral fat. The images in Figure 4.2 highlight this difficulty. Image a) shows the pelvic nodes which sit in a layer of fat which provides a good contrast between the two tissues. This

4. Abdominal Lymph Nodes

makes the identification of the lymph nodes relatively easy. Image b) shows the abdomen, which in this volunteer has very little visceral fat. The lack of fat meant that no contrast was provided between the nodes and the surrounding tissue, thus making the identification of lymph nodes difficult.

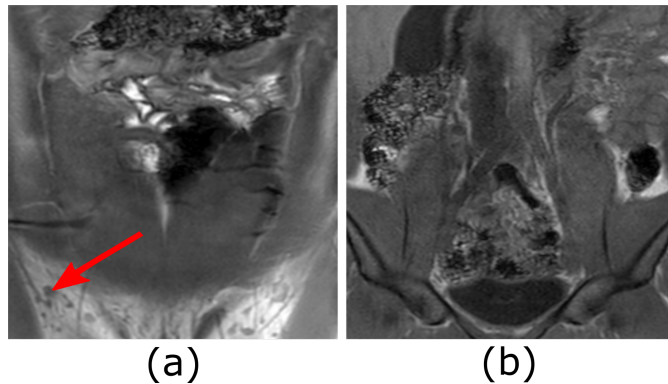


Figure 4.2: a) Coronal Dixon scan taken of the pelvis and abdomen. The pelvic nodes (indicated by red arrow) sit in a layer of fat, which provides a contrast between the nodes and surrounding fat tissue. In this image the nodes can be easily identified. b) A slice taken from the same scan located further back in the abdomen which shows a lack of visceral fat. The lack of surrounding fat would make identifying the lymph nodes difficult as they do not have the bright surrounding fat against which they would contrast.

Due to the difficulty in visualising nodes on non-DWI images the focus of this chapter is on the development and use of DWI to visualise and take quantitative measures of abdominal lymph nodes. The work then moves on to compare quantitative measures of T2, ADC and size of lymph nodes in healthy volunteers and patients with a range of chronic or recurrent inflammatory gastrointestinal diseases. This comparison will allow for the potential of abdominal lymph nodes to be used as a biomarker of abdominal inflammation to be evaluated.

4.4 Development of MRI of Abdominal Lymph Nodes

4.4.1 Abdominal Nodes at 1.5T

The starting point for the development of MRI to investigate lymph nodes was DWI scanning at 1.5T. Scanning parameters were taken from the 2012 paper written by Kwee et al (24) in which DWIBS was used to image tumours in the abdomen. As recommended in the paper free breathing was used with STIR fat suppression (TI=260ms), with a TR = 10000 ms and TE = 70 ms and a resolution of 2.5 x 3.6 x 4.0 mm with 25 slices. The paper recommends a b value of 1000 s/mm² however the images at this b value only contained noise and so the b value was reduced to 600 s/mm². Respiratory triggered and breath hold data was also acquired in order to determine the best method to allow visualisation of the lymph nodes. Diffusion gradients were applied in three directions with the results averaged.

In the respiratory triggered data nodes were identifiable in less than half of the initial images and the images had a low SNR. The data showed that tissue with low ADCs such as the kidneys, the vertebrae and the gall bladder were visible, as expected. A repeatability test showed that the few lymph nodes that were identified on the first scan could not be done so on subsequent scans. Figure 4.3 highlights the non-reproducibility of the original imaging sequence. These images were acquired during the same scanning session without moving the participant between scans.

Visualising the individual dynamics (rather than the averaged data) revealed that during free breathing the lymph nodes moved in and out of the imaging plane. This resulted in a low signal in the nodes due to the averaging of noise and node signal over all the dynamics, resulting in the signal in the location of the node being lowered to a level similar to the surrounding noise. This problem was not restricted to small objects, the kidneys for example (Figure 4.4) also moved in and out of the imaging slice however they had sufficient signal to exceed the noise when averaged across the dynamics. For the visualisation of the nodes to be repeatable the acquisition would have to be during the same

4. Abdominal Lymph Nodes

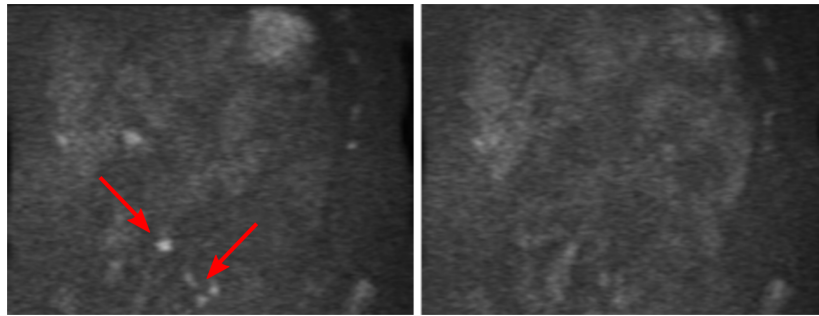


Figure 4.3: Two coronal abdominal images taken using the same DWI sequence. The images, taken consecutively, show that imaging abdominal lymph nodes (red arrows) with this sequence does not give reproducible results.

part of the breathing cycle as the previous acquisition, which is not guaranteed with free breathing.

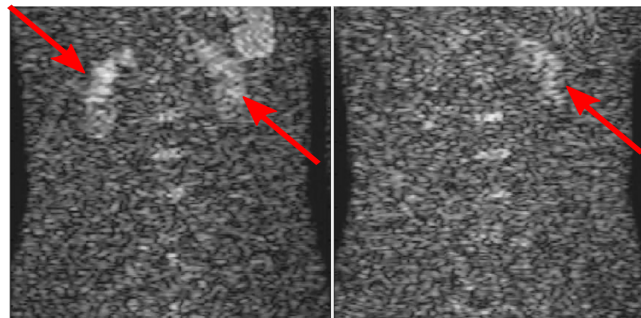


Figure 4.4: Coronal DWI dynamics taken during free breathing. The kidneys (red arrows) move in and out of plane, highlighting the amount of respiratory based motion present in the abdomen during free breathing.

Using respiratory triggering, it was found that the nodes again appeared to exhibit a significant amount of motion (Figure 4.5). Using breath holds it was found that motion of the nodes was minimised however it limited the number of slices that could be acquired during the scan. The image stack had to be reduced from 25 to 5 slices in order to be within a breath hold time that was realistically achievable. Here the nodes were visible but the SNR was low, again making optimisation of the sequence difficult (Figure 4.6).

4. Abdominal Lymph Nodes

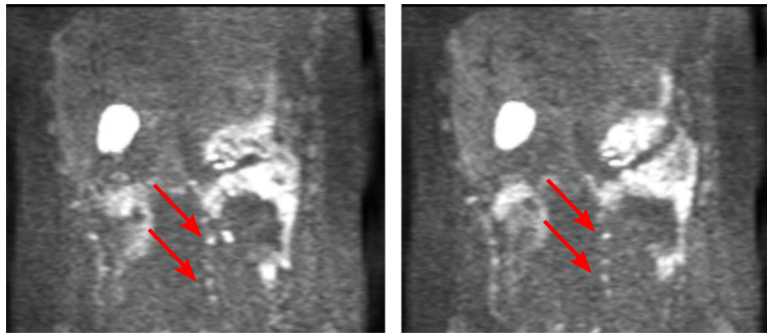


Figure 4.5: Coronal DWI images acquired using respiratory triggering at 1.5T. The background suppression is poor and nodes (red arrows) appear to move in and out of plane.

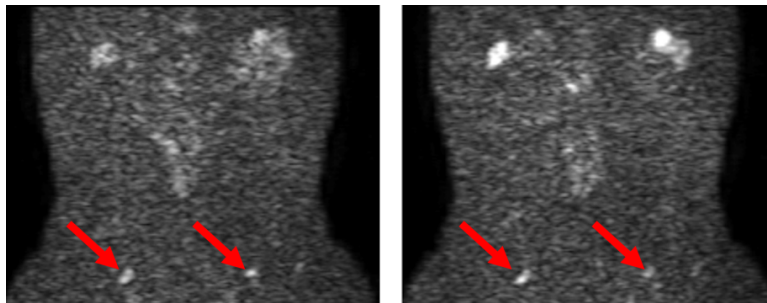


Figure 4.6: Coronal breath hold DWIs showing two nodes towards the lower section of the abdomen (red arrows). The SNR is low making the identification of any smaller nodes impossible.

After these three trials it was deemed that the need for higher SNR to allow visualisation of the nodes outweighed the problem of field inhomogeneities that exist at higher field strengths. It also highlighted the difficulty in optimising a sequence based on small movable objects. Thus the decision was made to move the optimisation to a 3T scanner to increase the SNR and to also use pelvic nodes which had the benefit of being unaffected by respiratory motion and peristalsis.

4.4.2 Pelvic Nodes at 3T

Pelvic nodes, as expected, produced repeatable and well defined images when imaged on a 3T Philips Achieva. The inversion delay time and b value were

4. Abdominal Lymph Nodes

then varied to determine the optimal values for visualising the lymph nodes. A b value of 600 s/mm^2 was chosen as it is commonly used in the literature and upon visual inspection of images acquired in-house, a b value higher than this (800 or 1000 s/mm^2) often produced images in which the lymph node signal was completely suppressed. A b value of 600 s/mm^2 consistently gave high signal in the lymph nodes with good background suppression. In a single participant the signal in the lymph nodes was also compared to that of the muscle tissue in the leg to confirm that background suppression was optimal at a b value of 600 s/mm^2 . This b value produced the highest value of lymph node to muscle ratio as it provided a compromise between high lymph node signal and high background suppression (defined as low signal in the surrounding leg muscle).

The second parameter in the sequence to be optimised was the inversion delay time for fat suppression. Three inversion delay times were tested, 220, 240 and 260 ms, these were chosen as they were all in the range of inversion delay times which are known to suppress the majority of the background body signal (fat and bowel). The ratio of lymph node signal to the surrounding fat was calculated and used to determine the optimal inversion delay time. No significant difference was found in the background suppression in the pelvis when comparing the three different inversion delay times, therefore an inversion delay time of 260 ms was chosen to be consistent with previous literature.

Once the optimal values were decided the images acquired using the 3T Achieva were compared to those acquired using a 3T Ingenia. The 3T Ingenia, being a digital system, was expected to give a higher SNR in comparison to the Achieva which is an analogue system. The higher SNR on the 3T Ingenia produced images in which the lymph nodes appeared to have sharper edges with less blurring (Figure 4.7). From these results it was decided to move all imaging to the 3T Ingenia.

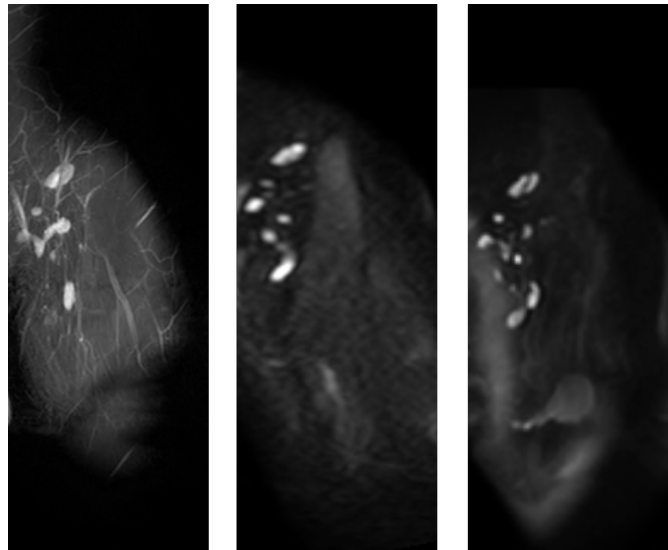


Figure 4.7: Left: A coronal T2 weighted image taken with a 3T Ingenia. Fat suppression was used to highlight the pelvic lymph nodes and lymphatic vessels joining the nodes. Middle: A coronal DWI image taken on the 3T Achieva showing good agreement with the positioning of the nodes when compared with the T2 weighted image. Right: A coronal DWI image taken on a 3T Ingenia which also highlights the lymph nodes but gives better definition of the edges of the nodes due to the higher SNR.

4.4.3 Abdominal Nodes at 3T

Once the sequence was optimised the imaging was then moved back to the abdominal lymph nodes. Figure 4.8 shows dynamics taken during a respiratory triggered acquisition. The lymph nodes were more easily identified when compared with those taken at 1.5T. However, the problem of blurring due to respiratory and digestive motion was still present. In order to overcome the loss of signal due to nodes moving through the imaging plane, sagittal slices were used. In a sagittal acquisition the motion of the nodes was in the plane of the image rather than through the plane. Whilst this caused some blurring it did reduce the signal loss from through plane motion. Figure 4.9 shows dynamics taken from a sagittal DWI acquisition. The dynamics showed some movement of the nodes up and down the plane. This could be overcome by using some form of navigator or motion correction, however the movements observed were

4. Abdominal Lymph Nodes

small and the use of a navigator or motion correction was not deemed necessary.

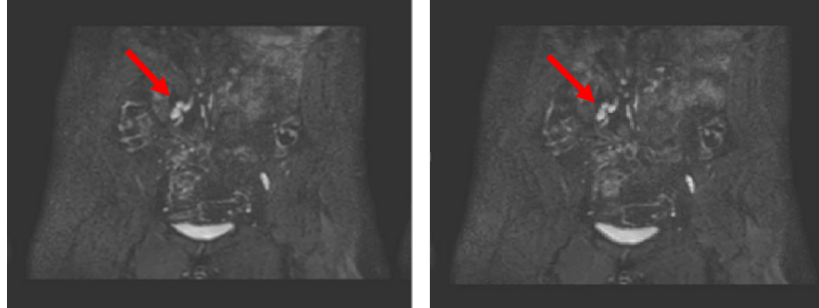


Figure 4.8: Two coronal single average DWI images that were acquired on a 3T Ingenia using respiratory triggering with lymph nodes indicated by arrows.

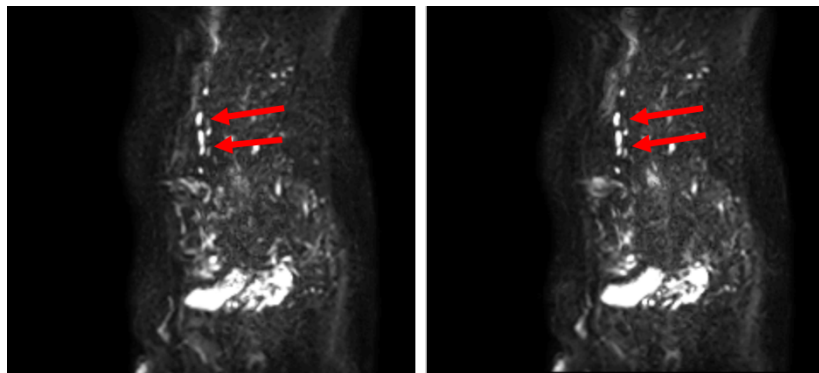


Figure 4.9: DWI dynamics taken with a sagittal orientation, nodes (red arrows) show no motion through the plane and minimal motion up and down the plane.

Figure 4.10 shows a sagittal DWI and T2 weighted image alongside each other. The nodes in the DWI image do appear to be present on the T2 weighted image which has the benefit of containing more anatomical information. However, the DWI image is necessary to distinguish nodes from vessels in the T2 weighted image. In order to confirm these locations the two images need to be overlaid which is difficult due to the distortion in the EPI image.

Acquiring a DWI with the echo time increased (with fixed gradients around the DWI inversion pulse) as described in section 2.3.6 would allow the T2 signal decay to be acquired by applying a fixed diffusion weighting, keeping the diffusion

4. Abdominal Lymph Nodes

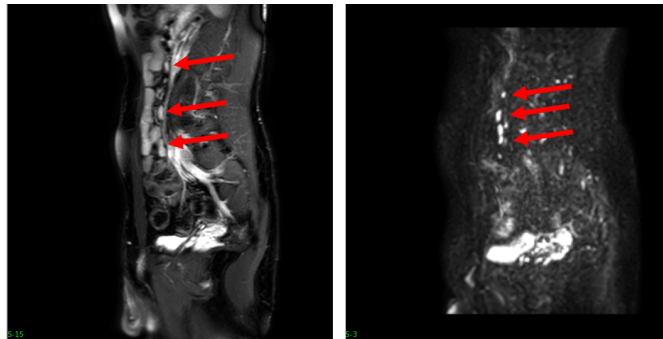


Figure 4.10: Left: T2 weighted anatomical image highlighting potential lymph nodes. Right: DWI showing nodes in a similar location to the suspected nodes in the T2 weighted SPAIR.

time constant and changing the echo time. This method allows for T2 to be measured from images in which lymph nodes can be distinguished from the surrounding tissue. This is not easily done on normal T2 weighted images due to the similar contrast in the nodes and the surrounding tissue and the similar appearance of nodes and vessels in anatomical images.

In order to check that this long-TE DWI method of measuring T2 was accurate a phantom study was conducted in which the T2 of the phantom was calculated using a spin echo EPI sequence as well as the long-TE DWI sequence. The phantom used had four different segments, each with different relaxation times. Table 4.1 shows the T2 measured from each segment of the phantom using the spin echo EPI sequence and the long-TE DWI sequence. One of the four segments failed to fit for a T2 using the long-TE DWI sequence as the diffusion weighting suppressed the signal in that segment to the noise floor. The results show that T2 can be accurately measured on a long-TE DWI scan providing that the signal is high in the diffusion weighted scans.

The developments made in the work presented in this section have allowed for lymph nodes to firstly be identified in healthy volunteers which was not previously possible in the abdomen and secondly made T2 and ADC measurements in the nodes possible. These two measurements along with the size and location of nodes have the possibility of being biomarkers of inflammation in patients with inflammatory disease. In order to evaluate the differences in lymph nodes

4. Abdominal Lymph Nodes

Scan/Segment	SE-EPI	Long-TE DWI
Segment 1	83 ms	81 ms
Segment 2	52 ms	-
Segment 3	49 ms	53 ms
Segment 4	69 ms	68 ms

Table 4.1: T2s measured from the quadrature phantom using spin echo EPI and long-TE DWI are given. The T2 for segment 2 could not be measured with DWI as the diffusion weighting suppressed the signal to the noise floor.

in patients with inflammatory disease and healthy volunteers the methods developed here were put to use in a healthy volunteer study aiming to characterise abdominal lymph nodes.

4.5 Measuring Healthy Abdominal Lymph Nodes

In order to investigate whether non-contrast enhanced MR measures could provide a biomarker of inflammatory disease a pilot study was set up with the aim of investigating a wide range of MR measures, firstly in a healthy volunteer group, and then in a patient study. We hypothesised that there would be detectable differences in quantitative MR measures of the lymph nodes between healthy volunteers and patients. Specifically, the aim of the study was to characterise, using non-contrast enhanced MRI, the size, ADC and T2 of lymph nodes in healthy volunteers and then to compare these with patient data to be taken in a later study. Initially 4 healthy volunteers were recruited to test a wide range of echo times for the T2 measurements, from these echo times a smaller set of optimal echo times was then chosen to allow the collection of the full T2 decay curve whilst reducing the number of echo times acquired. The size of the lymph nodes was measured by the major and minor axis lengths of each node which is the standard method for measuring node size in imaging studies and diagnostics, with a minor axis length above a given size used to indicate malignancy (25).

4. Abdominal Lymph Nodes

In this section the details of the small pilot study of four healthy volunteers are given.

4.5.1 Study Design and Healthy Volunteer Cohort

Four healthy volunteers were recruited (2 male and 2 female) with a mean age of 25 years with a standard deviation of 2 years. Each volunteer was asked to fast overnight and then to undergo a 1 hour 15 minute MRI. The overnight fast was requested to minimise any motion that the nodes may undergo due to peristalsis of the surrounding bowel. The following inclusion/exclusion criteria was set for the healthy volunteer cohort.

- Aged 18-75
- Male or Female
- Able to give informed consent.

The following exclusion criteria were set

- Pregnancy
- Gastrointestinal disorders or symptoms (e.g. coeliac disease, Crohn's disease, diverticulitis)
- Absolute contraindications for MRI.

4.5.2 Scanning Protocol

All healthy volunteers were scanned on a Philips 3T Ingenia (Best, Netherlands). Participants lay in the prone position. The purpose of this positioning was to cause the bowel to drop forward and away from the mesenteric lymph nodes which sit near the spine which was the target area of scanning. The diffusion and T2 images were acquired with 8 slices. The number of slices was limited by the number that could fit within the expiration phase of the respiratory cycle. The slices were orientated sagittally to reduce the through plane motion of the

lymph nodes. The scanning protocol and scan parameters are detailed in Table 4.2. As discussed in Section 2.3.6 the diffusion gradients must be fixed to ensure that the diffusion time is constant for all measurements, therefore they were fixed for all acquisitions throughout this chapter with $\delta = 11$ ms, $\Delta = 44$ ms and the gradient strength fixed at 20 mT/m. These were based off the gradients used at the shortest echo time. Previous data acquired with b values ranging from 0 - 1000 s/mm² had shown that between 200 s/mm² and 600 s/mm², ADC and b value had a linear relationship, therefore 3 b values were chosen in this range from which the ADC was to be measured.

A free breathing DWIBS sequence was acquired with two b values 0 and 600 s/mm² to obtain a guide as to the location of the abdominal lymph nodes. This was used to position the slices of the standard DWI (for ADC measurements) and long-TE DWI (for T2 measurements). The protocol lasted approximately 1 hour 15 minutes. The length was made longer than necessary due to an error in the triggering which meant that triggering only occurred on every other expiration even when a short TR was used. This error was corrected for the patient study. The difference in triggering may result in a higher SNR in the case where triggering was on every other breath rather than every breath. However the need to perform the patient scanning in a single 1 hour session outweighed the need for the higher SNR that may be achieved by triggering on every other breath. In most tissue the TR used (1.9 s) is likely to be sufficiently long to allow full T1 recovery before the next acquisition however in the case of necrosis T1 can be up to 2 s which would therefore not allow full recovery of the signal between acquisitions.

4.5.3 Analysis Methods

For both the standard DWI and long-TE DWI the same analysis methods were applied to obtain the signal from the lymph nodes. Firstly the $b = 600$ s/mm² standard DWI images were used to identify lymph nodes. The locations of the nodes were noted so that the T2 and ADC could be compared in the same

4. Abdominal Lymph Nodes

Scan parameters	T2 anatomical	DWIBS	Standard DWI (ADC measurement)	Long-TE DWI (T2 measurement)
TE (ms)	80	85	76	70, 80, 90, 100, 110, 120, 130, 150 and 200
Minimum TR (ms)	1676	2258	1938	3000
Voxel size (mm ²)	1.56 x 1.56	2.5 x 2.5	2.5 x 2.5	2.5 x 2.5
Slice thickness (mm)	3.12	4.68	4.68	4.68
Number of slices	40	20	8	8
Slices orientation	Coronal	Coronal	Sagittal	Sagittal
Reconstruction in-plane (mm ²)	0.78 x 0.78	1.56 x 1.56	1.56 x 1.56	1.56 x 1.56
Half Fourier factor	-	-	-	0.69
SENSE factor	2	2.3	2.3	2.3
<i>b</i> values (s/mm ²)	0	0, 600	400, 500, 600	300
EPI/TSE factor	120	69	53	53
Number of sequence averages	1	1	5	4
Motion correction	Triggered	Free breathing	Triggered	Triggered

Table 4.2: Table detailing the parameters of the acquired scans.

4. Abdominal Lymph Nodes

node from the two acquisitions. An ROI was drawn on the lowest b value/echo time in the node using MIPAV (medical image analysis package (26)) and was then propagated all other b values/echo times. The ROI was rigidly moved to account for motion of the lymph node where necessary. As the acquisition was multi-slice (not 3D) and the nodes did not traverse two slices they were only defined in two dimensions. For the ADC calculation a linear fit was applied in MATLAB using a linear least squares fit to the log of the signal, fitting for M_0 and ADC. For the long-TE DWI T2 calculation a linear fit was also applied to the log of the signal, fitting for T2 and M_0 . For the T2 data some of the nodes showed significant motion. To remove points that were likely to have undergone significant motion the linear fit was performed and the percentage difference in the predicted value at each echo time was compared to the measured value. If the two values differed by more than 10% then the node was deemed to have undergone significant motion at that echo time and the data point was removed. This value was chosen by looking at a subset of data to see which points fell away from the line and why. Points with $>10\%$ difference in predicted and measured value had all undergone a significant amount of motion and the nodes seem to have shifted so that they were between slices rather than sitting wholly within a slice, reducing the signal from the nodes in the ROI. This movement between image slices results in the signal being lower than expected causing a non-linear relationship between the ADC and b value. Removing these points so that only nodes that were constant in their positioning within the slice provides data with less noise contamination and therefore a higher R squared. The linear fit was then reapplied. If a fit was then found to have an R squared less than 0.9 it was not included in the analysis, as the results from these fits are less reliable. In MIPAV when an ROI is drawn the major and minor axis of the ROI are automatically calculated. These were taken as a measurement of the size of the lymph node. The axis lengths were taken from the ROIs drawn on the ADC images as these had the best SNR in the nodes.

4.5.4 Results

Figure 4.11 shows lymph nodes identified on a standard diffusion weighted image and a long-TE diffusion weighted image (used for the T2 measurement). The mean and standard deviation of number of nodes that were visible on both the standard and long-TE DWI images was 27 ± 17 nodes per participant. The number of nodes from which T2 was measured fell to 10 ± 3 after removal due to low R-squared of the fit. Figure 4.12 shows a diffusion decay and a T2 decay collected using diffusion weighted imaging. Figure 4.13 shows the ADC (mean $1.6 \pm 0.2 \times 10^{-3} \text{ mm}^2/\text{s}$) and T2 (mean $117 \pm 21 \text{ ms}$). Using Pearson's correlation coefficient no correlation was found between ADC and T2 in these healthy participants ($N = 15$ nodes, $p = 0.14$). Figure 4.14 shows the lengths of the major and minor axis of the nodes measured in the healthy volunteers. The mean major and minor axis length calculated for all four volunteers were $7.5 \pm 0.3 \text{ mm}$ and $5.0 \pm 0.4 \text{ mm}$ respectively.

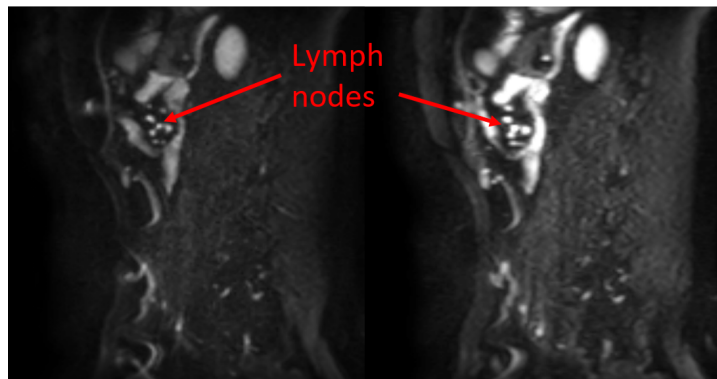


Figure 4.11: Red arrows indicate a cluster of lymph nodes that were identified on a standard DWI image ($b = 400 \text{ s}/\text{mm}^2$, $\text{TE} = 76 \text{ ms}$) on the left and the shortest echo time acquired as part of the long-TE DWI images on the right ($b = 300 \text{ s}/\text{mm}^2$, $\text{TE} = 70\text{ms}$).

4. Abdominal Lymph Nodes

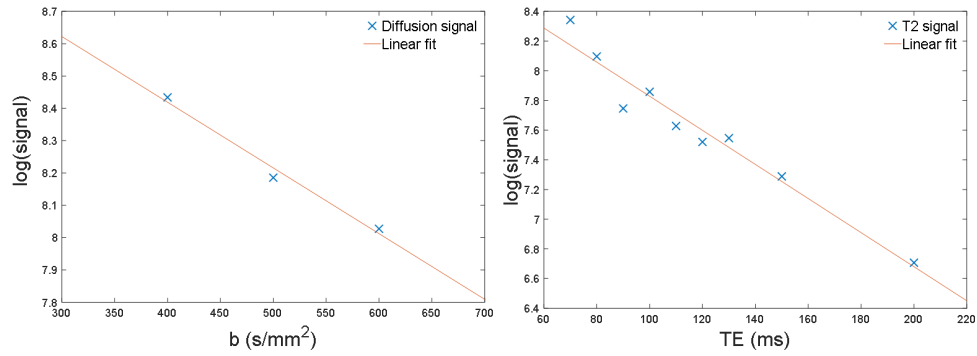


Figure 4.12: A linear fit was applied to the signal collected from a single lymph node on a standard DWI sequence (left) and a long-TE DWI sequence (right).

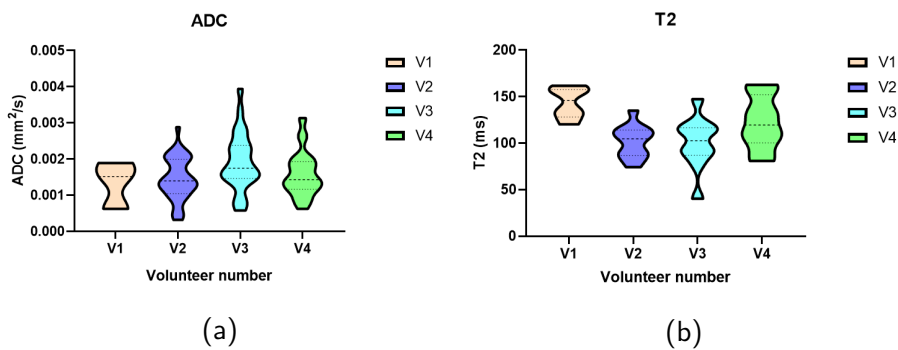


Figure 4.13: a) Violin plot showing the individual ADC measurements from each participant. b) Violin plot showing the individual T2 measurements from each participant.

4. Abdominal Lymph Nodes

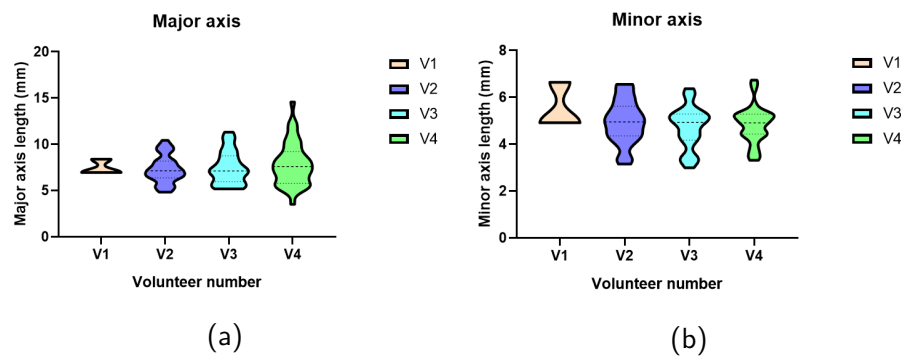


Figure 4.14: a) Violin plot showing the individual major axis measurements from each participant. b) Violin plot showing the individual minor axis measurements from each participant.

4.5.5 Discussion

Imaging of the abdominal lymph nodes in healthy participants presented a challenge due to their small size and respiratory and digestive motion. Here a modified diffusion weighted sequence was used to identify nodes and measure the size, ADC and T2 of abdominal lymph nodes. The mean ADC measured in the healthy volunteers was $1.7 \pm 0.2 \times 10^{-3} \text{ mm}^2/\text{s}$. This value is lower than that of the abdominal nodes measured in patients with a range of GI diseases by Akduman *et al* ($2.38 \pm 0.29 \times 10^{-3} \text{ mm}^2/\text{s}$ for benign nodes and $1.84 \pm 0.37 \times 10^{-3} \text{ mm}^2/\text{s}$ in malignant nodes) (19). It is expected that the ADC in the nodes of healthy volunteers would be higher than this however in their study ADC was calculated using b values of 0 and $600 \text{ s}/\text{mm}^2$. Using a b value of $0 \text{ s}/\text{mm}^2$ in the ADC calculation includes the effects of perfusion in the tissue. This increases the ADC measured and so it is to be expected that the ADC calculated is higher when using b values of 0.

The mean T2 measured in the healthy lymph nodes was $120 \pm 18 \text{ ms}$. T2 has not before been measured in lymph nodes and the values measured here are higher than other abdominal tissue such as liver tissue (around 40 ms) and kidney tissue (around 80 ms). The nodes do however carry lymph fluid which could lead to a higher T2 than that of other tissue found in the abdomen. No correlation was found between the T2 and ADC of the lymph nodes however the sample size for the correlation test was small ($N = 15$).

The average length of the major and minor axis of the lymph nodes was $7.5 \pm 0.3 \text{ mm}$ and $5.0 \pm 0.4 \text{ mm}$ respectively. The axis length measured was shorter than those nodes measured by Akduman *et al* who measured the nodes in patients with inflammatory GI diseases to be 16.8 mm and 11.5 mm for benign nodes. It is known that nodes in healthy volunteers are smaller than those in patients and the size of the healthy nodes measured here corresponds with the expected values quoted in the literature (around 6 - 10 mm (27)).

The main limitation of the technique used here was the significant motion of nodes between acquisitions which greatly restricted the number of nodes from which a full T2 decay could be measured. From these preliminary results an

optimal set of echo times to use in future measurements was chosen. For patient groups T2 is expected to be higher due to inflammation however using long echo times is not beneficial as the signal often becomes comparable to the noise floor. It was also noted that the start of the decay curve was not being sampled and thus using shorter echo times would better define the decay curve. To try to minimise the effect that motion has on the fit it was noted that interleaving the echo times may prove beneficial if a participant moves or the time available to scan is limited. Interleaving in these cases would mean that one pass from low to high echo times could be acquired as a minimum. A further limitation is the large voxel sizes and slice thickness which are likely to result in partial volume effects. This will cause noise to be included in the signal measured in the ROIs. Using smaller voxel sizes and thinner slices is not recommended due to the drop in SNR. However, using a thresholding mask to define the nodes as voxels containing signal above a certain value could minimise partial volume effects, the investigation of which is beyond the scope of this thesis.

4.6 Measuring Lymph Nodes in GI Diseases

In order to investigate differences in the lymph nodes between patients and healthy volunteers a study was set up with the aim of investigating the lymph nodes in a range of chronic/recurrent inflammatory gastrointestinal diseases. The study, titled “Magnetic resonance imaging of Abdominal Lymph nodes (MAL)”, was approved by the NHS Research Ethics Committee and adopted by the NIHR Biomedical Research Centre at the Queen’s Medical Centre. We hypothesised that there would be a decrease in the diffusion coefficient of lymph nodes, due to the fact that inflammation causes a decrease in ADC, and an increase in the T2 of lymph nodes, due to the fact that inflammation presents with a high intensity on T2 weighted images, when comparing healthy volunteers and patients (except in coeliac patients where we may find necrosis (8)). The aim of the study was to use the non-invasive MRI techniques described previously in a single, short scanning session to provide novel insights into lymph nodes in patients with inflammatory diseases. Previous literature has detailed some

quantitative ADC and size measures in inflammatory disease patients but these have typically been in small numbers ($n=1-3$) (19). The primary objective of the study was to collect pilot data from patients with a range of chronic/recurrent inflammatory diseases and healthy volunteers. The main quantitative measures to make were ADC, T2 and size of the nodes.

4.6.1 Cohort and Study Design

Patients were recruited by their clinical care team or by a member of the Biomedical Research Centre (BRC). They were initially given a short version of the Patient Information Sheet (PIS), if the patient then expressed interest they were invited to a screening visit. The screening visit provided the patient with the long version of the PIS and a medical screening to check that the patient was eligible for the study. After the screening visit the patient was invited to the MRI visit at which the necessary MRI safety checks were performed before the 1 hour MRI scan was carried out. The aim of the study was to recruit 10 patients from each of the following patient groups (at the time of writing 21/60 patients in total had been recruited, the results for which are presented in this chapter):

- Chronic viral Hepatitis B or C infection (N=0)
- Symptomatic coeliac disease (N=3)
- Symptomatic Crohn's disease (N=10)
- Diverticulitis (N=3)
- Active *Helicobacter pylori* infection (N=0)
- Clinical, radiological or histological diagnosis of liver cirrhosis (N=5).

6 healthy volunteers were also recruited to increase the overall healthy volunteer group size to 10 (at the time of writing 6/10 healthy volunteers had been recruited).

These diseases were chosen so that data from a range of anatomical locations within the abdomen was studied. Differences in the lymph nodes are expected to

4. *Abdominal Lymph Nodes*

be seen amongst the groups depending on the location of the inflamed tissue and the severity of the inflammation. All groups are expected to show an increase in size and decrease in the ADC of the lymph nodes surrounding the inflamed tissue with the exception of the coeliac group in which necrosis may be present in the lymph nodes which would cause an increase in the ADC. The cohort, whilst small, was deemed sufficient to provide pilot data for future studies. In order to minimise the risk of intolerance of the MRI scan, the patient not attending the MRI scan and to ensure the study followed ethical practises the following inclusion criteria were also set:

- Aged 18-75
- Male or Female
- Able to give informed consent
- Able to schedule the first MRI scan within 2 months of the screening visit.

The following exclusion criteria were set:

- Pregnancy declared by candidate
- Contraindications for MRI scanning i.e. metallic implants, pacemakers, history of metallic foreign body in eye(s) and penetrating eye injury
- Inability to lie flat or exceed weight <120kg
- Poor understanding of English language
- Participation in any medical trials for the past 3 months
- Judgement by the PI that the candidate will be unable to comply with the full study protocol e.g. severe COPD
- Asymptomatic coeliac disease or Crohn's disease.

4. Abdominal Lymph Nodes

The patient cohort was made up of 15 females and 6 males. The mean age was 46 ± 17 years. The healthy volunteer cohort was made up of 3 females and 3 males. The mean age was 32 ± 13 years. Participants were informed not to eat for a minimum of 8 hours prior to the MRI study visit.

4.6.2 MAL Protocol

All participants were scanned on a Philips 3T Ingenia (Best, Netherlands). Participants were scanned in the supine position rather than the prone position as the patients were less tolerant than healthy volunteers to the MRI scans and were therefore placed in the supine position which most patients find more tolerable. The scanning protocol and scan parameters are detailed in Table 4.3. As per the healthy volunteer pilot study the free breathing DWIBS was performed at two b values (0 and 600 s/mm^2) to obtain a guide as to the location of the abdominal lymph nodes. This was used to position the standard DWI and the long-TE DWI slices. For the long-TE DWI scans the echo times used were differed from those used in the healthy pilot group. The echo times were shortened to allow for the start of the decay curve to be better characterised. The echo times were also collected in two sweeps from a low TE to a high TE, this was done so that in the case of a patient moving during the scans or aborting the scan early the full decay curve was more likely to be sampled.

4.6.3 Analysis

The same analysis was used in this section as was used in Section 4.5.3. ROIs were drawn in the nodes and T2 and ADC were calculated respectively. Again for the T2 fit if the R-squared value for the fit was below 0.9 then the T2 measurement was not used in the final analysis. For the patient data 51% of nodes had an R2 higher than 0.9 in the T2 fit. This was due to the large amount of motion that was seen throughout the long-TE DWI scans. The increased amount of motion is likely due to the fact that the acquisition of these scans

4. Abdominal Lymph Nodes

Scan Parameter	T2 anatomical	DWIBS	Standard DWI (ADC measurement)	Long-TE DWI (T2 measurement)
TE (ms)	80	85	76	55, 95, 135, 175, 75, 115 and 155
Minimum TR (ms)	1676	2258	1938	4000
Voxel size (mm ²)	1.56 x 1.56	2.5 x 2.5	2.5 x 2.5	2.5 x 2.5
Slice thickness (mm)	3.12	4.68	4.68	4.68
Number of slices	40	20	8	8
Slices orientation	Coronal	Coronal	Sagittal	Sagittal
Reconstruction in-plane (mm ²)	0.78 x 0.78	1.56 x 1.56	1.56 x 1.56	1.56 x 1.56
Half Fourier factor	-	-	-	0.69
SENSE factor	2	2.3	2.3	2.3
<i>b</i> values (s/mm ²)	0	0, 600	400, 500, 600	300
EPI/TSE factor	120	69	53	53
Number of sequence averages	1	1	5	4
Motion correction	Triggered	Free breathing	Triggered	Triggered

Table 4.3: Table detailing the parameters of the scans for the MAL study.

4. *Abdominal Lymph Nodes*

took around 30 minutes providing a large time window for patient movement, and mis-triggering on the respiratory triggering.

A comparison between the measurements in healthy volunteers and the patient groups was performed in two ways. Firstly all of the lymph nodes from a single patient group were pooled and compared with the healthy volunteer group (for example median of all Crohn's nodes compared with median of all healthy nodes). This method was chosen as the number of patients in each group was low. Secondly the average values for each individual were calculated and then the groups compared.

For the pooled group analysis, each group was tested for normality, if both the healthy group and patient group passed a normality test then the two were compared using a two tailed Welch's t test which allowed for the assumption that the groups may not have the same standard deviation. If one or both of the groups being compared did not pass a normality test then the two were compared using a two-tailed Mann-Whitney test which accounts for the two groups not following a Gaussian distribution.

For the individual analysis the median values were calculated for each individual participant as the measurements did not follow a normal distribution. The medians for the participants within each group were then tested for normality and were found to have a normal distribution. Therefore the means for each group were then calculated and were compared using the two tailed Welch's t test.

4.6.4 Results

Figure 4.15 shows lymph nodes identified on DWI images at standard and long echo times in a healthy participant and a Crohn's patient. On average 29 nodes (varying between 13 and 39) were identified in patients and 29 (varying between 15 and 31) in healthy volunteers, however the number of nodes seen was highly dependent on the quality of respiratory triggering. The results for the group analysis are shown in Table 4.4 and the results for the individual analysis are shown in Table 4.5 with plots of the results in Figures 4.16, 4.17, 4.18 and 4.19.

4. Abdominal Lymph Nodes

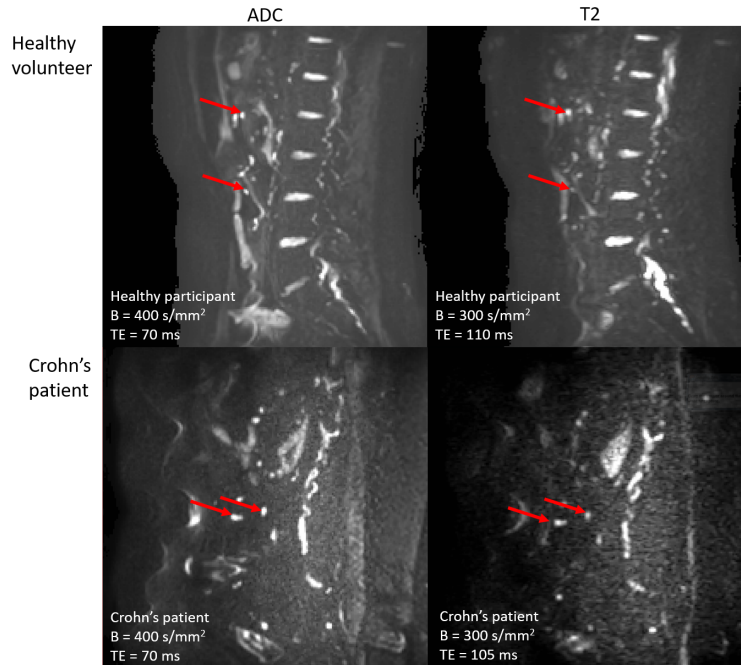


Figure 4.15: Top: Healthy volunteer taken from the pilot data set, two lymph nodes shown by the red arrows on a standard diffusion weighted image on the left and the same two nodes on a long-TE (TE = 110ms) diffusion weighted image on the right. Below: Crohn's patient, two lymph nodes shown by the red arrows on a standard diffusion weighted image on the left and the same two nodes on a long-TE (TE = 105ms) diffusion weighted image on the right. Nodes in the Crohn's patient appear larger.

4. Abdominal Lymph Nodes

Measurement Group	Total Number of nodes	ADC (10^{-3} mm ² /s)	T2 (ms)	Major axis (mm)	Minor axis (mm)
Healthy volunteers	150	1.4 (0.7)	101 (29)	7.1 (2.3)	4.8 (1.1)
Crohn's disease	176	1.3 (0.9) p = 0.03 *	107 (31) p = 0.08	7.4 (2.2) p = 0.02 *	5.0 (1.7) p <0.001 ***
Coeliac disease	95	1.7 (0.9) p <0.001 ***	106 (27) p = 0.30	7.1 (1.9) p = 0.71	4.8 (1.7) p = 0.22
Diverticulitis	55	1.2 (0.7) p <0.01 **	108 (33) p = 0.67	7.9 (2.1) p = 0.01 *	5.2 (1.5) p <0.001 ***
Liver cirrhosis	84	1.4 (0.8) p = 0.38	106 (20) p = 0.30	8.1 (2.0) p <0.001 ***	5.9 (1.6) p <0.001 ***

Table 4.4: Number of nodes in each group with the median and interquartile range (in brackets) of the ADC, T2 and length of the major and minor axis calculated for each group as a whole. The p values for comparisons between the healthy volunteer group and each patient group are shown for each measure and each patient group, with significant changes indicated (p <0.05 = *, p <0.01 = **, p <0.001 = ***).

4. Abdominal Lymph Nodes

Measurement Group	Number of nodes	ADC (10^{-3} mm ² /s)	T2 (ms)	Major axis (mm)	Minor axis (mm)
Healthy volunteers	30 ± 4	1.4 ± 0.1	112 ± 24	7.2 ± 0.3	4.7 ± 0.3
Crohn's disease	22 ± 4	1.3 ± 0.4 p = 0.41	112 ± 22 p = 0.97	7.9 ± 1.4 p = 0.14	5.2 ± 0.9 p = 0.16
Coeliac disease	38 ± 2	1.7 ± 0.1 p = 0.10	105 ± 7 p = 0.57	7.3 ± 0.7 p = 0.80	4.4 ± 0.9 p = 0.69
Diverticulitis	26 ± 1	1.2 ± 0.1 p = 0.01 *	108 ± 18 p = 0.83	8.0 ± 0.9 p = 0.28	5.3 ± 0.6 p = 0.21
Liver cirrhosis	28 ± 1	1.3 ± 0.1 p = 0.18	118 ± 19 p = 0.66	8.1 ± 0.4 p = 0.02 *	6.1 ± 0.8 p = 0.04 *

Table 4.5: Mean and standard deviation of number, ADC, T2 and length of the major and minor axis calculated for each individual. The p values for comparisons between the healthy volunteer group and each patient group are shown for each measure and each patient group, with significant changes indicated (p <0.05 = *, p <0.01 = **, p <0.001 = ***).

Apparent Diffusion Coefficient

When comparing the ADC of healthy volunteers and patients using a group comparison all groups excluding the liver cirrhosis patients showed a significant change in ADC. The Crohn's disease and diverticulitis groups both showed a reduction in ADC. Patients with coeliac disease showed an increase in ADC.

When the data was analysed using the median ADC value for each participant only the diverticulitis group showed a significant change in the ADC value when compared with the healthy volunteers. The coeliac group did show a trend towards a higher ADC but this did not reach significance ($p=0.1$).

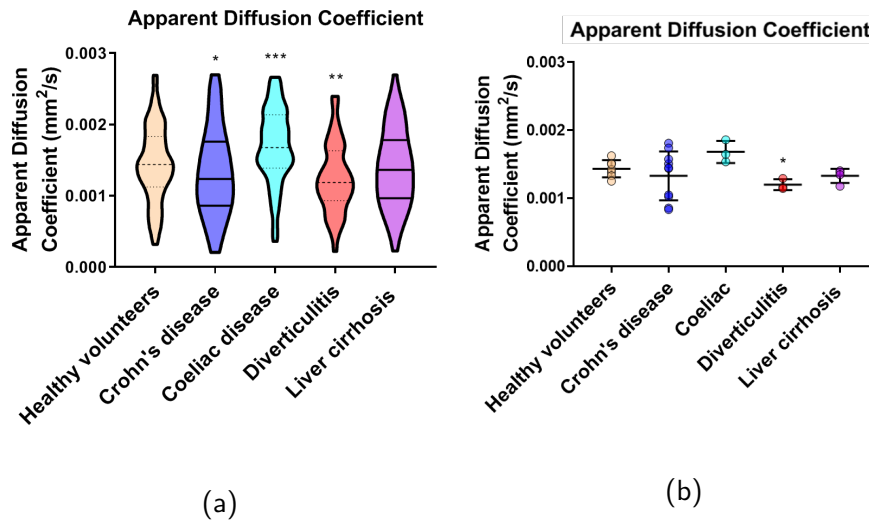


Figure 4.16: a) Violin plot showing the distribution of ADC measurements from all participants within each group. b) Median ADC value for each participant plotted for each group. The bars indicate the mean \pm 1 SD for each group. Statistically significant differences between the healthy volunteer group and the patient group are indicated by an asterisk above the patient group ($p < 0.05 = *$, $p < 0.01 = **$, $p < 0.001 = ***$).

T2

Using a group comparison no patient group showed a statistically significant difference in T2 when compared with the healthy volunteers. The Crohn's patients showed a trend towards higher T2, however this did not reach significance ($p =$

4. Abdominal Lymph Nodes

0.08).

When the data was analysed using the median T2 value for each participant no significant differences were seen in the mean of the values when comparing with the healthy volunteer group.

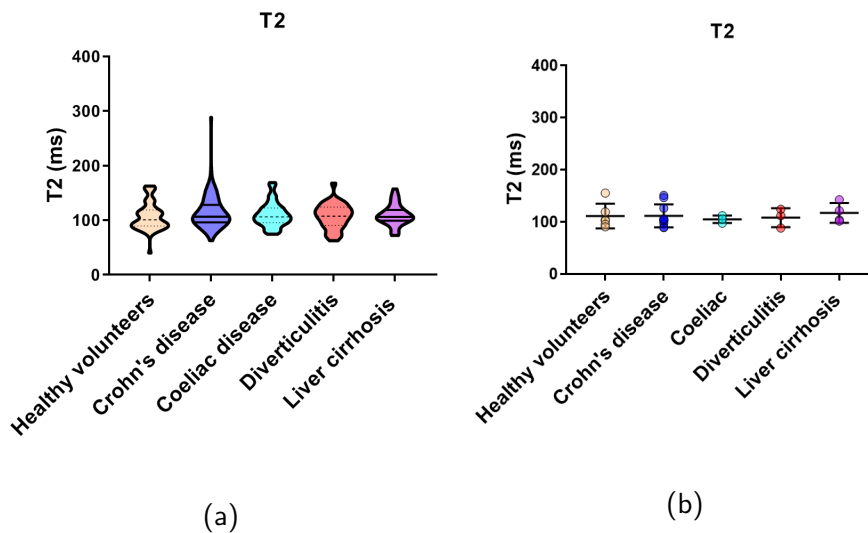


Figure 4.17: a) Violin plot showing the distribution of T2 measurements from all participants within each group. b) Median T2 value for each participant plotted for each group. The bars indicate the mean \pm 1 SD for each group. Statistically significant differences between the healthy volunteer group and the patient group are indicated by an asterisk above the patient group ($p < 0.05 = *$, $p < 0.01 = **$, $p < 0.001 = ***$).

Size of Lymph Nodes

When using a group comparison all patient groups, except for the coeliac group, showed an increase in major and minor axis length when compared with the healthy volunteers. The coeliac group showed no change in the length of the major or minor axis of the lymph nodes.

When the data was analysed using the median major and minor axis lengths for each participant, only the liver cirrhosis group showed a significant increase in length when compared with the healthy volunteers. All other patient groups

4. Abdominal Lymph Nodes

did not show a change in major or minor axis length when compared with healthy volunteers.

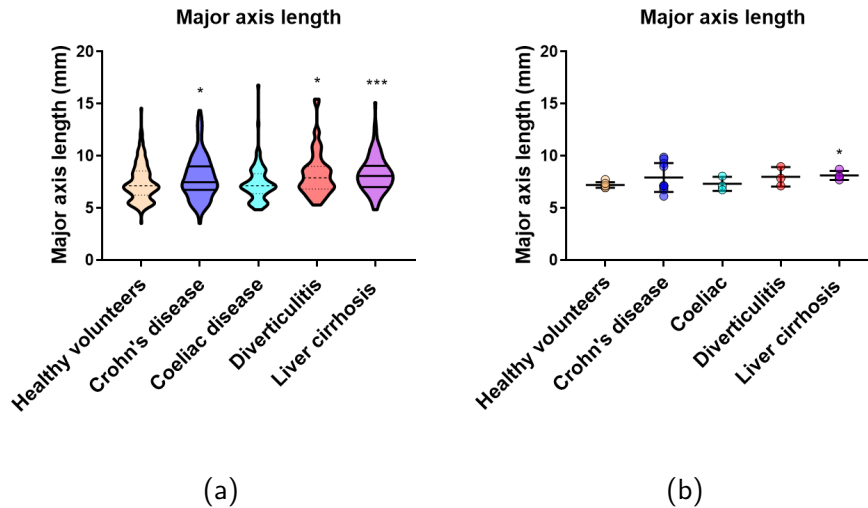


Figure 4.18: a) Violin plot showing the distribution of major axis length measurements from participants within each group. b) Median major axis length value for each participant plotted for each group. The bars indicate the mean \pm 1 SD for each group. Statistically significant differences between the healthy volunteer group and the patient group are indicated by an asterisk above the patient group ($p < 0.05 = *$, $p < 0.01 = **$, $p < 0.001 = ***$).

4. Abdominal Lymph Nodes

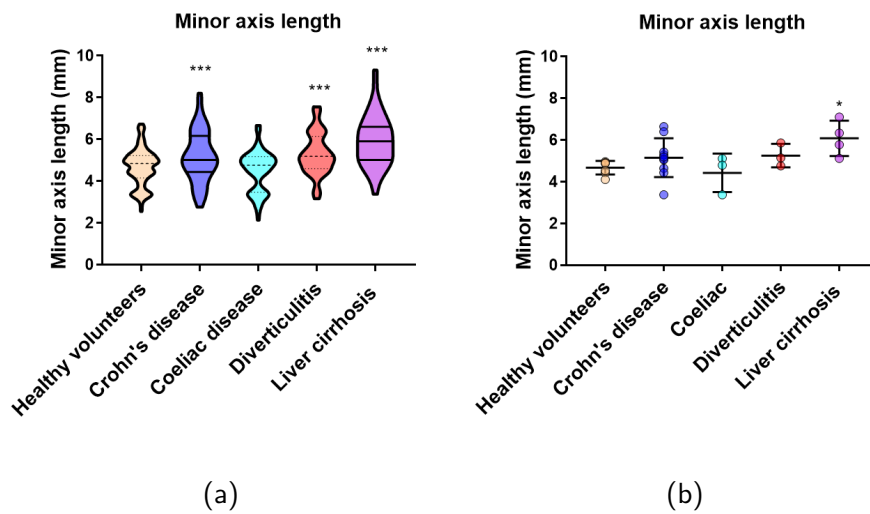


Figure 4.19: a) Violin plot showing the distribution of minor axis length measurements from all participants within each group. b) Median minor axis length value for each participant plotted for each group. The bars indicate the mean \pm 1 SD for each group. Statistically significant differences between the healthy volunteer group and the patient group are indicated by an asterisk above the patient group ($p < 0.05 = *$, $p < 0.01 = **$, $p < 0.001 = ***$).

4.6.5 Inter Observer Reproducibility

Inter observer reproducibility was tested using 10 patient data sets and two observers. Both observers were blinded to the patients disease and followed the same rules to identify and draw around nodes as discussed in section 4.5.3. Prior to the reproducibility test 5 different patient data sets were used as a training data set to ensure both observers had some experience in identifying lymph nodes and drawing the ROIs. Figure 4.20 shows the Bland Altman plot for the inter observer reproducibility of the ADC measurements. Figure 4.21 shows the Bland Altman plot for the inter observer results for T2 and Figures 4.22 and 4.23 show the Bland Altman plot for the major and minor axis lengths.

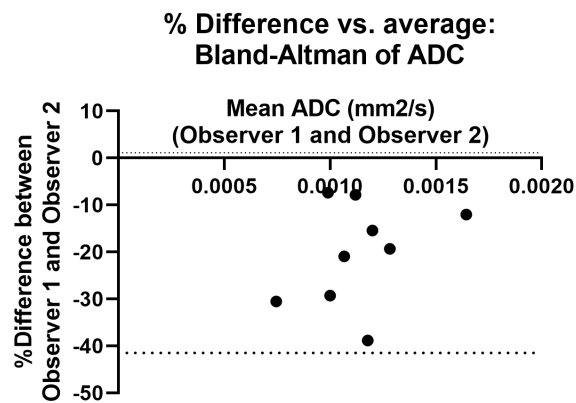


Figure 4.20: Bland-Altman plot for the ADC measured by Observer 1 and Observer 2. Dashed lines indicate the 95% confidence intervals.

4. Abdominal Lymph Nodes

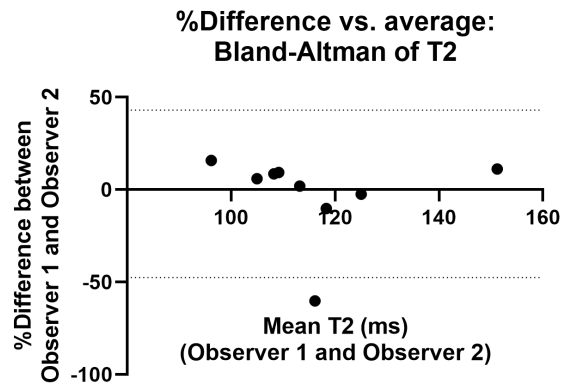


Figure 4.21: Bland-Altman plot for the T2 measured by Observer 1 and Observer 2. Dashed lines indicate the 95% confidence intervals.

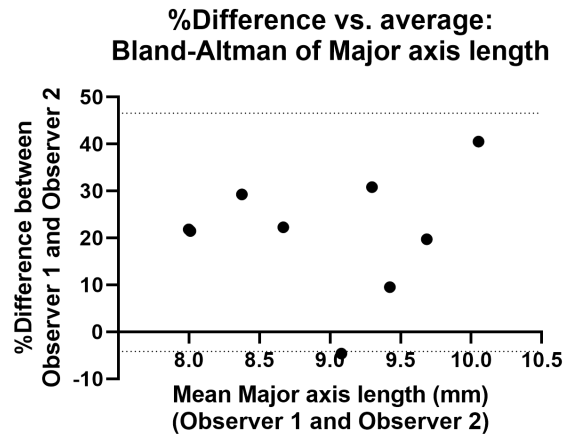


Figure 4.22: Bland-Altman plot for the major axis length measured by Observer 1 and Observer 2. Dashed lines indicate the 95% confidence intervals.

4. Abdominal Lymph Nodes

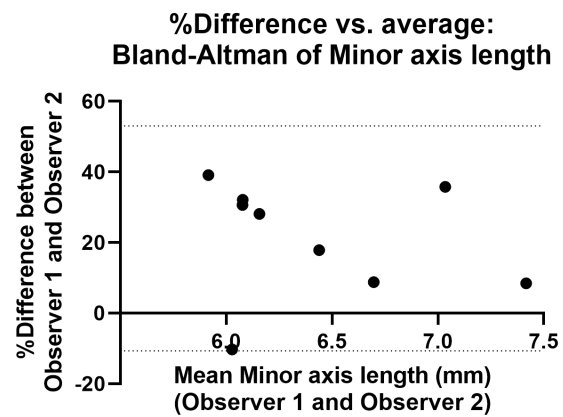


Figure 4.23: Bland-Altman plot for the minor axis length measured by Observer 1 and Observer 2. Dashed lines indicated the 95% confidence intervals.

From Figures 4.20, 4.21, 4.22 and 4.23 it can be seen that the inter observer variability is high. This is likely due to the fact that the analysis method is not automated and a large amount of observer input is required in determining which lymph nodes to draw around. The observer must determine which objects in the image are lymph nodes, whether the same nodes are present in the T2 and ADC images and whether the node is present in the same location throughout the image acquisition. Automating a method for drawing around the lymph nodes would prove to be difficult due to the subjective nature of determining what is/isn't a lymph node in the image. This type of analysis would be well suited to a machine learning algorithm providing reliable training data can be used.

4.7 Discussion

As expected from the literature significant changes were measured in size and diffusion coefficient in patients with inflammatory gastrointestinal diseases.

In patients with Crohn's disease nodes were significantly larger than those seen in healthy volunteers. ADC was also decreased which is likely to be an indication of an increase in cellularity in the lymph nodes which could be associated with migration of immune system cells to the active lymph nodes (similar changes have been reported in cancer). T2 showed no significant difference between the patients and the healthy volunteers ($p = 0.08$). This could be due to inflammation or other changes associated with lymph nodes in this condition however the number of patients may have been too small in this pilot study to observe this.

Similar changes were found in patients with diverticulitis with the size significantly increasing and the diffusion coefficient significantly decreasing when compared with healthy volunteers. Again this is likely related to increased cellularity resulting from inflammation of the surrounding tissue.

Patients with coeliac disease presented with an interesting finding that the size of the lymph nodes did not change however the diffusion coefficient increased when compared with healthy volunteers. This increase in ADC is the opposite effect to that seen in the lymph nodes of patients with Crohn's disease

4. *Abdominal Lymph Nodes*

and diverticulitis. The increase in diffusion coefficient is likely due to necrosis occurring in the lymph nodes which has been previously documented (8). This finding could provide a very useful non-invasive biomarker of coeliac disease which has the potential of differentiating coeliac disease from other inflammatory diseases as well as healthy volunteers. This may be of particular benefit in the diagnosis of children with coeliac disease as the current diagnosis method is via a biopsy which is invasive and carries higher risks than those associated with undergoing an MRI scan.

Patients with liver cirrhosis were found to have a significant increase in lymph node size but no changes were detected in the diffusion coefficient. The fact that no change is seen may be due to the fact that the nodes imaged were not draining inflamed tissue. The size increase with lack of diffusion changes may potentially be explained by the increase in permeability of the bowel wall that can occur in patients with liver cirrhosis. The increase in permeability causes a larger amount of substance to flow from the intestines and through the lymph nodes in cirrhosis patients than in healthy volunteers. This increase rather than change in drainage content may cause the nodes to swell.

The current method of analysis looks at the median measurements in each patient group, however this may not be the optimal way of comparing the groups. If, for example, a sample of lymph nodes are measured in which only a small sub-sample were linked to diseased tissue then only the small sub-sample of the nodes would differ from those in healthy volunteers. There is a potential for this to become masked in the averaging process. Perhaps a better method of comparing results would be to have a large sample of nodes measured in healthy volunteers and to then compare how many nodes a patient has that lie outside of this normal range. It is expected that a healthy person would have very few or no nodes outside of this range whilst a person with wide spread inflammatory disease would be expected to have many nodes outside of this range. The data collection in this study is not yet complete and so this type of analysis will be investigated once all data is collected.

The main limitation of this study was that only a limited number of imaging

slices could be acquired in a reasonable scan time and the fact that there were only a small number of patients in each group. Multiband imaging was trialled for this study to allow for an increase in the number of slices however the SNR loss due to the use of Multiband meant that the SNR became too low to visualise the lymph nodes. A second limitation of the study is that lymph nodes are not spherical in shape and so the true major and minor axis are not likely to have been measured in this analysis. It is unlikely that this limitation will be overcome as changing the orientation of the slices to achieve a cross sectional image of the true major and minor axis for each node is infeasible. Despite this being considered a limitation the major and minor axis lengths are the commonly used measures of size of lymph nodes in imaging studies and diagnostics with a minor axis length above a given size used to indicate malignancy.

The TR used for the diffusion imaging may have caused a decrease in SNR in the nodes of the coeliac patients. This is due to the necrotic tissue having a longer T1 and therefore not undergoing full recovery before the next acquisition. The coeliac patient data was compared to the healthy volunteer data and a ratio of the signal in the nodes to the surrounding noise taken for each participant. No significant changes were found between the SNR in the coeliac group when compared with the patient group. Therefore it was concluded that the T1 of the nodes was not long enough to impact on the SNR of the images.

The subjectivity of the ROI drawing in the analysis method is another limitation of the study. As this is a pilot study, the data here could be used to determine a more robust analysis method. Writing an automated analysis programme would be difficult due to the subjective nature of identifying lymph nodes in images. A machine learning algorithm may be a better method of analysis and the data presented here could serve as a training data set for such an algorithm.

4.8 Conclusion

In this section the development work performed to enable the visualisation and quantitative measurements of abdominal lymph nodes without the use of a

contrast agent has been shown. The first non-invasive MRI study which has compared quantitative measures of abdominal lymph nodes in healthy volunteers with patients with a range of inflammatory gastrointestinal diseases was also performed. The measurements show that there is potential for lymph nodes to be used as a biomarker of inflammatory disease. The progression of this work that goes beyond the scope of this thesis, is to first complete the data collection for this study at which point the best method to compare nodes can be evaluated and second to evaluate intra participant reproducibility.

References

- [1] J S Alexander, V C Ganta, P A Jordan, and M H Witte. Gastrointestinal lymphatics in health and disease. *Pathophysiology*, 17(4):315–335, 2010. doi: <http://dx.doi.org/10.1016/j.pathophys.2009.09.003>.
- [2] L Van den Bergh, S Joniau, K Haustermans, C M Deroose, S Isebaert, R Oyen, F M Mottaghy, F Ameye, J Berkers, H Van Poppel, and E Lerut. Reliability of Sentinel Node Procedure for Lymph Node Staging in Prostate Cancer Patients at High Risk for Lymph Node Involvement. *Acta oncologica (Stockholm, Sweden)*, 54(6):896–902, 2015. ISSN 1651-226X. doi: 10.3109/0284186X.2014.987354.
- [3] A Perrone, P Guerrisi, L Izzo, I D Angeli, S Sassi, L Lo, M Marini, D Mazza, and M Marini. Diffusion-weighted MRI in Cervical Lymph Nodes : Differentiation Between Benign and Malignant Lesions. *European Journal of Radiology*, 77(2):281–286, 2011. ISSN 0720-048X. doi: 10.1016/j.ejrad.2009.07.039.
- [4] P Y von der Weid and K J Rainey. Review article: lymphatic system and associated adipose tissue in the development of inflammatory bowel disease. *Aliment Pharmacol Ther*, 32(6):697–711, 2010. doi: 10.1111/j.1365-2036.2010.04407.x.

References

- [5] H L Bockus. *Gastroenterology*. WB Saunders, Philadelphia, 1946.
- [6] J Rimola, I Ordás, S Rodriguez, O García-Bosch, M Aceituno, J Llach, C Ayuso, E Ricart, and J Panés. Magnetic Resonance Imaging for Evaluation of Crohn's Disease. *Inflammatory Bowel Diseases*, 17(8):1759–1768, aug 2011. ISSN 1078-0998. doi: 10.1002/ibd.21551.
- [7] C J Tutein Nolthenius, S Bipat, B Mearadji, A M Spijkerboer, C Y Ponsioen, A D Montauban van Swijndregt, and J Stoker. MRI Characteristics of Proctitis in Crohn's Disease on Perianal MRI. *Abdominal Radiology*, 41(10): 1918–1930, oct 2016. ISSN 2366-004X. doi: 10.1007/s00261-016-0802-z.
- [8] H J Freeman. Mesenteric Lymph Node Cavitation Syndrome. 16(24): 2991–2993, 2010. doi: 10.3748/wjg.v16.i24.2991.
- [9] H Takahashi, S Kuboyama, H Abe, T Aoki, M Miyazaki, and H Nakata. Clinical Feasibility of Noncontrast- Enhanced Magnetic Resonance Lymphography of the Thoracic Duct. *Chest*, 124(6):2136–2142, 2003. ISSN 00123692. doi: 10.1378/chest.124.6.2136.
- [10] T C Kwee, T Takahara, M A Vermoolen, M B Bierings, W P Mali, and R A J Nivelstein. Whole-body diffusion-weighted imaging for staging malignant lymphoma in children. *Pediatric Radiology*, 40(10):1592–1602, 2010. ISSN 03010449. doi: 10.1007/s00247-010-1775-7.
- [11] P Kos, C Tekinbas, M Erol, A Sari, H Kavgaci, and O Funda. Mediastinal Lymph Nodes : Assessment With Diffusion-Weighted MR Imaging. 297: 292–297, 2009. doi: 10.1002/jmri.21850.
- [12] M Hasbahceci, A Akcakaya, N Memmi, I Turkmen, G Cipe, P Yildiz, D S Arici, and M Muslumanoglu. Diffusion MRI on Lymph Node Staging of Gastric Adenocarcinoma. 5(3):392–400, 2015. doi: 10.3978/j.issn.2223-4292.2015.03.06.
- [13] C Mesmann, M Sigovan, L Berner, A Abergel, F Tronc, Y Berthezène, P Douek, and L Bousset. Evaluation of image quality of DWIBS versus DWI

References

- sequences in thoracic MRI at 3 T. *Magnetic Resonance Imaging*, 32(10): 1237–1241, 2014. doi: <http://dx.doi.org/10.1016/j.mri.2014.08.015>.
- [14] F E Lecouvet, J El Mouedden, L Collette, E Coche, E Danse, F Jamar, J Machiels, B Vande Berg, P Omoumi, and B Tombal. Can Whole-body Magnetic Resonance Imaging with Diffusion-weighted Imaging Replace Tc 99m Bone Scanning and Computed Tomography for Single-step Detection of Metastases in Patients with High-risk Prostate Cancer? *European Urology*, 62(1):68–75, 2012. doi: <http://dx.doi.org/10.1016/j.eururo.2012.02.020>.
- [15] T C Kwee, M A Vermoolen, E A Akkerman, M J Kersten, R Fijnheer, I Ludwig, F J A Beek, M S Van Leeuwen, M B Bierings, M C A Bruin, J Zsíros, H M E Quarles Van Ufford, J M H De Klerk, J Adam, J Stoker, C S Uiterwaal, and R A J Nieuwstein. Whole-body MRI, Including Diffusion-Weighted Imaging, for Staging Lymphoma: Comparison with CT in a Prospective Multicenter Study. *Journal of Magnetic Resonance Imaging*, 40(1):26–36, 2014. ISSN 15222586. doi: 10.1002/jmri.24356.
- [16] P Reimer, P M Parizel, J F M Meaney, and F A Stichnoth. *Clinical MR Imaging: A Practical Approach*. Springer Berlin Heidelberg, 2010. ISBN 9783540745044.
- [17] M F Reiser, W Semmler, and H Hricak. *Magnetic Resonance Tomography*. Springer Berlin Heidelberg, 2007. ISBN 9783540293552.
- [18] L Arrivé, S Derhy, S E Mouhadi, Y Menu, C Becker, and L Monnier-cholley. Noncontrast Magnetic Resonance Lymphography. pages 80–85, 2016.
- [19] E I Akduman, A J Momtahn, N C Balci, N Mahajann, N Havlioglu, and M K Wolverson. Comparison between Malignant and Benign Abdominal Lymph Nodes on Diffusion-Weighted Imaging. *Academic radiology*, 15(5): 641–6, 2008. ISSN 1076-6332. doi: 10.1016/j.acra.2007.12.023.

- [20] Y Ohno, H Hatabu, D Takenaka, T Higashino, H Watanabe, C Ohbayashi, M Yoshimura, M Satouchi, Y Nishimura, and K Sugimura. Metastases in mediastinal and hilar lymph nodes in patients with non-small cell lung cancer: quantitative and qualitative assessment with STIR turbo spin-echo MR imaging. *Radiology*, 231(3):872–879, 2004. doi: 10.1148/radiol.2313030103.
- [21] L Xu, J Tian, Y Liu, and C Li. Accuracy of diffusion-weighted (DW) MRI with background signal suppression (MR-DWIBS) in diagnosis of mediastinal lymph node metastasis of nonsmall-cell lung cancer (NSCLC). *Journal of Magnetic Resonance Imaging*, 40(1):200–205, 2014. doi: 10.1002/jmri.24343.
- [22] G C Doms, H Hricak, M E Moseley, K Bottles, M Fisher, and C B Higgins. Characterization of Lymphadenopathy by Magnetic Resonance Relaxation Times: Preliminary Results. *Radiology*, 155(3):691–697, jun 1985. ISSN 0033-8419. doi: 10.1148/radiology.155.3.4001371.
- [23] C Li, S Meng, X Yang, J Wang, and J Hu. The Value of T2* in Differentiating Metastatic from Benign Axillary Lymph Nodes in Patients with Breast Cancer - A Preliminary In Vivo Study. *PLoS ONE*, 9(1):e84038, jan 2014. ISSN 1932-6203. doi: 10.1371/journal.pone.0084038.
- [24] T C Kwee, T Takahara, R Ochiai, R A J Nivelstein, and P R Luijten. Diffusion-weighted whole-body imaging with background body signal suppression (DWIBS): features and potential applications in oncology. *European Radiology*, 18(9):1937–1952, 2008. doi: 10.1007/s00330-008-0968-z.
- [25] S Ganeshalingam and D-M Koh. Nodal Staging. *Cancer imaging : the official publication of the International Cancer Imaging Society*, 9(1):104–11, dec 2009. ISSN 1470-7330. doi: 10.1102/1470-7330.2009.0017.
- [26] M J McAuliffe, F M Lalonde, D McGarry, W Gandler, K Csaky, and B L Trus. Medical Image Processing, Analysis and Visualization in Clinical Re-

References

- search. In *Proceedings 14th IEEE Symposium on Computer-Based Medical Systems. CBMS 2001*, pages 381–386, MIPAV. IEEE Comput. Soc. ISBN 0-7695-1004-3. doi: 10.1109/CBMS.2001.941749.
- [27] R E Dorfman, M B Alpern, B H Gross, and M A Sandler. Upper Abdominal Lymph Nodes: Criteria for Normal Size Determined with CT. <http://dx.doi.org/10.1148/radiology.180.2.2068292>, aug 1991. doi: 10.1148/RADIOLOGY.180.2.2068292.

5 Bowel Wall and the PerMinH Study

5.1 Introduction

The bowel wall has two main functions, it provides a barrier between the content of the bowel and the body, allowing certain substances to pass through into the body whilst blocking others, and it works to propel and mix the contents of the bowel. The bowel wall (described in section 3.7) is affected by many gastrointestinal diseases, including coeliac disease, inflammatory bowel disease (IBD), liver cirrhosis, irritable bowel syndrome (IBS), obesity, diabetes and Human Immunodeficiency Viruses (HIV) (1).

The permeability of the bowel wall is implicated in many diseases (2). A healthy bowel wall allows digested food to pass through into the blood and lymphatic vessels supplying the wall by two different methods. Substances can either move through the cells of the bowel wall (transcellular transport) or move through the spaces between the cells (paracellular transport) (Figure 5.1). Paracellular transport is restricted by tight junctions. These tight junctions are made up of proteins that hold the cells lining the wall together. When intact these tight junctions act as a selective barrier, preventing the free passage of bowel content through the bowel wall (2). If these become damaged the barrier becomes impaired, the permeability of the bowel wall is increased, and the bowel wall is said to be 'leaky' (Figure 5.1). Once the wall permeability is increased a process called increased bacterial translocation can occur (3). In the healthy bowel the passage of a small amount of bacteria from the bowel content through the wall is a normal immunological process which allows for the contents of the bowel to be screened for harmful substances. If the amount of transfer is increased then the chance of bacteria spreading throughout the body is increased, leading to an increased risk of bacterial infection (4). Therefore a marker of changes related to the structure or permeability of the bowel wall would have two main benefits: firstly a marker of structure would potentially allow for early disease manifestations to be identified and disease progression to be measured.

5. Bowel Wall and the PerMinH Study

Secondly a marker of the bowel wall permeability could allow for those at a high risk of bacterial infection to be identified.

All image acquisitions were performed by Hannah Williams, with initial assistance from Dr Caroline Hoad. Ethical approval and image sequence optimisation was performed by members of the gastrointestinal research group prior to the start of the authors PhD. Recruitment was carried out by Dr Robert Scott (Hepatologist). The work presented in this chapter has been presented as a poster presentation at the annual conference of the International Society of Magnetic Resonance Imaging (ISMRM) 2017 and 2018, and oral presentations at the Nottingham Digestive Diseases annual showcase 2018 and the East Midlands Doctoral Conference 2018. All image analysis was performed by the author of this thesis. Additional analysis to allow inter observer reproducibility to be evaluated was performed by Ali Alymami (PhD Student).

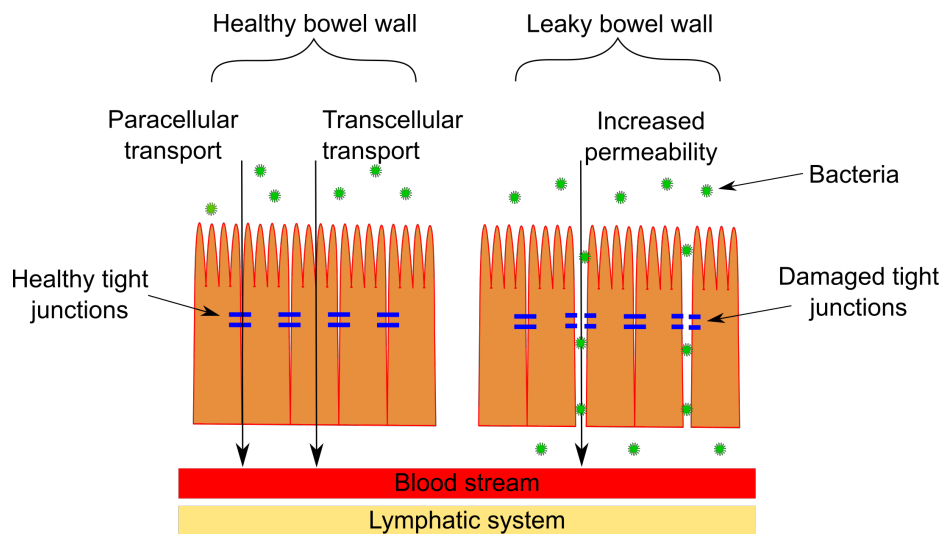


Figure 5.1: Diagram of the healthy and leaky bowel wall. In the healthy bowel wall substances are transported across the bowel wall barrier either via paracellular (between the cells) or transcellular transport (through the cells). The paracellular pathway is restricted by tight junctions which are made up of proteins. When the bowel wall is damaged these tight junctions can be broken, allowing substances from the bowel to pass much more freely through the bowel wall. Included in this is an increase in the amount of bacteria that can pass through, this is known as bacterial translocation.

5.2 Measuring Bowel Wall Permeability

Several methods exist for measuring the permeability of the bowel wall however, none currently meet the STARD initiative (5) (STAndards of Reporting of Diagnostic accuracy), meaning that they do not employ standardised methods, and the reported results are heterogeneous. The two main methods that are currently used are direct visualisation using confocal laser endoscopy (CLE) and the Lactulose:Mannitol urine test (LMR) (1, 6). CLE involves placing an endoscope down the oesophagus and into the intestines where a fluorescent dye is injected allowing the cell lining of the intestinal wall to be visualised (7). Whilst CLE has the benefit of providing direct visualisation of the bowel wall, the amount of wall that can be sampled is limited and the test requires deep sedation, limiting it to highly selected patients in specialised centres.

The Lactulose:Mannitol urine test involves measuring the amount of two different sized sugars, lactulose and mannitol, that are present in urine. The two sugars are absorbed by the bowel but are poorly metabolised meaning the majority of the sugar is passed straight out of the body in the urine. An increase in the ratio of the two sugars in the urine would indicate an increase in the permeability of the bowel wall.

Changes in the bowel wall structure and permeability have been observed in many patient groups including patients with Crohn's disease, diverticulitis and coeliac disease amongst others (1). IBS patients have been shown to have an increased bowel permeability in comparison to healthy controls (8). Increased bowel permeability has also been associated with active Crohn's disease (9), and may occur prior to the onset of disease in susceptible individuals (10). It is well documented that patients with liver cirrhosis present with an increase in bacteria in their mesenteric lymph nodes and that the integrity of the bowel wall is impaired, in particular the small bowel wall (8, 11, 12, 13, 14).

Due to the involvement of the bowel wall in many gastrointestinal diseases and the current lack of a gold standard quantitative marker of the permeability of the bowel wall there is a strong case for the development of a standardised, non-invasive, widely available biomarker associated with the permeability of the bowel

wall. Such a measure would potentially allow for early disease manifestations to be investigated along with the effect of interventions aimed at altering the structure of the bowel wall.

MRI is an obvious choice for the development of such a test as it is already used as a qualitative marker of the bowel wall structure in Crohn's disease amongst other gastrointestinal diseases and has the potential to provide quantitative markers of the structure and permeability of the bowel wall.

5.3 MRI and the Bowel Wall

MRI is commonly used both quantitatively and qualitatively to measure several aspects of the bowel wall including bowel wall thickness, oedema and inflammation (using T2), for instance in relation to Crohn's disease activity (15). In the literature surrounding Crohn's disease the most commonly reported MR measures that have a high sensitivity are wall T2 hyper-intensity, bowel wall thickness and motility of the bowel (16). Contrast-based Magnetic Resonance Enterography is also used in Crohn's disease to detect ulcer healing with an accuracy of up to 90% (17).

Whilst MRI measures are commonly used as qualitative and quantitative markers of the inflammation of the bowel wall in Crohn's disease, quantitative MRI measures of the bowel wall that is non-enlarged has, to our knowledge, not been reported. More specifically no quantitative T1 or T2 measurements of the healthy bowel wall have been made and no relationship between MR markers and the permeability of the bowel wall has been reported.

Many MRI assessments of the bowel rely on the use of gadolinium as a contrast agent. However the use of gadolinium contrast agents in healthy volunteers has currently been limited due to an FDA safety alert regarding its use in humans (18). This restriction inhibits the ability to use the majority of current MRI investigative tools to look at differences in bowel wall structure between healthy controls and patients. In order to evaluate the potential of an MRI measure as a biomarker, the base line values of that marker in healthy controls is needed for a comparison. Thus the FDA safety alert inherently restricts any

current research which aims to evaluate the potential use of any MRI measure requiring a gadolinium contrast agent as a biomarker.

Therefore there is an urgent clinical need for a standardised, widely available, biomarker associated with increased bowel wall permeability to enable characterisation of the changes to test both mechanisms and the effect of interventions in patient groups. Due to the restriction of the use of gadolinium in healthy volunteers the logical approach to this problem is to develop a non-contrast enhanced marker of permeability in order to allow for future research into changes in bowel wall permeability to be carried out without being limited to certain patient groups only.

5.4 Study Overview and Design

In order to investigate whether non-contrast enhanced MRI markers could provide a minimally invasive and regionally specific biomarker for bowel wall permeability a pilot study was set up with the aim of investigating a wide range of MRI measures in a healthy volunteer group. The study titled "Characterization of the structural changes associated with small bowel permeability using MRI in Healthy Volunteers (PerMinH)" was approved by the University of Nottingham School of Medicine ethics board.

We hypothesised that there would be detectable differences in quantitative MRI measures of the small bowel in healthy volunteers between placebo and provocation with indomethacin. Two relatively small doses of oral indomethacin, a drug similar to aspirin, provides a well validated and safe provocation that increases small bowel permeability (19). A two week washout period has been demonstrated to be adequate in preventing cross-contamination (6). Specifically, the aim of the study was to characterise, using non-contrast enhanced MRI, any objective differences between the small bowel wall thickness, T1, T2 and motility under both conditions. These measures were chosen based on published data from MRI studies in which bowel wall changes have been observed in patients with Crohn's disease before and after treatment (20, 21, 22). A LMR urine test was also performed as this is the current standard measure of bowel wall

permeability. The study was carried out as part of this thesis and the thesis of Dr Robert Scott (a hepatologist). Dr Scott's thesis focuses on the bowel wall thickness and motility measures whilst this thesis focuses on the development of methods to measure T1 and T2 in the small bowel wall. For details of the small bowel wall thickness and motility measures please refer to Dr Scott's thesis (not yet published).

5.4.1 Study Objectives

The main purpose of the study was to use quantitative MRI techniques in two short scanning sessions to investigate the structure and characteristics of the small bowel wall and the changes that occur in these with increased intestinal permeability. The objectives were to describe the changes in MRI parameters (T1 and T2) related to the small bowel wall and oedema and inflammation, and to describe differences in the small bowel motility and small bowel wall thickness. In particular the aims of this section were to firstly develop an analysis method which would allow for the T1 and T2 of the small bowel wall to be measured, secondly to investigate the variation of these measures along the bowel wall and thirdly to evaluate the methods used in this pilot study to allow for further optimisation of these measures in future studies.

5.4.2 Study Design

The study was designed as a 2x2 crossover healthy volunteer provocation study. In a 2x2 crossover study there are two arms to the study, in this case a placebo arm and an indomethacin arm. Each volunteer was randomly allocated to start on one arm of the study and, after a given washout period, was then swapped to the other arm (Figure 5.2). The provocation was, in this case, the administration of the drug indomethacin which is known to increase the permeability of the bowel wall in healthy volunteers. By having patients following both arms of the study, allowances were made for individual baseline differences in bowel permeability. Investigators and participants were blinded to the allocation until the completion of the trial. The participants were split into two groups, participants

5. Bowel Wall and the PerMinH Study

1-8 were allocated as a training data set with the remaining 9-24 as a validation cohort. Participants attended three study days in total, a screening/consent day and then two scan days.

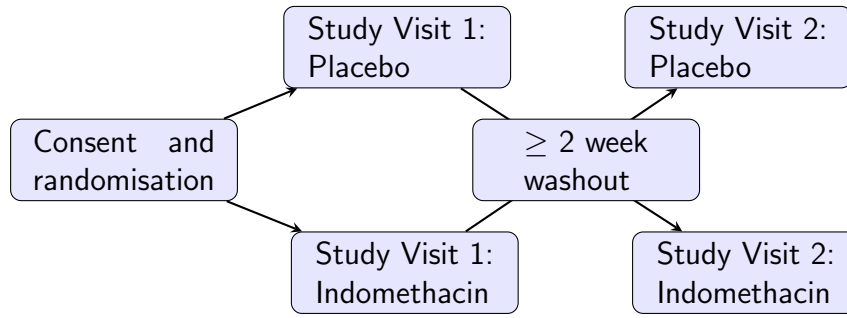


Figure 5.2: PerMinH study design, participants start on either the placebo or indomethacin arm of the study. After a washout period of two weeks they then swap to the opposite arm.

On the MRI study days (Figure 5.3) the participants were given 75 mg of either indomethacin or a placebo which was taken on the day of and the day preceding the MRI day. They were instructed to fast over night. Upon arrival a 2 hour LMR test was performed. After the LMR test the participants were then asked to consume an oral bowel preparation drink. This consisted of 1 litre of water containing 2.5% Mannitol, required for bowel distention, reduction of water absorption in the small bowel and to provide contrast between the content of the bowel and the wall of the bowel (23), and 0.2% locust bean gum, to slow the transition of the solution through the gastrointestinal tract. The participants then underwent a 1 hour MRI scan.

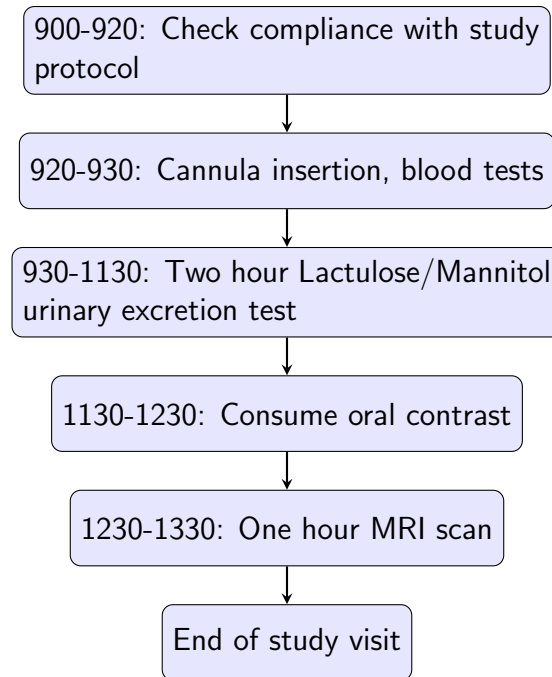


Figure 5.3: Schematic of participant experience during each study visit.

5.4.3 Studied Cohort

24 participants were recruited with the following inclusion/exclusion criteria.

Inclusion criteria:

- Aged 18-65
- Male or Female
- Able to give informed consent

The following exclusion criteria were set:

- Pregnancy
- Psychiatric disease
- Chronic gastrointestinal disorders or symptoms
- First degree relative with inflammatory bowel disease

5. *Bowel Wall and the PerMinH Study*

- Diabetes (type 1 or type 2)
- Active smoker
- Coeliac disease
- Food allergy
- Atopy
- Allergy or intolerance to imaging contrast agents
- Impaired renal function (eGFR <45 mls/min)
- Regular medications apart from oral contraception drugs
- Alcohol dependency
- Absolute contraindications for MRI
- Use of laxatives, antibiotics, NSAIDs, anti-cholinergics or opiates within two weeks of the first MRI study visit until the end of the final study visit.

The final participant cohort was made up of 15 females and 9 males. The median age was 23 years (interquartile range 22-25). The median body mass index was 23.7 (21.8-27.8) kg/m². The median interval between study visits was 21 (18-27) days. Two participants were excluded from the final analyses as one was non-compliant with the study protocol and one had an incidental finding of an asymptomatic thickened terminal ileum on review of the MRI data. Participants were informed to not smoke, drink alcohol and to refrain from ingestion of all artificial sweeteners for 72 hours prior to the MRI study days. The consumption of artificial sweeteners was required as they may contain lactulose or mannitol, which could affect the results of the LMR test, and there is also some evidence to suggest that they may change gastrointestinal permeability (24).

5.4.4 PerMinH Imaging Protocol

All subjects were scanned on a Philips 3T Achieva (N=46) or Ingenia (N=2). The Philips 3T Ingenia was used on two occasions where technical problems meant that the Achieva was unavailable. Participants lay in the prone position with their arms by their head. After the anatomical locator and motility scans subjects were given two 20 mg doses of intravenous Buscopan separated by 10 minutes. Buscopan is an antispasmodic drug that temporarily reduces peristalsis of the gut wall. The purpose of the Buscopan was to enable T1, T2 and wall thickness acquisitions to be carried out without peristalsis. Buscopan remains effective for around 8-10 minutes and thus the time over which the T1 and T2 scans could be acquired was restricted. This limited the T1 scans to 6 inversion times and the T2 scans to 6 echo times, each performed with separate breath holds. The scanning protocol consisted of the following acquisitions with the scan parameters of the T1 and T2 acquisitions detailed in Table 5.1:

- Survey
- B1 calibration
- Anatomical bTFE
- Anatomical axial T2W TSE
- Motility
- Buscopan administered
- mDIXON High Resolution
- T1 prepared FLASH (6 different inversion preparation times for T1 measurement)
- B1 map
- Buscopan administered

5. *Bowel Wall and the PerMinH Study*

- mDIXON lower resolution
- T2 prepared bTFE (6 different preparation echo times for T2)
- B1 map
- mDixon (for fat volume measurements)
- bTFE (High resolution for bowel wall thickness measurements)

In this thesis the T1 prepared FLASH sequence and T2 prepared bTFE are used to measure the T1 and T2 of the small bowel wall, these sequences were optimised by Dr Caroline Hoad prior to the start of this PhD. Each FLASH acquisition and bTFE acquisition for the T1 and T2 measurements was performed in a single breath hold with a 15 second wait time between each acquisition to allow for full recovery of the longitudinal magnetization. The acquisitions were single slice with the slice placed coronally in the plane where the terminal ileum enters the cecum. This location was chosen to provide consistency in the positioning of the slice across the two study days.

5. Bowel Wall and the PerMinH Study

Scan Parameters	T1	T2
Acquisition	Single slice IR - FLASH	Single slice Spin echo prepared bTFE
T1 prep (s)	0.5,0.8,1.2, 1.8,2.5,4.0	-
TE prep (ms)	-	20,50,80, 120,180,300
TE (ms)	2.3	1.68
Minimum TR (ms)	10	3.4
Voxel size (mm ²)	1.5 x 1.8 x 5	1.3 x 1.5 x 5
Reconstructed in-plane (mm ²)	0.98 x 0.98	1 x 1
Half Fourier factor	-	0.7
SENSE factor	2	1.5
Motion	Breath held	Breath held

Table 5.1: Details of the parameters of the T1 and T2 acquisitions taken as part of the PerMinH study.

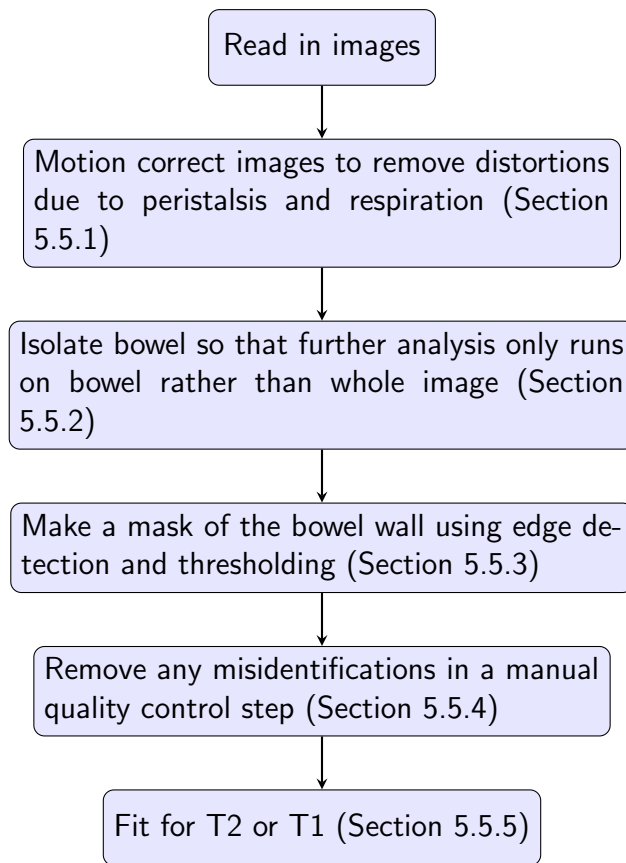
5.4.5 Lactulose:Mannitol Ratio Test

The *in vivo* permeability test is a standard differential urinary sugar excretion test (1, 25). In brief, after collection the total urine volume was noted and 1.5 mL sample aliquots were filtered with 450 nm filters (Merck Millipore, Billerica, Massachusetts, USA) and stored at -20°C until batch analysis was performed. All the samples were coded without reference to the test condition and the measurements were performed by a lab technician blinded to the test condition. The LMR in the urine collection of the first two hours after ingestion of the respective sugars was used to quantify the small bowel permeability (26, 27).

5.5 Calculating T1 and T2 of the Small Bowel Wall

In order to measure T1 and T2 of the small bowel wall the signal from the wall had to be extracted from the image. To do this code, was developed in Matlab which allowed for the signal along the wall to be automatically extracted, followed by a manual quality control step. The quality control step allowed for

any misidentifications to be removed (such as vessels, colon wall, etc). This section describes the process to obtain the signal from the bowel wall. A brief outline of the process is given below for reference. The development of each step was performed on the same training data set (participants 1-8). The training data set allowed for different motion correction, edge detection and thresholding techniques to be investigated. The analysis method was then finalised and used on all data sets. All development was performed prior to unblinding.



5.5.1 Motion Correction

The first step in the image analysis was to motion correct the images. Initially manual warping was trialled as a form of motion correction however this was time consuming and required a significant amount of user input. Therefore an

automated method based on Matlab's registration of MRI images was used.

The motion correction method used Matlab's inbuilt image registration function, `imregister`, which is an intensity-based image registration process. Several types of transformation were applied in order to motion correct the images. Firstly a similarity transformation was applied which uses translation, rotation and scale. Secondly an affine transformation was used which applies translation, rotation, scale and shear to match the images.

The images, at this stage, had been mainly corrected for large shifts in the image due to respiration, however small image distortions due to peristalsis still appeared in the images. Therefore the images underwent a second motion correction step. This motion correction was a non-linear registration problem solved by using Matlab's function for estimating displacement fields in images. The process was aimed at correcting local image distortions which were not fixed with rigid motion correction. The process takes two images and estimates the displacement field which would best minimise the intensity differences in the images, and then applies the field to the second image. The displacement field algorithm is based on image matching models proposed by Thirion and Vercauteren et al (28, 29).

The motion correction steps take around 5 minutes for each data set and requires no user input and so can be performed as a batch analysis. Following the motion correction a mask of the bowel wall was created. Figures 5.4 and 5.5 show the original T1/T2 images, the motion corrected images and the difference between the two for all inversion/echo times for a single data set.

5. Bowel Wall and the PerMinH Study

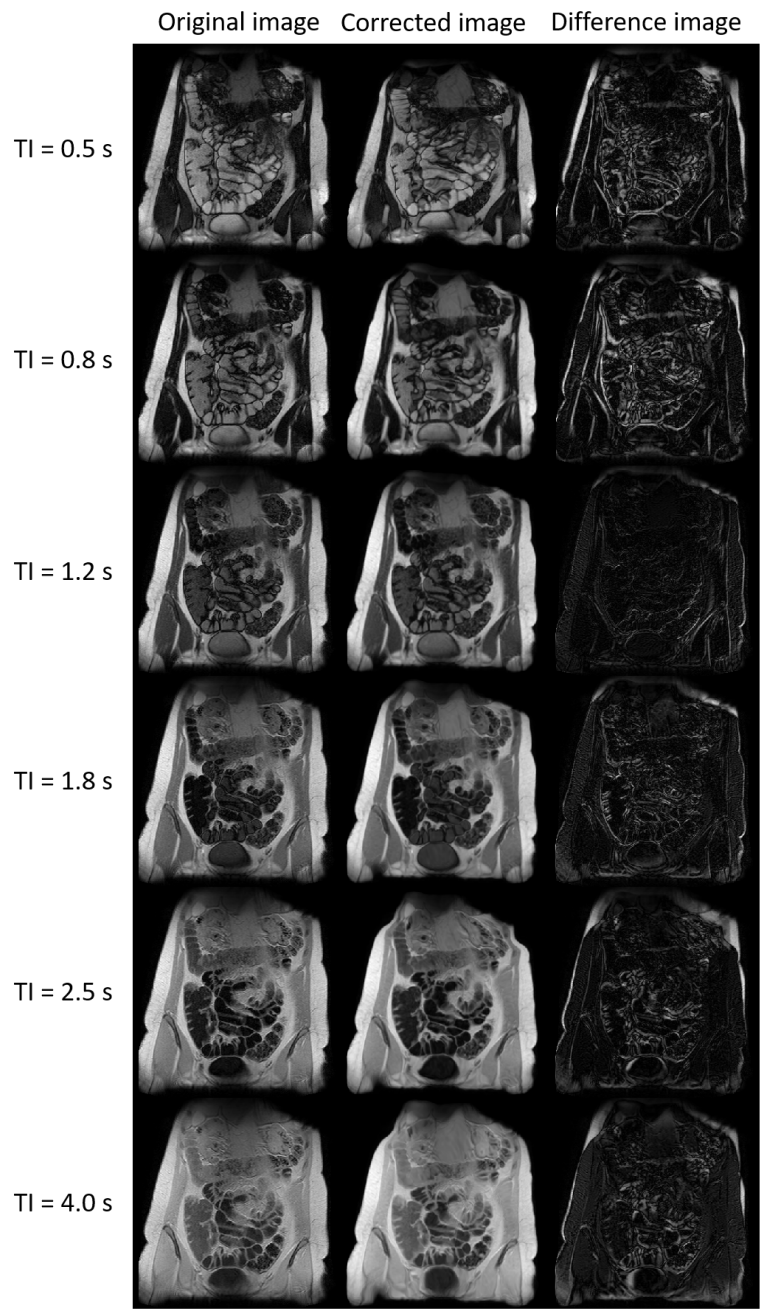


Figure 5.4: Images showing the an example set of T1 images before and after motion correction with the differences between the two images shown in the third column.

5. Bowel Wall and the PerMinH Study

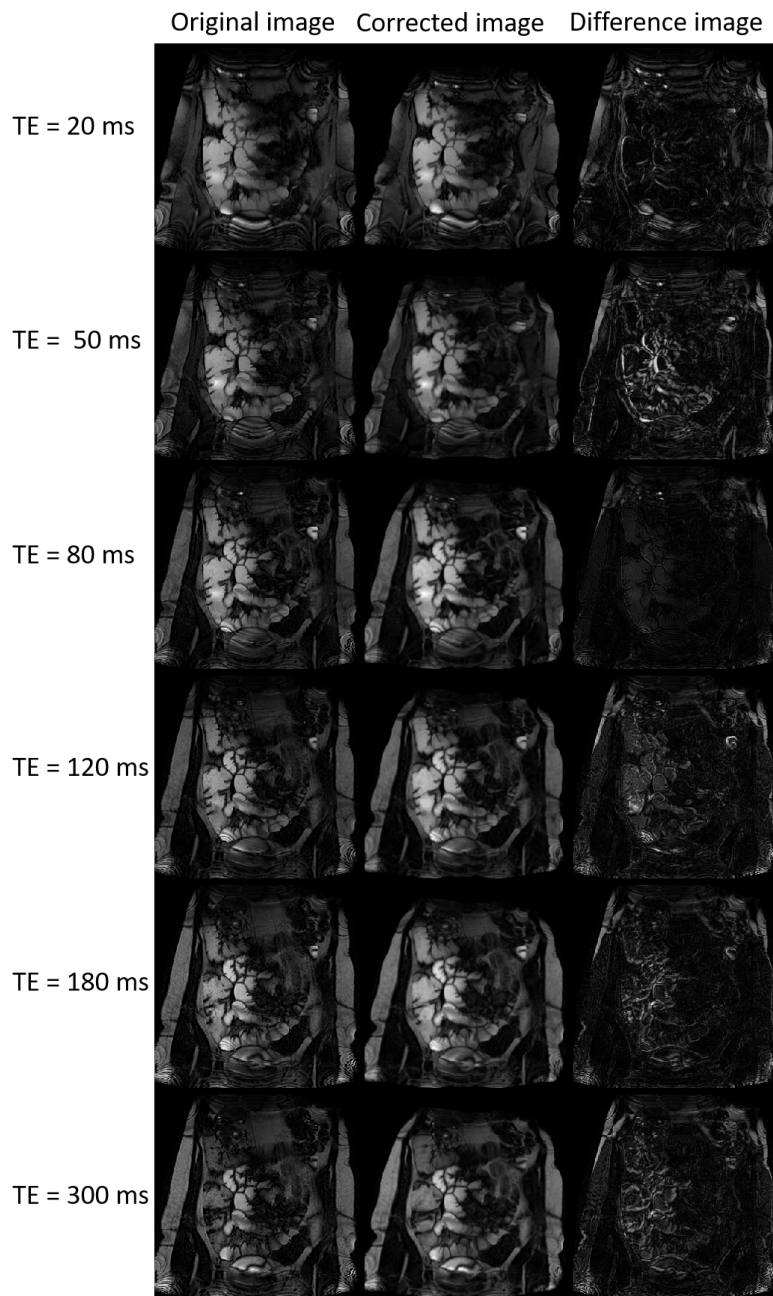


Figure 5.5: Images showing the an example set of T2 images before and after motion correction with the differences between the two images shown in the third column.

5.5.2 Masking the Bowel

In order to reduce the analysis time and to minimise the amount of misidentifications of structures such as vasculature or tissue interfaces as bowel wall, code was written which allowed for a mask of the bowel to be generated. The code was a step wise sequence that removed tissue from the image starting from the outer edges and working inwards, leaving only the bowel. A single mask is created that can be applied to all the images in the series. The process of isolating the bowel wall used thresholding and boundary conditions to remove specific tissues in the abdomen with each step, the process use to remove each tissue type is summarised in Figure 5.6.

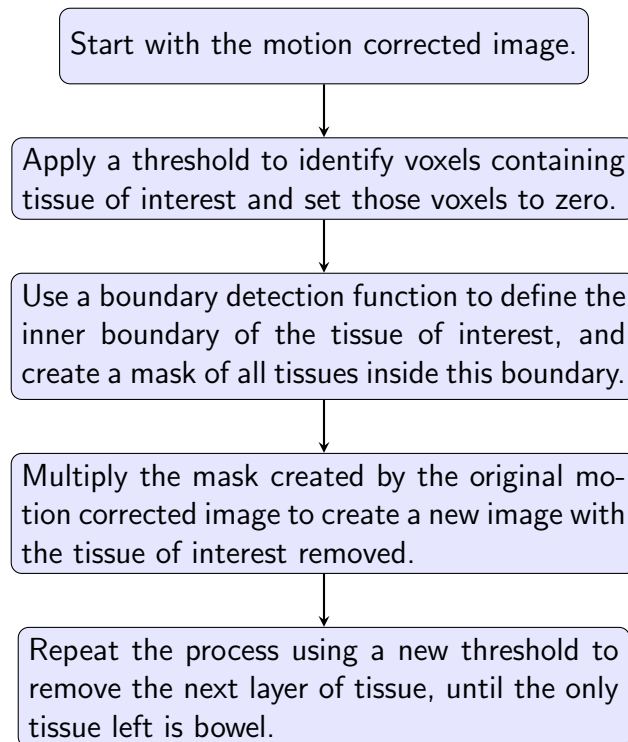


Figure 5.6: Flow chart illustrating the process to isolate the bowel. The effect of the thresholding, boundary detection and mask creation is to strip away the abdominal tissue one layer at a time, working from the outer edge of the body and working inwards. This resulting in the only remaining tissue being that of the small bowel.

5. *Bowel Wall and the PerMinH Study*

The images were normalised to allow for consistent threshold values to be used throughout the analysis, the high intensity values were also saturated to limit the impact of bright artefacts on the processing steps (30). Firstly the high intensity images were saturated at the 95th percentile of the original image, such that any signal intensity above the 95th percent of the maximum signal intensity was set to the 95th percent intensity. This allowed for the histogram of signal intensities to be redistributed with less weight on the higher signal intensities. Secondly the image intensities were then scaled to the range 0 - 1024. This scaling allowed for the same threshold values to be used across all data sets as the signal intensity varied from person to person. This scaled image was then used to create a mask of the bowel (Figure 5.7a).

The next step in creating a mask of the bowel was to remove the noise surrounding the image (Figure 5.7a). This was done by setting any voxels with a signal under a given threshold to zero (Figure 5.7b). To find the edge of the body from this image Matlab's inbuilt Boundary function was used. The function identifies all boundaries in an image as seen in Figure 5.7c, as well as providing the length of each detected boundary. The largest boundary was used to create a mask of the body which excluded any surrounding noise. Multiplying this binary mask by the original image (Figure 5.7a) provided an image in which the background noise was set to zero (Figure 5.7d).

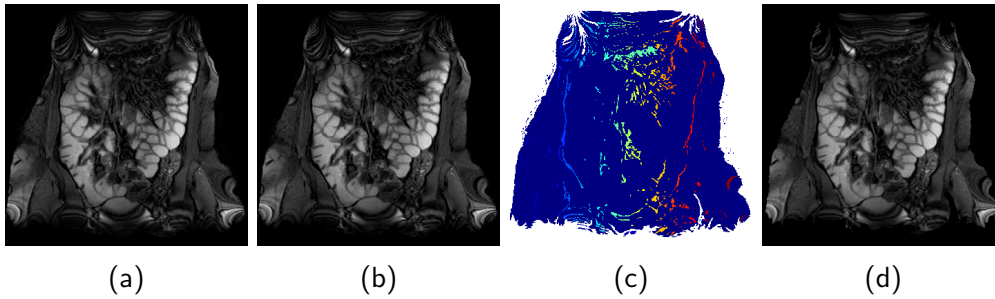


Figure 5.7: a) T2 image after motion correction was performed. b) Any voxels containing a signal below a set threshold in image a are set to zero. c) The boundaries in image b are then identified to produce a mask of the boundaries as seen in image c. The different colours indicate areas within a boundary with the white indicating the areas not within a boundary. d) The largest boundary is used to produce a mask of the body excluding the surrounding noise.

The process was then used to remove subcutaneous fat (Figure 5.8) using different threshold values, resulting in Figure 5.8b. Again the boundaries in the image were identified (Figure 5.8c), and the largest boundary was used to remove the subcutaneous fat from the image (Figure 5.8d).

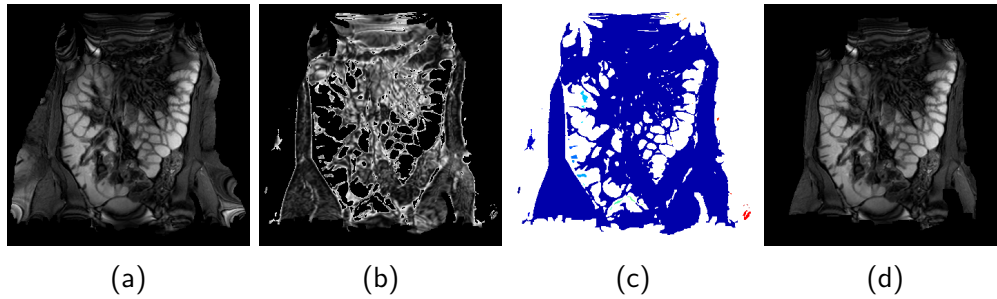


Figure 5.8: a) T2 image with surrounding noise removed. b) T2 image where all voxels with a signal within a given threshold were set to zero. This set all voxels containing fat to zero. Bowel content was also set to zero as a bi-product of the thresholding. c) Boundaries identified from image b. This allowed for subcutaneous fat to be removed from the image. The bowel content is included within the large blue area and so is not excluded from the image. d) Image resulting from the multiplication of the largest bound area in image c with the original image. This resulted in the subcutaneous fat being removed from the image.

This process was then repeated twice more, firstly to remove muscle (Figure 5.9) and then to remove visceral fat (Figure 5.10). The resulting image was one in which only the bowel was left. The mask was then dilated by 30 voxels to ensure that the outer bowel wall had not been removed. Figure 5.11 shows an example of a final mask overlaid with the original image.

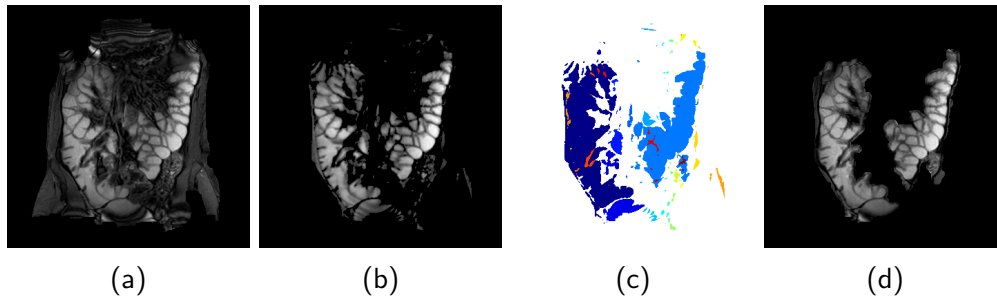


Figure 5.9: a) T2 image with noise and subcutaneous fat removed. b) T2 image where all voxels within a given threshold range are set to zero. This set all voxels containing muscle to zero. c) Boundaries identified in Matlab from image b. This allowed for muscle to be removed from the image. d) Image resulting from the multiplication of the largest bound area in image c with the original image. This allowed the muscle to be removed.

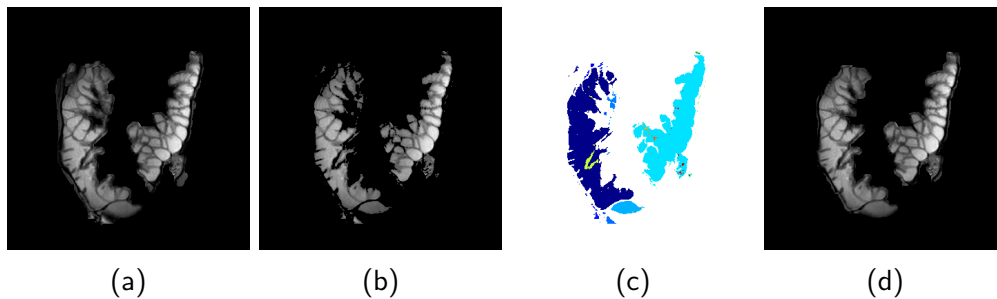


Figure 5.10: a) T2 image after surrounding noise, subcutaneous fat and muscle have been removed. b) T2 image where all voxels within a given threshold range are set to zero. This set all voxels containing visceral fat to zero. c) Boundaries identified from image b. d) Image resulting from the multiplication of the largest bound areas in image c with the original image. This allowed visceral fat to be removed from the image.



Figure 5.11: Mask of the bowel overlaid on the image from which the mask was created.

5.5.3 Creating a Mask of the Bowel Wall

A mask of the bowel wall was then created from the isolated bowel image. Initially a manual line of interest method was also tested however it was found to be time consuming and restricted the amount of bowel that could be feasibly sampled. Therefore the mask was created by using an automatic edge detection method which is detailed below.

The wall masking method was developed in Matlab and used edge detection and thresholding to obtain larger regions of interest in a much shorter amount of time than is possible with manual line of interest drawing. Edge detection is a common image segmentation tool, and is included in Matlab's image processing toolbox under the function name 'edge', which identifies edges as places in the image where the intensity changes abruptly. More specifically the canny method of edge detection is used which identifies both strong and weak edges. The method was originally describe by Canny (31). The below method was initially developed on the allocated training data sets from the study. The steps demonstrated in Figures 5.12:5.17 are performed on the image from each TE/TI and

the results combined to form a single mask that can be applied to all the images in the series (Figure 5.19).

Starting image (Figure 5.12): The motion corrected images in which the bowel had been isolated were used as the starting point for isolating the bowel wall.

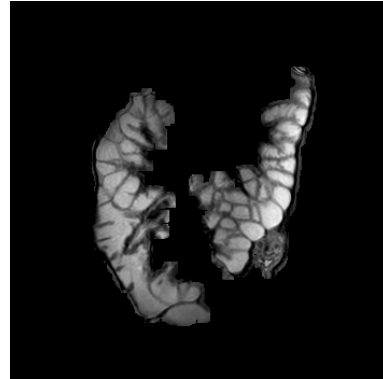


Figure 5.12

Edge detection (Figure 5.13): Edge detection was then applied to all 6 images in the image series. The edge detection produced a binary mask of voxels that are considered to be walls (i.e. voxels containing wall were given a value of 1 and those without wall were given a value of 0). The required edge detection input thresholds were optimised to reduce the amount of false positives in the mask (structures that are not bowel wall that are identified as bowel wall, such as vasculature in the surrounding mesentery). This optimisation was performed by visually inspecting the edges produced in the training data sets when using different thresholds in the edge detection function.

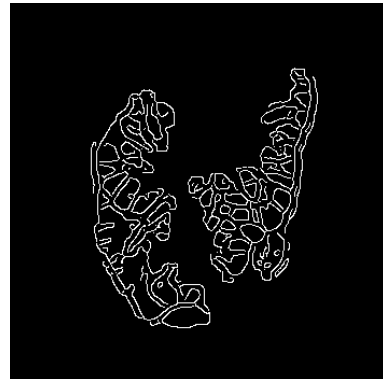


Figure 5.13

Edge dilation (Figure 5.14): To ensure that these edges covered the whole wall they were then dilated by 2 voxels on either side, using Matlab's inbuilt dilation function.

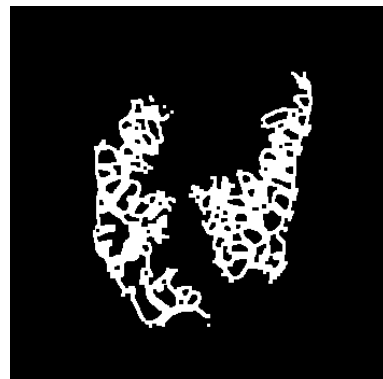


Figure 5.14

Create a threshold mask of the content (Figure 5.15): The next step isolated the contents of the bowel using thresholding. The threshold was chosen by histogram analysis of the training data set to determine a threshold that would only include the contents of the bowel and not the wall.



Figure 5.15

Invert the threshold mask (Figure 5.16): By inverting the threshold image of the content a mask of all voxels not containing bowel content was produced.



Figure 5.16

Multiply threshold mask with wall mask (Figure 5.17): The inverted threshold mask was then multiplied by the dilated edge detection image to provide a mask of the bowel wall at every echo time/inversion time.

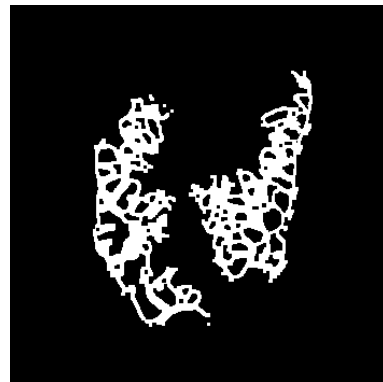


Figure 5.17

Multiply masks from each time point (Figure 5.18): The binary masks of the wall from each time point, were then multiplied together. The result of this multiplication was that only voxels that were considered to contain bowel wall in all of the multiplied images were contained in the final mask. This created a mask of bowel wall voxels that had a consistent spatial location across all images.

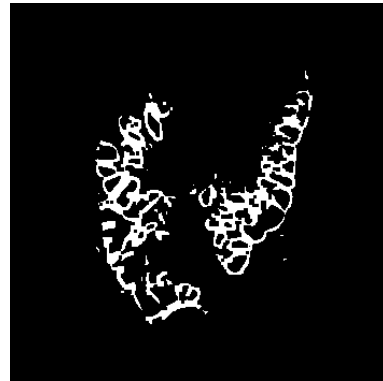


Figure 5.18

Fill in missing voxels (Figure 5.19): After creating the mask there were some imperfections that were corrected. The first correction was to fill any missing voxels along the walls. This was performed by first identifying all segments of wall in the binary mask. A continuous segment was defined as all voxels connected by their eight nearest neighbours. The end points of these segments were then located. If another end point was found to be within a 2 voxel radius of the end point the empty voxels between were filled and the segments joined. Figure 5.20 shows the mask overlaid with the original T2 image.

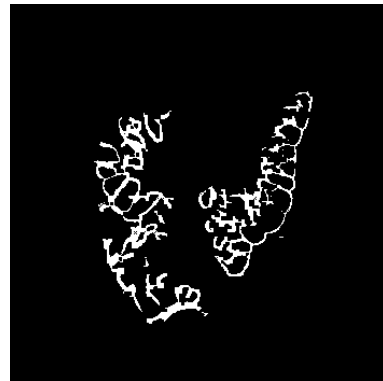


Figure 5.19

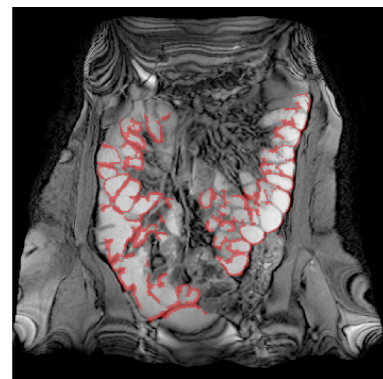


Figure 5.20

Remove large areas: In some masks large dense areas were identified as being part of the wall due to the dilation process joining two walls that were close together or several walls that joined in one location (Figure 5.21). These areas would often include a large amount of bowel content and were therefore removed. In order to remove these areas the solidity and eccentricity of each segment was calculated. The solidity gave the density of the segment and the eccentricity gave the shape of the segment. For example a completely filled circle will have a solidity of 1 and an eccentricity of 0, a straight line will have a solidity of 1 and an eccentricity of 1. The walls were often arched in shape giving a low solidity but a high eccentricity which is why both the solidity and eccentricity were used. If an area was found to have a high solidity and a high eccentricity then it was removed from the mask.

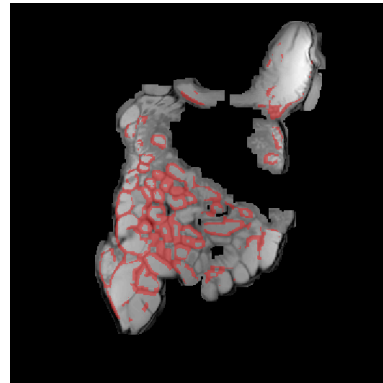


Figure 5.21

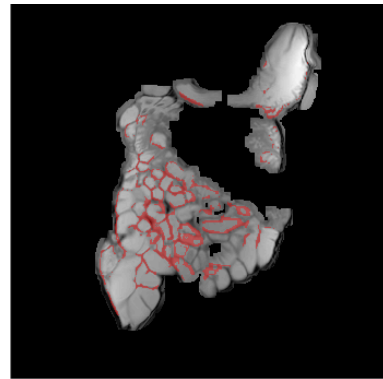


Figure 5.22

This solution had one situation in which it was not effective, the case was when a high density area had protruding arms in several directions. For example if 5 walls intersected (similar to an asterisk), when dilated a dense area in the mask would be created at the intersection. Such areas have a low solidity and eccentricity due to the protruding arms. To remove the central cross over zone but maintain the protruding arms, any area that could fit a square larger than 7×7 inside was set to zero, this was decided from the training data set. Figure 5.23 shows an example of this. The final mask of the bowel wall overlaid with the original image can be shown in Figure 5.22.

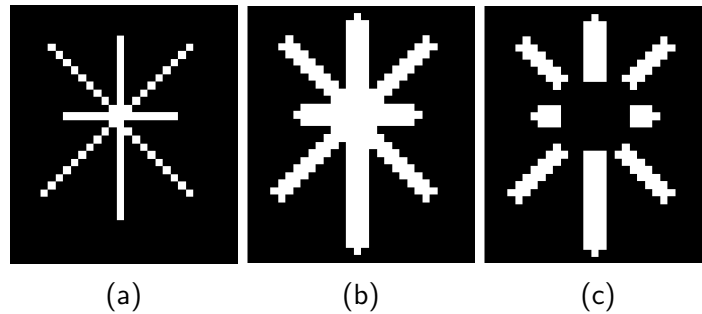


Figure 5.23: a) Mask of intersecting bowel walls. b) Dilated mask of the intersecting bowel walls, the central region merges and covers part of the bowel content. c) Merged middle section removed from intersecting walls.

5.5.4 Manual Quality Control Step

The above stages were run automatically as a batch process for all data sets. Once the batch process was complete a manual quality control step was used to ensure that only small bowel wall was included in the final mask. The removal process was done by first visually inspecting the mask overlaid on all 6 images (from the different inversion/echo times) and then drawing around areas that did not cover the bowel wall. Misidentifications often included the wall of the colon, stomach, uterus and bladder (Figure 5.24). Automated methods to remove these types of misidentifications were not developed as they have similar characteristics to the small bowel making the development of an automated method difficult. It was decided that at this stage manual removal of these misidentifications was a reasonable solution as they did not appear in all data sets and could be easily removed by manual methods.

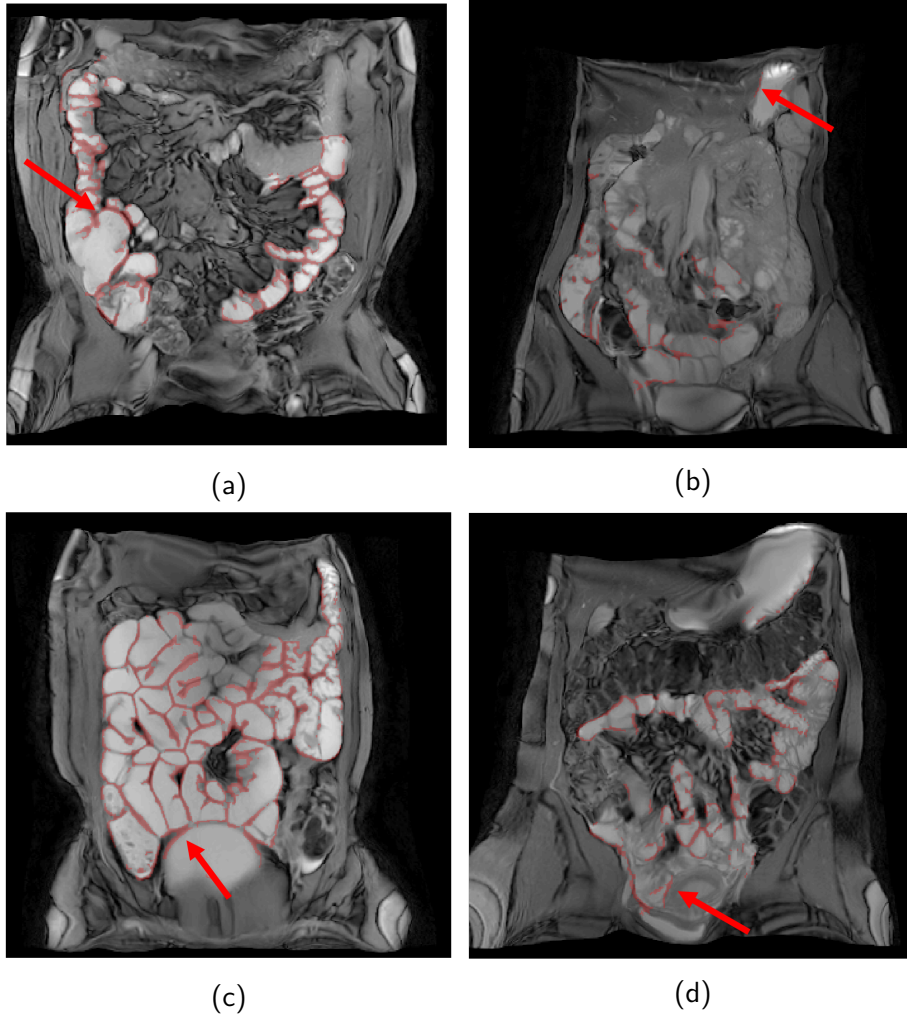


Figure 5.24: Misidentifications that had to be manually removed a) Colon wall b) Stomach wall c) Bladder wall d) Uterus wall.

5.5.5 Fitting to the Data

After the signal was extracted from the wall from the T1 and T2 data sets the signal had to be fit for T1 and T2 respectively.

For the T1 fit, an exponential inversion recovery (Equation 5.1) was fitted using a non-linear least-squares fit in Matlab.

$$S(TI) = S_0 \left(1 - 2\exp\left(-\frac{TI}{T1}\right) \right). \quad (5.1)$$

Here S_0 is the equilibrium magnetization, and $S(TI)$ is the magnetization at the measured inversion time. As the magnitude data is absolute, the part of the curve that is before the null point must be inverted. However it is unknown, due to the presence of Riccian noise, whether the point closest to zero should be before or after the null point. Therefore two separate fits were performed. The first fit had all the points before the one closest to zero inverted, and the second had all the points before and including the one closest to zero inverted. The T1 from the fit with the highest R squared was taken as the T1 of the bowel wall.

For the T2 fit a text file containing the signal was transferred onto the High Performance Computer and read into a c programme which fitted a numerical model, using the Powell algorithm, to the data (32). The numerical model described the full bTFE read out which includes T1, T2 and M_0 to the data. The code takes initial starting guesses for the T1, T2 and M_0 and then models the magnetization change as every RF pulse is applied and the recovery of the magnetization between the pulses. The resulting signal at each echo time is then compared with the measured signal and the sum of squares calculated. If the minima found by the Powell algorithm gives a sum of squares below a set threshold then the T1, T2 and M_0 from the Powell algorithm are accepted, if not the process is repeated with new starting guesses for T1, T2 and M_0 . The code was originally written for a single exponential decay, full details of which can be found in (33).

Partial Volume

During the analysis it was noted that regions of interest often contained partial volume effects which are shown below in Figure 5.25.

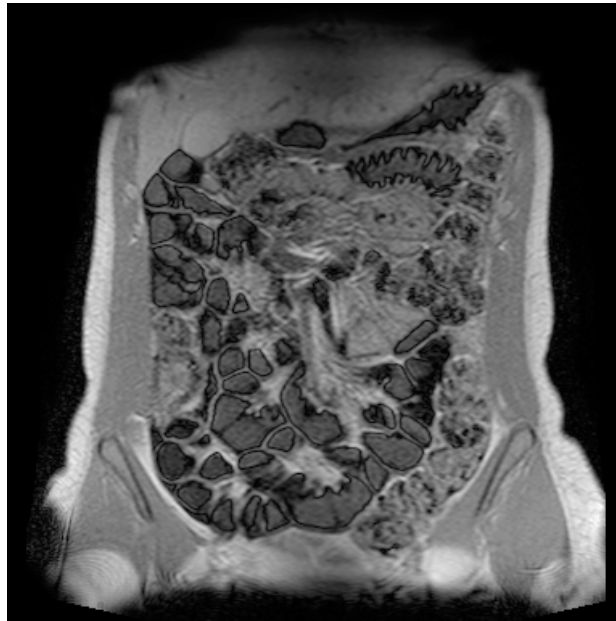
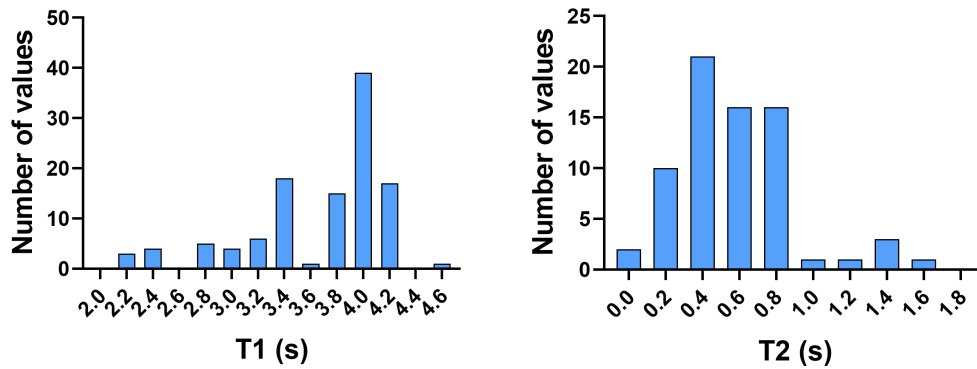


Figure 5.25: Partial volume effects seen as the dark line between the content of the bowel and the bowel wall.

Partial volume effects cause the signal to follow a bi-exponential decay/recovery with the dual T_1/T_2 being those of the wall and the contents of the bowel. Excluding these partial volume effects could not be guaranteed as the partial volume effects were only visible in the T_1 recovery at one inversion time. Therefore the fitting described above was altered to account for a bi-exponential T_1 recovery and bi-exponential T_2 decay respectively, with the dual T_1 s and T_2 s being those of the content and the wall. To reduce the number of parameters that were fit for, the T_1 and T_2 of the content were fixed. A single ROI was drawn in the bowel content on the T_1 and T_2 images respectively for each participant on both visits. A mono-exponential (decay for the T_2 signal and recovery for the T_1 signal) was then fitted to the mean signal in the ROI to calculate the T_1 and

5. Bowel Wall and the PerMinH Study



(a) T1 of bowel content measured from 3 ROIs in each participant. (b) T2 of bowel content measured from 3 ROIs in each participant.

Figure 5.26: Histograms showing the measurements of a) T1 and b) T2 of the bowel content measured from 3 separate ROIs in each participant.

T2 for each data set. The T1 and T2 of the contents were measured for all data sets and the results averaged to get a mean T1 (3.68 ± 0.05 s) and T2 (0.58 ± 0.04 s) of the content across the group (Figure 5.26). The bowel content T1 and T2 values were then fixed in the bi-exponential fitting code. The use of a single T1 and T2 for the content in all participants was justified by the fact that all participants consumed the same bowel prep prior to the scan making the content similar across the group. Figure 5.27 demonstrates a T1 and T2 data set and the bi-exponential fit on each respectively.

After the data was fitted the results were first looked at as a whole before unblinding. In the unblinded review any T1 or T2 fit that had an R squared value that was less than 0.9 was removed. An R squared value of 0.9 or less indicated that the simulated data did not match well with the measured data and thus the T1 or T2 from the fit was likely to be unreliable.

For the training data sets the fits were performed with and without the B1 map taken into account. Overall the B1 map showed little variation across the images. This difference was taken into account by multiplying the angle used in the fit with the percentage difference given in the B1 map. It was found that the B1 map caused a $<0.1\%$ change in the output T1 and T2 values and thus

the B1 map was not included in the full analysis.

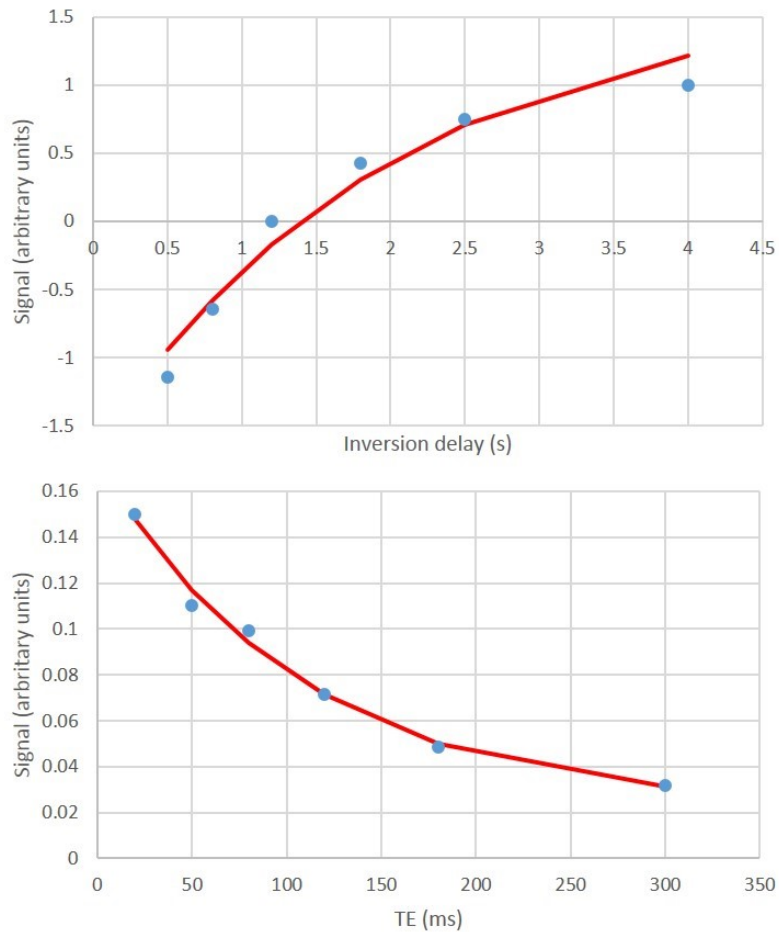


Figure 5.27: T1 recovery (top) and T2 decay (bottom), the red line demonstrates the fit to a single ROI taken from the T1 and T2 data sets respectively that follow a bi-exponential recovery/decay.

5.5.6 Bowel Wall Segment Size

Once the bowel wall extraction method was set, a maximum number of voxels per ROI was chosen due to the fact that if heterogeneity exists along the wall then averaging over a large area would not allow for the heterogeneity to be investigated. In order to determine the appropriate maximum limit on ROI size

all data was pooled together to produce Figure 5.28.

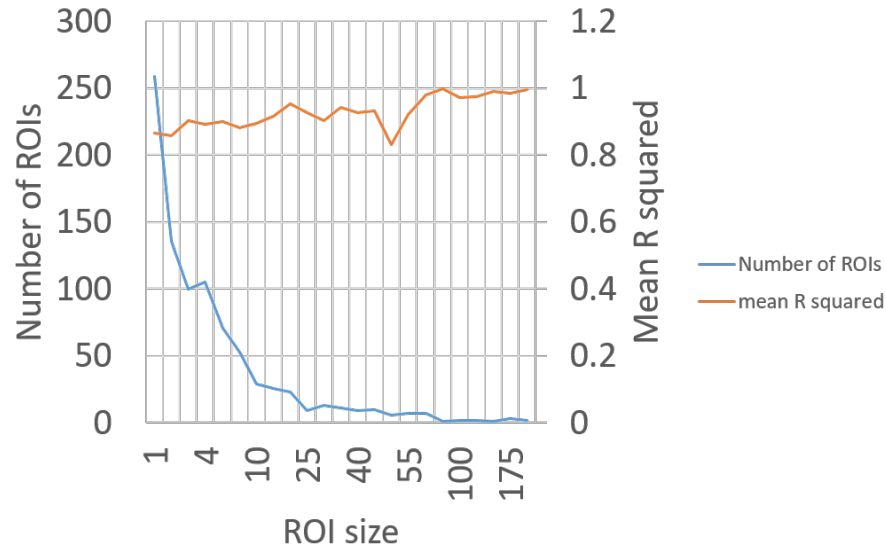


Figure 5.28: Mean R squared is shown for ROIs containing a given number of voxels. Also plotted is the number of ROIs containing each number of voxels.

From Figure 5.28 it can be seen that as expected the R squared of the fit increases with the number of voxels. The R squared is seen to be high (above 0.9) and stable at around 25 voxels and so 25 voxels was chosen as the upper limit of voxels per ROI. This limit was deemed small enough to allow any heterogeneity along the wall to be seen but not so small that the time to analyse the data would be excessive.

To investigate the effect of choosing this limit over a larger one the analysis of the data was performed again with two different upper limits (25 and 50) on the number of voxels per ROI. To impose the upper limits the original ROIs were fit again but any ROI that contained more than the upper limit of voxels was split into smaller ROIs.

Splitting of the ROIs was performed by moving a kernel along each ROI and, once the number of voxels in the ROI reached the upper limit, the ROI was split at that point, creating two ROIs. The moving kernel then continued along the ROI and if the upper limit of voxels per ROI was again reached, the ROI was

split again. This process was repeated until all the original ROIs were split into smaller ROIs, none of which contained more voxels than the upper limit. Figure 5.29 shows the weighted median for each subject with a maximum of 50 voxels per ROI plotted against a maximum of 25 voxels per ROI (with the weight being the number of voxels per ROI). The weighted median was used rather than the mean as the distribution of the data was not normal. The data as expected follows the line of identity in most cases. However a few points lay far away from the line of identity, the four main outliers were investigated to determine why there was such a discrepancy in the T2s.

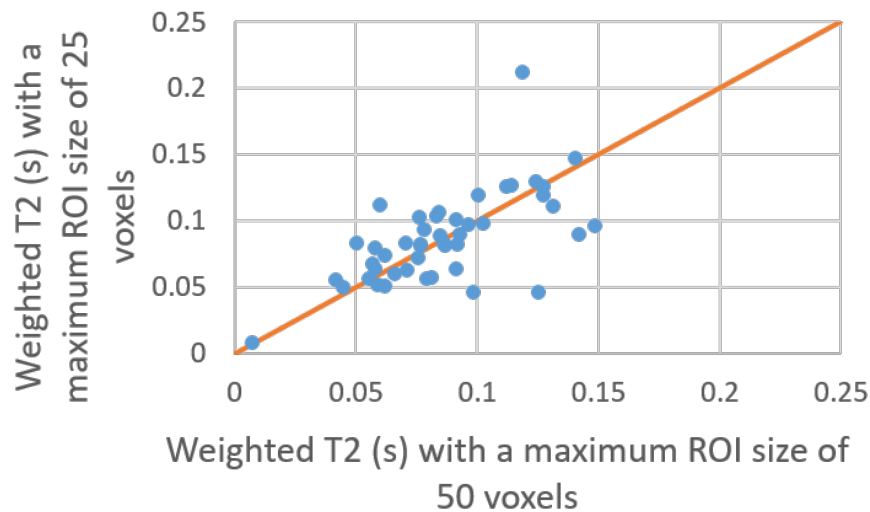


Figure 5.29: Weighted median T2 for each participant with the maximum number of voxels per ROI set as 25 and 50 respectively.

In all four cases it was found that the difference in weighted median originated in an ROI with between 25 and 50 voxels that had been split into smaller ones when the 25 limit was applied. When the ROI was split into two ROIs, it was found that one of the ROIs had a very low R squared, and was therefore not included in the weighted median, whilst the other had a high R squared and remained. This implied that the ROI containing all the voxels was partly contaminated with noise but not enough for the R squared to fall below the 0.9 cut off. Splitting the ROI allowed for the noisy section to be removed. Therefore it was decided

that using an upper limit of 25 was appropriate, as in the majority of cases it did not affect the weighted median but did allow for more noise to be removed from the fit data.

5.6 PerMinH Results

Here the results of the PerMinH study are discussed. The bowel wall thickness and motility measurements showed no differences between the placebo and indomethacin arms of the study. For full details of the bowel wall thickness and motility analysis and results please refer to Dr Scott's thesis once published.

5.6.1 T1

On analysis of the T1 images it was apparent that the inversion times used to measure the T1 of the bowel wall were not optimal. Because of this in many cases the signal was measured close to the null point in either 1 or two inversion times (Figure 5.30). The phase data was not collected and therefore it could not be determined whether the signal measured lay before or after the null point. Due to this the number of data points that were used to fit for T1 was reduced to 4 in many cases resulting in an unreliable fit (3 variables fit to 4 data point). Therefore the T1 results for the study were not analysed further but were used to find an optimal set of inversion to measure T1 (Section 5.9.1).

5. Bowel Wall and the PerMinH Study

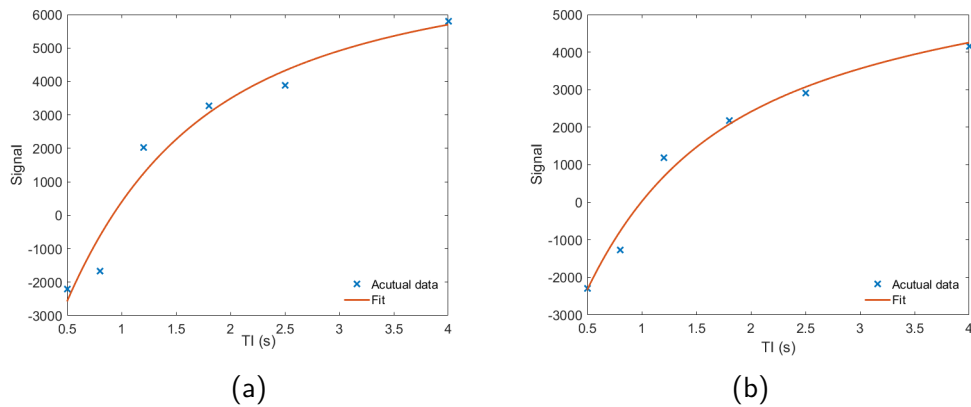


Figure 5.30: a) T1 fit to a single ROI. b) T1 fit to a separate ROI. Both data sets do not appear to follow a smooth inversion recovery curve. It is believed that this is due to some of the time points measuring Riccian noise.

5.6.2 T2

In total 16 participants were used in the final analysis. One participant was removed due to non-compliance with the study protocol and one was removed due to an incidental finding of Crohn's disease. A further 5 were removed as they exhibited significant motion of the bowel which was due to the breath hold being in a significantly different location. One participant was removed as the slice positioning of the two study days was significantly different. This could potentially be improved by collecting data using respiratory triggering, which unlike breath holds encourages shallower breathing rather than larger exaggerated breaths.

Figure 5.31 shows the weighted median T2 for the placebo and indomethacin arms of the study. The T2 for each participant is given by the median and interquartile range taken from all the ROIs which have a T2 fit with R squared above 0.9. The median and interquartile range were used as the T2 measurements within each individual were found to not follow a Gaussian distribution. The median T2s across the participants had a normal distribution and so the change in T2 between the two study days was calculated using a paired t test. Indomethacin provocation induced a statistically significant increase in small bowel wall T2 compared to placebo (Figure 5.32), from 0.070 s (standard deviation

5. *Bowel Wall and the PerMinH Study*

0.036 s) to 0.115 s (standard deviation 0.063 s) with a p value of 0.017.

The interquartile range showed a trend towards an increased interquartile range (0.097 s to 0.147 s) with the administration of indomethacin, however this was not significant with a p value of 0.065 (Figure 5.33). Figure 5.34 shows the change in T2 with the change in interquartile range. Most of the participants who exhibited a drop in T2 upon the administration of indomethacin also exhibited a drop in the interquartile range. There was a significant correlation between change in T2 and change in the interquartile range (tested with a Pearson's correlation coefficient $R = 0.67$, $p < 0.01$).

There was a significant positive correlation between LMR and small bowel wall T2 (Pearson correlation coefficient 0.68, $p < 0.01$ (Figure 5.35)). There was also a significant positive correlation between change in T2 and change in LMR (Pearson correlation coefficient 0.63, $p < 0.01$).

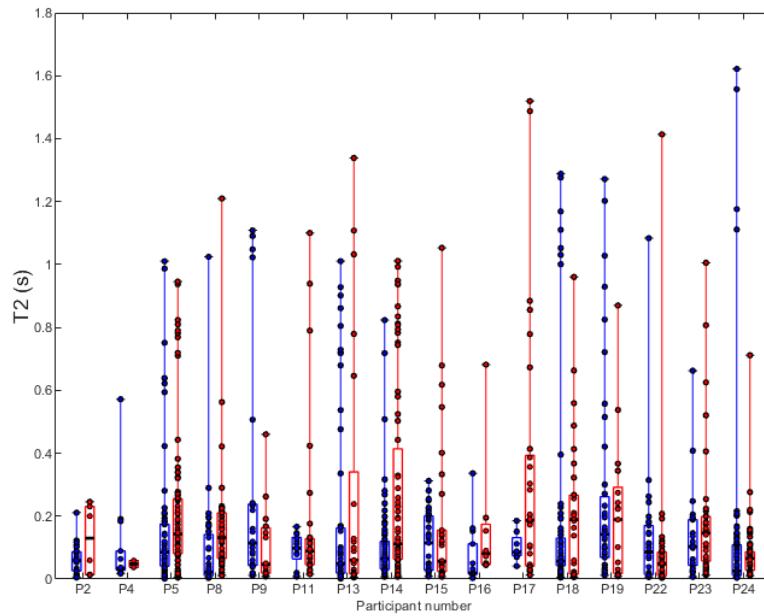


Figure 5.31: Box plot shows median placebo (blue) and median indomethacin (red) values of T2 measurements with the lower and upper quartiles marked by the limits of the box. Circles show individual results for each ROI. Overall placebo median T2 from all subjects is 0.070 ± 0.036 s and for indomethacin is 0.115 ± 0.063 s. The median range of T2 was 0.097 s for placebo and 0.147 s for indomethacin.

5. Bowel Wall and the PerMinH Study

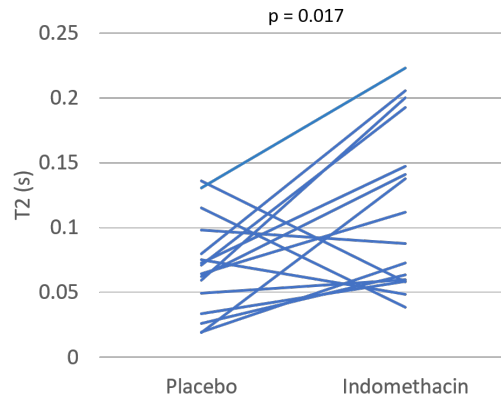


Figure 5.32: Median T2 for each participant shown for the placebo and indomethacin arms of the study. A statistically significant difference in T2 was found using a two-tailed paired t test ($p = 0.017$).

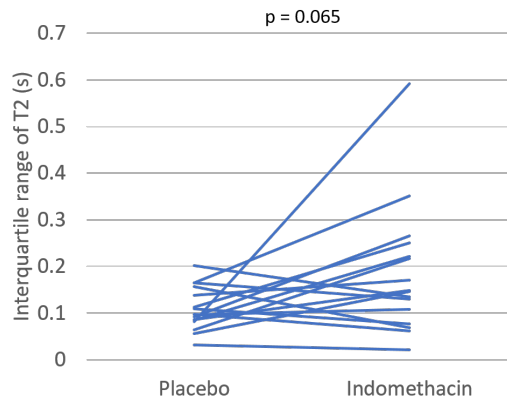


Figure 5.33: Range of T2 across regions of interest for each participant. A trend was found towards a higher range of T2 values in the indomethacin case but this did not reach significance ($p = 0.065$).

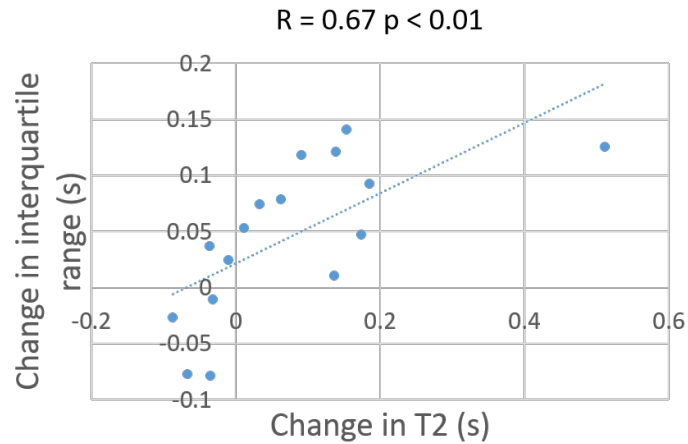


Figure 5.34: Change in T2 with the change in range of T2 upon the administration of indomethacin.

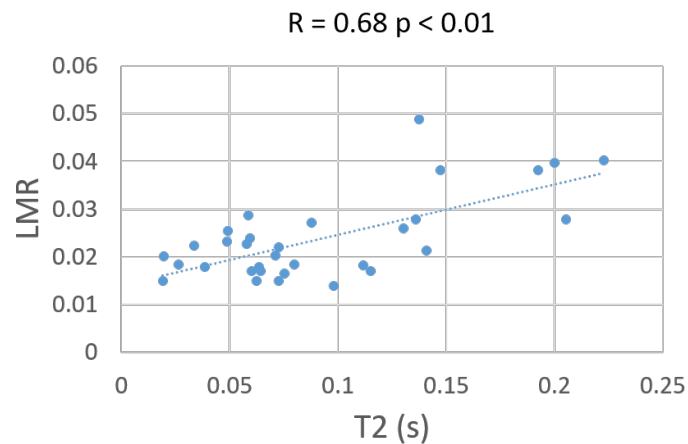


Figure 5.35: Correlation of median T2 and LMR for each participant. A strong positive correlation was found between T2 and LMR ($R = 0.68$) which was found to be significant using a Pearson's correlation coefficient ($p < 0.01$).

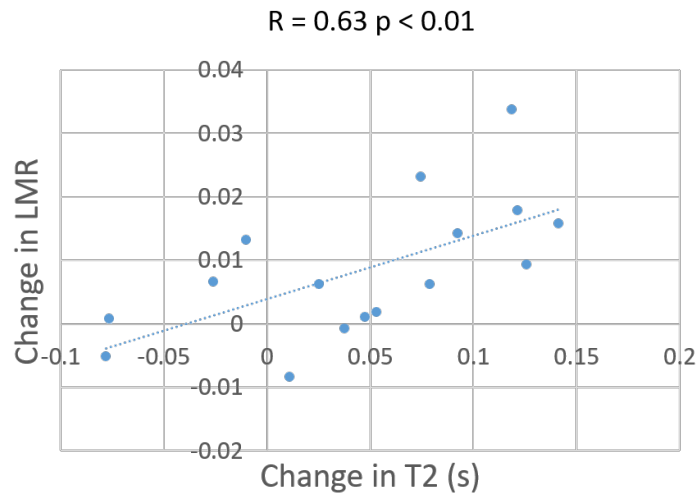


Figure 5.36: Correlation of change in median T2 and change in LMR for each participant. A strong positive correlation was found between T2 and LMR ($R = 0.63$) which was found to be significant using a Pearson's correlation coefficient ($p < 0.01$).

5.7 Inter Observer and Intra Subject Reproducibility

A second healthy volunteer study was carried out to look at the intra subject reproducibility of various gastrointestinal measures in healthy volunteers, including T2 of the bowel wall. The analysis was performed by two observers to also allow for the inter observer reproducibility to be tested. Figure 5.37 shows the results obtained from 6 healthy volunteers who all underwent the same protocol as mention in section 5.4.2, the only change being that the slice of the T2 image was not restricted to the plane where the terminal ileum enters the cecum. This restriction was lifted so that the image slice could be placed in the plane deemed to have the highest amount of small bowel. Figure 5.38 shows the Bland Altman plot for the inter observer reproducibility. Figures 5.39 and 5.40 show the Bland Altman plots for the intra subject reproducibility performed by the two different observers.

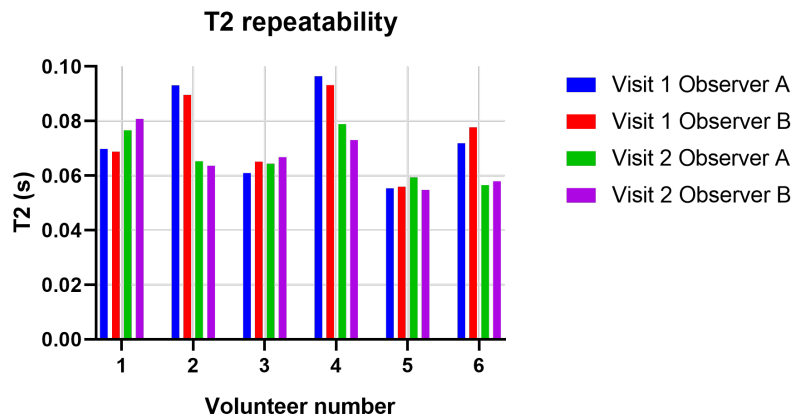


Figure 5.37: Inter observer and intra subject reproducibility of T2 measurements in healthy volunteers. The solid bar indicates the median T2 calculated by each observer with the standard deviation given by the error bars.

From Figure 5.38 it is clear that the the analysis method is robust to use by different observers, the mean difference between the measurements by the two observers was 5% with a range of -8% to +7%. The automated section of the analysis is user independent so the differences seen here originate from the

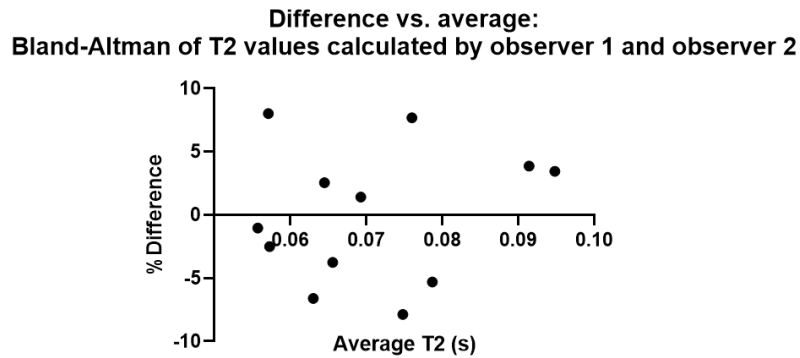


Figure 5.38: Bland-Altman plot to show the difference in the T2's measured by observer 1 and those measured by observer 2.

non-automated section of the analysis which requires the user to remove any part of the bowel wall mask that they judge to be non-small bowel material.

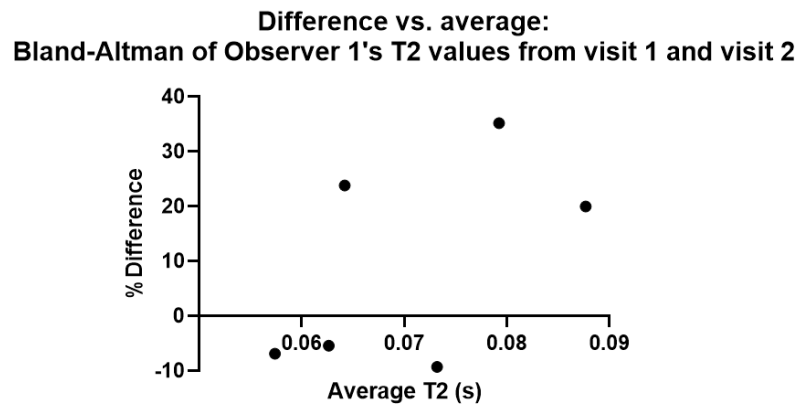


Figure 5.39: Bland-Altman plot for observer 1's T2 measurements from visit 1 and visit 2.

From both of the above plots it is clear that in some cases T2 changed by a significant amount between visits. It is believed that this change might be due to the imaging slice being in a different place, or the bowel sitting differently in the two scans. Figure 5.41 shows the two imaging slices used for visit 1 and visit 2 in the participant with the largest T2 change (subject 2). It can be seen that the imaging slice is in a different location for the two visits. In the first

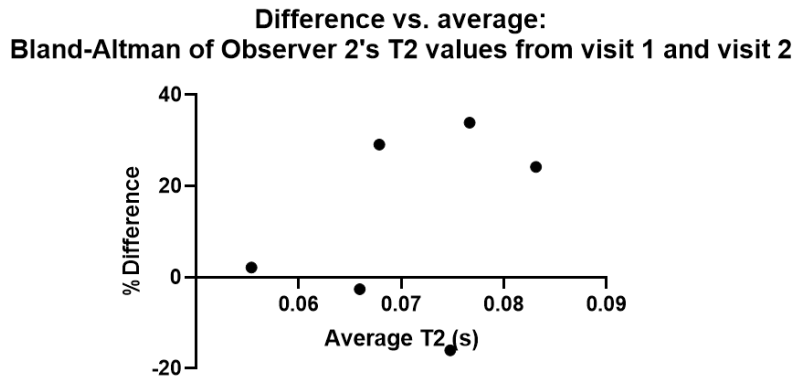


Figure 5.40: Bland-Altman plot for observer 2's T2 measurements from visit 1 and visit 2.

visit the bowel wall sampled is across a large area mainly towards the right of the abdomen. In the second visit the bowel is taken from the lower and upper section of the abdomen. This difference may be the reason as to why the T2 changes so dramatically.

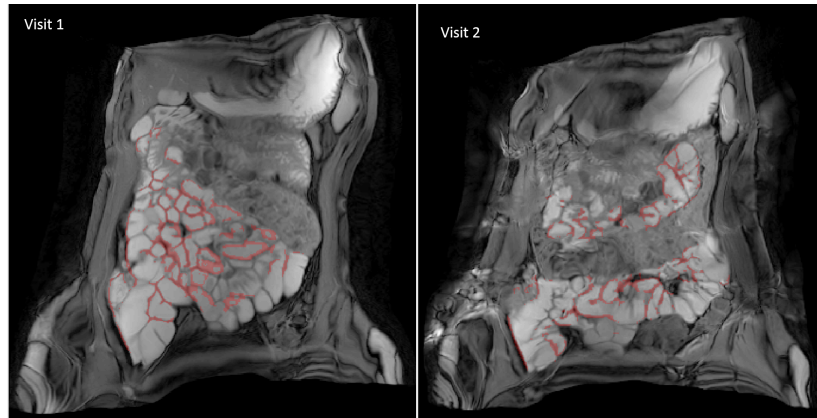


Figure 5.41: The slice acquired for the T2 measurement in a participant on two separate study days.

In order to truly evaluate the intra subject reproducibility of this analysis method the same imaging slice must be used or alternatively a multi slice version of the acquisition would allow for full coverage of the bowel and a better evaluation of intra subject reproducibility to be performed.

5.8 Discussion of PerMinH

In a randomised, double blind, placebo controlled, prospective cross-over provocation study with indomethacin in healthy volunteers, we have shown that objective MRI measures of small bowel wall T2 increased following indomethacin provocation and these correlated with increased permeability as demonstrated by a 2 hour Lactulose/Mannitol urinary excretion ratio (LMR) test, the current standard method of evaluating intestinal permeability. The correlation between T2 and LMR, as well as change in T2 with change in LMR, suggest that T2 is a surrogate marker for the results measured in the LMR test. T2 also has the advantage that it could in future be used to visualise the location of changes in bowel permeability as well as overall changes which are measured in the LMR test. One participant was found to have an abnormal LMR result (Figure 5.35) that did not correlate with T2. This could be due to inadvertent consumption of lactulose or mannitol in the diet, but no information was collected on this.

The MRI measures of small bowel thickness and motility remained unchanged with indomethacin provocation. This is likely to be due to the fact that the dose of indomethacin given was low and unlikely to cause large changes in the gut.

This study had several strengths. A prospective double blind cross-over study design minimises confounding factors and increases the power of the study. The observed differences were therefore most likely caused by provocation with indomethacin. All analysis was performed blinded to treatment allocation and compared to small bowel permeability as defined by 2 hour LMR, the current standard measure of small bowel permeability (1, 34). Each MRI measure was quantitative bringing an objective marker to the study that could allow for transfer between systems. These MRI techniques did not require the administration of intravenous contrast and are therefore safe and appropriate for repeated measurements - especially in the context of recent FDA warnings which restrict the use of gadolinium in healthy volunteers (18). The protocols were based on widely available scan sequences and as such could be rapidly adopted into clinical pathways and research programs. The analysis whilst not currently available is largely automated and could be used on a wide scale.

5. *Bowel Wall and the PerMinH Study*

Whilst two doses of indomethacin is safe and does increase small bowel permeability (6, 19) the relatively low dose is small and may be too transient and subtle to cause changes in bowel wall thickness and motility. The given dosage of indomethacin is considered safe however higher or more frequent doses of oral indomethacin is known to cause variable patchy small bowel erosions (35, 36). Combined with previous MR data in Crohn's (15, 16, 20, 37, 38), it is reasonable to assume that increased small bowel wall T2 reflects inflammation causing the integrity of the barrier function to become impaired.

Both MRI parameters and 2 hour lactulose/mannitol urinary excretion ratio (LMR) changed significantly following the indomethacin provocation test, supporting our choice of the later method. Although LMR is the most validated measure of small bowel permeability, it does have known shortcomings. Firstly, up to 30% of participants have detectable urinary mannitol at baseline (prior to administration of test sugars) or disproportionate excretion relative to the mass of mannitol administered for the test. This is hypothesised to be as a result of inadvertent ingestion of mannitol in diet or medications (39). Secondly, 0-2 hours is mostly, but not exclusively a measure of small bowel permeability, and may partially reflect colonic permeability.

The developed analysis tool required a manual quality control step to remove misidentified regions of wall, this is an inherent weakness. Whilst the quality control step does not incur a large time penalty, taking around 30 seconds per subject, it does introduce an element of observer variability. The difficulty in removing these structures automatically originates in the fact that they are not always present in the imaging slice and look similar to the small bowel, making the removal with a traditional algorithm difficult. This could potentially be overcome in the future with a machine learning algorithm trained to automatically remove structures such as the stomach, bladder, uterus and colon. Lastly, inherent to the non-invasive study design, we are unable to elucidate the molecular mechanisms at the tight junction level underlying increased permeability.

The main limitation of the study was the number of data points used to measure T1 and T2. Before the start of this study it was assumed that only a

5. *Bowel Wall and the PerMinH Study*

mono-exponential recovery/decay would need to be fit for to measure T1 and T2. However, throughout the process it became apparent that partial volume effects were present in the data and that a bi-exponential would need to be used. Because of this the fitting algorithm fits 3 variables to 6 data points. This combined with noise in the data is likely to reduce the accuracy in the results. In future studies more data points should be used to allow an increase in the accuracy of the fitting. In addition to this using a multi-slice or 3D imaging technique could provide full coverage of the small bowel. This could provide further insights into local changes in bowel permeability caused by disease or drug administration. These methods do however present challenges to the acquisition of the data. Whilst 3D acquisition is possible, using a centre out k space trajectory would result in the outer edges of k space being collected when the signal is low. This would lead to blurred edges and may not allow for accurate identification of the bowel walls, which in this case rely on sharp edges. Currently the imaging pulses used in the T1/T2 preparation steps excite the whole body. Because of this multi-slice imaging would either require more complex modelling which takes this into account or would require new pulse sequences to be developed to only excite the slice in question. The impact of fitting with fixed T1/T2 values for the bowel content rather than measured values for each individual will also be investigated by re-running a sub-sample of the data presented in this chapter using individual values rather than the group average.

Intra observer and intra subject reproducibility of the methods used in this chapter showed low variability in the results providing that the imaging slice used was consistent for both visits. One PerMinH data set was removed from the study due to the slice positing being different between the two visits, all other data sets showed consistent slice positioning. Therefore if the PerMinH study was repeated in such a fashion that inter observer and intra subject reproducibility were able to be tested, the results would like show a low variability.

For the first time, this study suggests non-contrast quantitative MR measures of small bowel wall T2 could be a sensitive biomarker associated with increased permeability. If validated in patients, a newly developed MRI tool associated

with small bowel permeability has far reaching implications. This hypothesis will need to be tested in patient populations where increased small bowel permeability and bacterial translocation contribute significantly to pathogenic processes, and are associated with clinical manifestations or outcomes. A widely available, non-invasive, *in vivo* measure of small bowel structure and integrity would be an important tool for mechanistic studies as well as evaluations of specific interventions. Arguably the lack of robust, accessible and affordable biomarkers of these potentially pathophysiological changes has hampered research in this area.

In summary, we have developed non-contrast MRI techniques that can sensitively measure T2 in healthy volunteers. MR measures of small bowel wall T2 were significantly increased and associated with increased permeability following indomethacin provocation. The method used here for mapping the small bowel wall is not restricted to T2 weighted images but can be applied, with minor adjustments, to any images in which the small bowel content and wall have different signal intensities. The findings need to be validated and the hypothesis will be tested in future studies with patients in whom increased permeability is thought to be clinically significant.

5.9 Improving on the PerMinH Study Design

At the outset of the PerMinH study it was unknown as to what the T1 and T2 of the bowel wall would be and thus the echo times and inversion times used were set to best cover a wide range of T1s and T2s. The PerMinH study gave the first measurements of T1 and T2 of the bowel wall. It was also not known that a bi-exponential would be required when fitting for T1 and T2 due to the presence of partial volume effects. This section describes Monte Carlo simulations that were used to optimise the echo times and inversion times to improve sensitivity to the T1 and T2 of the bowel wall. In order to do this data was simulated for a range of T1 and T2 values. Rician noise was then added to the simulated signal and the data fit for T1 and T2 respectively. By changing the echo times and inversion times, an optimal set of times to measure T1 and T2 of the small

bowel wall was determined.

5.9.1 Optimising Inversion Times to Measure T1

Optimal T1 values were estimated using Monte Carlo simulations. The optimal times were found by identifying a set of inversion times that would minimise the difference between the simulated and fitted T1s across a range of T1 values that are expected in the bowel wall. Several factors were taken into account when simulating the data:

- T1 of the bowel wall
- Inversion times
- Noise in the images
- Partial volume effects

T1 values that were evenly spaced between 0.6 s and 1.5 s (the range identified in PerMinH) in steps of 0.01 s were simulated. Riccian noise was also added to the data which was estimated from the PerMinH data to be around 2.5% of the equilibrium magnetization. Partial volume effects were taken into account by combining wall and content signal in different percentages from 100% wall down to 70% wall with 30% content in steps of 10%. This range was estimated by looking at the range of wall fractions that were fit in the PerMinH data. The same bi-exponential recovery was fitted to the simulated data as was used in the PerMinH T1 measurements. The inversion times were varied as follows with the results for each shown in Figure 5.42.

- Inversion times from the PerMinH study were used to estimate the error the fit would produce on the current data.
- The same inversion times as the PerMinH study were used with the addition of a long inversion time at 12 s to achieve a good estimate of M_0 in the fitting.

5. *Bowel Wall and the PerMinH Study*

- 8 inversion times logarithmically spaced between 0.5 s and 12 s were used to evenly sample the recovery curve using an achievable number of acquisition in the restricted time frame.
- A set of 1000 inversion times between 0.5 s and 12 s were used to determine the best possible fit with the given noise.

From Figure 5.42 it can be seen that the addition of a long inversion time to the PerMinH inversion times provides a large reduction in the potential error on the fit T1 values from a range of 33% to 14%. Further to this if the inversion times are logarithmically spaced between 0.5s and 12 s a further, albeit small, reduction in the range of errors is achieved. As expected with a heavily sampled inversion recovery curve a very small error on the fit T1 values is seen ($\approx 1\%$). Therefore in future studies it is recommended that the use of logarithmically spaced inversion times between 0.5 s and 12 s be used.

5. Bowel Wall and the PerMinH Study

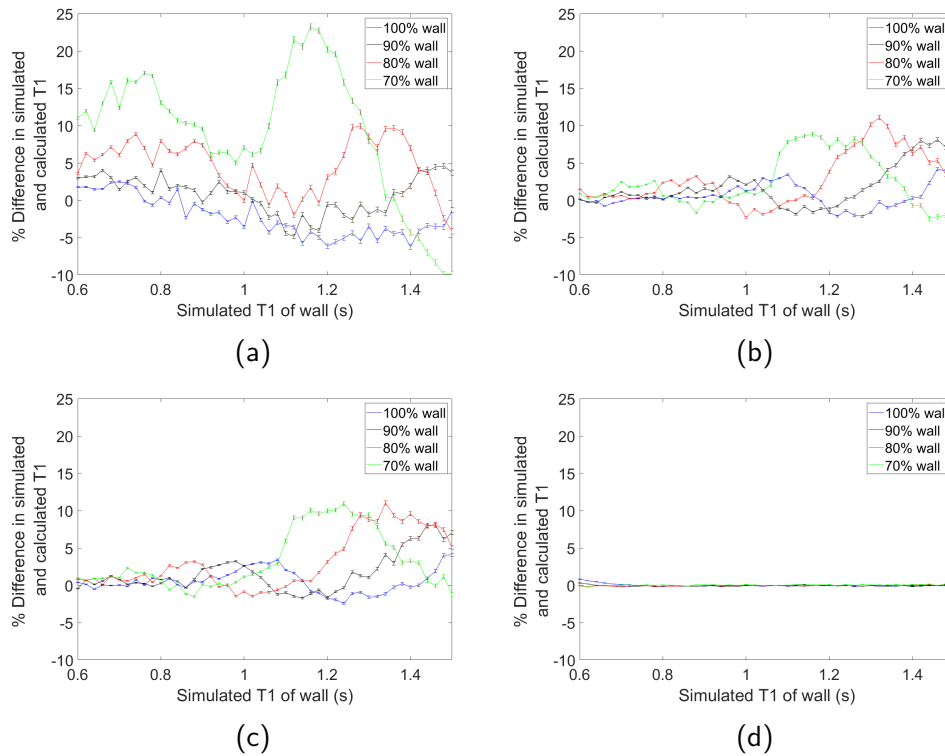


Figure 5.42: Simulated T1 with the percentage difference in the simulated and calculated T1 shown when using a) the same inversion times as PerMinH, b) the same inversion times as PerMinH with an extra inversion time at a long TI, c) logarithmically spaced inversion times between 0.5 s and 12 s d) 1000 inversion times between 0.5 s and 12 s to estimate the best possible fit to the data with the given noise level. The range in percentage difference between the simulated and fit T1 was a) -9.9% to 23.2% b) -3.3% to 11.1% c) -2.4% to 11.0% d) -0.2% to 0.8%.

5. Bowel Wall and the PerMinH Study

In order to better understand the origin of the error on the fitted T1 the least accurate fitting scenario was looked at in more detail. Figure 5.43 shows the results when a fit is applied to signal simulated with 70% wall and a T1 of 1.6 s using the original PerMinH inversion times. The fitted curve matches well with the simulated data, giving an R squared of 0.98, however the results from the fit do not match the input results as shown in Table 5.2. The error originates from the fitting algorithm finding a local minima which produces a sum of squares error below the tolerance level of the fit. If the starting guesses for the fit are set to match the simulated values, then the algorithm produces a T1 and wall fraction close to the simulated values. This problem, as demonstrated by the simulations shown in Figure 5.42, can be overcome by using an additional inversion time which gives a good estimate of M_0 , reducing the number of variables in the fit and therefore reducing the likelihood of the algorithm finding a local minima.

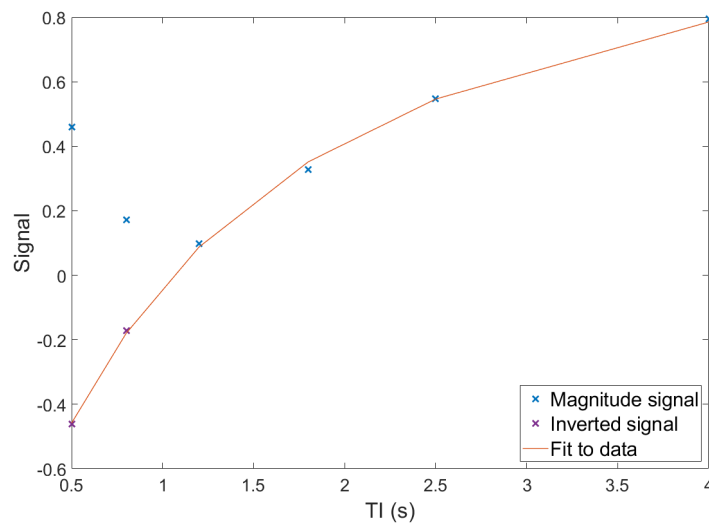


Figure 5.43: Fitted curve to simulated T1 recovery with Riccian noise added, simulated and fitted parameters are given in Table 5.2.

5. Bowel Wall and the PerMinH Study

Parameter	Simulation value	Fitted value
T1 (s)	1.6	0.8
M_0	1.0	1.2
Wall fraction	0.7	0.5

Table 5.2: Table detailing the parameters of the simulation and the fitted values.

Similar simulations were run to see if an improvement could be made on the T2 measurement however the only method of significantly improving the T2 result was to use an earlier echo time. Unfortunately the shortest echo time is restricted by the scanner and was already in use in the T2 measurement, thus the results cannot be significantly improved without altering the acquisition sequence.

5.9.2 Discussion

From the Monte Carlo simulations it has been determined that the precision of the T2 measurements cannot be improved by altering the echo times as predicted by the simulations because a shorter echo time than the one used in the PerMinH study cannot be achieved with the current scan parameters. The accuracy of the T1 measurements however can be improved. This can be achieved by the collection of an inversion time that is sufficiently long that the signal measured is effectively M_0 . By measuring the signal at a long inversion time the M_0 parameter is well estimated leaving 1 variable to fit for. A further increase in accuracy can be achieved by logarithmically spacing the inversion times. The number of inversion times that should be collected was increased from 6 to 8 to allow an increase in the accuracy. It is believed that acquiring 8 inversion times is now achievable as the scanner operators are more familiar with the protocol and the method in which they are acquired than at the beginning of the study.

5.10 Conclusion and future work

In this section we have presented the development of a new clinically viable tool to measure T1 and T2 of the small bowel wall. T2 was shown to increase with

5. *Bowel Wall and the PerMinH Study*

the administration of indomethacin which is known to increase the permeability of the bowel wall. This is the first study which has measured T1 and T2 of the small bowel wall. The methods developed in this section allowed for the first non-invasive marker of bowel permeability to be assessed and will also allow for further investigations into spatial variations of the small bowel wall to be carried out.

The inter observer and intra subject reproducibility of the newly developed T2 analysis have also been presented. The inter observer reproducibility showed that the analysis method is robust to different observers however the reproducibility results showed that T2 can vary between subject visits. This is likely due to different areas of the bowel wall being imaged which highlights the need for the T2 acquisition to be made into a multi slice sequence to allow for full coverage of the bowel wall.

Monte Carlo simulations were used to determine a set of inversion times and echo times which would allow for better accuracy of the T1 and T2 measurements. The accuracy of the T2 measurements could not be improved due to the limitation on the shortest echo time available on the scanner. It was shown that the T1 accuracy could be greatly improved by acquiring an image with a long inversion time effectively giving the value of M_0 and effectively removing it as a variable from the fitting. In future studies these improved echo times will be used to measure T1.

The analysis method for measuring T2/T1 may prove to be a useful clinical tool and the potential for this to be developed into a commercial tool is being investigated. It would provide the first method of measuring quantitative structural changes to the small bowel wall which is of great interest in both clinical and pharmaceutical applications.

T1 and T2 measurements are currently being made in patient groups including patients with Crohn's disease and, in the future, Liver cirrhosis patients with and without portal hypertension. The liver cirrhosis group is of particular interest as it is believed that increased permeability is associated with portal hypertension. This hypothesis can now be tested using T2 measurements.

References

- [1] M Camilleri, K Madsen, R Spiller, B G Van Meerveld, and G N Verne. Intestinal Barrier Function in Health and Gastrointestinal Disease. *Neurogastroenterology & Motility*, 24(6):503–512, jun 2012. ISSN 13501925. doi: 10.1111/j.1365-2982.2012.01921.x.
- [2] M S Balda and K Matter. Tight Junctions in Health and Disease. *Seminars in Cell & Developmental Biology*, 36:147–148, dec 2014. ISSN 1084-9521. doi: 10.1016/J.SEMCDB.2014.11.001.
- [3] R D Berg and A W Garlington. Translocation of Certain Indigenous Bacteria from the Gastrointestinal Tract to the Mesenteric Lymph Nodes and Other Organs in a Gnotobiotic Mouse Model. *Infection and immunity*, 23(2): 403–11, feb 1979. ISSN 0019-9567.
- [4] V I Nikitenko, A A Stadnikov, and V A Kopylov. Bacterial Translocation from the Gastrointestinal Tract in Healthy and Injured Rats. *Journal of Wound Care*, 20(3):114–122, mar 2011. ISSN 0969-0700. doi: 10.12968/jowc.2011.20.3.114.
- [5] P M Bossuyt, J B Reitsma, D E Bruns, C A Gatsonis, P P Glasziou, L M Irwig, J G Lijmer, D Moher, D Rennie, H C W De Vet, and Standards for Reporting of Diagnostic Accuracy. Towards Complete and Accurate Reporting of Studies of Diagnostic Accuracy: the STARD Initiative. *BMJ (Clinical research ed.)*, 326(7379):41–4, jan 2003. ISSN 1756-1833.
- [6] E Smecuol, J C Bai, E Sugai, H Vazquez, S Niveloni, S Pedreira, E Mauriño, and J Meddings. Acute Gastrointestinal Permeability Responses to Different Non-Steroidal Anti-Inflammatory Drugs. *Gut*, 49(5):650–5, nov 2001. ISSN 0017-5749. doi: 10.1136/GUT.49.5.650.
- [7] R Kiesslich, C A Duckworth, D Moussata, A Gloeckner, L G Lim, M Goetz, D M Pritchard, P R Galle, M F Neurath, and A J M Wat-

References

- son. Local barrier Dysfunction Identified by Confocal Laser Endomicroscopy Predicts Relapse in Inflammatory Bowel Disease. *Gut*, 2011. doi: 10.1136/gutjnl-2011-300695.
- [8] U C Ghoshal, R Shukla, U Ghoshal, K Gwee, S C Ng, and E M M Quigley. The Gut Microbiota and Irritable Bowel Syndrome: Friend or Foe? *International journal of inflammation*, 2012:151085, 2012. ISSN 2042-0099. doi: 10.1155/2012/151085.
- [9] D Hollander, C M Vadheim, E Brettholz, G M Petersen, T Delahunty, and J I Rotter. Increased Intestinal Permeability in Patients with Crohn's Disease and Their Relatives. A Possible Etiologic Factor. *Annals of internal medicine*, 105(6):883–5, dec 1986. ISSN 0003-4819.
- [10] E J Irvine and J K Marshall. Increased Intestinal Permeability Precedes the Onset of Crohn's Disease in a Subject with Familial Risk. *Gastroenterology*, 119(6):1740–4, dec 2000. ISSN 0016-5085.
- [11] I H Koh, R Guatelli, E F Montero, R Keller, M H Silva, S Goldenberg, and R M Silva. Where is the Site of Bacterial Translocation—Small or Large Bowel? *Transplantation proceedings*, 28(5):2661, oct 1996. ISSN 0041-1345.
- [12] D W Powell. Barrier Function of Epithelia. *American Journal of Physiology-Gastrointestinal and Liver Physiology*, 241(4):G275–G288, oct 1981. ISSN 0193-1857. doi: 10.1152/ajpgi.1981.241.4.G275.
- [13] J MacFie, C O'Boyle, C J Mitchell, P M Buckley, D Johnstone, and P Sudworth. Gut Origin of Sepsis: A Prospective Study Investigating Associations Between Bacterial Translocation, Gastric Microflora, and Septic Morbidity. *Gut*, 45(2):223–8, aug 1999. ISSN 0017-5749.
- [14] J C Marshall, N V Christou, R Horn, and J L Meakins. The Microbiology of Multiple Organ Failure. The Proximal Gastrointestinal Tract as an Occult

- Reservoir of Pathogens. *Archives of surgery (Chicago, Ill. : 1960)*, 123(3): 309–15, mar 1988. ISSN 0004-0010.
- [15] J Rimola, I Ordás, S Rodriguez, O García-Bosch, M Aceituno, J Llach, C Ayuso, E Ricart, and J Panés. Magnetic Resonance Imaging for Evaluation of Crohn's Disease. *Inflammatory Bowel Diseases*, 17(8):1759–1768, aug 2011. ISSN 1078-0998. doi: 10.1002/ibd.21551.
- [16] P C Church, D Turner, B M Feldman, T D Walters, M-L Greer, M M Amitai, A M Griffiths, and ImageKids Study Group. Systematic Review with Meta-Analysis: Magnetic Resonance Enterography Signs for the Detection of Inflammation and Intestinal Damage in Crohn's Disease. *Alimentary Pharmacology & Therapeutics*, 41(2):153–166, jan 2015. ISSN 02692813. doi: 10.1111/apt.13024.
- [17] I Ordás, J Rimola, S Rodríguez, J M Paredes, M J Martínez-Pérez, E Blanc, J A Arévalo, M Aduna, M Andreu, A Radosevic, A M Ramírez-Morros, S Pinó, M Gallego, A Jauregui-Amezaga, E Ricart, and J Panés. Accuracy of Magnetic Resonance Enterography in Assessing Response to Therapy and Mucosal Healing in Patients With Crohn's Disease. *Gastroenterology*, 146(2):374–382.e1, feb 2014. ISSN 00165085. doi: 10.1053/j.gastro.2013.10.055.
- [18] Center for Drug Evaluation and Research. Drug Safety and Availability - FDA Drug Safety Communication: FDA Evaluating the Risk of Brain Deposits with Repeated Use of Gadolinium-Based Contrast Agents for Magnetic Resonance Imaging (MRI). pages 4–6, 2015. URL <https://www.fda.gov/Drugs/DrugSafety/ucm455386.htm>.
- [19] T Vanuytsel, S van Wanrooy, H Vanheel, C Vanormelingen, S Verschueren, E Houben, S Salim Rasoel, J Toth, L Holvoet, R Farré, L Van Oudenhove, G Boeckxstaens, K Verbeke, and J Tack. Psychological Stress and Corticotropin-Releasing Hormone Increase Intestinal Permeability in Hu-

References

- mans by a Mast Cell-Dependent Mechanism. *Gut*, 63(8):1293–1299, aug 2014. ISSN 0017-5749. doi: 10.1136/gutjnl-2013-305690.
- [20] J Rimola, S Rodriguez, O Garcia-Bosch, I Ordas, E Ayala, M Aceituno, M Pellise, C Ayuso, E Ricart, L Donoso, and J Panes. Magnetic Resonance for Assessment of Disease Activity and Severity in Ileocolonic Crohn's Disease. *Gut*, 58(8):1113–1120, aug 2009. ISSN 0017-5749. doi: 10.1136/gut.2008.167957.
- [21] A A Plumb, A Menys, E Russo, D Prezzi, G Bhatnagar, R Vega, S Halligan, T R Orchard, and S A Taylor. Magnetic Resonance Imaging-Quantified Small Bowel Motility is a Sensitive Marker of Response to Medical Therapy in Crohn's Disease. *Alimentary Pharmacology & Therapeutics*, 42(3):343–355, aug 2015. ISSN 02692813. doi: 10.1111/apt.13275.
- [22] M Zappa, C Stefanescu, D Cazals-Hatem, F Bretagnol, L Deschamps, A Attar, B Larroque, X Tréton, Y Panis, V Vilgrain, and Y Bouhnik. Which Magnetic Resonance Imaging Findings Accurately Evaluate Inflammation in Small Bowel Crohn's Disease? A Retrospective Comparison with Surgical Pathologic Analysis. *Inflammatory Bowel Diseases*, 17(4):984–993, apr 2011. ISSN 1078-0998. doi: 10.1002/ibd.21414.
- [23] J Zhu, J Xu, H Gong, and Y Zhou. Updating Magnetic Resonance Imaging of Small Bowel: Imaging Protocols and Clinical Indications. *World journal of gastroenterology*, 14(21):3403–9, jun 2008. ISSN 1007-9327. doi: 10.3748/WJG.14.3403.
- [24] N Bueno-Hernández, B L Jiménez-Cruz, M Zavala-Solares, and G Meléndez-Mier. Association of Natural and Artificial Nonnutritive Sweeteners on Gastrointestinal Disorders: A Narrative Review. *J Nutr Food Sci*, 8(4):711, 2018. ISSN 2155-9600. doi: 10.4172/2155-9600.1000711.
- [25] P Kubica, A Kot-Wasik, A Wasik, J Namieśnik, and P Landowski. Modern Approach for Determination of Lactulose, Mannitol and Sucrose in Human

- Urine using HPLC–MS/MS for the Studies of Intestinal and Upper Digestive Tract Permeability. *Journal of Chromatography B*, 907:34–40, oct 2012. ISSN 15700232. doi: 10.1016/j.jchromb.2012.08.031.
- [26] I Bjarnason, A Macpherson, and D Hollander. Intestinal Permeability: An Overview. *Gastroenterology*, 108(5):1566–1581, may 1995. ISSN 00165085. doi: 10.1016/0016-5085(95)90708-4.
- [27] M Camilleri, A Nadeau, J Lamsam, S Linker Nord, M Ryks, D Burton, S Sweetser, A R Zinsmeister, and R Singh. Understanding Measurements of Intestinal Permeability in Healthy Humans with Urine Lactulose and Mannitol Excretion. *Neurogastroenterology & Motility*, 22(1):e15–26, jul 2009. ISSN 13501925. doi: 10.1111/j.1365-2982.2009.01361.x.
- [28] J Thirion. Image matching as a diffusion process: An analogy with Maxwell’s demons. *Medical Image Analysis*, 2(3):243–260, 1998. ISSN 13618415. doi: 10.1016/S1361-8415(98)80022-4.
- [29] T Vercauteren, X Pennec, A Perchant, and N Ayache. Diffeomorphic demons: efficient non-parametric image registration. *NeuroImage*, 45(1 Suppl), 2009. ISSN 10959572. doi: 10.1016/j.neuroimage.2008.10.040.
- [30] C Solomon and T Breckon. *Fundamentals of digital image processing*. 2011. doi: 10.1007/978-981-10-7272-7_1.
- [31] John Canny. A Computational Approach to Edge Detection. *IEEE Transactions on Pattern Analysis and Machine Intelligence*, PAMI-8(6):679–698, 1986. ISSN 01628828. doi: 10.1109/TPAMI.1986.4767851.
- [32] W H Press, S A Teukolsky, W T Vetterling, and B P Flannery. *Numerical Recipes in C: The Art of Scientific Computing*. Fortran numerical recipes. Cambridge University Press, 1996. ISBN 9780521576086.
- [33] C L Hoad, E F Cox, and P A Gowland. Quantification of T2 in the Abdomen at 3.0 T using a T2 -Prepared Balanced Turbo Field Echo Sequence. *Mag-*

References

- netic Resonance in Medicine*, 63(2):356–364, feb 2010. ISSN 07403194. doi: 10.1002/mrm.22203.
- [34] S C Bischoff, G Barbara, W Buurman, T Ockhuizen, J Schulzke, M Serino, H Tilg, A Watson, and J M Wells. Intestinal Permeability—A New Target for Disease Prevention and Therapy. *BMC gastroenterology*, 14:189, nov 2014. ISSN 1471-230X. doi: 10.1186/s12876-014-0189-7.
- [35] C J Hawkey, C Ell, B Simon, J Albert, M Keuchel, M McAlindon, P Fortun, S Schumann, W Bolten, A Shonde, J L Hugot, V Yu, U Arulmani, G Krammer, R Rebuli, and E Toth. Less Small-Bowel Injury With Lumiracoxib Compared With Naproxen Plus Omeprazole. *Clinical Gastroenterology and Hepatology*, 6(5):536–544, may 2008. ISSN 15423565. doi: 10.1016/j.cgh.2007.12.023.
- [36] I Bjarnason, C Scarpignato, E Holmgren, M Olszewski, K D Rainsford, and A Lanas. Mechanisms of Damage to the Gastrointestinal Tract From Nonsteroidal Anti-Inflammatory Drugs. *Gastroenterology*, 154(3):500–514, feb 2018. ISSN 00165085. doi: 10.1053/j.gastro.2017.10.049.
- [37] C Hordonneau, A Buisson, J Scanzi, F Goutorbe, B Pereira, C Borderon, D Da Ines, P F Montoriol, J M Garcier, L Boyer, G Bommelaer, and V Petitcolin. Diffusion-Weighted Magnetic Resonance Imaging in Ileocolonic Crohn's Disease: Validation of Quantitative Index of Activity. *The American Journal of Gastroenterology*, 109(1):89–98, jan 2014. ISSN 0002-9270. doi: 10.1038/ajg.2013.385.
- [38] A Buisson, A Joubert, P-F Montoriol, D D Ines, C Hordonneau, B Pereira, J-M Garcier, G Bommelaer, and V Petitcolin. Diffusion-Weighted Magnetic Resonance Imaging for Detecting and Assessing Ileal Inflammation in Crohn's Disease. *Alimentary Pharmacology & Therapeutics*, 37(5):537–545, mar 2013. ISSN 02692813. doi: 10.1111/apt.12201.
- [39] M Grover, M Camilleri, J Hines, D Burton, M Ryks, A Wadhwa, W Sundt, R Dyer, and R J Singh. 13 C Mannitol as a Novel Biomarker for Measure-

References

ment of Intestinal Permeability. *Neurogastroenterology & Motility*, 28(7): 1114–1119, jul 2016. ISSN 13501925. doi: 10.1111/nmo.12802.

6 Fat Quantification using Multi-Echo MRI in Non Standard Situations

6.1 Introduction

Fat quantification is increasingly being used in MRI especially in relation to metabolic disorders and gastrointestinal diseases. For instance Non-Alcoholic fatty liver disease (NAFLD), which is the most common cause of chronic liver disease, affects around 20% of the US population (1). It is currently diagnosed from the histology of a sample obtained using a biopsy, which is subject to errors due to the heterogeneity of the liver in NAFLD and hence has the potential to misdiagnose or incorrectly stage the disease, and also comes with significant risk to the patient (1). MRI has a much lower risk and could therefore provide a safer alternative to biopsy for the diagnosis of NAFLD. Magnetic Resonance Spectroscopy (MRS) has similar benefits to MRI fat quantification and has been shown to have high sensitivity and specificity for liver fat quantification. However, MRS only provides a fat fraction measurement from a finite single location and so can produce errors in fat quantification similar to biopsy (2).

Various methods are currently used to quantify abdominal fat (3), but Proton Density Fat Fraction (PDFF) is an important measure in abdominal imaging that can be quantified robustly and repeatedly (4, 5, 6, 7). It has been shown that at 1.5T and 3T PDFF correlates with steatosis assessed by histology in patients with NASH (8), and the degree of steatosis, iron accumulation and fibrosis in chronic liver disease (9). It could not however distinguish between higher histology scores in NASH meaning that a biopsy would still be required (1). Good linear relationships have been found between CT, histology and MRI PDFF however this does not hold true when iron overload is present (10, 11, 12, 13). In liver transplants it is important to determine the fat content of a liver before transplant and PDFF has shown good sensitivity and specificity in this case at 1.5T (14).

Whilst fat quantification has mainly been focused in the liver, outside of

6. Fat Quantification using Multi-Echo MRI in Non Standard Situations

the liver it has been used in the spine to detect bone marrow involvement in Gaucher disease (spinal disorder), showing a decrease in fat in the vertebrae from untreated to treated patients and a further decrease in fat levels in healthy volunteers (15).

Most scanner vendors now offer a fat quantification package that uses Dixon imaging (e.g. Liver Multi Scan IDEAL and mDIXON Quant). Vendor products for fat quantification are optimised to work mainly in the liver at 1.5T and 3T where the *in vivo* conditions are well known. Outside of the liver and at higher field strengths it is unlikely that vendor products use appropriately optimised algorithms which could result in a decreased accuracy and precision in fat quantification. A fat quantification toolbox for use in Matlab was developed by the members of the International Society for Magnetic Resonance in Imaging (ISMRM) (16). Whilst this toolbox allows much more user control over the fitting method than the vendor products it is still optimised for use in the liver at 1.5T and 3T. The toolbox also uses the assumption that fat and water have the same $T2^*$ which may reduce the accuracy of fat quantification in cases where there is a large difference in the $T2^*$ of fat and water. The aim of this chapter was to use fat quantification in regions which do not fall into the target areas for vendor fat quantification products. Two key areas of fat quantification which are unlikely to have optimal results when using vendor products are the liver at 7T and the colon.

The liver at 7T was chosen as an area of interest as 7T has the potential to provide increased sensitivity to detect changes related to conditions such as NAFLD.

The colon was chosen as an area of interest as patients with Cystic Fibrosis are known to have compromised gastrointestinal systems and suffer from fat malabsorption. Fat malabsorption which is currently diagnosed by looking at stool samples over the course of several hours or days (17). MRI has the potential to provide an alternative method of detecting fat malabsorption in the colon which is faster and less intrusive than current methods.

An in-house fitting method was developed that could be optimised for non-

standard situations. Firstly Monte Carlo simulations were used to theoretically test the performance of in-house fat quantification. Simulations were run for both the liver at 3T and 7T and the colon at 3T. In-house fitting at 3T and 7T over the liver was compared to fat maps produced by Philip's mDixon Quant and using the ISMRM toolbox.

All image acquisitions were performed by Hannah Williams, with assistance from Dr Stephen Bawden (Post doctoral researcher) and Emma Doran (PhD student). All analysis was performed by the author of this thesis. The work presented in this chapter has been presented as a poster presentation at the annual conference of the International Society of Magnetic Resonance Imaging (ISMRM) 2019, the Post Graduate Symposium of the British Chapter of ISMRM 2019 and the British Chapter of ISMRM in 2016.

6.2 Quantification using the Dixon Method

Chemical shift causes fat and water to resonate at different frequencies (see Section 2.1.10 and fat quantification using Dixon imaging (see Section 2.3.9) makes use of these differences. The simplest Dixon fat quantification algorithms assume that there is one peak in the fat spectra whilst more complete models take account of up to 9 peaks (Figure 6.1). Different Dixon techniques also make use of different numbers of echo times at different relative phases of fat and water (Figure 6.2), and more complex algorithms also take account of several confounding factors. The different Dixon methods are discussed here.

6.2.1 Two Point Dixon

The original form of fat quantification proposed by Dixon (19) is the two point Dixon method. It requires the acquisition of two echoes, one in which fat and water are out of phase and one in which they are in phase. From the in-phase and opposed-phase images, fat only and water only images can be calculated, along with a fat fraction map. This method restricts the measured fat quantity to <50% and can also lead to negative fat fraction estimates if there has been

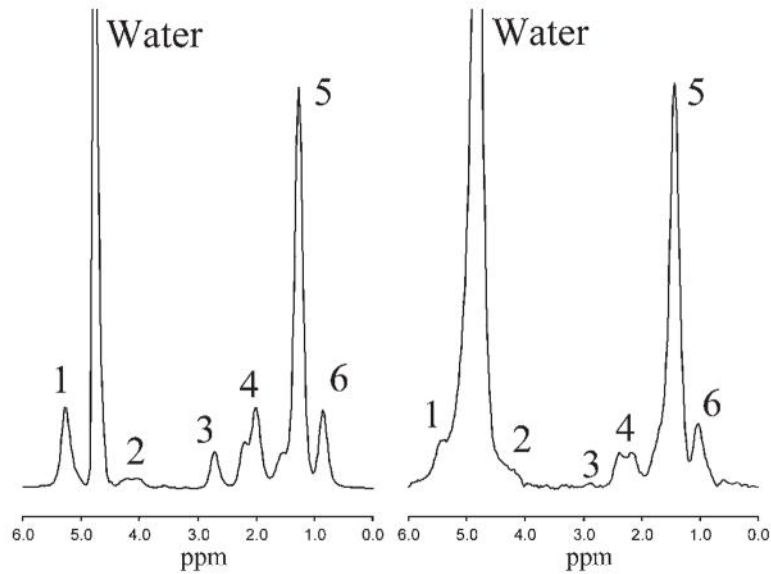


Figure 6.1: Fat spectra taken from Hamilton *et al* (18) showing the spectra in a fat emulsion phantom (left) and the liver from a patient with fatty liver disease (right). Fat peak assignment: 1, $-\text{CH}=\text{CH}-$ and $-\text{CH}-\text{O}-\text{CO}-$; 2, $-\text{CH}_2-\text{O}-\text{CO}-$; 3, $-\text{CH}=\text{CH}-\text{CH}_2-\text{CH}=\text{CH}-$; 4, $-\text{CO}-\text{CH}_2-\text{CH}_2-$ and $-\text{CH}_2-\text{CH}=\text{CH}-\text{CH}_2-$; 5, $-\text{CO}-\text{CH}_2-\text{CH}_2-$ and $-(\text{CH}_2)_n-$; 6, $-(\text{CH}_2)_n-\text{CH}_3$. Of the six fat peaks resolvable by spectroscopy at 3T, *in vivo* peaks 1 and 2 are buried within the water peak, and peak 3 is small and rarely seen in the human liver clinically.

signal decay due to T_2^* between the opposed-phase and in-phase echoes. This method also does not take account of phase changes due to B_0 inhomogeneities leading to errors in quantification.

6.2.2 Three Point Dixon

The two point method was succeeded by the three point Dixon method which uses a third echo acquired when water and fat are at opposed phases at a later echo time. The collection of the third echo allows for the correction of B_0 inhomogeneities. Most vendors offer a product that performs this scan for fat quantification as part of a commercial package (on Philips' it is known as modified Dixon or mDIXON). Two and three point Dixon do not take into account the spectral complexity of fat (Figure 6.1) i.e. assume one spectral peak,

6. Fat Quantification using Multi-Echo MRI in Non Standard Situations

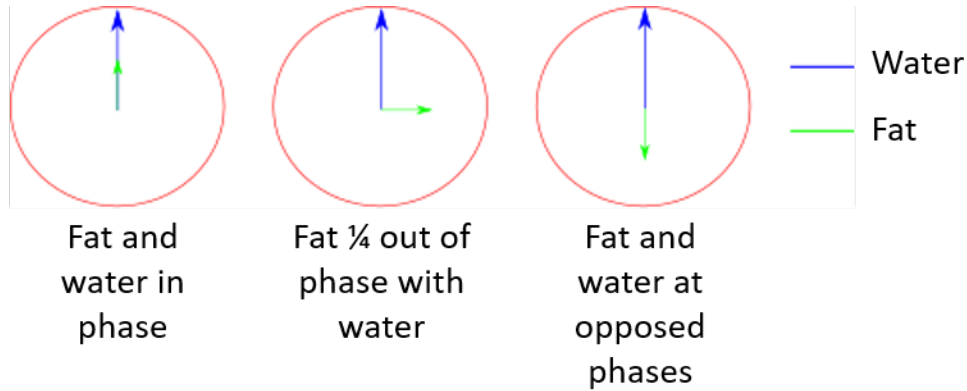


Figure 6.2: Phases of fat and water shown at different points in the phase cycles of fat and water.

making it a simplification of the true spectra which can reduce the accuracy of the fat quantification at high fat levels (20).

6.2.3 Multi-Echo Dixon

The next progression in Dixon fat quantification was the 6 point Dixon technique. This technique allows fat quantification along with T2* calculation. The 6 point technique fits the signal measured in a voxel to a more complete model:

$$S = \left[W e^{-R2_w^* t} + \sum_1^n F_n e^{i\Delta\omega_n t} e^{-R2_f^* t} \right] e^{i\psi t} e^{i\phi} \quad (6.1)$$

where $\Delta\omega$ is the offset resonant frequency, $R2^* = 1/T2^*$, ψ is the field map (the deviation of the magnetic field from B_0) and ϕ is the phase offset. Figure 6.3 shows the magnitude, phase, real and imaginary signals that were produced from 100% fat for three different values of T2*. Examples of the magnitude, phase, real and imaginary signal simulated using Dixon imaging from 100% water, 100% fat and 50\50 water and fat are shown in Figure 6.4. The fat (simulated with 6 fat peaks) and the water were simulated as having the same T2*.

A significant amount of work has been done to develop Multi-echo Dixon

6. Fat Quantification using Multi-Echo MRI in Non Standard Situations

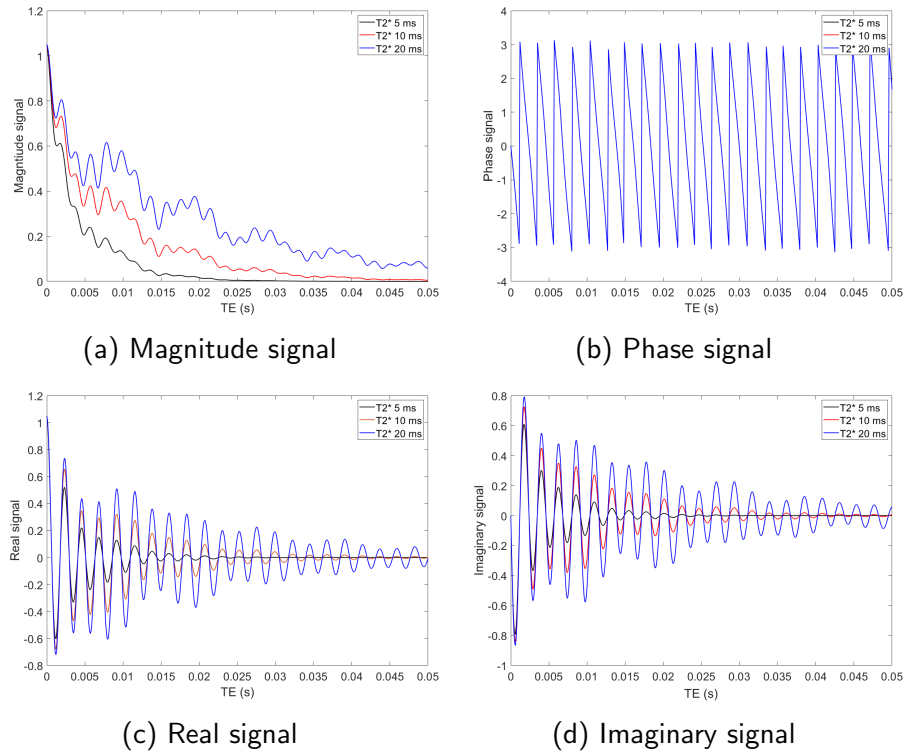


Figure 6.3: Example a) magnitude b) phase c) real and d) imaginary signals simulated using Dixon imaging for 100% fat with T2* values of 5 ms (black line), 10 ms (red line) and 20 ms (blue line).

sequences and fitting algorithms that account for the confounding factors that may influence the fat quantification (21). The main confounding factors are the T2* of the fat and the water, the T1 dependence of the signal, the flip angle used, the echo times at which the data is acquired and B₀ inhomogeneities (22). Whilst the issue of some of these confounding factors have mainly been resolved, some are still subject to much debate and probably depend on circumstance. Each factor is discussed below (23).

6. Fat Quantification using Multi-Echo MRI in Non Standard Situations

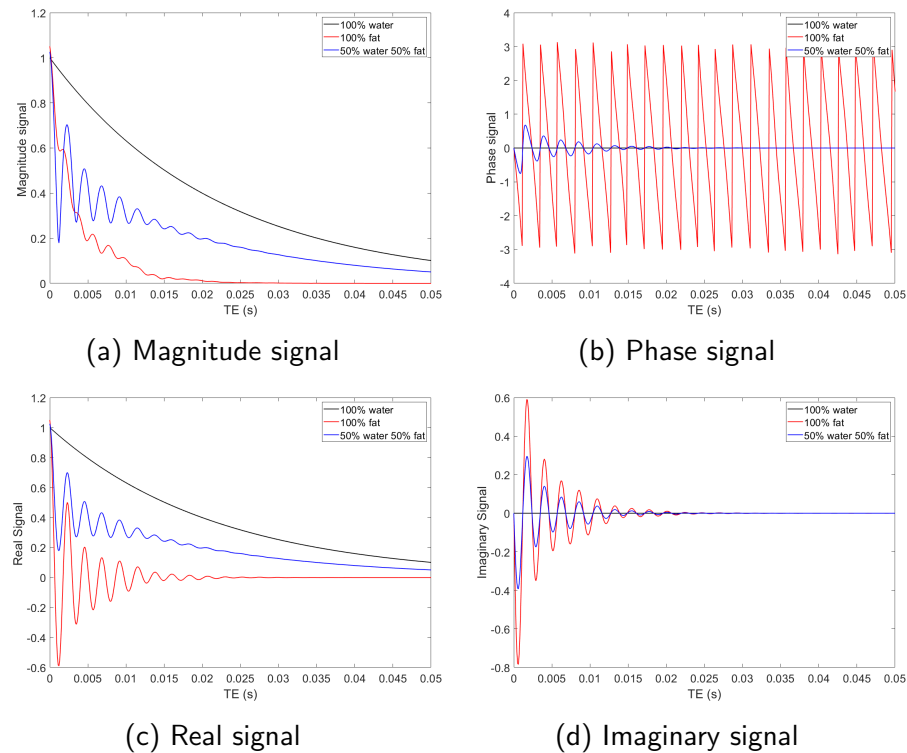


Figure 6.4: Example a) magnitude b) phase c) real and d) imaginary signals simulated using Dixon imaging for 100% water (black line), 100% fat (red line) and 50% water 50% fat (blue line). The fat and water were simulated with the same $T2^*$.

$T2^*$ of Fat and Water: At 1.5T most of the literature now agrees that $T2^*$ should be included as a fitting parameter when quantifying fat. However, at 1.5T in most situations the $T2^*$ of fat and water are similar enough that fitting for a common $T2^*$ (assumes that fat and water have the same $T2^*$) for both species is more beneficial than fitting for them separately. Fitting for the $T2^*$ s separately introduces more instability into the fitting algorithms by adding an additional variable (24, 25). It is known that accurate MRS measurements of fat fraction require correction for the $T2^*$ of fat and water, suggesting that it should also be important in Dixon methods, especially at high fields where the differences are larger. However the Dixon model is rather underdetermined and so adding more variables to the fit may reduce precision. Reeder *et al* concluded

6. Fat Quantification using Multi-Echo MRI in Non Standard Situations

that a common $T2^*$ produces more precise results but does introduce a bias in the results leading to less accurate fat quantification compared to using separate $T2^*$ s (26, 27).

At 3T the question as to whether separate $T2^*$ values should be incorporated into the fitting algorithm is dependent on the patient group or phantom that is scanned. Bydder *et al* have shown that using a common $T2^*$ value produced more reproducible results with a better noise performance (28). However, Deng *et al* have shown that in pediatric patients with NAFLD separate $T2^*$ values produced better results using magnitude fitting with in-phase and opposed-phase echo times compared to using a common $T2^*$ (29). Hernando *et al* have noted the reverse problem where the presence of fat has introduced bias into $T2^*$ calculations and that the inclusion of corrections for the presence of fat increased the accuracy of $T2^*$ measurements (30).

From these results it is clear that the optimal approach taken when fitting for $T2^*$ values is dependent on the scenario. In areas such as the liver during iron overload where the $T2^*$ is expected to vary much more than in a healthy liver a separate $T2^*$ approach would be more appropriate. However in areas where there is not expected to be a large difference then a common $T2^*$ would be more appropriate.

T1 and Flip Angle Dependence: The signal measured in a Multi-echo fast field echo sequence depends on both the T1 and the flip angle (α) used (as seen in Equation 6.2 (23)) and introduces different T1 weightings into the fat and water signals.

$$S(TR, \alpha) = \frac{(1 - e^{-TR/T1}) \sin(\alpha)}{1 - e^{-TR/T1} \cos(\alpha)}. \quad (6.2)$$

Provided that a long TR (compared to the T1 of fat and water) and low flip angle are used then it can be assumed that total T1 recovery occurs and this does not need to be factored into the fat quantification algorithm. At 7T T1 is longer and so the TR will need to be increased accordingly.

Field Inhomogeneities: Field inhomogeneities (e.g. caused by shim errors or tissue/air interfaces) result in poor performance of fat quantification (31). Correction methods for field inhomogeneities vary from a voxel-by-voxel estimation to more complex methods such as graph cut algorithms (used in the ISMRM toolbox) which include smoothing functions to create a continuous field map (32, 33). In this chapter the field map is included as a variable in the fitting however no iterative methods or smoothing functions were used when estimating the field map. At 7T where the field is expected to be less homogeneous, more sophisticated methods of field map estimation would be beneficial.

Phase Errors: The other main confounding factor in the quantification of fat is related to the phase errors that can occur (e.g. due to eddy currents or gradient timing misregistrations). At higher field strengths shorter TEs are required as fat and water come in and out of phase in a shorter time. This requires higher gradients with faster slew rates which may cause higher eddy currents and hence larger phase errors than those found at lower field strengths. These errors relate to a debate as to whether fitting to magnitude only or complex only data provides a more robust fitting method. Complex fitting has the benefit of including both the magnitude and phase data. Magnitude fitting discards the phase data, leaving half the number of data points, however this results in the magnitude fitting being insensitive to phase errors (see Section 6.3.1). Magnitude fitting also has the disadvantage of being unable to distinguish which signal originates from the fat and which from the water.

Several studies have looked at whether using the magnitude data or the complex data provides the most robust fitting for fat quantification and the results are varied. At both 1.5T and 3T it appears that the two methods produce similar results in phantoms and *in vivo* and hence the use of both methods is commonly found in the literature (4, 34, 3). In cases where the fat content is above 50%, for example adipose tissue, fat infiltration in the pancreas due to obesity or in bone marrow, complex fitting would be required (35). It has also been shown that whilst magnitude data is less sensitive to system variations it

6. Fat Quantification using Multi-Echo MRI in Non Standard Situations

did have a lower SNR in patients with NASH (36).

Hybrid approaches to fat quantification are also reported which use both the magnitude and complex data. The majority of these hybrid methods firstly use the magnitude data to get an estimate of the fat fraction and then use the outputs from a magnitude fit as the starting parameters for a complex fit. These hybrid methods give robust results at very low and very high fat fractions which are not achieved when using solely magnitude fitting (37).

Echo Times: The echo times that should be used for fat quantification have been the subject of several studies. The IDEAL paper investigated the variation in SNR with echo times from an analytical point of view when fitting to the complex data (38). They found that using asymmetric echo times rather than the commonly used in-phase and opposed-phase echo times (as used in the original Dixon method) produced the highest noise performance. Figure 6.5 illustrates the echo times that were found to produce the highest noise performance.

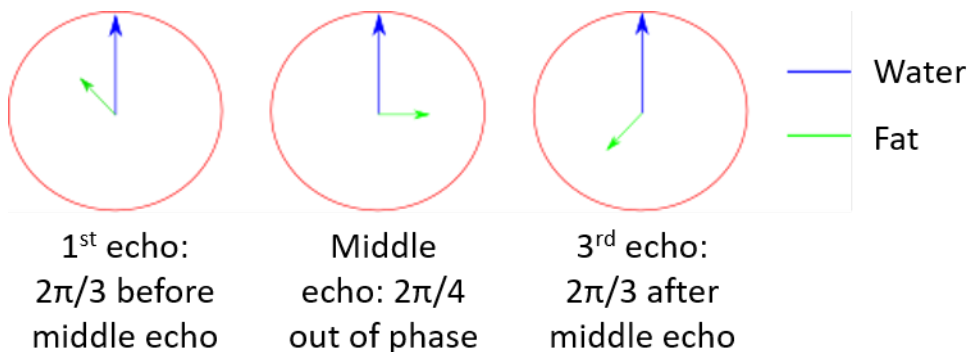


Figure 6.5: Relative phases of water (blue) and fat (green) for the first three echo times used in IDEAL 6 echo Dixon imaging.

The general format for these echo times is to separate the echos by $2\pi/3$ with the middle of the first three echoes (m) occurring when fat and water are $1/4$

6. Fat Quantification using Multi-Echo MRI in Non Standard Situations

out of phase. These follow the general equation, where k is any integer:

$$\begin{aligned}m &= \pi/2 + \pi k \\TE_1 &= m - 2\pi/3 \\TE_3 &= m + 2\pi/3.\end{aligned}\tag{6.3}$$

This method has come to be known as IDEAL (Iterative Decomposition of water and fat with Echo Asymmetric and Least-squares estimation) and is used in the majority of fat quantification studies. Studies have shown that it is more robust than in-phase opposed-phase imaging especially in cases of iron overload (39, 40). IDEAL fits to the signal to obtain an estimate of the field map and the phase shift. These estimates are then used as the starting guess for a second fit to the signal, again producing estimates for the field map and phase shift. This process is continued until the minimisation reaches a certain threshold. The field map is then smoothed and a final fit performed using the smoothed map.

In the ISMRM toolbox a graph cut algorithm is used to quickly estimate the field map in the IDEAL method. The graph cut method is a minimisation technique used to find the global minimum solution for the field map. This method makes use of mixed magnitude and complex fitting. The iterative methods used in the toolbox mean that computational time is greatly reduced when compared with non-linear fitting on a voxel-by-voxel basis.

In order to reduce the impact of the confounding factors, increasingly sophisticated methods for fat quantification have been developed over recent years including graphcut algorithms (aimed at tackling errors due to large field inhomogeneities) (33) and complex field maps (used to try to reduce the impact of the $T2^*$ and field inhomogeneities (2, 41)). Magnetic resonance fingerprinting has been used to produce $T1$ and PDF maps using Multi-echo Dixon scans in a single breath hold (42).

At 7T to our knowledge *in vivo* fat quantification has not been performed on human participants. One paper exists that has made use of fat quantification in rats at 7.1T (31). The authors used magnitude rather than complex fitting

6. Fat Quantification using Multi-Echo MRI in Non Standard Situations

as the complex data is sensitive to phase errors. At higher field strengths phase errors may be larger than at lower field strengths due to the need for higher gradients with faster slew rates. Similarly to 3T the authors use a common $T2^*$ value. At 7T the difference in $T2^*$ values of water and fat is expected to be much higher and therefore it would be expected that a common $T2^*$ approach to fat quantification would not be suitable. The International Society for Magnetic Resonance in Medicine (ISMRM) 2019 meeting contained an abstract based on human *in vivo* fat quantification on a clinical scanner (43). The authors found large discrepancies in the fat fraction measured at 3T and at 7T when using complex data. They concluded that the inaccuracies were caused by signal loss due to B1 inhomogeneities and increased magnetic susceptibility effects.

At 3T the methods by which fat is quantified in the liver are relatively robust and repeatable, and in most cases the methods by which the fat is quantified do not have a significant impact on the quantification itself. Most scanner vendors now offer a fat quantification package (e.g. Liver Multi Scan IDEAL and mDIXON Quant). Whilst the exact methods of quantification are unknown to the user it is believed that they employ hybrid fitting, using both magnitude and complex data, and assume a common $T2^*$ for fat and water (44). The assumption of a common $T2^*$ will lead to some inaccuracies in the fat quantification. This is of particular concern at 7T where the $T2^*$ of fat and water are expected to have larger differences than at 3T and in the colon at 3T. The established methods of quantification have not been tested under these circumstances and it cannot be assumed that the currently used methods are applicable for fat quantification in the more challenging circumstances in the liver at 7T and in the colon at 3T.

The aim of this chapter was to make liver fat measurements outside the normal use of Dixon imaging, at 7T and colonic fat measurements at 3T. It was hypothesised that in the liver at 7T and in the colon the assumption of a common $T2^*$ reduces the accuracy of the fat quantification. Monte Carlo simulations were carried out with a range of conditions including variable field inhomogeneities,

variable $T2^*$ values for both fat and water and variable fat fractions to test the accuracy and precision of in-house fitting. In-house fitting was first tested on the liver at 3T and 7T as reliable fat maps could be obtained for comparison over the liver using mDixon Quant and the ISMRM toolbox at 3T. The difference in fitting with complex and magnitude data was also investigated. Finally Philip's mDixon method, the ISMRM toolbox and in-house fitting were used to make colonic fat measurements at 3T.

6.3 Methods

The overall aim of the work in this section was to test, using simulations and *in vivo* data, the currently used fat quantification methods for use in the liver at 7T and in the colon at 3T, where the current vendor products provide non-optimised fat quantification. Where possible results of *in vivo* in-house fat quantification were compared to fat quantification maps produced by vendor products and using the graphcut algorithm in the ISMRM toolbox (33). The algorithm considers each voxel and its neighbours in a minimisation function which produces a smooth field map. The graphcut algorithm was chosen from the ISMRM toolbox as it provides robust fitting for 6 echo Dixon data and takes account of field inhomogeneities. The others methods either use three or two point Dixon, do not take into account $T2^*$ decay or are computationally slower than the graphcut algorithm. The ISMRM toolbox has several benefits over in-house fitting as it uses both the magnitude and complex data and fits for the field map first, then $T2^*$ and finally the fat and water fractions which can overcome the instabilities in a single fitting algorithm. Fat quantification was performed using Monte Carlo simulations and *in vivo* data for the liver at 3T and 7T and the colon at 3T. The exact details of each simulation are given in the sections below but all simulations followed the same structure which is detailed here.

6.3.1 General Simulation Method

The general signal generated from a voxel containing both fat and water using an FFE scan (neglecting T1 and flip angle) can be calculated as:

$$S = \left[W e^{-R2_w^* t} + F \sum_1^n c_n e^{i\omega_n t} e^{-R2_f^* t} \right] e^{i\psi t} e^{i\phi} \quad (6.4)$$

where W is the water signal at $t = 0$, F is the fat signal at $t=0$, n is the number of fat peaks, c is the relative amplitudes of each fat peak, ω the offset frequency of each fat peak, ψ the field offset and ϕ is the phase offset. 6 fat peaks were simulated with the frequencies and relative peaks taken from Hamilton *et al* (18). Currently the fat spectra for different types of fat within the body is unknown and so the liver spectra was used for colonic fat quantification. Fat fraction is calculated as $FF = F/(W+F)$. The proton density of fat and water are not equal and therefore to calculate the PDFF a correction must be applied to the calculated fat fraction. However, as the correction for *in vivo* fat is small and usually within experimental measurement errors no correction is required (45).

In order to test whether magnitude or complex fitting provides a more robust quantification method Equation 6.4 was modified to match the data that is generated firstly from magnitude data:

$$S_{mag} = \sqrt{S \cdot S^*} \quad (6.5)$$

where

$$\begin{aligned} S &= \left[W e^{-R2_w^* t} + F \sum_1^n c_n e^{i\omega_n t} e^{-R2_f^* t} \right] \\ S^* &= \left[W e^{-R2_w^* t} + F \sum_1^n c_n e^{-i\omega_n t} e^{-R2_f^* t} \right]. \end{aligned} \quad (6.6)$$

Note that the field map and phase shift are not included here as they cancel out in the SS^* calculation. Secondly for the complex data, the real and imaginary

6. Fat Quantification using Multi-Echo MRI in Non Standard Situations

parts were calculated and the fit applied to both simultaneously:

$$S_{complex} = S_{real} + iS_{imaginary} \quad (6.7)$$

where

$$\begin{aligned} S_{real} &= We^{-R2_w^*t} \cos \psi t + Fe^{-R2_f^*t} \sum_{n=1}^6 c_n \cos ((\psi + w_n)t + \phi) \\ S_{imaginary} &= We^{-R2_w^*t} \sin \psi t + Fe^{-R2_f^*t} \sum_{n=1}^6 c_n \sin ((\psi + w_n)t + \phi). \end{aligned} \quad (6.8)$$

For both the magnitude and complex fitting either a common T2* for both fat and water can be used or separate T2*s (fitting for them separately). In the literature common and separate T2*s are used with both complex and magnitude fitting and therefore four different fitting types were tested (with the brackets indicating the short notation used to refer to the fitting types in the results section):

- Complex with a common T2* for fat and water (C1)
- Complex with separate T2*s for fat and water (C2)
- Magnitude with a common T2* for fat and water (M1)
- Magnitude with separate T2*s for fat and water (M2)

The factors in Equations 6.6 and 6.8 that were varied throughout the simulations are listed below, although the details of values used are in the individual simulation sections:

- Fat fraction
- T2* of water
- T2* of fat
- Field inhomogeneities (of particular importance in the colon)

6. Fat Quantification using Multi-Echo MRI in Non Standard Situations

- Echo times used

For each simulation the fat fraction was varied between 0 and 100% and Rician noise was added at 2% of M_0 which was estimated from experimental data.

The issue of which echo times to use has largely been resolved by Reeder *et al* (38) as detailed in Section 6.2. From the generalised results,

$$\begin{aligned}m &= \pi/2 + \pi k \\TE_1 &= m - 2\pi/3 \\TE_3 &= m + 2\pi/3\end{aligned}\tag{6.9}$$

the echo times to use at 3T and 7T were calculated, here 2π refers to the in-phase time of fat and water (2.3 ms at 3T and 0.99 ms at 7T). Three different sets of echo times, each of which followed the IDEAL recommendations were used (these will be referred to as IDEAL1, IDEAL2 and IDEAL3) along with the traditional in-phase opposed-phase (IPOP) echo times. The echo times were all chosen to be achievable on the scanners and able to be acquired in a single breath hold.

3T Echo Times: At 3T the in phase time, or time for a full phase evolution, is 2.3 ms. Using the general formula from Equation 6.9, if $k=0$, $m = 2.3/4 = 0.575$ ms. Here m is too short to be achievable on the 3T Ingenia, so one full phase is added to the middle echo giving $m = 2.875$ ms. This results in $TE_1 = 2.875 - 2.3/3 = 2.108$ ms. Using these ΔTE would be too short to be achievable. To overcome this a 2π phase shift is added to the second echo resulting in:

IDEAL1: $TE_1 = 2.108$ ms and $\Delta TE = 3.067$ ms.

Using a similar method for $k = 1$ gives:

IDEAL2: $TE_1 = 3.258$ ms and $\Delta TE = 3.067$ ms.

Alternatively, the first and third echoes can be set as $2/3$ of a phase either side of m which, when using $k = 0$ results in:

IDEAL3: $TE_1 = 1.34$ ms and $\Delta TE = 1.53$ ms

6. Fat Quantification using Multi-Echo MRI in Non Standard Situations

The traditional in-phase opposed-phase method uses echo times of:

IPOP: $TE_1 = 1.15$ ms and $\Delta TE = 1.15$ ms.

7T Echo Times: Using the same method the echo times at 7T can be calculated as:

IDEAL1: $TE_1 = 1.89$ ms and $\Delta TE = 1.32$ ms for $k = 0$

IDEAL2: $TE_1 = 1.40$ ms and $\Delta TE = 1.32$ ms for $k = 1$

IDEAL3: $TE_1 = 1.56$ ms and $\Delta TE = 1.645$ ms using $k = 0$ and the first and third echo $2/3$ out of phase with the middle echo.

IPOP: $TE_1 = 1.48$ ms and $\Delta TE = 2.97$ ms.

Whilst these echo times are achievable they do not measure the signal during each phase evolution.

6.3.2 General In Vivo Methods

Several fitting options were available for the *in vivo* data depending on the anatomical area and field strength. The exact details of each acquisition are given in the sections below with a summary of the fitting methods used for each area/field strength given in Table 6.1. Unfortunately in the case of the 7T acquisitions complex fitting was unable to be performed. This is due to the fact that the scan control parameter "Echo Phase Determination" was not switched off. The result of this is that the phase evolution overtime is not preserved by the scanner and thus cannot be used for quantification. Therefore magnitude fitting was only used in these cases, this also ruled out the use of complex fitting using the ISMRM toolbox. Magnitude only data was used in the toolbox at 7T however the creators do recommend the use of complex data as the toolbox is optimised for complex data.

6. Fat Quantification using Multi-Echo MRI in Non Standard Situations

Anatomical area	Field Strength	mDixon Quant / mDixon 3 point	ISMRM toolbox	Complex fitting	Magnitude fitting
Phantom	3T	✓	✓	✓	✓
Liver	3T	✓	✓	✓	✓
Colon	3T	✓	✓	✓	✓
Liver	7T	✓	✓*	✗	✓

Table 6.1: Table detailing fitting types that were used for the different *in vivo* cases that were explored in this chapter. * Note that for the 7T data only the magnitude data was used in the ISMRM toolbox.

6.3.3 Simulations for the Liver a 3T

In the liver at 3T the variables in the fat quantification are fairly well defined. The $T2^*$ of fat and water have been measured separately as water = 16.0 ± 4.1 ms and fat = 7.4 ± 2.1 ms for patients with liver cirrhosis and water = 21.8 ± 11.7 ms and fat = 4.6 ± 1.8 ms in healthy volunteers (46). Based on these values two simulations were run for the liver at 3T. One in which the $T2^*$ s of fat and water were very similar (around the middle of the fat and water range *in vivo*) and one in which they had a large difference (at the extremes of the range measured *in vivo*). The field inhomogeneities in the liver at 3T are expected to be small and therefore were varied between -80Hz and +80Hz (estimated from Hernando et al (33)). The parameters used in the simulations are given in Table 6.2.

Simulation parameters	3T liver	
Fat fraction	0, 0.03, 0.05, 0.1, 0.2, 0.4, 0.6, 0.8, 1.0	
$T2^*$ water (s^{-1})	10	2
$T2^*$ of fat (s^{-1})	9.5	4
Noise (percentage of M_0)	2	
B_0 field inhomogeneity (Hz)	- 80, 0, 80	

Table 6.2: Table detailing the parameters of the Monte Carlo simulations to determine the accuracy of fat quantification in the liver at 3T

6.3.4 Fat Phantom Measurements at 3T

A fat phantom was built to test the in-house fat quantification methods used in the simulation section and to also compare with the ISMRM toolbox and the Philips mDixon Quant package. The phantom consisted of a spherical plastic ball filled with agar. Four table tennis balls each filled with sunflower oil, water and two emulsifiers (Span 80 and Tween 60) were set in the centre of the ball (a schematic of the phantom is shown in Figure 6.6). The contents of each ball are listed in Table 6.3.

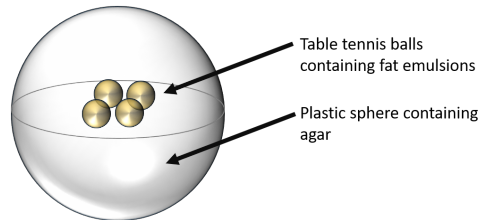


Figure 6.6: Schematic diagram of the fat phantom consisting of a spherical plastic ball filled with agar. Four table tennis balls containing fat emulsions were set within the agar. Two emulsifiers (Span 80 and Tween 60) were used to bind the fat and water together to make a stable emulsion.

Fat Percentage	Fat (g)	Water (g)	Span (g)	Tween (g)
5 %	5	95	0.38	0.16
10 %	10	90	0.75	0.25
20 %	20	80	1.50	0.50
40 %	40	60	3.00	1.00

Table 6.3: Table detailing the contents of the four table tennis balls within the fat phantom. Two emulsifiers (Span 80 and Tween 60) were used to bind the fat and water together to make a stable emulsion.

The phantom was scanned using mDixon Quant and 6 echo Dixon, the scan parameters are shown in Table 6.4. The four fitting methods detailed in Section 6.3.4 were used to fit for the fat fraction on a voxel by voxel basis in the

6. Fat Quantification using Multi-Echo MRI in Non Standard Situations

phantom to produce four different fat maps. The ISMRM toolbox was also used to produce fat maps from the 6 echo dixon data. An ROI was drawn in each of the table tennis balls on the fat maps produced by the in-house fitting and mDixon Quant.

Scan parameters	mDixon Quant	6 point Dixon
First TE (ms)	0.95	1.34
Δ TE (ms)	0.70	1.53
Voxel size (mm ²)	2.2 x 2.5	2.0 x 1.6
Number of slices	77	31
Slice orientation	coronal	axial
Reconstruction in-plane (mm ²)	2.0 x 2.0	0.98 x 0.80
Number of echoes	6	6
Flip angle (degrees)	3	5
Motion	Breath held	Breath held

Table 6.4: Table detailing the parameters of phantom scans at 3T.

6.3.5 Liver Fat Measurements at 3T

In vivo liver fat measurements were tested on four healthy volunteers at 3T. An mDixon Quant scan was run along with a Multi-echo Dixon with 6 echoes. The details of the acquisitions are given in Table 6.5.

Both magnitude and complex fitting were applied to the 6 point Dixon data, firstly with a common T2* value for fat and water. Following this any voxel containing more than 5% fat from the single T2* fit then underwent a second fit with separate T2*s for fat and water. Three ROIs were then drawn in the same location on each map and compared with the same ROIs drawn on the maps produced by mDixon Quant and the ISMRM toolbox. Similar ROIs were used for all four healthy volunteers.

6. Fat Quantification using Multi-Echo MRI in Non Standard Situations

Scan parameters	mDixon Quant	6 point Dixon
First TE (ms)	0.95	2.10
Δ TE (ms)	0.70	0.7
Voxel size (mm ²)	2.2 x 2.5 x 6.0	1.7 x 2.0 x 4.0
Number of slices	77	10
Slice orientation	axial	axial
Reconstruction in-plane (mm ²)	2.0 x 2.0	0.9 x 0.9
Number of echoes	6	6
Flip angle (degrees)	3	15
Motion	Breath held	Breath held

Table 6.5: Table detailing the parameters of *in vivo* liver scans at 3T.

6.3.6 Simulations for the Liver at 7T

In the liver at 7T the variables in the fat quantification are relatively unknown due to the fact that *in vivo* human scanning at 7T has only recently been achieved in the abdomen. At 7T separate T2* values of fat and water in the liver have not to our knowledge been measured and so estimates of the range were taken from Doran *et al* who produced the first *in vivo* liver T1 and T2* maps at 7T. They showed that the T2* of the liver at 7T was 7.9 ± 0.5 ms or 8.6 ± 0.9 ms, depending on the acquisition method (47). From these measurements and by comparing them with the 3T values, estimates of the fat and water T2* in the liver were made. The field inhomogeneities at 7T are expected to be larger than those at 3T and so were estimated at between -160 Hz and +160 Hz. At 7T the separation of the fat and water resonant frequencies increases, causing the fat and water to come into and out of phase at a faster rate than at 3T. The consequence of this is that the echo times required are shorter than those at 3T, however acoustic noise limitations on the 7T mean that the echo spacing is limited. The parameters used in the simulations are given in Table 6.6.

6. Fat Quantification using Multi-Echo MRI in Non Standard Situations

Simulation parameters	7T liver
Fat fraction	0, 0.03, 0.05, 0.1, 0.2, 0.4, 0.6, 0.8, 1.0
T2* water (s ⁻¹)	85
T2* fat (s ⁻¹)	250
Noise (percentage of M ₀)	2
B0 field inhomogeneity (Hz)	0, 160

Table 6.6: Table detailing the parameters of the Monte Carlo simulations to determine the accuracy of fat quantification in the liver at 7T.

6.3.7 Liver Fat Measurements at 7T

The first *in vivo* fat quantification measurements of the liver at 7T were performed on 4 healthy human participants. The details of the scan parameters are given in Table 6.7. The mDixon Quant package is unavailable on a Philips 7T system as they do not produce commercial coils that enable body scanning. Therefore the three point mDixon fat quantification was used with a body coil from MR Coils (MR Coils, Zaltbommel, Netherlands) that is compatible with the 7T. The same four participants were also scanned at 3T to provide a comparison of the fat quantification across the two field strengths. The scanning parameters used at 3T were the same as those used in section ??.

Similarly to the 3T data the 7T data underwent a two stage fitting process to the magnitude data. Initially the data was fitted using a common T2* for fat and water. Then any voxel containing a fat fraction higher than 5% was refitted using a separate T2* values for fat and water. A fit to the complex data was unable to be performed as the scan control parameter, "Echo Phase Determination", was not switched off prior to scanning. The result of this is that the phase evolution over echo times is not preserved and thus cannot be used. The magnitude data from the 6 echo dixon scan was used to produce fat maps from the ISMRM toolbox as well.

6. Fat Quantification using Multi-Echo MRI in Non Standard Situations

Scan parameters	mDixon	6 point Dixon
First TE (ms)	0.49	1.40
Δ TE (ms)	0.5	1.32
Voxel size (mm ²)	1.5 x 1.5	2 x 2
Slice thickness (mm)	5	5
Number of slices	8	4
Slice orientation	axial	axial
Reconstruction in-plane (mm ²)	0.93 x 0.93	0.93 x 0.93
Number of echoes	3	6
Flip angle (degrees)	15	15
Motion	Breath held	Breath held

Table 6.7: Table detailing the parameters of *in vivo* liver scans at 7T.

6.3.8 Simulations for the Colon at 3T

In the colon the T2* values for fat and water are likely to be shorter due to the surrounding micro-bubbles of gas that are produced by bacteria in the colon. Therefore the T2* of fat and water were set as the shorter values used in the liver simulations at 3T and a much larger field inhomogeneity was used (estimated from Hernando et al (33)). The details of the parameters used in the simulations are given in Table 6.8.

Simulation parameters	3T colon
Fat fraction	0, 0.03, 0.05, 0.1, 0.2, 0.4, 0.6, 0.8, 1.0
T2* water (s ⁻¹)	45
T2* fat (s ⁻¹)	230
Noise (percentage of M ₀)	2
B0 field inhomogeneity (Hz)	500

Table 6.8: Table detailing the parameters of the Monte Carlo simulations to determine the accuracy of fat quantification in the colon at 3T.

6. Fat Quantification using Multi-Echo MRI in Non Standard Situations

Scan parameters	6 point Dixon	mDixon
First TE (ms)	1.34	1.06
Δ TE (ms)	1.53	1.09
Voxel size (mm ²)	2.0 x 2.0 x 4.00	2.0 x 2.0 x 4.00
Slice thickness (mm)	5	5
Number of slices	20	20
Slice orientation	sagittal	sagittal
Reconstruction in-plane (mm ²)	0.99 x 0.99	0.99 x 0.99
Number of echoes	6	2
Flip angle (degrees)	5	5
Motion	Breath held	Breath held

Table 6.9: Table detailing the parameters of the fat quantification scans taken as part of the cystic fibrosis study.

6.3.9 Colonic Fat Measurements at 3T

Multi-echo Dixon data was collected as part of a wider cystic fibrosis study. At the time of writing 5 participants with cystic fibrosis had been recruited and scanned. The volunteers underwent a full day study in which they were scanned at baseline and after the consumption of a fatty meal. As the Dixon scans were collected at baseline and the main outcomes of this section were only related to a very small part of the whole study, only the relevant scan details are given here. The scan parameters are given in Table 6.9. The colonic fat data was fitted using a in-house magnitude and complex fitting, using the ISMRM toolbox and using Philip's mDixon method.

6.4 Results

In this section the results from the Monte Carlo simulations and preliminary results of *in vivo* data are given. The results for the simulations are shown in 2D plots which show the simulated fat fraction along the x axis and the fitting method along the y axis. The color indicates either the percentage difference in the simulated and fitted fat fraction or the standard deviation in the fitted fat

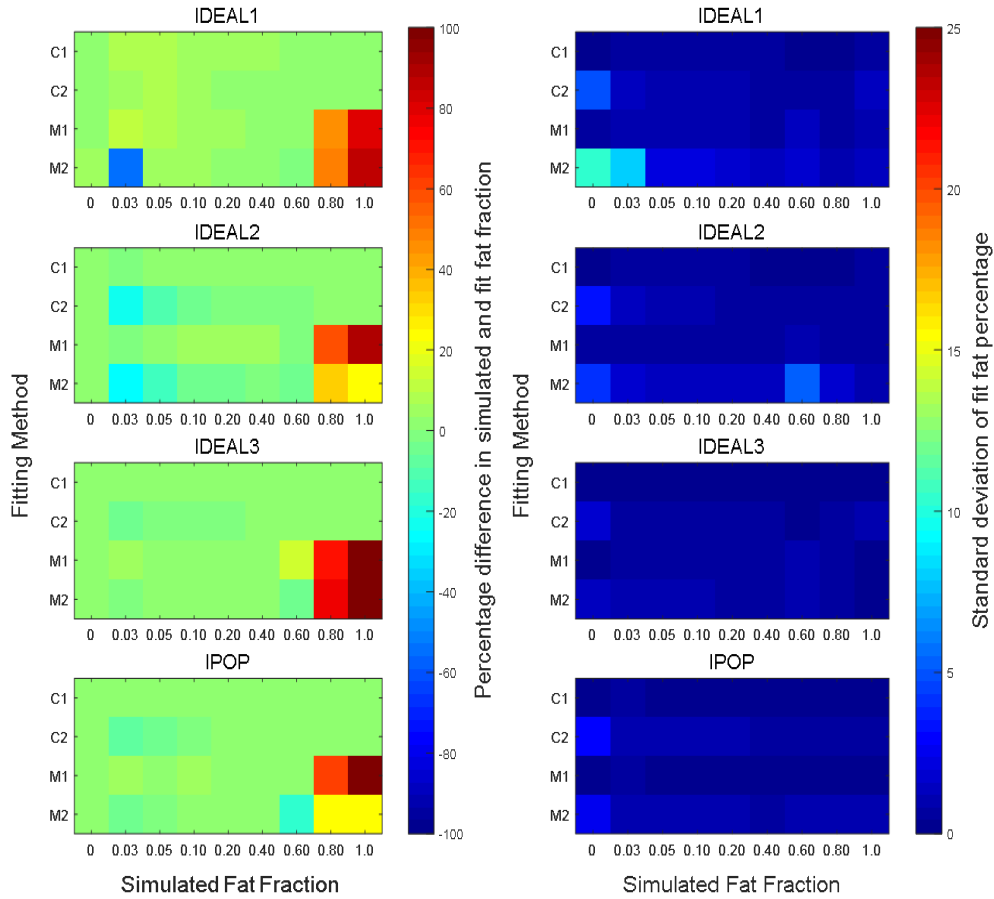
percentage depending on the chart. The results are given for each of the four echo times tested.

6.4.1 Simulations in the Liver a 3T

Figure 6.7 shows the results when two similar $T2^*$ values for fat and water (105 s^{-1} and 100 s^{-1}) are simulated and no field inhomogeneities included.

All sets of echo times showed similar results (differences mainly $<2\%$) with complex fitting consistently performing better than the magnitude fitting. It was found that at low fat fractions ($<5\%$) using a common $T2^*$ was more accurate than using separate $T2^*$ s however the difference in the errors between using a common and separate $T2^*$ was small. At high fat fractions it was expected that magnitude fitting would misregister water and fat (swap water and fat signals) which did happen in some cases however at fat fractions of 80% it was common for the fitting algorithm to find an alternative fat fraction that better matched the data rather than misregister the water and fat fraction. It was determined by further simulations that this was due to the fitting algorithm finding a local minima which can be avoided by using different starting parameters for the fitting algorithm. However it may not be known in advance what starting parameters would work best and so a particle swarm type approach to the fitting would be needed if using magnitude fitting with fat fractions about 60% (48).

6. Fat Quantification using Multi-Echo MRI in Non Standard Situations



(a) Percentage difference in simulated and fitted fat fraction. (b) Standard deviation of fitted fat fraction.

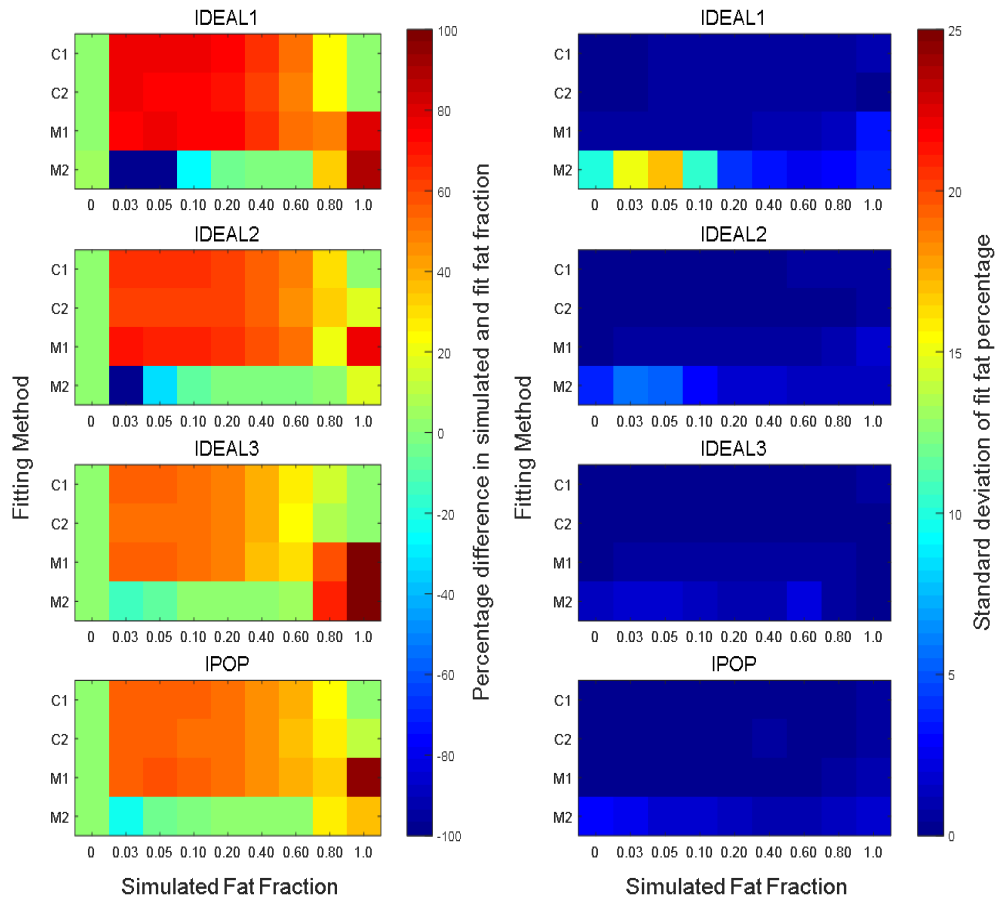
Figure 6.7: Monte Carlo simulation results for the liver at 3T when fat and water have similar $T2^*$ values (105 s^{-1} and 100 s^{-1}) and no field inhomogeneities are included. a) Percentage difference between the simulated and fitted fat fraction. b) Standard deviation of the fitted fat percentage. Magnitude fitting is not as accurate as complex fitting. At low fat fractions ($<5\%$ common $T2^*$ fitting is more accurate and precise than separate $T2^*$ fitting).

6. Fat Quantification using Multi-Echo MRI in Non Standard Situations

The next simulation for the liver at 3T used the extreme values of $T2^*$ of fat and water that were found *in vivo* (45 s^{-1} and 230 s^{-1}). Figure 6.8 shows the results of these simulations. It was found that the fitting was less accurate than in the previous simulation. The only method which produced results with a high accuracy ($<5\%$ error on fat fractions of more than 10%) and precision were those performed using the magnitude data, using separate $T2^*$ values with the IDEAL3 or IPOP echo times. The other methods introduced an error on the fitted $T2^*$ s of fat and the fat fraction. Changing the starting parameters of the fitting algorithm to be closer to the simulated value improved the accuracy of the fitting for all echo times and fitting methods (the original starting parameters were 50% fat, $T2^*$ fat and water = 100 ms with no field inhomogeneity). This suggests that the fitting algorithm is finding a local minima rather than the global minima which could be overcome by using a particle swarm method. Alternatively altering the starting parameters to be approximate for anatomical location could provide a computationally faster solution than using a particle swarm method.

The final scenario considered was in the case of field offsets (Figure 6.9). Again a large difference in the $T2^*$ of fat and water was simulated. The error on the fitted fat fraction was dependent on the fitting method used as well as the echo times. All echo times performed poorly when complex fitting was used. IDEAL3 and IPOP echo times performed with a high accuracy ($<10\%$ error when the fat fraction is higher than 3%) when magnitude fitting was used with separate $T2^*$ s except at high fat fractions ($>60\%$).

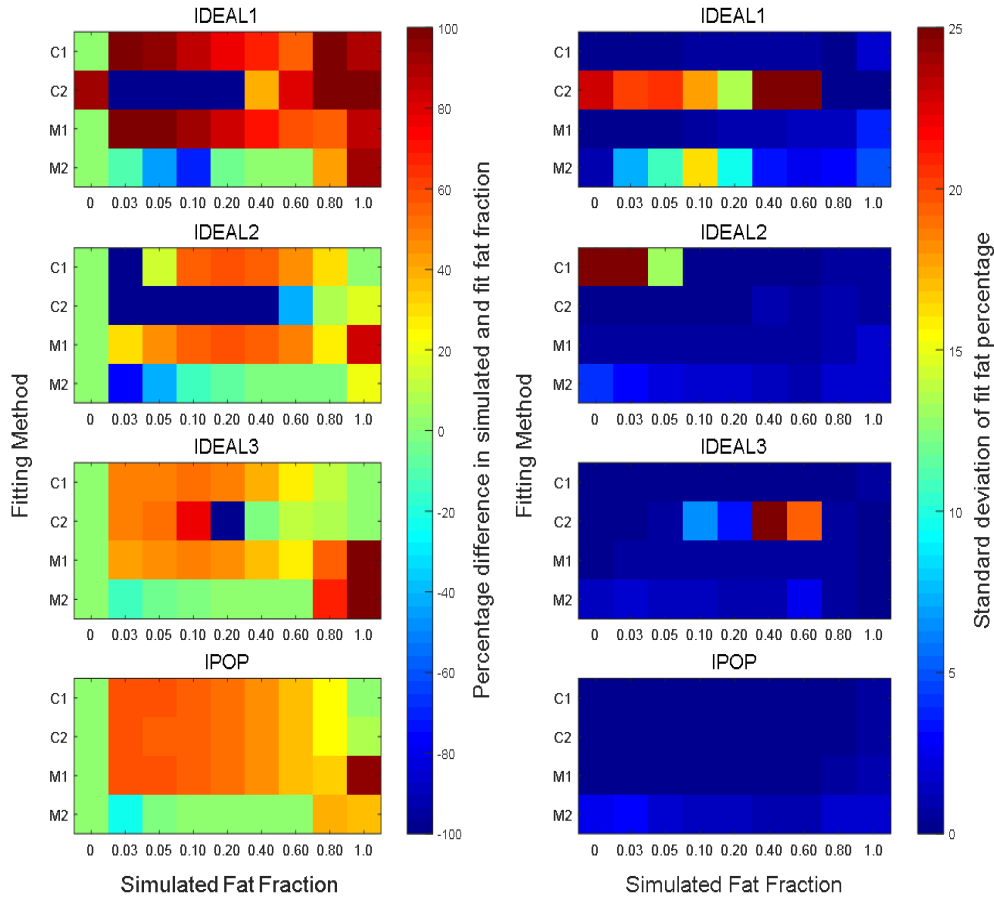
6. Fat Quantification using Multi-Echo MRI in Non Standard Situations



(a) Percentage difference in simulated and fitted fat fraction. (b) Standard deviation of simulated and fitted fat fraction.

Figure 6.8: Monte Carlo simulation results for the liver at 3T when fat and water have different $T2^*$ values and no field inhomogeneities are included. a) Percentage difference between the simulated and fitted fat fraction. b) Standard deviation of the fitted fat percentage.

6. Fat Quantification using Multi-Echo MRI in Non Standard Situations



(a) Percentage difference in simulated and fitted fat fraction. (b) Standard deviation of fitted fat fraction.

Figure 6.9: Monte Carlo simulation results for the liver at 3T when fat and water have different T2* values and large field inhomogeneities are included. a) Percentage difference between the simulated and fitted fat fraction. b) Standard deviation of the fitted fat percentage.

6.4.2 Fat Phantom Measurements at 3T

Fat quantification was performed using a phantom containing emulsions with four different fat percentages. In-house fitting, and fitting using the ISMRM toolbox were performed on 6 echo Dixon data. A fat map was generated using the mDixon Quant package for comparison. A single ROI was drawn in each table tennis ball encompassing as much of the content as possible. The first echo time image taken using the 6-point Dixon acquisition is shown in Figure 6.10 with the fat fraction measured for all four balls given in Table 6.10.

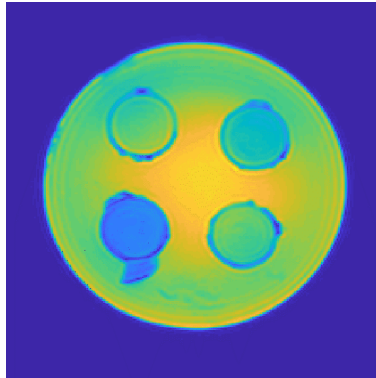


Figure 6.10: Magnitude image of the phantom with a cross section slice covering all table tennis balls.

In-house fitting assuming a common $T2^*$ produced accurate results at low fat fractions (5%). At high fat fractions ($>20\%$) assuming separate $T2^*$ s produced accurate results. Neither methods produced accurate results at 20% fat, this is likely due the algorithm finding a local minima (however further experiments were not performed to determine the source of this error). Based on these results and the simulations a two step fitting process was employed for the *in vivo* data, initially a common $R2^*$ was fit, followed by a separate $R2^*$ fit for voxels that contained fat fractions $>5\%$. The ISMRM toolbox produced accurate fat measurements at the three lower fat fractions but over estimated the fat fraction at 40%. This may be due to the fact that the toolbox is limited to using a single $T2^*$ in the fitting which can introduce and bias on the fitted fat fraction.

6. Fat Quantification using Multi-Echo MRI in Non Standard Situations

Fat %	In-house complex fitting 1T2*	In-house complex fitting 2T2*	In-house magnitude fitting 1T2*	In-house magnitude fitting 2T2*	mDixon Quant	ISMRM toolbox
5%	3.4±0.8	5.8±1.2	2.9±0.9	16.5±1.2	4.3±0.5	5.8±0.1
10%	4.7±0.5	6.4±0.8	7.4±0.7	19.2±6.2	11.1±0.8	9.1±1.3
20%	11.2±0.7	15.6±0.8	10.9±0.6	26.6±3.2	20.3±2.2	20.3±0.1
40%	42.0±2.0	42.3±0.9	28.1±1.2	46.6±4.7	45.7±7.5	50.1±0.2

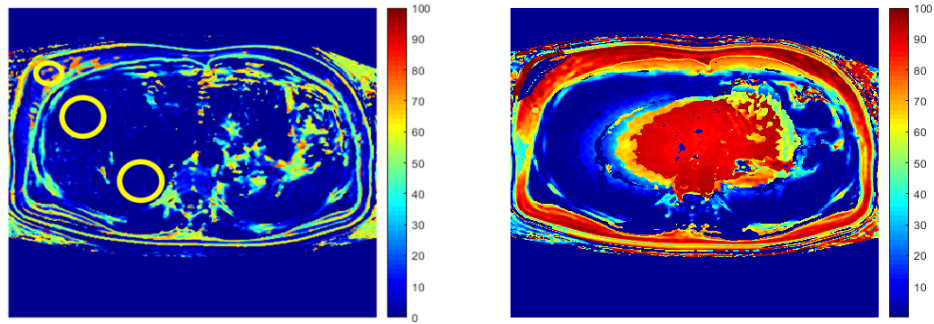
Table 6.10: Table detailing the mean and standard deviation fat measurements from the fat phantom. All measurement are given as the mean and standard deviation fat percentage.

The T2*s that were fitted for the fat and water were variable with fat percentage and had an average of 167 ms for water and 197 ms for fat. These results are likely to be inaccurate as the echo times are too short to measure the T2* of free water and the oil that are used in the phantom which much longer than those found *in vivo*.

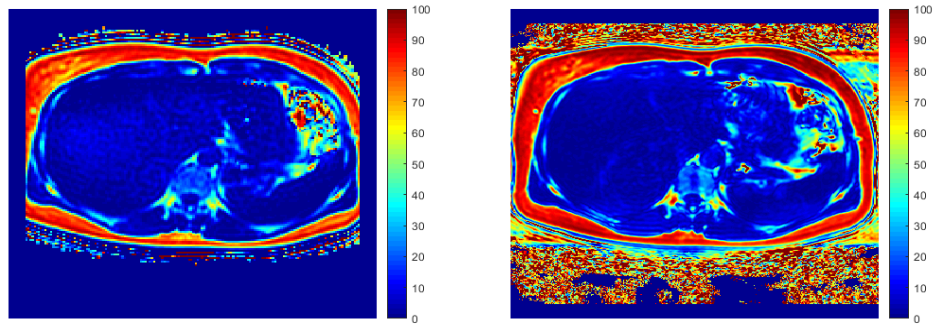
6.4.3 In Vivo Liver Fat Measurements at 3T

In vivo liver fat quantification was performed on four subjects using in-house fitting, Philips' mDixon Quant package and the ISMRM toolbox. Three ROIs (one in the subcutaneous (SC) fat and two in the liver) were used to measure the fat fraction from the three different methods. The ROIs for a participant are shown in Figure 6.11 a) with the fat fraction measured for all four participants in each ROI given in Table 6.11. Similar ROIs were used for all participants. It is clear from the fat fraction maps produced by in-house fitting to the complex data that the fitting method used for the complex data fails to provide accurate fat fractions. This is probably due to the fact that a large number of variables are fitted to few data points.

6. Fat Quantification using Multi-Echo MRI in Non Standard Situations



(a) In-house fat map created using mag- (b) In-house fat map created using com-
pitude data plex data



(c) ISMRM toolbox fat map

(d) mDixon Quant fat map

Figure 6.11: a) Fat map generated using in-house fitting and magnitude data. b) Fat map generated using in-house fitting and complex data. c) Fat map generated using Philip's mDixon Quant package. d) Fat map generated using the ISMRM toolbox which utilises a combination of magnitude and complex data. ROIs are named 1,2 and 3 with ROI 1 in the subcutaneous fat, ROI 2 on the left of the image in the liver and ROI 3 at the bottom of the image in the liver.

6. Fat Quantification using Multi-Echo MRI in Non Standard Situations

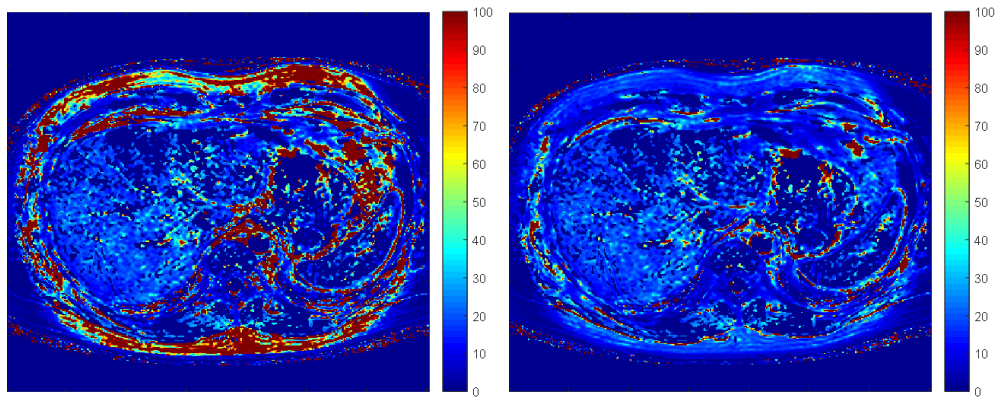
The same ROIs were used to compare the $T2^*$ measured by the mDixon Quant sequence and the in-house fitting when a common $T2^*$ was used and when separate $T2^*$ s were used for magnitude data, the $T2^*$ maps are shown in Figure 6.12 with the fitted values of $T2^*$ in Table 6.12. The complex data did not produce accurate fat maps when using in-house fitting and so the $T2^*$ maps are not shown.

6. Fat Quantification using Multi-Echo MRI in Non Standard Situations

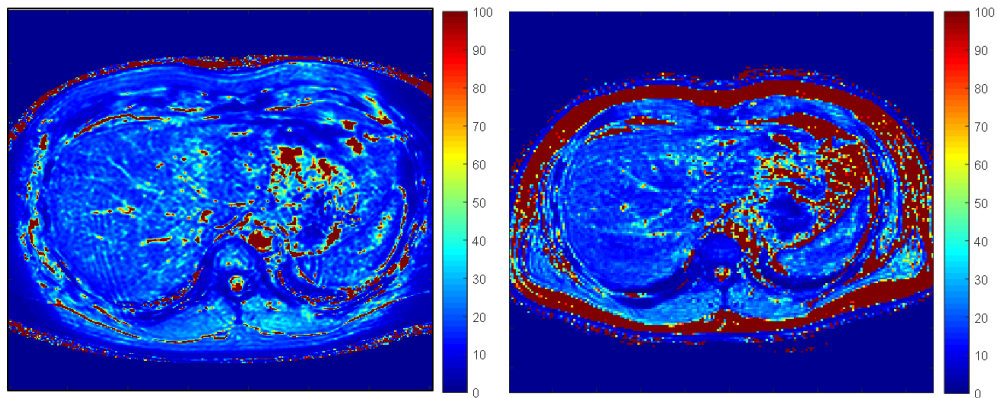
Participant	ROI 1 - Subcutaneous fat			
	In-house fitting magnitude data	In-house fitting complex data	mDixon Quant	ISMIRM toolbox
P1	22.0±29.1%	48.8±30.8%	80.4±6.8%	85.3±5.5%
P2	86.5±8.7%	14.2±2.4%	89.8±2.8%	94.3±3.6%
P3	35.9±38.6%	27.7±19.9%	92.0±2.3%	100±1.5%
P4	85.6±6.3%	12.8±5.8%	85.0±3.9%	88.4±4.4%
	ROI 2 - liver fat (anterior)			
	In-house fitting magnitude data	In-house fitting complex data	mDixon Quant	ISMIRM toolbox
P1	2.0±3.2%	25.7±24.2 %	3.9±2.0%	2.5±1.3%
P2	1.2±1.0%	40.0±15.3%	2.2±1.8%	2.8±1.5%
P3	5.6±8.7%	81.1±10.1%	8.4±3.5%	6.9±2.0%
P4	3.1±1.3%	49.7±1.8 %	1.6±1.3%	3.5±1.1%
	ROI 3 - liver fat (posterior)			
	In-house fitting magnitude data	In-house fitting complex data	mDixon Quant	ISMIRM toolbox
P1	1.0±1.3%	5.0±4.9 %	5.2±3.1%	4.0±1.0%
P2	0.3±0.5%	33.2±20.0%	1.8±1.9%	2.6±1.5%
P3	4.6±0.4%	46.1±34.1%	8.3±4.9%	5.9±2.2%
P4	1.6±0.9%	30.4±16.7%	1.0±1.3 %	1.7±0.9%

Table 6.11: Table detailing the fitted fat fraction and standard deviation from four participants at 3T in three different ROIs.

6. Fat Quantification using Multi-Echo MRI in Non Standard Situations



(a) 3T - In-house separate T2* fitting - T2* of water map (b) 3T - In-house separate T2* fitting - T2* of fat map



(c) 3T - In-house common T2* fitting - T2* map (d) 3T - mDixon Quant (assumed single T2*) - T2* map

Figure 6.12: T2* map for water (a) and fat (b) from in-house fitting. T2* map using a common T2* (c) using in-house fitting. T2* map from mDixon Quant (d) (All performed at 3T).

6. Fat Quantification using Multi-Echo MRI in Non Standard Situations

ROI	In-house fitting single T2* (ms)	In-house fitting dual T2* - water (ms)	In-house fitting dual T2* - fat (ms)	mDixon Quant (ms)
ROI 1	17±4	67±11	18±4	100±11
ROI 2	15±4	27±9	32±9	17±8
ROI 3	19±4	20±7	23±6	16±3

Table 6.12: Table detailing the parameters of the T2* measurements from an *in vivo* data set.

6.4.4 Simulations for the Liver at 7T

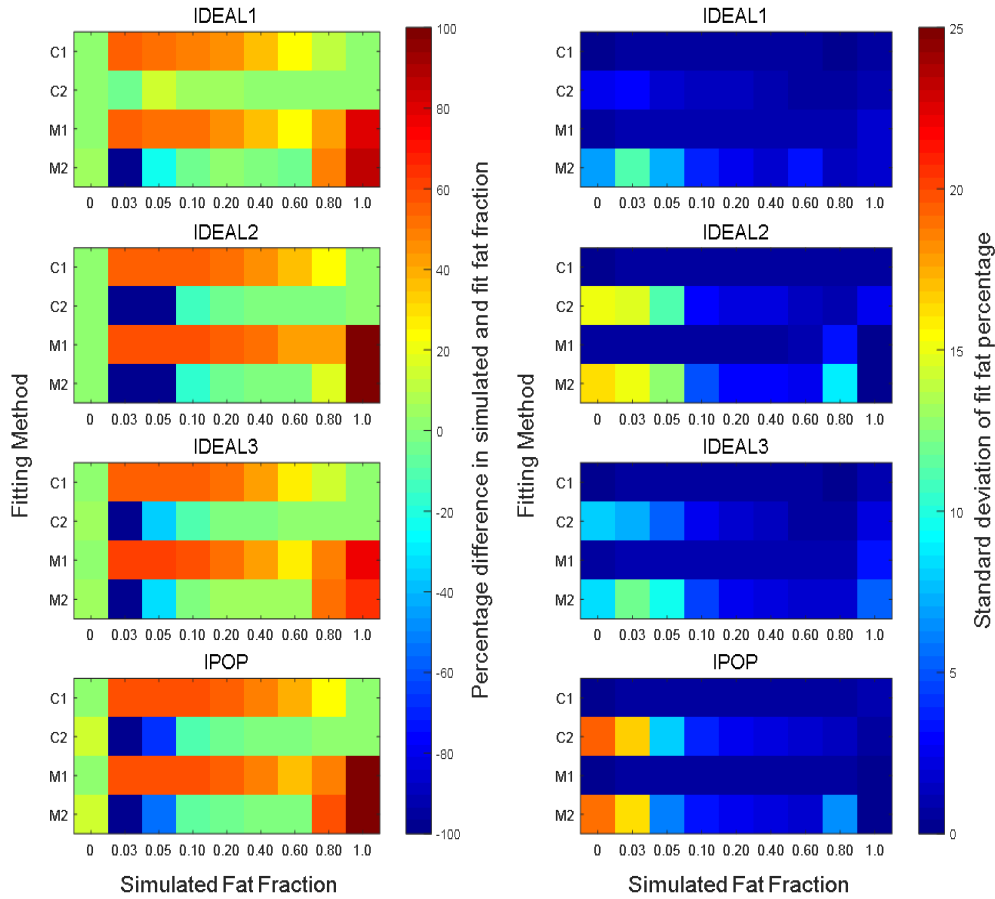
A set of simulations were run to test the accuracy and precision of fitting at 7T similar at 3T. The first set of Monte Carlo simulations used T2*s for fat and water that had a large difference, with no field inhomogeneities assumed. The results are shown in Figure 6.13.

The accuracy of the results seen at 7T were variable depending on the echo times used and the fitting method. All echo times had a similar accuracy using separate T2*s (<10% error on fat fractions >10%). With all echo times, using a combination of common T2* fitting for low fat fraction and separate T2* fitting for higher fractions can produce more accurate results than using one method alone ($\approx 50\%$ error on fat fractions <10% and $\approx 10\%$ error on fat fractions >10%).

The second set of Monte Carlo simulations ran for the liver at 7T was again using T2*s with a large difference but this time a large field inhomogeneity was included. From the results in Figure 6.14 it can be that the seen accuracy of the fit depends on the fitting method and the echo times used. For some echo times used, using a common T2* fitting followed by a separate T2* fitting for those voxels with a high fat fraction could provide a higher overall accuracy.

Similarly to the 3T simulations further simulations showed that altering the starting parameters of the fit provided more accurate results for all fitting methods and echo times.

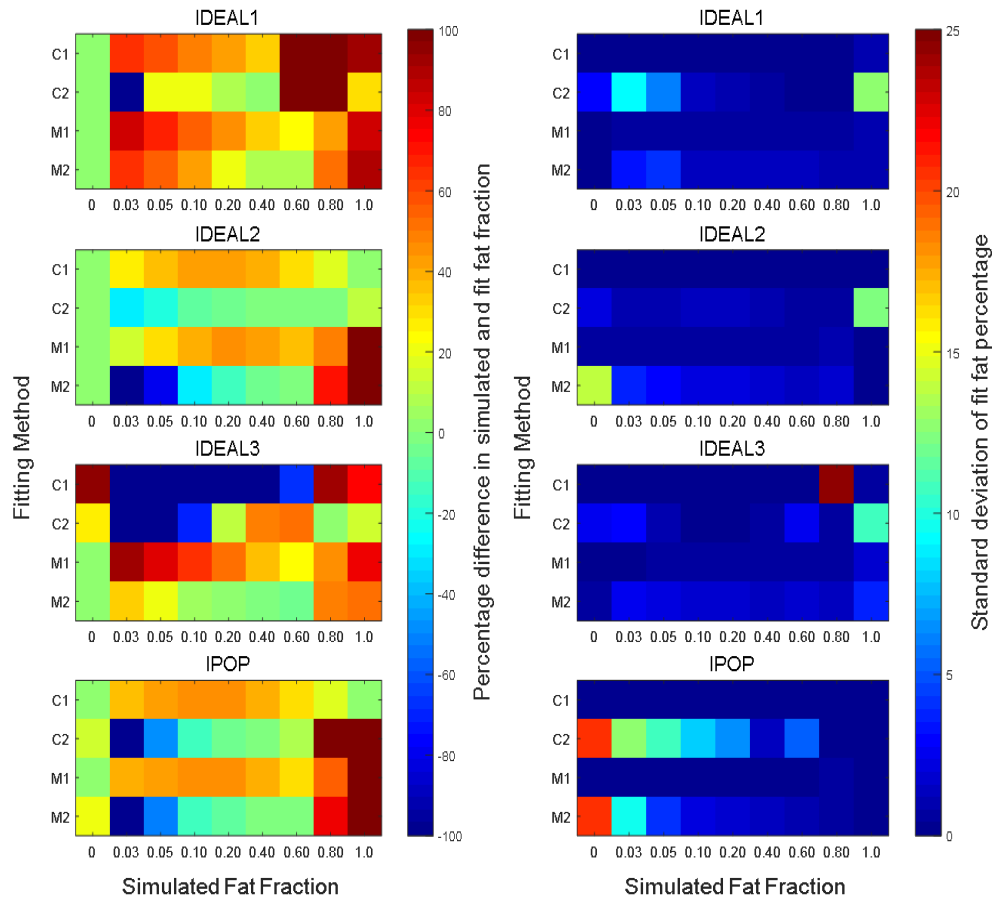
6. Fat Quantification using Multi-Echo MRI in Non Standard Situations



(a) Percentage difference in simulated and fitted fat fraction. (b) Standard deviation of fitted fat fraction.

Figure 6.13: Monte Carlo simulation results for the liver at 7T when fat and water have different $T2^*$ values and no field inhomogeneities are included. a) Difference between the simulated and fitted fat fraction. b) Standard deviation of the fitted fat percentage.

6. Fat Quantification using Multi-Echo MRI in Non Standard Situations



(a) Percentage difference in simulated and fitted fat fraction. (b) Standard deviation of fitted fat fraction.

Figure 6.14: Monte Carlo simulation results for the liver at 7T when fat and water have different $T2^*$ values and field inhomogeneities are included. a) Difference between the simulated and fitted fat fraction. b) Standard deviation of the fitted fat percentage.

6.4.5 In Vivo Liver Fat Measurements at 7T

Four subjects were scanned both at 3T and 7T to provide a comparison of fat quantification across the two field strengths. Figures 6.15 and 6.16 show fat maps produced from mDixon (three echos), the ISMRM toolbox and in-house fitting (6 echo) Dixon data. The 3 point mDixon does not quantify fat accurately or precisely. The ISMRM toolbox appears to overestimate the fat fraction in the liver and misregister the fat and water in the subcutaneous fat as is expected when using magnitude only data. The in-house fitting appears to give more accurate fat fractions however the maps are noisy and could benefit from smoothing. Again as expected from magnitude fitting the fat and water in the high fat areas such as the subcutaneous fat are misregistered giving a low fat fraction. The overall in-house fat maps show that volunteer 1 has a higher fat fraction in the liver than volunteer 2 which is to be expected due to the higher amount of abdominal fat seen in volunteer 1.

For both the 3T and 7T data the phase information could not be used for complex fitting due to the scan control parameter "Echo Phase Determination" not being switched off. Three ROIs were drawn on the mDixon Quant maps acquired at 3T, and the toolbox and in-house fat maps produced using magnitude data. Figure 6.17 shows an example map produced by the mDixon Quant sequence at 3T as well as the in-house fitting and toolbox fat maps, with the average fat in each ROI from each of the maps given in Table 6.13. The central slice of the image plane was planned on the same spinal disc in order to match the location of the slices across the two field strengths.

6. Fat Quantification using Multi-Echo MRI in Non Standard Situations

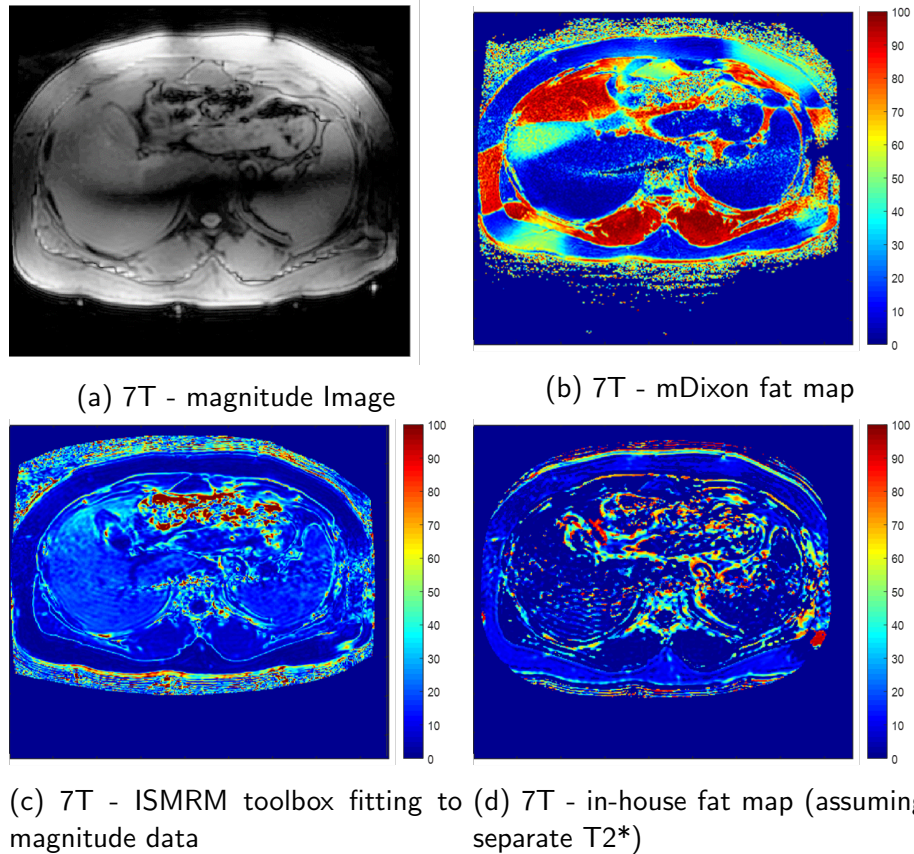


Figure 6.15: a) Magnitude image from first echo of 6 echo Dixon. b) Fat fraction map from 3 point mDixon. The fat and water have been misregistered on the scanner causing the fat and water to be switched in the calculated images. c) Fat fraction from a magnitude fit using the ISMRM toolbox. d) Fat fraction from a two stage magnitude fit. Initially a common T2* was used, followed by separate T2*s for voxels with more than 5% fat in the initial fat map. The in-house fitting swapped the fat and water signals in the subcutaneous fat resulting in a fat fraction around 10% rather than around 90% which is expected.

6. Fat Quantification using Multi-Echo MRI in Non Standard Situations

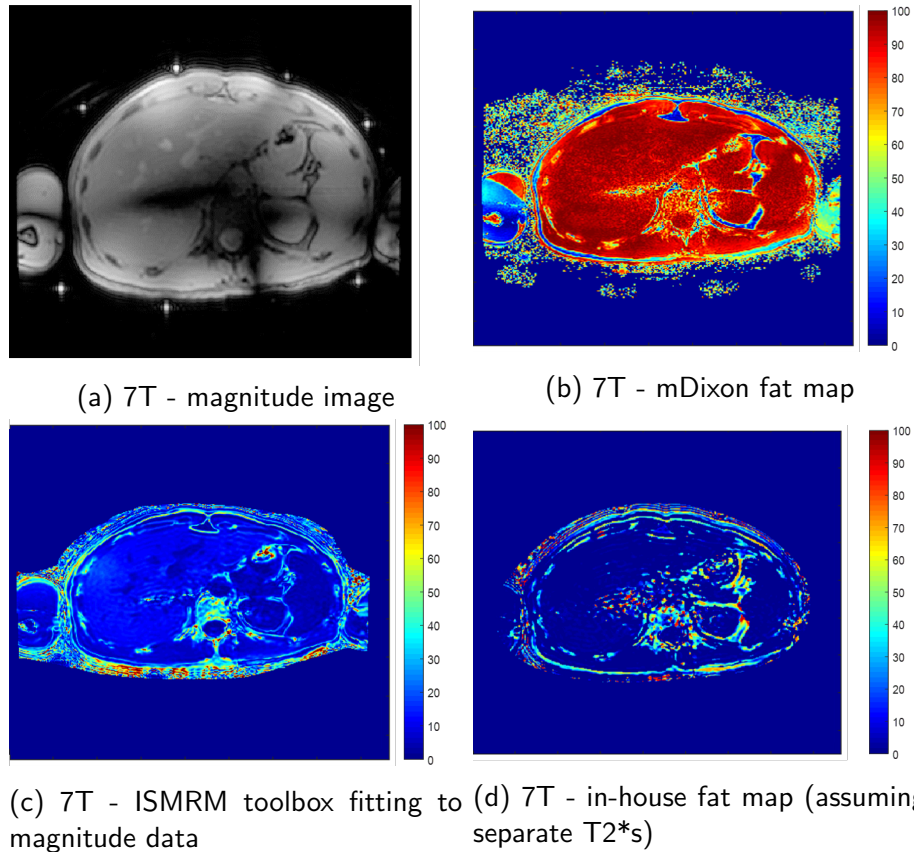


Figure 6.16: a) Magnitude image from first echo. b) 3 point mDixon fat fraction calculation. The fat and water have been misregistered on the scanner c) Fat fraction from a magnitude fit using the ISMRM toolbox. d) Fat fraction from a two stage magnitude fit. Initially a common T2* was used, followed by separate T2*s for voxels with more than 5% fat in the initial fat map. The in-house fitting swapped the fat and water signals in the subcutaneous fat resulting in a fat fraction around 10% rather than around 90% which is expected. The three echo mDixon has swapped the water and fat signals across the whole image.

6. Fat Quantification using Multi-Echo MRI in Non Standard Situations

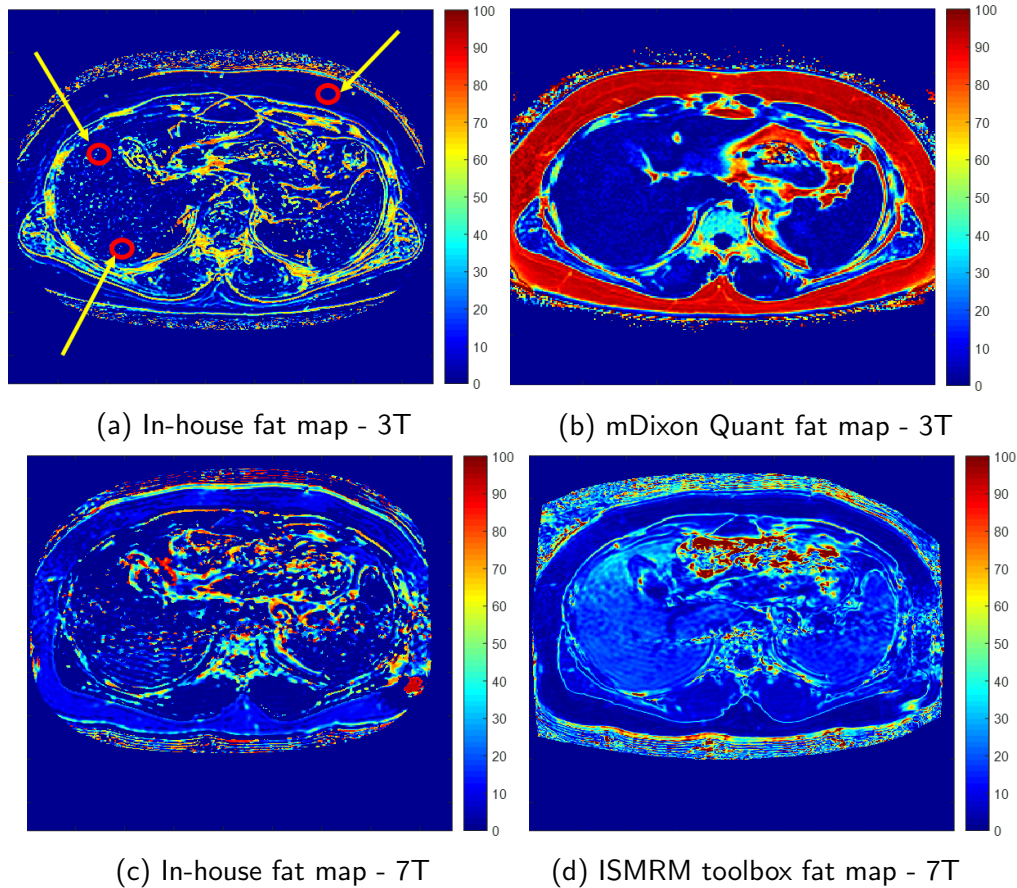


Figure 6.17: a) Fat map generated using in-house fitting at 3T. b) Fat map generated using Philip's mDixon Quant package at 3T. c) Fat map generated using in-house fitting at 7T. d) Fat map generated using the ISMRM toolbox at 7T. ROIs are named 1,2 and 3 with ROI 1 in the subcutaneous fat, ROI 2 on the left of the image in the liver and ROI 3 at the bottom of the image in the liver. The in-house fitting at 3T and 7T swapped the fat and water signals in the subcutaneous fat resulting in a fat fraction around 10% rather than around 90% which is expected.

6. Fat Quantification using Multi-Echo MRI in Non Standard Situations

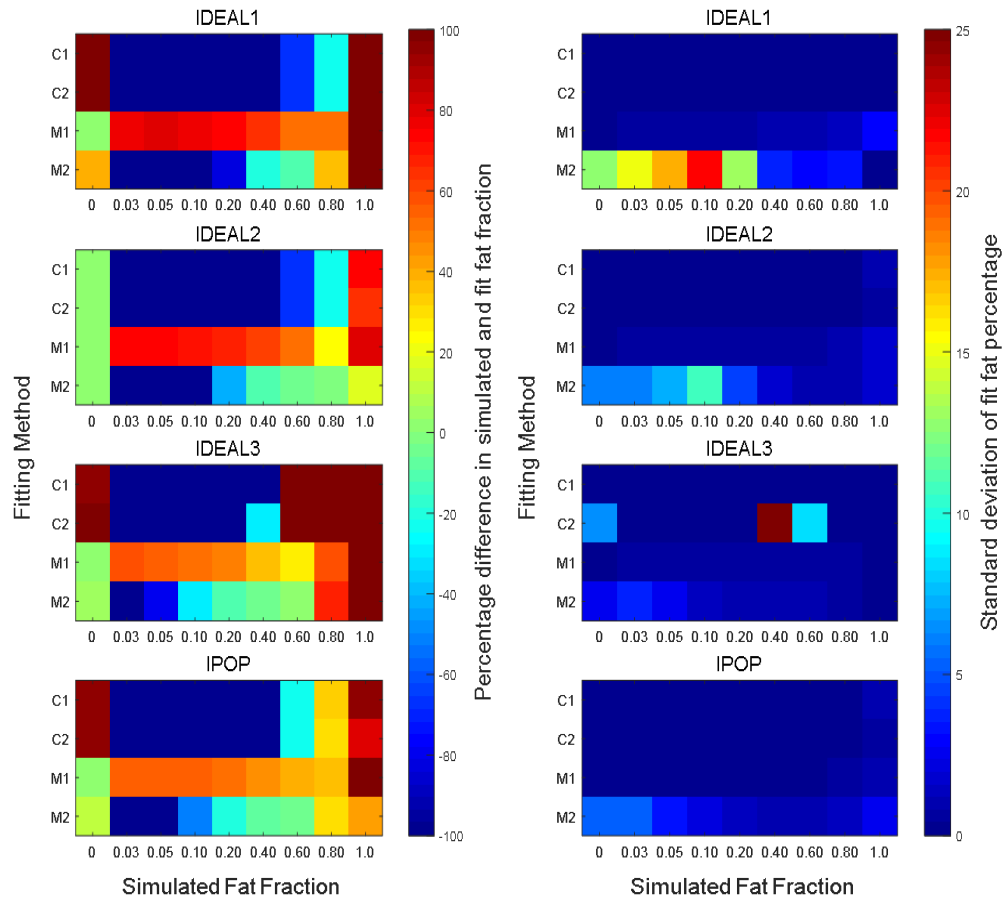
Participant	ROI 1 - SC fat			
	mDixon Quant at 3T	In-house fitting to magnitude data at 3T	In-house fitting to magnitude data at 7T	ISMRM toolbox fitting to magnitude data at 7T
P1	93.0±6.8%	0.3±5.4%	2.7±4.6%	2.9±1.7%
P2	67.7±11.6%	53.9±11.6%	17.8±5.6%	4.0±1.9%
P3	87.1±6.3%	12.1±19.8%	41.3±2.4%	6.9±5.2%
P4	84.2±6.0%	57.4±20.1%	9.2±6.7%	3.1±2.0%
	ROI 2 - liver fat			
	mDixon Quant at 3T	In-house fitting to magnitude data at 3T	In-house fitting to magnitude data at 7T	ISMRM toolbox fitting to magnitude data at 7T
P1	3.1±2.2%	6.7±4.3%	1.2±7.5%	15.9±2.1%
P2	2.0±1.8%	1.2±1.3%	1.9±2.7%	14.4±1.1%
P3	3.0±2.2%	1.3±2.2%	4.4±2.5%	13.9±2.2%
P4	2.2±1.9%	1.4±1.9%	2.4±0.1%	12.2±3.1%
	ROI 3 - liver fat			
	mDixon Quant at 3T	In-house fitting to magnitude data at 3T	In-house fitting to magnitude data at 7T	ISMRM toolbox fitting to magnitude data at 7T
P1	3.2±2.5%	6.6±4.5%	6.3±9.4%	15.6±2.1%
P2	3.0±2.0%	1.4±5.2%	2.2±4.1%	14.7±1.5%
P3	2.7±2.4%	1.5±1.1%	3.7±7.0%	14.8±1.5%
P4	1.5±2.2%	2.0±1.4%	1.2±1.3%	10.0±1.8%

Table 6.13: Table detailing the fat fractions measured using mDixon quant, in-house fitting and the ISMRM toolbox at 3T and 7T.

6.4.6 Simulations for the Colon at 3T

For the simulations of the colon at 3T, higher field inhomogeneities were simulated than those investigated in the liver. The results (Figure 6.18) show that complex fitting swaps fat and water in the presence of very large field inhomogeneities. The magnitude fitting with a single $T2^*$ overestimates the fat fraction by around 50% when IPOP and IDEAL3 echo times are used. The highest overall accuracy was given by using the magnitude data and assuming a common $T2^*$ although the accuracy is around 50%. From these results it can be seen that whilst true quantitative measurements may not be possible in the colon the presence of fat should be detectable and a semi quantitative method of measuring the fat is possible (as the fitting algorithm consistently overestimates the fat percentage except in the case of 0% fat where it accurately fitted 0% fat).

6. Fat Quantification using Multi-Echo MRI in Non Standard Situations



(a) Percentage difference in simulated and fitted fat fraction. (b) Standard deviation of fitted fat fraction.

Figure 6.18: Monte Carlo simulation results for the colon at 3T when fat and water have different $T2^*$ values and large field inhomogeneities are included. a) Difference between the simulated and fitted fat fraction. b) Standard deviation of the fitted fat percentage.

6.4.7 In Vivo Colonic Fat Measurements at 3T

As the colonic fat study is still ongoing only 5 complete data sets were available for analysis. Figure 6.19 show an example of *in vivo* colonic fat map created using in-house fitting, the ISMRM toolbox and Philip's mDixon method. The four methods gave significantly different fat fraction in the colon. This is likely due to the fact that all methods make certain assumptions which can lead to inaccuracies in the fat quantification. The mDixon only uses two echoes which is know to produce inaccurate fat estimations in the case of field inhomogeneities and T2* decay. The ISMRM toolbox smooths the field inhomogeneities which may introduce errors on the fat quantification in the colon as the field is likely to have large inhomogeneities around pockets of gas. The in-house fitting is on a voxel-by-voxel basis which lead to noisy fat maps and fits (in the case of complex fitting) 5 variables to 6 echo times which can also lead to errors in the fitted fat fraction.

ROIs were drawn in the colon on the fat map images and the median and interquartile range fat fractions were calculated, the details of which are given in Table 6.14.

Volunteer number	mDixon	ISMRM toolbox	Complex fitting	Magnitude fitting
1	41.7 (10.0)	22.8 (24.0)	0 (11.9)	0 (20.5)
2	30.0 (22.8)	20.5 (17.5)	12.2 (41.3)	5.7 (25.2)
3	11.3 (9.1)	20.8 (16.4)	12.2 (29.3)	3.9 (18.1)
4	22.3 (14.0)	26.4 (25.4)	19.9 (65.7)	6.5 (26.3)
5	24.0 (15.9)	37.8 (29.4)	41.7 (88.1)	0 (12.7)

Table 6.14: Table detailing the median and inter quartile range colonic fat measurements calculated using the mDixon methods, the ISMRM toolbox, and in-house fitting using magnitude and complex data.

6. Fat Quantification using Multi-Echo MRI in Non Standard Situations

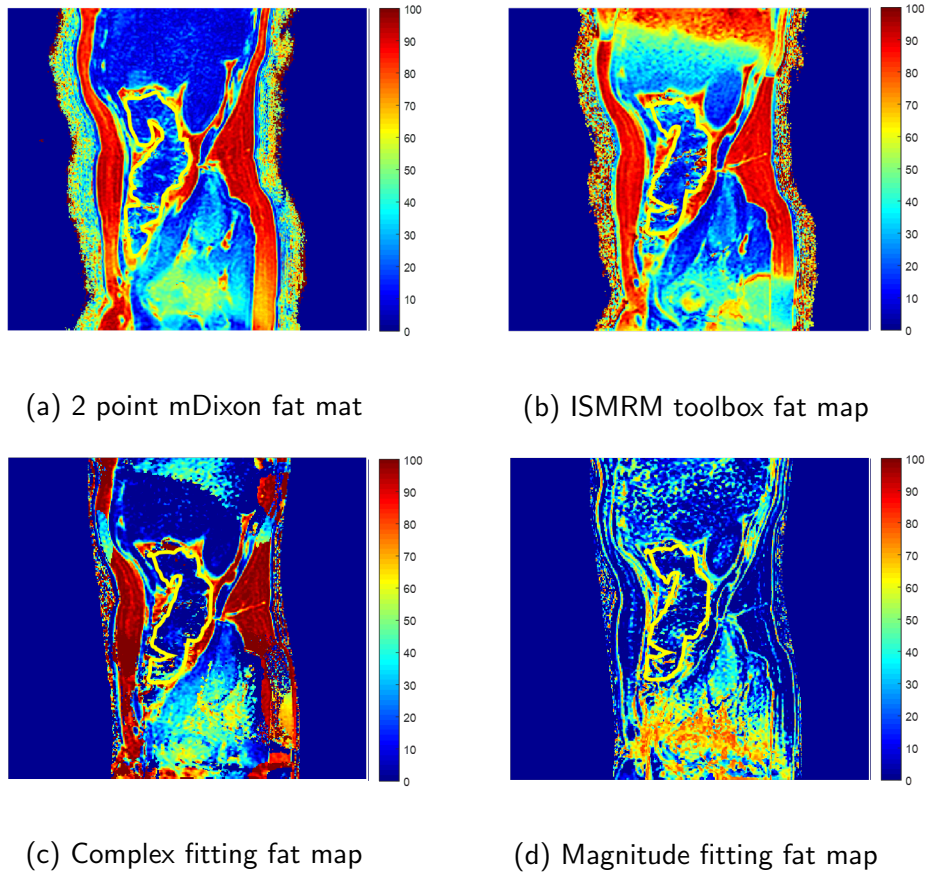


Figure 6.19: Fat quantification maps calculated using the mDixon method, the ISMRM toolbox and in-house fitting using complex and magnitude fitting. The colon ROI is outlined in yellow.

6.5 Discussion

If fat quantification were to be performed in the liver the Monte Carlo simulations show that, as expected from the literature, separate and common T2* fitting methods perform to a similar standard at fat fractions <50% using all echo times. However in the case of large differences in the T2* of fat and water fitting for separate T2*s performs with the highest accuracy at all echo times.

The measurements of fat taken using the fat phantom show that the mDixon Quant method accurately measures the fat fraction in each of the four fat percentages tested (5%, 10%, 20% and 40%) with <1% absolute difference between the actual and measured fat fraction up to 20% fat and 5% absolute difference at 40% fat. The ISMRM toolbox also gave accurate fat percentages, except in the case of the 40% fat fraction where there was a 10% difference between actual and measured fat fraction. The in-house fitting gave a similar accuracy when fitting for separate T2*s except in the case of the 20% fat where the fat fraction was underestimated in the complex fitting and magnitude fitting with a single T2* and over estimated in the magnitude fitting with separate T2*s. The reason for this discrepancy is unclear but may be due to the fitting algorithm finding a local minima. Therefore for *in vivo* cases where a fat fraction <40% is present the mDixon Quant and ISMRM toolbox method can be used as a standard measurement.

In-house fitting (using magnitude data) to *in vivo* liver data has been shown to match well (<4% different in fat percentage measured, except in the case of high fat percentage) with the results from Philips' mDixon Quant fat quantification (which may assume a common T2*). The ISMRM toolbox consistently produced fat fractions similar to those produced by the mDixon Quant sequence. The fat fraction maps produced using the complex data did not match well and failed to provide accurate fat fractions, this is likely due to the fact that a large number of variables are fit to few data points. The ISMRM toolbox has the benefit of fitting firstly for the field map, then T2* and finally the fat and water fractions which can overcome the instabilities in a single fitting algorithm. It also makes use of both the magnitude and complex data. The T2* measure-

6. Fat Quantification using Multi-Echo MRI in Non Standard Situations

ments from in-house common $T2^*$ fitting and mDixon Quant match well (≈ 2 ms discrepancy except in the case of high fat). In the subcutaneous fat where the fat fraction is much higher, the in-house fitting produced a slightly lower fat fraction and much shorter $T2^*$ than that given by mDixon Quant (18 ms compared to 100 ms). The subcutaneous fat is known to have a $T2$ of 68 ms and the $T2^*$ would be shorter than this (49). A crude estimate of $T2^*$ was measured by fitting an exponential decay to the subcutaneous fat showing the $T2^*$ to be around 13 ms. From this we can conclude that it is unlikely that mDixon Quant is producing accurate $T2^*$ measures in the subcutaneous fat. This may be due to the fact that mDixon Quant was developed for liver fat quantification rather than whole body fat quantification where the $T2^*$ and fat fraction are more variable. Despite the need for $T2^*$ inclusion in the fitting algorithm the echo times that are used here and throughout the literature may not be long enough to provide accurate estimates of $T2^*$.

At 7T the in-house simulations showed that using a combination of fitting with a common $T2^*$ followed by fitting with separate $T2^*$ s provides the most accurate results. *In vivo* in-house fitting at 7T has been shown to produce reasonable fat quantification maps. The accuracy of these maps cannot be confirmed using mDixon Quant at 7T as it is not available on the 7T and the three point Dixon performs poorly due to the field inhomogeneities. As mDixon Quant is unlikely to become available on the 7T due to the fact that body imaging is not widely available on Philips' 7T systems, the in-house method and the ISMRM toolbox are the only fat quantification tools available. The toolbox however is not optimised for use at 7T and the fat maps produced using the magnitude data in the toolbox consistently showed an over estimation of the fat fraction in the liver. The comparison of fat fractions measured using in-house fitting at 3T and 7T and mDixon Quant at 3T show similar fat fractions in the liver ($<5\%$ difference). In the subcutaneous fat large differences in the fat fraction were measured (e.g. 93% fat measured using mDixon Quant at 3T and 2.7% measured using in-house fitting at 7T and 2.9% using the toolbox) however this is probably due to the inability of magnitude fitting to distinguish

6. Fat Quantification using Multi-Echo MRI in Non Standard Situations

between water and fat using only magnitude data (i.e. the fat and water in this case have been swapped). To overcome this a mask of fat obtained from Dixon imaging could be used to inform the algorithm whether a given voxel contains fat and therefore the fat percentage should be switched if it is given as $<50\%$.

In the colon simulations showed that fitting using the complex data provided results where the fat and water were sometimes switched (probably due to large field inhomogeneities and the fitting algorithm finding local minima). Determining whether fat and water have been switched would be difficult in the colon as it is not always clear on Dixon images whether fat is present due to the short $T2^*$. Magnitude fitting did provide reliable results (probably due to the fact that the equation for the magnitude signal does not include a term for the field inhomogeneities, see section 6.3.1). At fat fractions less than 60%, when using in-phase opposed-phase imaging the magnitude fit with a common $T2^*$ for fat and water performed the best ($\approx 50\%$ error on the fitted fat fraction). Therefore *in vivo* fat quantification should be performed using the magnitude data assuming a common $T2^*$ for fat and water. Whilst the quantification was not as accurate as those performed for lower field inhomogeneities the results were still precise.

The four fitting methods used on the *in vivo* all produced significantly different fat fractions. The differences are likely due to the different limitations of each method. The mDixon quant only used two echoes which is known to give errors in the presence of field inhomogeneities and $T2^*$ decay. The toolbox is limited to a single $T2^*$ and smooths out field inhomogeneities which are likely to be large but localised to areas of gas in the colon. Finally, the in-house data has a large number of parameters that are fitted to relatively few data points. Therefore none of the methods used are likely to provide accurate fat quantification in the colon.

Fat quantification using Dixon imaging uses an underdetermined model, whilst sophisticated methods of using the 6 echo data may provide better results of fat quantification than the method employed here, the model still remains underdetermined (mDixon Quant however we are not aware as to whether it may

use additional information such as fat segmentation to improve the fat quantification). Several solutions to the underdetermined model could in the future be considered. One avenue to explore is the effect of fixing the $T2^*$ of fat in the fitting algorithm to reduce the number of parameters that are fitted for, however it is currently unknown how much the $T2^*$ fat varies throughout the abdomen and how much it varies between subjects. A second possibility is the use of fat/water segmentation as a method of indicating which voxels contain fat or water in the magnitude fitting could be used to allow accurate fat quantification above 50%. Outside of the liver the fat spectrum used needs to be given more consideration. The currently used spectrum is based on fat in the liver which is unlikely to be applicable to all types of fat within the abdomen. Spectroscopy could be used to sample the fat giving a more accurate spectra and $T2^*$ values of the fat peaks present. Whilst this method would require extra scan acquisitions it could provide a much more accurate model of the fat being measured. These techniques all have the potential to improve the accuracy, precision and speed of the fitting performed here and will be explored in future work. These methods could all be included into the ISMRM toolbox code which has the benefit of using iterative fitting methods and sophisticated minimisation algorithms which can process data at much faster speeds than the currently used in-house methods and produce more robust results. The toolbox could be optimised for use at 7T and modified to allow different fat spectra and the inclusion of separate $T2^*$ s.

6.6 Conclusion

In this section it has been shown that fat quantification at 3T and 7T has a variable accuracy which is dependent on the *in vivo* conditions and the fit used. However, the first steps have been made to quantify fat at 3T in the colon which is likely to be the most difficult area in the abdomen to quantify fat. The first 7T fat quantification maps using human participants have also been acquired. Whilst the work presented here is preliminary it provides a foundation for quantification which should in future allow for malabsorption of fat to be

studied as well as high field fat quantification maps to be produced. As *in vivo* fat quantification is becoming a common biomarker for disease it is likely that vendors will continue to produce more and more sophisticated fat quantification methods that out perform the methods presented here. However it has been shown in this section that fitting for a common $T2^*$ reduces the accuracy of the fat quantification when fat and water have different $T2^*$ values except in the case of the colon where local field inhomogeneities are large and the $T2^*$ is very short. Fitting for separate $T2^*$ values is not currently an option on most vendor products and therefore in-house fitting may provide more accurate results under these circumstances. Further to this in-house fitting is likely to be the only reliable method of fat quantification at 7T due to the absence of body imaging as a product offered the scanner vendor. At 7T the use of a short ΔTE is limited due to acoustic noise limitations and gradient capabilities. In future these could be overcome by using two acquisitions with interleaved echo times. In the future in-house fitting will make use of the code provided as part of the ISMRM toolbox. Optimisation of the toolbox will need to be performed in areas outside its intended purpose of liver fat quantification at 1.5T and 3T.

References

- [1] B Wildman-Tobriner, M M Middleton, C A Moylan, S Rossi, Flores, Z A Chang, M F Abdelmalek, C B Sirlin, and M R Bashir. Association Between Magnetic Resonance Imaging–Proton Density Fat Fraction and Liver Histology Features in Patients With Nonalcoholic Fatty Liver Disease or Nonalcoholic Steatohepatitis. *Gastroenterology*, 155(5):1428–1435.e2, nov 2018. ISSN 00165085. doi: 10.1053/j.gastro.2018.07.018.
- [2] C D G Hines, A Frydrychowicz, G Hamilton, D L Tudorascu, K K Vigen, H Yu, C A McKenzie, C B Sirlin, J H Brittain, and S B Reeder. T1 Independent, $T2^*$ Corrected Chemical Shift Based Fat-Water Separation with Multi-Peak Fat Spectral Modeling is an Accurate and Precise Measure

- of Hepatic Steatosis. *Journal of Magnetic Resonance Imaging*, 33(4):873–881, apr 2011. ISSN 10531807. doi: 10.1002/jmri.22514.
- [3] T Yokoo, S D Serai, A Pirasteh, M R Bashir, G Hamilton, D Hernando, H H Hu, H Hetterich, J P Kühn, G M Kukuk, R Loomba, M S Middleton, N A Obuchowski, J S Song, A Tang, X Wu, S B Reeder, C B Sirlin, and RSNA-QIBA PDFF Biomarker Committee. Linearity, Bias, and Precision of Hepatic Proton Density Fat Fraction Measurements by using MR Imaging: A Meta-Analysis. *Radiology*, 286(2):486–498, feb 2018. ISSN 0033-8419. doi: 10.1148/radiol.2017170550.
- [4] B D Pooler, D Hernando, J A Ruby, H Ishii, A Shimakawa, and S B Reeder. Validation of a Motion-Robust 2D Sequential Technique for Quantification of Hepatic Proton Density Fat Fraction During Free Breathing. *Journal of Magnetic Resonance Imaging*, 48(6):1578–1585, dec 2018. ISSN 10531807. doi: 10.1002/jmri.26056.
- [5] C A Campo, D Hernando, T Schubert, C A Bookwalter, A J V Pay, and S B Reeder. Standardized Approach for ROI-Based Measurements of Proton Density Fat Fraction and R2* in the Liver. *American Journal of Roentgenology*, 209(3):592–603, sep 2017. ISSN 0361-803X. doi: 10.2214/AJR.17.17812.
- [6] A Grimm, H Meyer, M D Nickel, M Nittka, E Raithel, O Chaudry, A Friedberger, M Uder, W Kemmler, K Engelke, and H H Quick. Repeatability of Dixon Magnetic Resonance Imaging and Magnetic Resonance Spectroscopy for Quantitative Muscle Fat Assessments in the Thigh. *Journal of Cachexia, Sarcopenia and Muscle*, 9(6):1093–1100, dec 2018. ISSN 21905991. doi: 10.1002/jcsm.12343.
- [7] G H Kang, I Cruite, M Shiehorteza, T Wolfson, A C Gamst, G Hamilton, M Bydder, M S Middleton, and C B Sirlin. Reproducibility of MRI-Determined Proton Density Fat Fraction Across Two Different MR Scanner

References

- Platforms. *Journal of Magnetic Resonance Imaging*, 34(4):928–934, oct 2011. ISSN 10531807. doi: 10.1002/jmri.22701.
- [8] I S Idilman, H Aniktar, R Idilman, G Kabacam, B Savas, A Elhan, A Celik, K Bahar, and M Karcaaltincaba. Hepatic Steatosis: Quantification by Proton Density Fat Fraction with MR Imaging Versus Liver Biopsy 1. *Radiology*, 267. doi: 10.1148/radiol.13121360.
- [9] C L Hoad, L Marciani, P Kaye, I N Guha, C Costigan, A Austin, R C Spiller, M W James, P A Gowland, S Francis, and G P Aithal. Quantitative Magnetic Resonance Imaging (MRI) in the Evaluation of the Degree of Steatosis, Iron Accumulation and Fibrosis in Chronic Liver Diseases (MRKER STUDY). *Gut*, 60(Suppl 1):A55–A56, apr 2011. ISSN 0017-5749. doi: 10.1136/gut.2011.239301.110.
- [10] P J Pickhardt, P M Graffy, S B Reeder, D Hernando, and K Li. Quantification of Liver Fat Content With Unenhanced MDCT: Phantom and Clinical Correlation With MRI Proton Density Fat Fraction. *American Journal of Roentgenology*, 211(3):W151–W157, sep 2018. ISSN 0361-803X. doi: 10.2214/AJR.17.19391.
- [11] T Hayashi, S Saitoh, J Takahashi, Y Tsuji, K Ikeda, M Kobayashi, Y Kawamura, T Fujii, M Inoue, T Miyati, and H Kumada. Hepatic Fat Quantification Using the Two-Point Dixon Method and Fat Color Maps Based on Non-Alcoholic Fatty Liver Disease Activity Score. *Hepatology Research*, 47(5):455–464, apr 2017. ISSN 13866346. doi: 10.1111/hepr.12767.
- [12] M A Fischer, D A Raptis, M Montani, R Graf, P-A Clavien, D Nanz, H Alkadhi, and H Scheffel. Liver Fat Quantification by Dual-echo MR Imaging Outperforms Traditional Histopathological Analysis. *Academic Radiology*, 19(10):1208–1214, oct 2012. ISSN 10766332. doi: 10.1016/j.acra.2012.05.009.
- [13] C D G Hines, H Yu, A Shimakawa, C A McKenzie, J H Brittain, and S B Reeder. T1 Independent, T2* Corrected MRI with Accurate Spectral Mod-

References

- eling for Quantification of Fat: Validation in a Fat-Water-SPIO Phantom. *Journal of Magnetic Resonance Imaging*, 30(5):1215–1222, nov 2009. ISSN 10531807. doi: 10.1002/jmri.21957.
- [14] H-J Chiang, L-H Lin, C-W Li, C-C Lin, H-W Chiang, T-L Huang, C-L Chen, and Y-F Cheng. Magnetic Resonance Fat Quantification in Living Donor Liver Transplantation. *Transplantation Proceedings*, 46(3):666–668, apr 2014. ISSN 00411345. doi: 10.1016/j.transproceed.2013.11.050.
- [15] A A K A Razek, A Abdalla, T Barakat, H El-Taher, and K Ali. Multi-Parametric MR Imaging using Apparent Diffusion Coefficient and Fat Fraction in Quantification of Bone Marrow in Pediatrics with Gaucher Disease. *Clinical Imaging*, 51:318–322, sep 2018. ISSN 08997071. doi: 10.1016/j.clinimag.2018.06.011.
- [16] ISMRM Fat-Water Toolbox. In *ISMRM Fat-Water Separation Workshop*, ISMRMTOOLBOX, 2012. URL <http://www.ismrm.org/workshops/FatWater12/>.
- [17] J Dorsey, D Buckley, S Summer, R J Jandacek, T Rider, P Tso, M R Narkewicz, and J E Heubi. Fat Malabsorption in Cystic Fibrosis: Comparison of Quantitative Fat Assay and a Novel Assay using Fecal Lauric/Behenic Acid. *Journal of pediatric gastroenterology and nutrition*, 50(4):441–6, apr 2010. ISSN 1536-4801. doi: 10.1097/MPG.0b013e3181b18308.
- [18] G Hamilton, T Yokoo, M Bydder, I Cruite, M E Schroeder, C B Sirlin, and M S Middleton. In Vivo Characterization of the Liver Fat ^1H MR Spectrum. *NMR in biomedicine*, 24(7):784–90, aug 2011. ISSN 1099-1492. doi: 10.1002/nbm.1622.
- [19] W T Dixon. Simple Proton Spectroscopic Imaging. *Radiology*, 153(1):189–194, oct 1984. ISSN 0033-8419. doi: 10.1148/radiology.153.1.6089263.
- [20] J Kühn, D Hernando, Al Muñoz del Rio, M Evert, S Kannengiesser, H Völzke, B Mensel, R Puls, N Hosten, and S B. Reeder. Effect of Multi-

- peak Spectral Modeling of Fat for Liver Iron and Fat Quantification: Correlation of Biopsy with MR Imaging Results. *Radiology*, 265(1):133–142, oct 2012. ISSN 0033-8419. doi: 10.1148/radiol.12112520.
- [21] X Zhong, M D Nickel, S A R Kannengiesser, B M Dale, B Kiefer, and M R Bashir. Liver Fat Quantification using a Multi-Step Adaptive Fitting Approach With Multi-Echo GRE Imaging. *Magnetic Resonance in Medicine*, 72(5):1353–1365, nov 2014. ISSN 07403194. doi: 10.1002/mrm.25054.
- [22] P Sharma, M Altbach, Jean P Galons, B Kalb, and D R Martin. Measurement of Liver Fat Fraction and Iron with MRI and MR Spectroscopy Techniques. *Diagnostic and Interventional Radiology*, 20(1):17–26, sep 2013. ISSN 13053825. doi: 10.5152/dir.2013.13124.
- [23] M Bydder, T Yokoo, G Hamilton, M S Middleton, A D Chavez, J B Schwimmer, J E Lavine, and C B Sirlin. Relaxation Effects in the Quantification of Fat Using Gradient Echo Imaging. *Magnetic Resonance Imaging*, 26(3):347–359, 2008. ISSN 0730725X. doi: 10.1016/j.mri.2007.08.012.
- [24] D E Horng, D Hernando, C D G Hines, and S B Reeder. Comparison of $R2^*$ Correction Methods for Accurate Fat Quantification in Fatty Liver. *Journal of Magnetic Resonance Imaging*, 37(2):414–422, feb 2013. ISSN 10531807. doi: 10.1002/jmri.23835.
- [25] H Yu, C A McKenzie, A Shimakawa, A T Vu, A C S Brau, P J Beatty, A R Pineda, J H Brittain, and S B Reeder. Multiecho Reconstruction for Simultaneous Water-Fat Decomposition and $T2^*$ Estimation. *Journal of Magnetic Resonance Imaging*, 26(4):1153–1161, oct 2007. ISSN 10531807. doi: 10.1002/jmri.21090.
- [26] S B Reeder, E K Bice, H Yu, D Hernando, and A R Pineda. On the Performance of $T2^*$ Correction Methods for Quantification of Hepatic Fat Content. *Magnetic Resonance in Medicine*, 67(2):389–404, feb 2012. ISSN 07403194. doi: 10.1002/mrm.23016.

- [27] V V Chebrolu, C D G Hines, H Yu, A R Pineda, A Shimakawa, C A McKenzie, A Samsonov, J H Brittain, and S B Reeder. Independent Estimation of T2* for Water and Fat for Improved Accuracy of Fat Quantification. *Magnetic resonance in medicine*, 63(4):849–57, apr 2010. ISSN 1522-2594. doi: 10.1002/mrm.22300.
- [28] M Bydder, T Yokoo, G Hamilton, M S Middleton, A D Chavez, J B Schwimmer, J E Lavine, and C B Sirlin. Relaxation Effects in the Quantification of Fat Using Gradient Echo Imaging. *Magnetic Resonance Imaging*, 26(3): 347–359, apr 2008. ISSN 0730725X. doi: 10.1016/j.mri.2007.08.012.
- [29] J Deng, M H Fishbein, C K Rigsby, G Zhang, S E Schoeneman, and J S Donaldson. Quantitative MRI for Hepatic Fat Fraction and T2* Measurement in Pediatric Patients with Non-Alcoholic Fatty Liver Disease. *Pediatric Radiology*, 44(11):1379–1387, nov 2014. ISSN 0301-0449. doi: 10.1007/s00247-014-3024-y.
- [30] D Hernando, J H Kramer, and S B Reeder. Multipeak Fat-Corrected Complex R2* Relaxometry: Theory, Optimization, and Clinical Validation. *Magnetic Resonance in Medicine*, 70(5):1319–1331, nov 2013. ISSN 07403194. doi: 10.1002/mrm.24593.
- [31] C Mahlke, D Hernando, C Jahn, A Cigliano, T Ittermann, A Mössler, M Kromrey, G Domaska, S Reeder, and J Kühn. Quantification of liver proton-density fat fraction in 7.1T preclinical MR systems: Impact of the fitting technique. *Journal of magnetic resonance imaging : JMRI*, 44(6): 1425–1431, 2016. ISSN 1522-2586. doi: 10.1002/jmri.25319.
- [32] H Yu, S B Reeder, A Shimakawa, J H Brittain, and N J Pelc. Field map estimation with a region growing scheme for iterative 3-point water-fat decomposition. *Magnetic Resonance in Medicine*, 54(4):1032–1039, 2005. ISSN 07403194. doi: 10.1002/mrm.20654.
- [33] D Hernando, P Kellman, J P Haldar, and Z-P Liang. Robust Water/Fat Separation in the Presence of Large Field Inhomogeneities using a Graph

- Cut Algorithm. *Magnetic Resonance in Medicine*, 63(1):NA–NA, jan 2009. ISSN 07403194. doi: 10.1002/mrm.22177.
- [34] N S Artz, W M Haufe, C A Hooker, G Hamilton, T Wolfson, G M Campos, A C Gamst, J B Schwimmer, C B Sirlin, and S B Reeder. Reproducibility of MR-based liver fat Quantification Across Field Strength: Same-Day Comparison Between 1.5T and 3T in Obese Subjects. *Journal of Magnetic Resonance Imaging*, 42(3):811–817, sep 2015. ISSN 10531807. doi: 10.1002/jmri.24842.
- [35] N S Sakai, S A Taylor, and M D Chouhan. Obesity, Metabolic Disease and the Pancreas - Quantitative Imaging of Pancreatic Fat. *The British Journal of Radiology*, page 20180267, jun 2018. ISSN 0007-1285. doi: 10.1259/bjr.20180267.
- [36] C Caussy, S B Reeder, C B Sirlin, and R Loomba. Noninvasive, Quantitative Assessment of Liver Fat by MRI-PDFP as an Endpoint in NASH Trials. *Hepatology*, 68(2):763–772, aug 2018. ISSN 02709139. doi: 10.1002/hep.29797.
- [37] D E Horng, D Hernando, C D G Hines, and S B Reeder. Comparison of R2* Correction Methods for Accurate Fat Quantification in Fatty Liver. *Journal of Magnetic Resonance Imaging*, 37(2):414–422, feb 2013. ISSN 10531807. doi: 10.1002/jmri.23835.
- [38] S B Reeder, A R Pineda, Z Wen, A Shimakawa, H Yu, J H Brittain, G E Gold, C H Beaulieu, and N J Pelc. Iterative Decomposition of Water and Fat with Echo Asymmetry and Least-Squares Estimation (IDEAL): Application with Fast Spin-Echo Imaging. *Magnetic Resonance in Medicine*, 54(3): 636–644, sep 2005. ISSN 0740-3194. doi: 10.1002/mrm.20624.
- [39] G Corrias, S Krebs, S Eskreis-Winkler, D Ryan, J Zheng, M Capanu, L Saba, S Monti, M Fung, S Reeder, and L Mannelli. MRI Liver Fat Quantification

- in an Oncologic Population: the Added Value of Complex Chemical Shift-Encoded MRI. *Clinical Imaging*, 52:193–199, nov 2018. ISSN 08997071. doi: 10.1016/j.clinimag.2018.08.002.
- [40] S Eskreis-Winkler, G Corrias, S Monti, J Zheng, M Capanu, S Krebs, M Fung, S Reeder, and L Mannelli. IDEAL-IQ in an Oncologic Population: Meeting the Challenge of Concomitant Liver Fat and Liver Iron. *Cancer Imaging*, 18(1):51, dec 2018. ISSN 1470-7330. doi: 10.1186/s40644-018-0167-3.
- [41] D Hernando, J P Haldar, B P Sutton, J Ma, P Kellman, and Z.-P Liang. Joint Estimation of Water/Fat Images and Field Inhomogeneity Map. *Magnetic Resonance in Medicine*, 59(3):571–580, mar 2008. ISSN 07403194. doi: 10.1002/mrm.21522.
- [42] M Cencini, L Biagi, J D Kaggie, R F Schulte, M Tosetti, and G Buonincontri. Magnetic Resonance Fingerprinting with Dictionary-Based Fat and Water Separation (DBFW MRF): A Multi-Component Approach. *Magnetic Resonance in Medicine*, dec 2018. ISSN 07403194. doi: 10.1002/mrm.27628.
- [43] R Konnek, E Korbinian, Z Starcuk, S Trattinig, and M Krssak. *Feasibility of Abdominal Quantitative Imaging at 7T: Pilot Study*. Montreal, 2019.
- [44] C Hutton, M L Gyngell, M Milanese, A Bagur, and M Brady. Validation of a Standardized MRI Method for Liver Fat and T2* Quantification. *PLOS ONE*, 13(9):e0204175, sep 2018. ISSN 1932-6203. doi: 10.1371/journal.pone.0204175.
- [45] S Reeder, C Hines, H Yu, C McKenzie, and J Brittain. On The Definition of Fat-Fraction for In Vivo Fat Quantification with Magnetic Resonance Imaging. *Proceedings 17th Scientific Meeting, International Society for Magnetic Resonance in Medicine*, Honolulu:211, 2009.

- [46] D P O'regan, M F Callaghan, M Wylezinska-Arridge, J Fitzpatrick, R P Naoumova, J V Hajnal, and S A Schmitz. Liver Fat Content and T2*: Simultaneous Measurement by using Breath-hold Multiecho MR Imaging at 3.0 T-Feasibility 1 Grants from Bayer Schering Pharma and Philips Medical Systems. *Radiology*, 247(2), 2008. doi: 10.1148/radiol.2472070880.
- [47] E Doran, S Bawden, S Francis, R Bowtell, and P Gowland. T1 and T2* Measurements in the Liver and Kidneys at 3 and 7 Tesla. In *BCISMRM Post Graduate symposium*, page 46, 2018.
- [48] S Wang, F Zheng, and L Xu. Comparison Between Particle Swarm Optimization and Genetic Algorithm in Artificial Neural Network for Life Prediction of Nc Tools. *Journal of Advanced Manufacturing Systems*, 07(01): 1–7, 2008. ISSN 0219-6867. doi: 10.1142/s0219686708001073.
- [49] Cedric M. J. de Bazelaire, Guillaume D. Duhamel, Neil M. Rofsky, and David C. Alsop. MR Imaging Relaxation Times of Abdominal and Pelvic Tissues Measured in Vivo at 3.0 T: Preliminary Results. *Radiology*, 230(3): 652–659, mar 2004. ISSN 0033-8419. doi: 10.1148/radiol.2303021331. URL <http://pubs.rsna.org/doi/10.1148/radiol.2303021331>.

7 Conclusions

The work presented throughout this thesis has shown that quantitative measurements in the gastrointestinal tract and abdomen are possible using non-invasive MRI. These findings will aid in the development of non-invasive tools to diagnose and monitor gastrointestinal diseases without the use of invasive procedures such as endoscopies, colonoscopies and biopsies.

The experimental work presented in Chapter 4 demonstrated that quantitative measures of the abdominal lymph nodes in healthy volunteers and patients without cancer are possible without the need of a contrast agent. The diffusion imaging techniques have been optimised allowing for the visualisation of nodes in healthy volunteer which has not previously been performed. Further to this it was shown that the measures made using diffusion weighted imaging are sensitive enough to show differences in the lymph nodes between healthy volunteers and patient groups with different gastrointestinal diseases. The patient study was the first to compare both patients and healthy volunteers in order to evaluate the potential of abdominal lymph nodes to be used as a non-invasive biomarker. The main limitation of the results presented in this chapter is the small number of patients recruited. Future work will aim to recruit a larger number of patients for a more robust analysis of the differences in lymph nodes between healthy volunteers and patients with inflammatory gastrointestinal diseases.

Chapter 5 described the first quantitative T1 and T2 measures of the healthy bowel wall. Whilst the T1 results could not be fully evaluated due to the sub-optimal inversion times used they did provide a basis for determining an optimal set of inversion times for future studies. The T2 results showed that small changes in the permeability of the bowel wall can be measured indirectly by T2. The T2 of the small bowel wall was found to correlate well with the current standard of measuring bowel permeability, the LMR test. The inter observer reproducibility was also evaluated and was found to produce no significant difference between observers. The intra subject reproducibility also showed no difference except in the case where the imaging slice was not consistent between

the two scans. Due to the fact that the imaging performed was single slice, the permeability of the whole bowel could not be evaluated. This inherently limits the use of T2 as changes in permeability that occur over a small spatial location may be missed if the slice is not placed in the correct imaging plane. Future work aims to extend the T2 measurements to multi slice imaging. Perhaps most importantly in Chapter 5 the method to analyse the data was carried out using an automated tool that was developed to require a minimal amount of user input. The tool greatly increases the ease of using T2 as a biomarker in the future due to the minimal amount of user input required to generate the results. This work in this chapter is currently being used to file a patent application for the use of T2 as a marker of permeability.

Finally in Chapter 6 the currently used *in vivo* methods of quantifying abdominal fat were tested to verify whether the assumptions made in the current methods are suitable for fat quantification both in and outside the liver at 3T and 7T. It was found that at 3T the assumptions made by vendor products that perform fat quantification are justified. However, if the conditions in the liver differed significantly from a healthy liver, such as large differences in the $R2^*$ of fat and water or there were large field inhomogeneities, then the vendor products may not produce accurate results. At 7T the only available vendor product, mDixon, was shown to perform poorly in the liver making in-house fat quantification necessary. The ISMRM fat toolbox was found at 7T to greatly over estimate the fat percentage in the liver which was likely due to the fact that the toolbox is optimised to work at 1.5T and 3T and only allows for a single $T2^*$ to be used for fat and water. Optimisation of the toolbox for use at 7T is likely to provide the best over all method for quantifying fat at 7T. In Chapter 6 the first *in vivo* fat quantification in the colon was also performed using in-house fitting on cystic fibrosis patients with fat malabsorption. Simulations showed that field inhomogeneities due to gas in the colon will mean that the fat quantification is less accurate than that performed in the liver when using vendor products. The preliminary *in vivo* results showed the current fitting methods all produce significantly different fat maps. This is likely due to the individual limitations

of each fitting method. Again optimisation of the ISMRM toolbox for use in areas with localised but high field inhomogeneities such as those found around gas bubbles in the colon is likely to produce the best over all method for fat quantification in the colon. The ISMRM toolbox provides a good starting base of code to fit for fat in non standard situations. It is computationally much faster than the in-house fitting method and therefore is much more applicable for use on large data sets. Adaption of the toolbox is possible and so could be used in the future for optimised fat quantification in non standard situations.

7.1 Future Work

The follow up work from this thesis would be to firstly complete the data collection for the lymph node patient study and to evaluate the best method to compare the nodes between the patient groups and the healthy volunteers. A more robust method of ROI drawing will also be investigated to reduce the inter observer variation. Further to this the imaging used to collect the information on lymph nodes will be further optimised to attempt to gain higher resolution and thinner imaging slices to reduce partial volume effects on the diffusion measurements. A reduction in the scan time will also try to be achieved in order to allow the imaging of lymph nodes to be added onto other studies in which the involvement of lymph nodes in disease progression is of interest. Second to this a study will be performed to look at whether fat uptake in the abdominal lymph nodes can be measured using the results presented in this thesis. The interest in the fat uptake has stemmed from a research group who attach cancer fighting drugs to lipids which are then delivered to the body through the abdominal lymph nodes. If visualisation of the uptake of the fat is possible then the group would be able to determine whether abdominal nodes containing cancer cells could be targeted by this method of drug delivery.

The T1 and T2 of the bowel wall has many possible applications. The analysis method developed here will allow for bowel walls which are healthy in appearance to be studied, not just the inflamed wall that is usually the focus in Crohn's studies. The methods presented here are currently being used in a

7. Conclusions

study which monitors the progress of Crohn's disease from base line and for a year after treatment. A second application of the analysis tool is to allow research in diseases which are suspected to have gut involvement but which are not defined as gastrointestinal diseases. Ankylosing Spondylitis (AS) is one such example which is a type of arthritis. It is currently believed that the gut may be a gateway for pathogens which may cause or worsen the disease. Having a non-invasive tool to study the involvement of the gastrointestinal system in non-GI disease may provide further insight into diseases such as AS. The T1 and T2 imaging methods will also be developed to allow for multi slice or 3D imaging. This development should allow for the full length of the bowel to be evaluated which would enable the variation in the whole bowel to be investigated in a single scanning session rather than using single slice imaging which has limited the investigation of changes in the bowel to small section. The use of machine learning to remove any misidentifications in the bowel wall mask will also be explored as this could enable the analysis to become fully automated, making its use in a clinical setting much more likely.

Finally for the fat quantification work the follow up from this thesis will be to optimise the ISMRM toolbox for use outside the liver and at 7T. In order to do this the possibility of creating a new fat phantom which better resembles the *in vivo* conditions will be considered. Such a phantom would allow for more robust comparisons of different fat quantification techniques in a controlled environment. Once optimised the full cystic fibrosis data set will be analysed to determine whether MRI has the capability to measure fat malabsorption non-invasively. Different methods of fitting for the fat quantification also need to be explored such as fixing the $T2^*$ of fat and using accurate fat spectra for the different anatomical locations. Further to this, patient studies are currently underway to compare the differences in fat quantification in patients with liver cirrhosis at 7T using MRI and MRS.